

**PATTERN-INTEGRATED INTERFERENCE LITHOGRAPHY
FOR TWO-DIMENSIONAL AND THREE-DIMENSIONAL
PERIODIC-LATTICE-BASED MICROSTRUCTURES**

A Thesis
Presented to
The Academic Faculty

By

Matthieu C. R. Leibovici

In Partial Fulfillment
Of the Requirements for the Degree
Doctor of Philosophy in Electrical and Computer Engineering

Georgia Institute of Technology
December 2015

Copyright © Matthieu C. R. Leibovici 2015

PATTERN-INTEGRATED INTERFERENCE LITHOGRAPHY
FOR TWO-DIMENSIONAL AND THREE-DIMENSIONAL
PERIODIC-LATTICE-BASED MICROSTRUCTURES

Approved by:

Professor Thomas K. Gaylord, Advisor
School of Electrical and Computer
Engineering
Georgia Institute of Technology

Professor Phillip N. First
School of Physics
Georgia Institute of Technology

Professor Bernard Kippelen
School of Electrical and Computer
Engineering
Georgia Institute of Technology

Professor Donald D. Davis
School of Electrical and Computer
Engineering
Georgia Institute of Technology

Professor Oliver Brand
School of Electrical and Computer
Engineering
Georgia Institute of Technology

Date Approved: November 6, 2015

A mes parents, Christine et Gérald

ACKNOWLEDGEMENTS

First and foremost, it has been a true privilege to work under the guidance of Professor Thomas K. Gaylord. His constant, unswerving positive attitude has always kept me optimistic. In both his private and professional life, he is a true gentleman and a role model. He will always be a source of inspiration in my future career and personal life.

I would like to extend my sincere thanks to my thesis committee members: Professor Bernard Kippelen, Professor Oliver Brand, Professor Phillip N. First, Professor Donald D. Davis, Dr. Justin L. Stay, and Dr. Sorin Tibuleac for their advice and for making the time within their busy schedules to participate.

I am deeply indebted to past and present members of the Georgia Tech Optics Laboratory: Dr. Chien-I Lin, Dr. Michael Hutsel, Dr. Jonathan Maikisch, Dr. Matt Burrow, Dr. Micah Jenkins, Donald Sedivy, Marc Beudet, Sylvain Lelievre, Joe Kummer, Shruthi Vadivel, Raymond Wong, and Congshan Wan. Thank you for your helpful contributions, the hours spent on reviewing manuscripts and refining oral presentations, the insightful Friday lunches, and the Pi-mile races.

I would like to thank Gary Spinner, Todd Walters, Eric Woods, Mikkel Thomas, and Hang Chen from the Institute for Electronics and Nanotechnology for their help and guidance in the cleanrooms. Thanks also to Marion Crowder from the ECE Digital Media Lab for video-taping my TI:GER presentation and my PhD defense.

I am also grateful to my TI:GER teammates as well as Margi Berbari and Professor Mary Thursby. Thanks to them, I gained new perspectives on my research and developed my entrepreneurial spirit.

Special thanks should go to all my friends in Atlanta and France. They have kept me level-headed and supported me outside (and even sometimes inside) the classrooms and the cleanrooms. I wish I could list all their names. Yet, I know they will recognize

themselves in these words. Thank you et merci!

Cette thèse n'aurait également pas pu être possible sans ma famille. Ma mère Christine et mon père Gérald ont été d'indéfectibles soutiens et de constantes sources d'encouragements tout au long de ma vie. Ils ont toujours été présents pour me guider et me soutenir dans mes choix. Ils m'ont également enseigné rigueur, méticulosité, et goût du travail bien fait. Papa, Maman, je vous aime, merci pour vos sacrifices et tout ce que vous m'avez appris.

Mon enfance aurait également été bien triste sans ma sœur Margot et mon frère Charles. Ils ont été sources d'inspiration et de courage durant ma thèse. Je remercie également toute ma famille à Paris et en province, ainsi que la famille Fabien/Hamel. Leur amour et encouragements ont rechargé mes batteries à chacun de mes retours en France. J'ai finalement une pensée pour ma grand-mère avec qui j'aurais aimé partager cette aventure.

Je garde enfin mes derniers remerciements, mais les plus importants, pour Chloé. En Avril 2011, nous décidâmes de nous lancer dans cette aventure. Tu as toujours été là pour moi depuis et finalement, cette thèse c'est aussi un peu la tienne. Alors que tes soucis étaient plus grands que les miens, tu n'as jamais hésité à relire mes papiers, venir me chercher tard sur le campus, ou bien m'emmener bruncher pour oublier les moments difficiles. Il y a eu de nombreux obstacles sur notre route. Mais nous les avons toujours franchis ensemble. Et c'est ensemble que nous franchirons les prochains.

MATTHIEU C. R. LEBOVICI

Georgia Institute of Technology

November 2015

TABLE OF CONTENTS

	Page
ACKNOWLEDGEMENTS	iv
LIST OF TABLES	xi
LIST OF FIGURES	xii
LIST OF ABBREVIATIONS.....	xix
LIST OF SYMBOLS	xxi
SUMMARY	xxvi
CHAPTER 1 INTRODUCTION	1
1.1 Periodic-Lattice-Based Microstructures	1
1.2 Fabrication Techniques for PLB Microstructures	2
1.2.1 Construction-Based Microfabrication Techniques	4
1.2.2 Multi-Beam Interference Lithography	6
1.2.3 Modified MBIL Techniques	9
1.3 Pattern-Integrated Interference Lithography	14
1.4 Research Objectives and Contributions	15
1.5 Thesis Overview	17
CHAPTER 2 THEORY OF PATTERN-INTEGRATED INTERFERENCE LITHOGRAPHY	19
2.1 PIIL Precursors	19
2.1.1 Optical Interference.....	19
2.1.2 Holography	21
2.2 PIIL Concept.....	23

2.3 PIIL Model.....	26
2.3.1 High-NA Optics Considerations	27
2.3.2 Vector Model of High-NA Imaging in Thin Films.....	28
2.3.3 MBIL Model	32
2.4 Time-Dependent Exposure Simulations	34
2.5 Summary.....	37
CHAPTER 3 PATTERN-INTEGRATED INTERFERENCE LITHOGRAPHY FOR TWO-DIMENSIONAL PERIODIC-LATTICE-BASED MICROSTRUCTURES.....	40
3.1 Photonic-Crystal Devices Design and Simulation Parameters	40
3.2 Photomask Improvement	45
3.3 Simulated PIIL Exposures and Estimated Fabrication	49
3.4 Photonic-Crystal Device Performance.....	54
3.5 Summary.....	57
CHAPTER 4 PATTERN-INTEGRATED INTERFERENCE LITHOGRAPHY FOR THREE-DIMENSIONAL PERIODIC-LATTICE-BASED MICROSTRUCTURES.....	58
4.1 Beam Configurations for 3D-PIIL.....	58
4.2 3D-PIIL Exposure Simulation Parameters	63
4.3 Simulated 3D-PIIL Exposures	65
4.3.1 Photomask-Integrated 3D Periodic Microstructure	65
4.3.2 Photomask-Shaped 3D Periodic Microstructure.....	70
4.3.3 Microcavity Integrated at the Top of a 3D Periodic Structure.....	72
4.3.4 Microcavity-Integrated 3D Periodic Microstructure.....	74
4.4 Summary.....	76

CHAPTER 5 PATTERN-INTEGRATED INTERFERENCE EXPOSURE SYSTEM DESIGN AND ANALYSIS	78
5.1 PIIES Implementation.....	78
5.2 Interference Pattern Formation Capability	81
5.2.1 Range of Feasible Angles of Incidence.....	81
5.2.2 Range of Feasible Interference Periods	83
5.2.3 Interference Pattern Sensitivity to Beam Misalignment	87
5.3 Photomask Imaging with the Prototype PIIES	92
5.3.1 COL Imaging Performance with Perfectly Aligned Lenses	93
5.3.2 Imaging Performance with Decentered or Tilted Lenses.....	95
5.3.3 Exposure Field Distortions	98
5.3.4 Image Shifting with Beam Tilting	102
5.4 Summary	104
CHAPTER 6 PIIL EXPERIMENTAL DEMONSTRATION	107
6.1 Experimental Procedure.....	107
6.1.1 PIIES Alignment Procedure.....	107
6.1.2 Photomask Design	111
6.1.3 Sample Processing	114
6.1.4 Sample Focusing Procedure.....	114
6.2 Experimental results	116
6.2.1 Integration of Double-Period-Blocking Photomask Patterns within a Square-Lattice Periodic Microstructure	116
6.2.2 Integration of Single-Period-Blocking Photomask Patterns within a Square-Lattice Periodic Microstructure	121

6.2.3 Integration of Single-Period-Blocking Photomask Patterns within a Hexagonal-Lattice Periodic Microstructure.....	123
6.2.4 Exposure Field Distortions	125
6.3 Summary.....	129
CHAPTER 7 CONCLUSIONS AND FUTURE WORK.....	130
7.1 Conclusions.....	130
7.1.1 PIIL Concept and Modeling.....	130
7.1.2 PIIL Exposure Simulations for 2D PhC Devices.....	132
7.1.3 PIIL Exposure Simulations for 3D Periodic-Lattice-Based Microstructures	133
7.1.4 PIIES Prototyping and Analysis	134
7.1.5 PIIL Experimental Demonstration.....	136
7.2 Future work.....	137
7.2.1 Multiple-Optical-Axis Pattern-Integrated Interference Exposure System.....	137
7.2.2 Partially Coherent Photomask Illumination in PIIL	140
7.2.3 Photomask Optimization.....	141
7.2.4 Photoresist processing improvement	143
7.2.5 3D-PIIL Experimental Demonstration.....	143
7.3 Concluding Remarks.....	144
APPENDIX A FRINGE ZERNIKE POLYNOMIALS AND COEFFICIENTS	146
APPENDIX B MATLAB SCRIPTS	150
B.1 Main script	150
B.2 Mask_Generation_Function.m.....	154
B.3 UnitMask_Generation_Function.m.....	155
B.4 shifted_fourier_transform.m	157

B.5	fourier_transform_5beams.m	158
B.6	stack_matrix_5beams.m	159
	REFERENCES	164
	VITA	179

LIST OF TABLES

	Page
Table 1.1: Comparison of characteristics of fabrication techniques for PLB microstructures. Dashes indicate conditional/limited yes.....	5
Table 2.1: Simulation parameters used for the simulation results of Figure 2.6.	30
Table 3.1: Comparison of transmission spectrum characteristics between the PIIL-produced and idealized PhC devices.....	56
Table 4.1: Field directions of the beams illuminating the photomask.....	60
Table 5.1: Lens parameters of EL, CL, OL1, and OL2 as given in the datasheets.....	82
Table 5.2: Numerical values of d_{beam} and the interference periods for the extreme values $\theta_{beam} = 5deg$ and $\theta_{beam} = 30deg$	85
Table 5.3: Beam parameters for the calculations of e_{Λ} and e_{Θ}	90
Table 5.4: RMS OPD for OL1, OL2, and COL at the design and exposure wavelengths.....	94
Table 5.5: Summary of PIIES capabilities.....	104
Table 5.6: Summary of PIIES sensitivity analysis compared to estimated experimental precision.....	105
Table 6.1: Experimental average lattice periods and lattice vector angles.	120

LIST OF FIGURES

	Page
<p>Figure 1.1: Example PLB microstructures. (a) PhC band edge laser array [38]. (b) Schematic description of PhC biosensors [27]. (c) pH-responsive 3D periodic microstructure for drug delivery [31]. (d) Microfluidic mixer [33]. (e) Microfluidic filter [35]. (f) 2D array of fibronectin domains to study murine osteoblast cells growth. (g) 3D PLB scaffold for cell culture [35]. (h) Lightweight and ultrastiff 3D mechanical metamaterials [36].</p>	3
<p>Figure 1.2: Multi-beam configurations and corresponding MBIL-produced periodic microstructures. (a) One-dimensional grating produced by two-beam interference [73]. (b) 2D PhC produced by three-beam interference [74]. (c) 3D periodic lattice produced by four-beam interference [75]. The lattice constant depends on the common beam incidence angle, θ_{beam}.</p>	8
<p>Figure 1.3: Example PLB microstructures produced by extrinsically-modified MBIL techniques, where MBIL is combined with (a) electron-beam lithography [45], (b) focused-ion-beam lithography [46], (c) direct laser writing [47], (d) projection lithography [48], and (e) two-photon polymerization [49].</p>	10
<p>Figure 1.4: (a) Mask-delimited two-beam interference system [50]. (b) Schematic illustration of a mask-delimited interference pattern produced with (a). (c) Implementation and (d) front-view of the modified diffractive mask with an amplitude mask in the center [51]. (e) Line-integrated 3D periodic lattice produced with (d). (f) Phase mask missing a single post (left) and resulting 3D cavity-integrated periodic structure (right).</p>	11
<p>Figure 1.5: (a) Implementation of phase-controlled MBIL and (b) SEM image of a resulting 2D PLB microstructure [54]. (c) DEMPI system [59]. (d) Bessel-Beam-Assisted MBIL CCD image. (e) 2D line- and cavity integrated periodic microstructure obtained by DEMPI [59]. (e) SEM image a line-integrated periodic microstructure produced by displaying a graded phase pattern on the SLM in (c) [87].</p>	13
<p>Figure 2.1: (a) Conventional optical interference as the superposition of two reference waves. (b) Canonical interference system configuration.</p>	20
<p>Figure 2.2: (a) Conventional holography as the interference of a subject wave with a reference wave. (b) Recording of the Fourier transform hologram of an Object A. (c) Reconstruction of Object A by illuminating the hologram with the reference wave.</p>	22
<p>Figure 2.3: PII as the superposition of two, three, or more reference/subject waves. The resulting interference patterns may be recorded in a photosensitive material.</p>	23

Figure 2.4: (a) A conceptual PIIL system consists of an $8f$ optical system, where multiple polarization- and amplitude-controlled laser beams project demagnified images of a photomask, which overlap and interfere at the image plane of the system. Only two beams are shown for clarity but, there may be three, or more beams. (b) By carefully adjusting the beam amplitudes, polarizations, and directions, 2D and 3D interference patterns that integrate the photomask pattern can be produced in a single exposure.	25
Figure 2.5: Illustration of light propagation and polarization rotation through a high-NA lens.	28
Figure 2.6: (a) Example photomask transmittance. (b) Magnitude of the complex projection of the diffraction pattern along the x-, y-, and z-axis. (c) Magnitude of the x-, y-, and z-component of \mathbf{E}_i at the photoresist surface ($z = 0\mu m$). (d) $ \mathbf{E}_i ^2$ at depths $z = 0\mu m$, $z = 1.5\mu m$, and $z = 3\mu m$ illustrating defocus, off-axis imaging, and photoresist absorption effects.	31
Figure 2.7: Flow chart of the calculation of the optical intensity distribution within the photoresist film produced by the PIIL exposure. The vector electric field distribution produced by each beam in the volume of the photoresist are first calculated with Equation (2.6) before being combined using the multi-beam interference model with Equation (2.7).	33
Figure 2.8: Screen capture of the PIIL simulator GUI.	35
Figure 2.9: Flow chart of the calculation of c_{PAC} and I_{PIIL} as a function of time.	37
Figure 2.10: Top and isometric views of simulated relative PAC concentration $c_{PAC}(\mathbf{r}, t)$ for a bottom threshold of 50% from $t = 0sec$ to $t_{end} = 1sec$	38
Figure 3.1: Schematic representations of the PhC (a) 90deg-bend waveguide, (b) passband filter, and (c) stopband filter.	41
Figure 3.2: (a) Configuration of the three interfering beams at the image plane where the photoresist, BARC, and substrate arrangement is located. (b) Normalized intensity contour for the unit cell of a square-lattice interference pattern with $p4m$ plane group symmetry [128].	42
Figure 3.3: (a) Elementary photomask for the 90deg-bend waveguide. Once projected, the waveguide width is Λ_{sq} . (b) Simulated PIIL exposure. The close-up view shows pillar distortions near the integrated waveguide.	43
Figure 3.4: (a) Estimated etched structure in the silicon substrate accounting for the 3D structural variations of the pillars. (b) Comparison between the estimated and reference pillars. White (black) pixels represent pixels that are present (absent) in the estimated pillars, but absent (present) in the reference pillars.	45

Figure 3.5: (a) Schematic representation of the photomask design problem in PIIL. (b) Five possible geometric shapes for the single-motif-blocking photomask. (c) Illustration of the symbols used in Equations (3.2) and (3.3).	47
Figure 3.6: (a) Average pillar-area error, \bar{e}_{area} . (b) Average pillar-displacement error, \bar{e}_{disp} . (c) Geometric mean of \bar{e}_{area} and \bar{e}_{disp} as figure of merit. The $0.9\Lambda_{sq}/M$ -wide $45deg$ -rotated square mitigates pillar distortions the most. Counter-intuitively, the elementary Λ_{sq}/M -wide square exhibits poor performance.	48
Figure 3.7: Improved photomasks designed with $0.9\Lambda_{sq}/M$ -wide $45deg$ -rotated squares as building blocks for the (a) PhC $90deg$ -bend waveguide, (b) passband filter, and (c) stopband filter. (d), (e), and (f) Corresponding simulated PIIL exposures with close-up views on selected pillars.	50
Figure 3.8: (a), (b), and (c) Estimated silicon pillar structures for the PhC $90deg$ -bend waveguide, passband filter, and stopband filter, respectively. In the insets, white (black) pixels represent pixels that are present (absent) in the estimated pillars, but absent (present) in the reference pillars. Pillar distortions are significantly reduced with the improved photomask design.	51
Figure 3.9: (a) Location of the pillars Λ_{sq} (yellow), $2\Lambda_{sq}$ (blue), and $3\Lambda_{sq}$ (red) from the waveguide. (b) Comparison of the averaged errors \bar{e}_{area} and \bar{e}_{disp} between the elementary and improved photomask. The averaged errors are calculated for pillars located at different distances from the waveguide.	52
Figure 3.10: Amplitude of Beam 1 at the surface of the photoresist produced with (a) the elementary and (b) improved photomask of the $90deg$ -bend waveguide. With $45deg$ -rotated squares, amplitude fluctuations interfere less with the formation of the interference motifs.	53
Figure 3.11: Transmission spectra between Port 1 and Port 2 of the PIIL-produced and idealized PhC (a) $90deg$ -bend waveguide, (b) passband filter, and (c) stopband filter.	55
Figure 4.1: (a) (3+1)-beam configuration and (b) resulting FCC unit cell. (c) (4+1)-beam configuration and (d) corresponding DC unit cell of the interference pattern. SU8 is used as photoresist and is coated on glass to minimize back reflections.	59
Figure 4.2: $\Lambda_z(3+1)\Lambda_{xy}(3+1)$ ratios as functions of $\theta_{beam}(q+1)$. Conditions for cubic unit cell are not be met due to refraction at the air/photoresist interface.	62
Figure 4.3: $\Lambda_z(q+1), IM\Lambda_{xy}(3+1)$ ratios as functions of $\theta_{beam}(q+1)$. With an index-matching material, conditions for cubic unit cell are met for $\theta_{beam}(3+1), FCC = 38.9deg$ and $\theta_{beam}(4+1), DC = 70.5deg$	63
Figure 4.4: (a) FCC lattice and simulated interference pattern with FCR lattice generated by the (3+1)-beam configuration. The ABC layer sequence is visible in the xz-plane. (b) DC lattice and simulated interference pattern with woodpile lattice	

generated by the (4+1)-beam configuration. Matching lattice motifs are superposed to the interference patterns. 64

Figure 4.5: Filling factor of the 3D interference pattern with FCR lattice as a function of the normalized intensity threshold. The interference pattern is bicontinuous for normalized intensity threshold ranging from 24% to 59%. 66

Figure 4.6: Filling factor of the 3D interference pattern with woodpile lattice as a function of the normalized intensity threshold. The interference pattern is bicontinuous for normalized intensity threshold ranging from 16% to 60%. 67

Figure 4.7: (a) Clear-field photomask with opaque GT logo. 3D and top views of the simulated 3D-PIIL exposures for the (b) (3+1)- and (c) (4+1)-beam configuration. 69

Figure 4.8: (a) Dark-field photomask with transparent GT logo. 3D and top views of the simulated 3D-PIIL exposures for the (b) (3+1)- and (c) (4+1)-beam configuration. 71

Figure 4.9: (a) Photomask with an opaque disc to create the cavity within the interference pattern. Exploded views of the simulated 3D-PIIL exposures for the (b) (3+1)- and (c) (4+1)-beam configuration. A microcavity is created at the surface of the 3D interference pattern. Side views of the central slice ($x = 0\mu m$) depict the interference pattern being reproduced below the microcavity. The intensity threshold is 35% of the maximum intensity produced with a blank mask. 73

Figure 4.10: Exploded views of the simulated 3D-PIIL exposures for the (a) (3+1)- and (b) (4+1)-beam configuration. A microcavity is successfully embedded within the 3D interference pattern. Above and below the image focal plane ($z = 10\mu m$), the 3D interference pattern is progressively reproduced by interference of the out-of-focus and non-overlapping images of the disc photomask. The intensity threshold is 35% of the maximum intensity produced with a blank mask. 75

Figure 5.1: (a) Schematic representation of the PIIES. (b) Picture of the prototype PIIES in the laboratory. Selected components from (a) are labeled. 79

Figure 5.2: Ray tracing of a single beam through the ZEMAX-modeled PIIES. 81

Figure 5.3: The EL, Cl, OL1, and OL2 can be positioned to satisfy the beam propagation constraints for the full range of feasible θ_{beam} . However, the distances d_{EL-CL} , $d_{OL1-OL2}$, and thus, d_{total} decrease as θ_{beam} increases. 84

Figure 5.4: Feasible periods for (a) 2D square- and hexagonal-lattice and (b) 3D FCR- and woodpile-lattice interference patterns. Equations fitting the data points are given as well and are practical in aligning the prototype PIIES to target a particular interference period. 86

Figure 5.5: (a) Example two-beam configuration propagating after OL2. (b) Corresponding fringe interference pattern in the xy-plane. 88

Figure 5.6: (a) Example two-beam configuration propagating after OL2, where the second beam is decentered relative to the z-axis. As a result, the period and orientation of the interference fringes are modified. (b) and (c) Relative fringe period error and fringe orientation error, respectively, as functions of the beam decentering in the xy-plane.....	91
Figure 5.7: ZEMAX modeling of (a) OL1, (b) OL2, and (c) COL.	94
Figure 5.8: (a) Illustration of lens decentering applied on OL1 in the COL. (b) and (c) Calculated RMS OPDs as functions of OL1 and OL2 decentering at λ_{des} and λ_{exp} wavelengths.....	96
Figure 5.9: (a) Illustration of lens tilting in the COL. (b) and (c) Calculated RMS OPDs as functions of OL1 and OL2 tilt angles at λ_{des} and λ_{exp} wavelengths.....	97
Figure 5.10: (a) 3D and (b) 2D representations of an example three-beam configuration at the COL image plane. (c), (d), and (e) Distortion error across the image plane for the first, second, and third beam, respectively. The three red dots correspond to the discussed example points. (f) RMS of the three distortion error maps. The exposure field area with $RMS < 0.5\mu m$ is smaller than $0.2mm^2$ and centered on the optical axis.	99
Figure 5.11: (a) 3D and (b) 2D representations of an example three-beam configuration at the COL image plane. (c), (d), and (e) Distortion error across the image plane for the first, second, and third beam, respectively. (f) RMS of the three distortion error maps. The exposure field area with RMS distortion errors $< 0.5\mu m$ is smaller than $0.2mm^2$ and centered on the optical axis.	100
Figure 5.12: (a) Schematic representation of the propagation of a non-tilted (solid line) and tilted (dotted line) beam chief ray through OL2. The tilted ray is shifted upward at the image plane. (b) Image shift as a function of the beam tilt. Tilt error as low as $10^{-3}deg$ can introduce a detrimental $1\mu m$ shift.....	103
Figure 6.1: Alignment of the HWPs, PBSCs, and central beam.	108
Figure 6.2: Alignment of the M3 to M8 mirrors to redirect the side beams along the z-axis with correct d_{beam}	109
Figure 6.3: Alignment of the Cl, OL1, OL2, photomask mount, and sample mount. ..	110
Figure 6.4: Addition of the ELs to complete the 8f prototype PIIES.	111
Figure 6.5: Schematic representations of the single- and double-period-blocking photomask elements contained in the photomask. The size scales are different in both columns.....	112
Figure 6.6: (a) Single- and double-period-blocking photomask elements are grouped as a pair. (b) 10×10 array of element pairs delimited by a solid frame and	

identification code. (c) Complete photomask containing 72 frames corresponding to the eight different photomask elements and their nine size scales.	113
Figure 6.7: Picture of an exposed, developed, and gold-coated sample containing nine individual PIIL exposures. Light diffraction from the gratings and integrated large photomask features are visible.....	115
Figure 6.8: Beam configuration at the PIIES image plane for the pattern-integrated square-lattice results.....	116
Figure 6.9: (a), (b), and (c). Low-magnification SEM image, high-magnification SEM image, and simulated PIIL exposure of the integration of the $90deg$ -bend waveguide within the square-lattice periodic microstructure, respectively. (d), (e), and (f). Low-magnification SEM image, high-magnification SEM image, and simulated PIIL exposure of the integration of the waveguide coupler within the square-lattice periodic microstructure, respectively.....	117
Figure 6.10: (a), (b), and (c). Low-magnification SEM image, high-magnification SEM image, and simulated PIIL exposure of the integration of the ring resonator within the square-lattice periodic microstructure, respectively. (d), (e), and (f). Low-magnification SEM image, high-magnification SEM image, and simulated PIIL exposure of the integration of the straight waveguide within the square-lattice periodic microstructure, respectively.....	118
Figure 6.11: SEM images of the periodic square-lattice produced with (a) $1sec$, (b) $1.5sec$, (c) $1.75sec$, and (d) $2sec$ exposure times.	120
Figure 6.12: SEM image of PIIL exposures using the single-period-blocking (a) waveguide coupler, (b) ring resonator, (c) $90deg$ -bend waveguide, and (d) straight waveguide. (e) and (f) Simulated PIIL exposures corresponding to the (c) and (d), respectively.	122
Figure 6.13: (a) Beam configuration at the PIIES image plane to generate the hexagonal-lattice 2D-PIIL experimental results. (b) SEM image of the single-period-blocking straight waveguide integrated within the lattice. (c) Corresponding simulated PIIL exposure. Residual motifs due to non-optimal conditions are visible in both experiments and simulations.....	124
Figure 6.14: (a) 3D AFM image of the single-period-blocking straight waveguide integrated within the hexagonal lattice of holes. (b) Corresponding simulated PIIL exposure. (c) and (d) Cross-sectional view of the simulated PIIL exposures with the depth profile (black dashed lines) measured by AFM.....	126
Figure 6.15: (a) Low-magnification microscope image of a complete frame containing a 10×10 array of $90deg$ -bend waveguides. (b) SEM image of the portion of the array containing the photomask elements that are the best integrated within the periodic lattice. (c) Representation of the outlines of the three frames extracted from (a). (d) Outlines of the projected frames simulated with ZEMAX. The center of the	

distortion grids for the three simulations are identical and fit the location of the best integrated element from the experiment. 128

Figure 7.1: (a) MOA Fourier-transform PII system configuration. The photomask is coherently illuminated and a double-objective lens system is employed in each optical axis. (b) MOA PII system configuration employing a single objective lens in each axis. In both systems, the optical elements in each axis may be the same or may differ. Only two beams are shown for clarity but, there may be three, or more beams [90]. 138

Figure 7.2: MOA-PIIES configuration without mirrors [157]. 139

Figure 7.3: (a) Top-view and (b) *25deg*-side-view SEM images of 3D-PIIL exposures. 144

Figure A.1: (a) Fringe Zernike coefficients calculated with ZEMAX (b) OPD accross the exit pupil. 149

LIST OF ABBREVIATIONS

1D	One-Dimensional
2D	Two-Dimensional
3D	Three-Dimensional
AFM	Atomic Force Microscope
BARC	Bottom Antireflective Coating
CL	Condenser Lens
DEMPI	Defect-Engineered Multiple Plane-Wave Interference
EL	Expander Lens
FWHM	Full Width at Half Maximum
GT	Georgia Institute of Technology
HWP	Half-wave plate
IM	Index Matching
IP	Image Plane
MBIL	Multi-Beam Interference Lithography
NA	Numerical Aperture
OL1	Objective Lens 1
OL2	Objective Lens 2
OP	Object Plane
OPC	Optical Proximity Correction
PAC	Photoactive Compound
PBSC	Polarizing Beam Splitter Cube
PhC	Photonic Crystal
PII	Pattern-Integrated Interference

PIES	Pattern-Integrated Interference Exposure System
PIIL	Pattern-Integrated Interference Lithography
PLB	Periodic-Lattice-Based
PR	Photoresist
RMS	Root-Mean Square
SEM	Scanning Electron Microscope
SLM	Spatial Light Modulator
TM	Transverse Mode

LIST OF SYMBOLS

A_D	First Dill's parameter (μm^{-1})
a_i	Coefficients of the i^{th} fringe Zernike polynomial
α	Direction cosines relative to the x-axis at the Fourier plane
α_{PR}	Photoresist absorption (μm^{-1})
B_D	Second Dill's parameter (μm^{-1})
β	Direction cosines relative to the y-axis at the Fourier plane
C	Energy conservation factor transfer function
C_D	Third Dill's parameter (m^2/J)
c_0	Homogeneity factor (W/V^2)
c_{PAC}	Relative concentration of photoactive compound
d	Distance from the center of mass of the estimated pillar and its expected location in the lattice (μm)
d_{beam}	Lateral beam displacement from the z-axis (mm)
d_{beam}^*	Lateral beam displacement from the z-axis for a decentered beam (mm)
d_{cav}	Depth of the integrated microcavity (μm)
d_{CL-OP}	Distance from the condenser lens to the object plane in the ZEMAX optimization (mm)
d_{EL-CL}	Distance from the expander lens to the condenser lens in the ZEMAX optimization (mm)
$d_{OL1-OL2}$	Distance from the objective lens 1 to the objective lens 2 in the ZEMAX optimization (mm)
d_{OL2-IP}	Distance from the objective lens 2 to the image plane in the ZEMAX optimization (mm)
d_{OP-OL1}	Distance from the object plane to the objective lens 1 in the ZEMAX optimization (mm)

\mathbf{E}_i	3×1 complex electric field vector of the i^{th} interfering beam in PIIL (V/m)
\mathbf{E}_i^{ill}	2×1 complex electric field vector of the i^{th} beam illuminating the photomask (V/m)
$\mathbf{E}_{pw,i}$	3×1 complex electric field vector of the i^{th} interfering plane wave in MBIL (V/m)
$E_{pw,i}$	Electric field norm of the i^{th} interfering plane wave in MBIL (V/m)
e_{area}	Relative pillar-area error
e_{disp}	Relative pillar-displacement error
$\hat{\mathbf{e}}_i$	Electric field direction
e_{Λ}	Relative fringe period error
e_{Θ}	Fringe orientation error (deg)
η	Azimuthal angle error (deg)
f_{EL}	Expender lens focal length of the objective lens 1 (mm)
f_{OL1}	Objective lens 1 focal length (mm)
f_{OL2}	Objective lens 2 focal length (mm)
φ_i	Azimuthal angle at the image plane of the i^{th} interfering beam (deg)
φ_i^*	Azimuthal angle at the image plane of the i^{th} interfering beam for a decentered beam (deg)
ϕ	Beam phase (rad)
γ	Direction cosines relative to the z-axis at the Fourier plane
I_{MBIL}	Optical intensity distribution of an MBIL exposure (W/m^2)
I_{PIIL}	Optical intensity distribution of a PIIL exposure (W/m^2)
\mathbf{k}_i	Wavevector of the i^{th} beam (nm^{-1})
\mathbf{k}_2^*	Propagation vector of the decentered beam (nm^{-1})
k_p	Process-dependent quantity
$\Delta\mathbf{k}$	Grating vector (nm^{-1})

$\Delta \mathbf{k}^*$	Modified grating vector in case of beam decentering (nm^{-1})
Λ_{ID}	Two-beam interference period (μm)
Λ_{ID}^*	Modified two-beam interference period in case of beam decentering (μm)
Λ_{hex}	Period of the hexagonal-lattice interference pattern (μm)
Λ_{sq}	Period of the square-lattice interference pattern (μm)
$\Lambda_{xy}^{(q+1)}$	(q+1)-beam interference period in the xy-plane (μm)
$\Lambda_z^{(q+1)}$	(q+1)-beam interference period along the z-axis (μm)
λ_{des}	Lens design wavelength (nm)
λ_{exp}	Exposure wavelength (nm)
M	Compound objective lens magnification
M1 to M8	Mirrors in the pattern-integrated interference exposure system
$\mathbf{M}_F^{3 \times 5}$	Film function matrix
$\mathbf{M}_P^{5 \times 2}$	Electric field correction matrix
NA	Numerical Aperture
\mathbf{n}_{BARC}	Bottom antireflective coating refractive index
n_g	Photonic-crystal group velocity index
\mathbf{n}_{glass}	Glass photoresist
n_{imm}	Refractive index of the immersion medium in immersion photolithography
\mathbf{n}_{PR}	Photoresist complex refractive index
n_{PR}	Real part of the photoresist complex refractive index
\mathbf{n}_{Si}	Silicon complex refractive index
n_{Si}	Real part of the silicon complex refractive index
\mathbf{n}_{SU8}	SU8 photoresist complex refractive index
n_{SU8}	Real part of the SU8 photoresist complex refractive index

\mathbf{n}_{sub}	Substrate complex refractive index
v	Binary pixel values (0 or 1) of the estimated pillar in PIIL photomask design
O	Fourier transform of the photomask object (m^{-2})
P	Pupil transmission function
ψ	Beam tilt angle (deg)
R	Critical dimension (μm)
\mathbf{r}	Cartesian coordinate (m)
r_{cav}	Integrated microcavity radius (μm)
r_p	Photonic-crystal pillar radius (m)
ρ	Radial distance error from the ideal intersection between \mathbf{k}_2 and the $z = -f_{OL2}$ plane (mm)
ρ_P	Normalized radial coordinate in the exit pupil
S	Off-axis beam propagation transfer function
S_{21}	Scattering parameter from Port 1 to Port 2
σ	Photomask projection lateral shift at the image plane (μm)
t	Time (sec)
t_{exp}	Exposure time (sec)
t_{PR}	Photoresist film thickness (μm)
t_{SU8}	SU8 film thickness (μm)
Θ	Grating vector orientation (deg)
Θ^*	Modified grating vector orientation in case of beam decentering (deg)
$\theta_{\text{beam}}^{(3+1),DC}$	Common beam incidence angle at the PIIES image plane in a (4+1)-beam configuration satisfying the condition for diamond cubic lattice
$\theta_{\text{beam}}^{(3+1),FCC}$	Common beam incidence angle at the PIIES image plane in a (3+1)-beam configuration satisfying the condition for face-centered cubic lattice

$\theta_{beam}^{(3+1)}$	Common beam incidence angle at the PIIES image plane for a (3+1)-beam configuration in 3D-PIIL (<i>deg</i>)
$\theta_{beam}^{(4+1)}$	Common beam incidence angle at the PIIES image plane for a (4+1)-beam configuration in 3D-PIIL (<i>deg</i>)
θ_{beam}	Common beam incidence angle at the PIIES image plane (<i>deg</i>)
θ_{beam}^*	Common beam incidence angle at the PIIES image plane for a decentered beam (<i>deg</i>)
θ_{max}	Lens acceptance cone angle (<i>deg</i>)
θ_P	Polar coordinate in the exit pupil (<i>deg</i>)
θ_{SU8}	Beam propagation within the SU8 photoresist film (<i>deg</i>)
τ	Binary pixel values (0 or 1) of the reference pillar
W	Normalized wavefront phase error
w	Width of the single-motif-blocking element in photomask design (Λ_{sq}/M)
x	Cartesian coordinate (μm)
y	Cartesian coordinate (μm)
Z_i	i^{th} fringe Zernike polynomial
z	Cartesian coordinate (μm)
z_0	Distance from the image focal plane to the photoresist film surface (μm)

SUMMARY

Two-dimensional (2D) and three-dimensional (3D) periodic-lattice-based microstructures have found multifaceted applications in photonics, microfluidics, tissue engineering, biomedical engineering, and mechanical metamaterials. To fabricate functional periodic microstructures, in particular in 3D, current available technologies have proven to be slow and thus, unsuitable for rapid prototyping or large-volume manufacturing. To address this shortcoming, the new innovative field of pattern-integrated interference lithography (PIIL) was introduced. PIIL enables the rapid, single-exposure fabrication of 2D and 3D custom-modified periodic microstructures through the non-intuitive combination of multi-beam interference lithography and photomask imaging. The research in this thesis aims at quantifying PIIL's fundamental capabilities and limitations through modeling, simulations, prototype implementation, and experimental demonstrations.

PIIL is first conceptualized as a progression from optical interference and holography. Then, a comprehensive PIIL vector model is derived to simulate the optical intensity distribution produced within a photoresist film during a PIIL exposure. Using this model, the fabrication of representative photonic-crystal devices by PIIL is simulated and the performance of the PIIL-produced devices is studied. Photomask optimization strategies for PIIL are also studied to mitigate distortions within the periodic lattice. The innovative field of 3D-PIIL is also introduced. Exposures of photomask-integrated, photomask-shaped, and microcavity-integrated 3D interference patterns are simulated to illustrate the richness and potential of 3D-PIIL. To demonstrate PIIL experimentally, a prototype pattern-integrated interference exposure system is designed, analyzed with the optical

design program ZEMAX, and used to fabricate pattern-integrated 2D square- and hexagonal-lattice periodic microstructures. To validate the PIIL vector model, the proof-of-concept results are characterized by scanning-electron microscopy and atomic force microscopy and compared to simulated PIIL exposures. As numerous PIIL underpinnings remain unexplored, research avenues are finally proposed. Future research paths include the design of new PIIL systems, the development of photomask optimization strategies, the fabrication of functional devices, and the experimental demonstration of 3D-PIIL.

CHAPTER 1

INTRODUCTION

1.1 Periodic-Lattice-Based Microstructures

Periodic-lattice-based (PLB) structures are material arrangements based on a one-dimensional (1D), two-dimensional (2D), or three-dimensional (3D) periodic lattice. At the microscale, PLB structures exhibit unique physical, optical, and mechanical properties [1]. As such, they have found applications in numerous areas. To exploit these properties, the shape of, and lattice modifications within PLB microstructures must be carefully engineered.

One of the most documented applications of PLB microstructures are photonic-crystal (PhC) devices that are made of dielectric materials with different refractive indices [2]. PhC devices exhibit photonic bandgaps and allow the control of light propagation and light-matter interaction at the wavelength scale [3, 4]. PhC can be engineered into waveguides [5, 6], resonators [7-9], filters [9-13], waveguide couplers [14-17], directional couplers [18], logic gates [19, 20], demultiplexers [21], antennas [22], switches [23, 24], and sensors [25]. PhC devices can further be integrated into dense integrated photonic circuits and systems for telecom or biomedical diagnostics applications [26, 27]. Even more compact, subwavelength-sized optical metamaterials enable new classes of optical devices including superlenses [28], split-ring resonators for second-harmonic generation [29], and metamaterial electromagnetic cloak [30].

PLB microstructures have also found unique applications in bioengineering. For drug delivery, a pH-responsive periodic network of pores has, for example, been demonstrated to deliver neurotrophins in neural prosthetic devices [31]. Compared to microstructures with random porosity, 3D PLB microfluidic mixers exhibiting 84% improved fluid mixing and 3D PLB microfluidic filters blocking submicron particles have been demonstrated [32, 33]. PLB microstructures also provide flexible analysis platforms to study biological mechanisms. Periodic arrays of sub-micrometer domains can be used to investigate the attachment and spreading of biological tissues in contact with specific material such as murine osteoblast cells with fibronectin [34]. Finally, 3D PLB scaffolds with periodic pore architectures exhibit better pore interconnectivity, improved wetting properties, and thus improved static cultures of cells and tissues [35].

Another application area of PLB microstructures are mechanical metamaterials that demonstrate large strength-to-weight ratios and better mechanical performance than most engineered cellular structures with random porosity [36]. Mechanical metamaterials find applications in catalyst supports, filtration devices, and micro heat-exchangers [1]. In addition to photonics, microfluidics, tissue engineering, biomedical engineering, and mechanical metamaterials applications illustrated in Figure 1.1, PLB structures have also been used in nanoelectronics, surface texturing, magnetic nanostructures, plasmonic structures, field-emission devices, and form-birefringent polarization elements [37].

1.2 Fabrication Techniques for PLB Microstructures

Significant efforts have been dedicated over the past decades toward the development of fabrication techniques to produce 2D and 3D PLB microstructures. These techniques

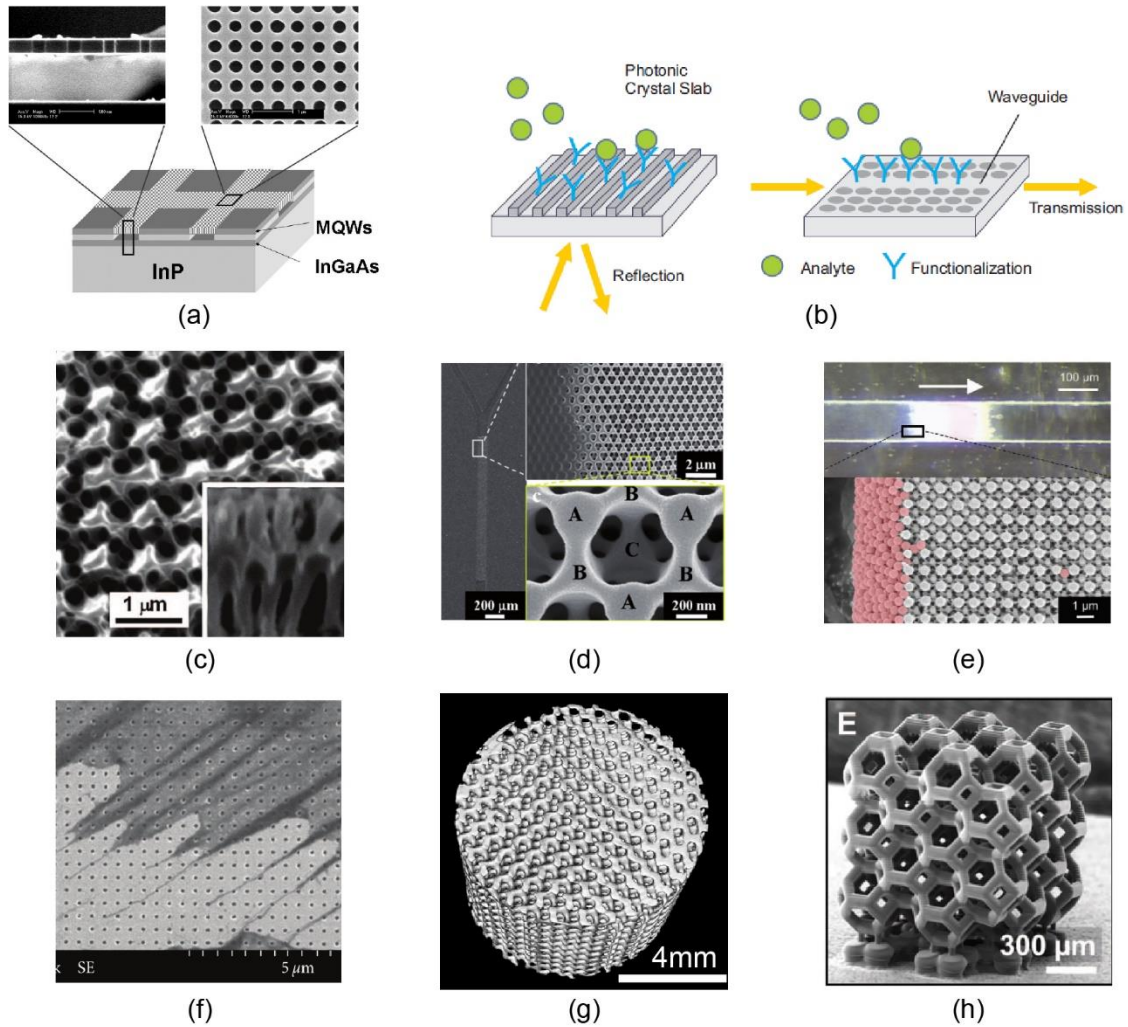


Figure 1.1: Example PLB microstructures. (a) PhC band edge laser array [38]. (b) Schematic description of PhC biosensors [27]. (c) pH-responsive 3D periodic microstructure for drug delivery [31]. (d) Microfluidic mixer [33]. (e) Microfluidic filter [35]. (f) 2D array of fibronectin domains to study murine osteoblast cells growth. (g) 3D PLB scaffold for cell culture [35]. (h) Lightweight and ultrastiff 3D mechanical metamaterials [36].

include construction-based methods and approaches derived from multi-beam interference lithography (MBIL).

1.2.1 Construction-Based Microfabrication Techniques

Numerous construction-based microfabrication techniques exist to fabricate PLB microstructures. Some of their characteristics are compared in Table 1.1. With electro-mechanical etching, a substrate with a pre-patterned surface is placed in a hydrofluoric acid solution under electrical bias such that current density drives selective etching through the substrate, resulting in a 2D periodic array of holes [39]. 3D PLB microstructures can be produced by modulating the electrical bias over time and thus, the etching through the substrate. Glancing angle deposition uses an analogous approach [40], where the substrate surface is also pre-patterned with seed posts before being exposed to a collimated vapor flux at large incident angle. During nucleation, the seed posts grow toward the incident vapor flux. 3D PLB microstructures can be grown by rotating and tilting the substrate during the growth. Yet, introducing custom modifications to the periodic lattice with the two aforementioned techniques is limited and challenging. Direct writing techniques are more flexible and include robotic ink writing [41], which employs a microscopic “pen” and an engineered ink, and two-photon polymerization [42], which involves the non-linear excitation of a photosensitive material in the focal spot of a focused laser beam. In both cases, arbitrary 3D patterns, including PLB microstructures, can be “written” in a serial fashion by controlling piezoelectric stages holding the photosensitive-material-coated substrate. More sophisticated, micro-manipulation requires the handling and assembly of pre-fabricated microscopic building blocks using optical tweezers or high-resolution robots

Table 1.1: Comparison of characteristics of fabrication techniques for PLB microstructures. Dashes indicate conditional/limited yes.

Fabrication Techniques	Lattice Customization	2D / 3D Lattice	Large Format	Sub-Micron Resolution	Rapid
<i>Construction-Based Fabrication Techniques</i>					
Electrochemical Etching [39]	—	✓	✓	×	×
Glancing Angle Deposition [40]	—	✓	✓	×	×
Robotic Ink Writing [41]	✓	✓	✓	×	×
Two-Photon Polymerization [42]	✓	✓	—	✓	×
Micromanipulation [43]	✓	✓	×	✓	×
Conventional Lithography [44]	✓	✓	✓	✓	×
<i>Extrinsically-Modified MBIL Techniques</i> [45-49]	✓	✓	✓	✓	× (multi-step)
<i>Intrinsically-Modified MBIL Techniques</i>					
Mask-Delimited MBIL [50]	✓	× (1D)	✓	✓	✓
Modified Diffractive-Mask [51]	✓	✓	✓	×	✓
Modified Phase-Mask [33]	—	—	✓	✓	✓
Phase-Controlled MBIL [52-55]	✓	—	×	×	✓
Bessel-Beam-Assisted MBIL [56-58]	—	—	✓	×	✓
Defect-Engineered Multiple Plane-Wave Interference (DEMPI) [59]	✓	—	✓	×	✓
Pattern-Integrated Interference Lithography	✓	✓	✓	✓	✓

under a microscope [43]. This technique enables the fabrication of arbitrary microstructures, but is extremely complex and slow. Finally, well-established conventional photolithography can be used to produce 2D PLB microstructures directly and 3D arrangements, yet with a layer-by-layer process [44].

Construction-based microfabrication techniques have the potential to produce large-format 2D and 3D PLB microstructures. However, they are time-consuming and prone to overlay and misalignment errors because the fabrication is typically performed layer-by-layer or even point-by-point [60, 61]. Therefore, they are usually not suitable for rapid prototyping or for large-volume manufacturing.

1.2.2 Multi-Beam Interference Lithography

A significantly more rapid approach to produce PLB microstructures employs the periodic interference pattern produced by multiple overlapping laser beams. The amplitude, wavelength, wavevector configuration, phases, and polarizations of the interfering beams can be adjusted to produce particular 2D or 3D periodic interference patterns. With three interfering laser beams, 2D periodic interference patterns including all five 2D Bravais lattices can be produced [62]. With four or more interfering beams, 3D periodic interference patterns including all fourteen 3D Bravais lattices can be achieved [63]. Complex 60-fold 2D quasi-periodic [64], 3D chiral-basis [65], icosahedral [66], spatially variant [67], and dual-lattice interference patterns [68] are furthermore feasible.

For microfabrication purposes, a 1D, 2D, or 3D optical interference pattern can be recorded within a photo-sensitive material (or photoresist) coated on a substrate. This method is known as MBIL and is sometimes referred to as “holographic” or “interferometric” lithography in the literature [1]. With sufficient optical power, the

exposure of the photoresist can be shorter than one second, making MBIL extremely rapid compared to construction-based techniques. Upon exposure, the solubility of the photoresist changes. A positive- (negative-) tone photoresist becomes more (less) soluble when exposed. After a development step, a latent image of the interference pattern is created in the photoresist. The photoresist structure can be used directly or serve as a sacrificial template for lift-off [34], substrate etching [69], infiltration/inversion steps [70], or double infiltration/inversion steps [71]. In addition, the pairing of the light-field (intensity maxima) or dark-field (intensity minima) interference pattern to positive- and negative-tone photoresist extends the variety of feasible PLB microstructures by MBIL.

As early as 1970, two-beam interference lithography was used to produce one-dimensional gratings used as optical couplers [72]. Two-beam interference lithography is also currently employed to fabricate dense line/space nanostructures in the study of the chemistry and performance of extreme-ultraviolet photoresists (Figure 1.2(a)) [73]. Using three laser beams, Berger *et al.* [74] recorded for the first time a 2D interference pattern with hexagonal symmetry within a photoresist film and transferred the pattern into a gallium arsenide substrate through reactive ion etching (Figure 1.2(b)). Later, 3D MBIL was demonstrated by using a four-beam configuration to produce 3D periodic microstructures with sub-micron periodicity as shown in Figure 1.2(c) [75]. Since the initial MBIL demonstrations, numerous MBIL methodologies have been developed using a diffractive beam splitter [76], a Lloyd's mirror [77], a prism [78], a phase-mask [79], optical fibers [80], or half-wave plates and beam-splitter cubes for individual beam control [81].

As a flexible, rapid, and cost-effective approach, MBIL has found numerous applications in photonics, microfluidics, tissue engineering, biomedical engineering, and optical metamaterials, where large-format periodic microstructures are needed [1, 82]. Unfortunately, MBIL in its current form only produces continuous periodic structures and does not enable the fabrication of periodic microstructures with controlled lattice modifications in a single step. As a result, MBIL-produced structures have limited functionalities and applications. To address this issue, extrinsically- and intrinsically-modified MBIL techniques have been developed to add functionalities to MBIL-produced structures.

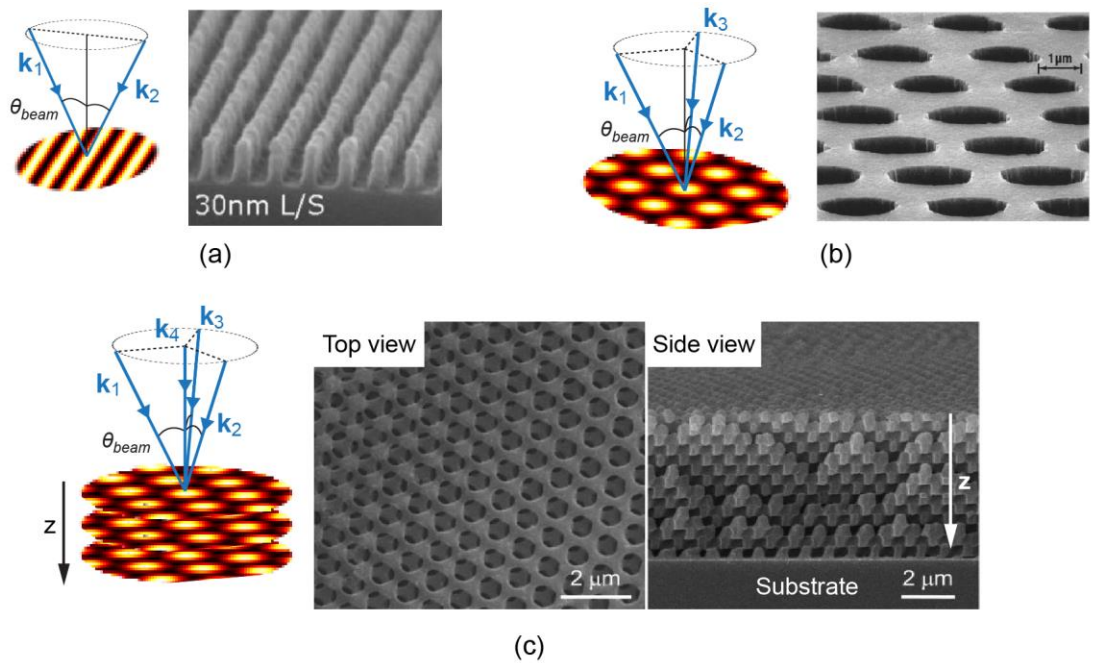


Figure 1.2: Multi-beam configurations and corresponding MBIL-produced periodic microstructures. (a) One-dimensional grating produced by two-beam interference [73]. (b) 2D PhC produced by three-beam interference [74]. (c) 3D periodic lattice produced by four-beam interference [75]. The lattice constant depends on the common beam incidence angle, θ_{beam} .

1.2.3 Modified MBIL Techniques

1.2.3.1 Extrinsically-modified MBIL

To address MBIL patterning limitations, MBIL-produced structures have been functionalized by using an additional microfabrication technique in a two-step process. This approach is hereafter referred to as *extrinsically-modified MBIL*. Characteristics of extrinsically-modified MBIL are listed in Table 1.1. The additional techniques include electron-beam lithography [45], focused ion beam lithography [46], direct laser writing [47], projection lithography [48], or multi-photon polymerization [49]. Various functional 2D and 3D PLB microstructures have been produced with extrinsically-modified MBIL as illustrated in Figure 1.3. However, modifying an already-constructed periodic lattice using an additional fabrication step is a time-consuming and expensive process. In addition, this two-step approach is prone to misalignment issues and sample deterioration. Therefore, extrinsically-modified MBIL does not address the rapidity issue of construction-based microfabrication techniques.

1.2.3.2 Intrinsically-modified MBIL

To avoid the need for multiple processing steps, the holy grail for experimentalists would be the single-step creation of an interference pattern with intrinsic lattice modifications [83]. *Intrinsically-modified MBIL* techniques have been introduced to address this need and produce custom-modified interference patterns in a single-exposure step. Characteristics of the described intrinsically-modified MBIL techniques are compared in Table 1.1.

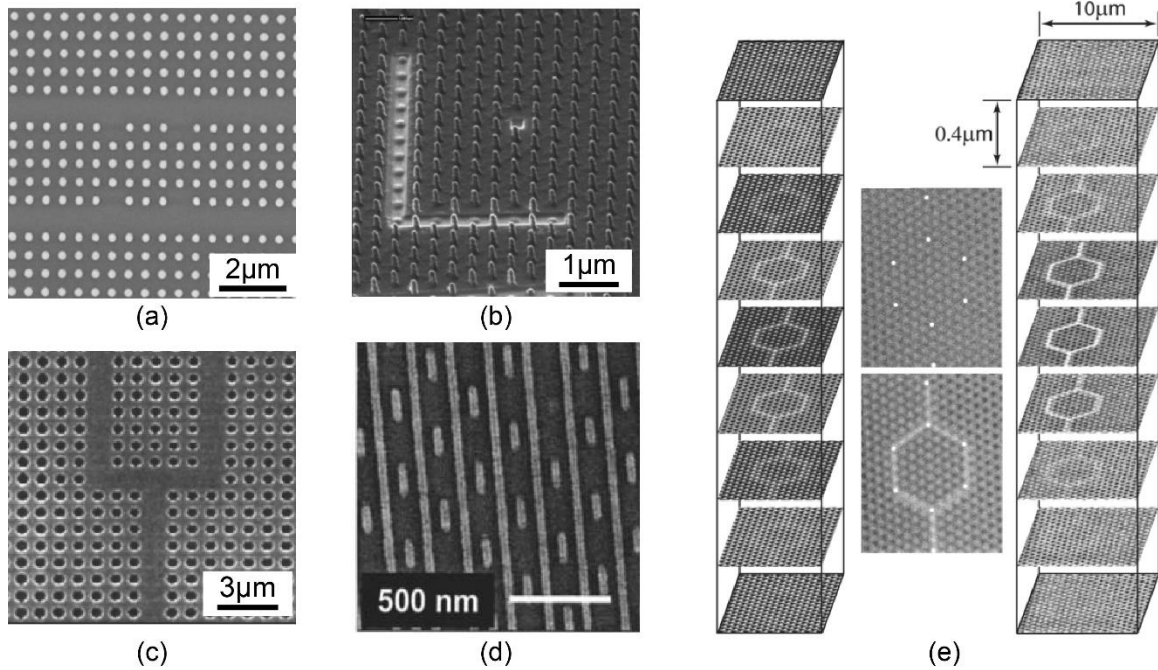


Figure 1.3: Example PLB microstructures produced by extrinsically-modified MBIL techniques, where MBIL is combined with (a) electron-beam lithography [45], (b) focused-ion-beam lithography [46], (c) direct laser writing [47], (d) projection lithography [48], and (e) two-photon polymerization [49].

Using two photomasks, a confocal two-lens system, and a Fresnel's double mirror, Chen *et al.* [50] produced a one-dimensional interference pattern delimited by the photomask opening as illustrated in Figures 1.4(a) and (b). However, this approach does not allow for more than two interfering beams and thus, is limited to one-dimensional fringes. Lin *et al.* [51] proposed a five-beam diffractive mask depicted in Figures 1.4(c) and (d) to produce a 3D interference pattern embedding a line as shown in Figure 1.4(e). However, the line is created by casting the shadow of a photomask within the 3D interference pattern. Therefore, the line width is orders of magnitude larger than the lattice constant of the 3D interference pattern.

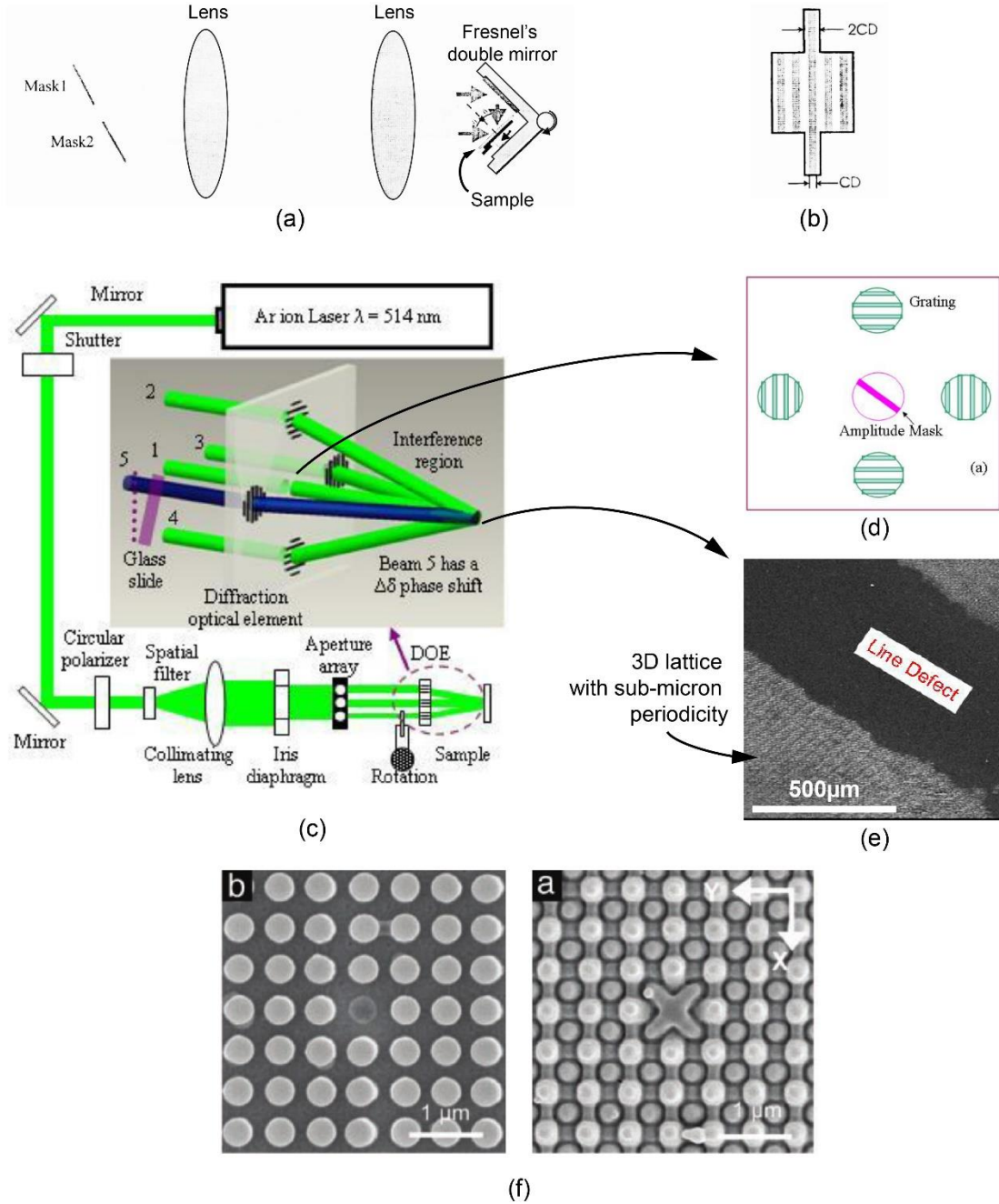


Figure 1.4: (a) Mask-delimited two-beam interference system [50]. (b) Schematic illustration of a mask-delimited interference pattern produced with (a). (c) Implementation and (d) front-view of the modified diffractive mask with an amplitude mask in the center [51]. (e) Line-integrated 3D periodic lattice produced with (d). (f) Phase mask missing a single post (left) and resulting 3D cavity-integrated periodic structure (right).

Phase masks are commonly used to implement MBIL and produce large areas of 3D periodic structures [84-86]. To modify locally the surface of the 3D interference pattern, Jeon *et al.* [33] removed a single post from a phase mask as shown in Figure 1.4(f). However, lattice modifications deeper in the photoresist are poorly controlled and more complex geometries seem limited since removing more posts from the phase mask would deteriorate the formation of the interference pattern.

Recently, several intrinsically-modified MBIL techniques employing a spatial light modulator (SLM) have been proposed. In phase-controlled MBIL, a phase-only SLM placed at the Fourier plane of a two-lens system is used to control the phase of tens of large-diameter (typically 2mm) beamlets as illustrated in Figure 1.5(a) [52-55]. The required phase and spatial distribution of the beamlets displayed on the SLM are pre-calculated using an optimization routine such as the genetic algorithm. The beamlets are then focused and superposed to produce a custom-modified interference pattern as shown in the scanning electron microscope (SEM) image in Figure 1.5(b). Zhang *et al.* [54] further improved this approach by updating the SLM pixels in real time using a simulated annealing algorithm and a feedback loop between a camera and the SLM. The integrated functional elements, however, are repeated periodically within the interference pattern and the size of the exposure spot is non-uniform and limited to about $500\mu\text{m}^2$. The exposure area can possibly be extended with a diffractive optical element but only to a few square millimeters [55].

Alternatively, the SLM can be placed at the object plane of a two-lens confocal system to display a phase pattern that produces upon illumination the interfering beams as

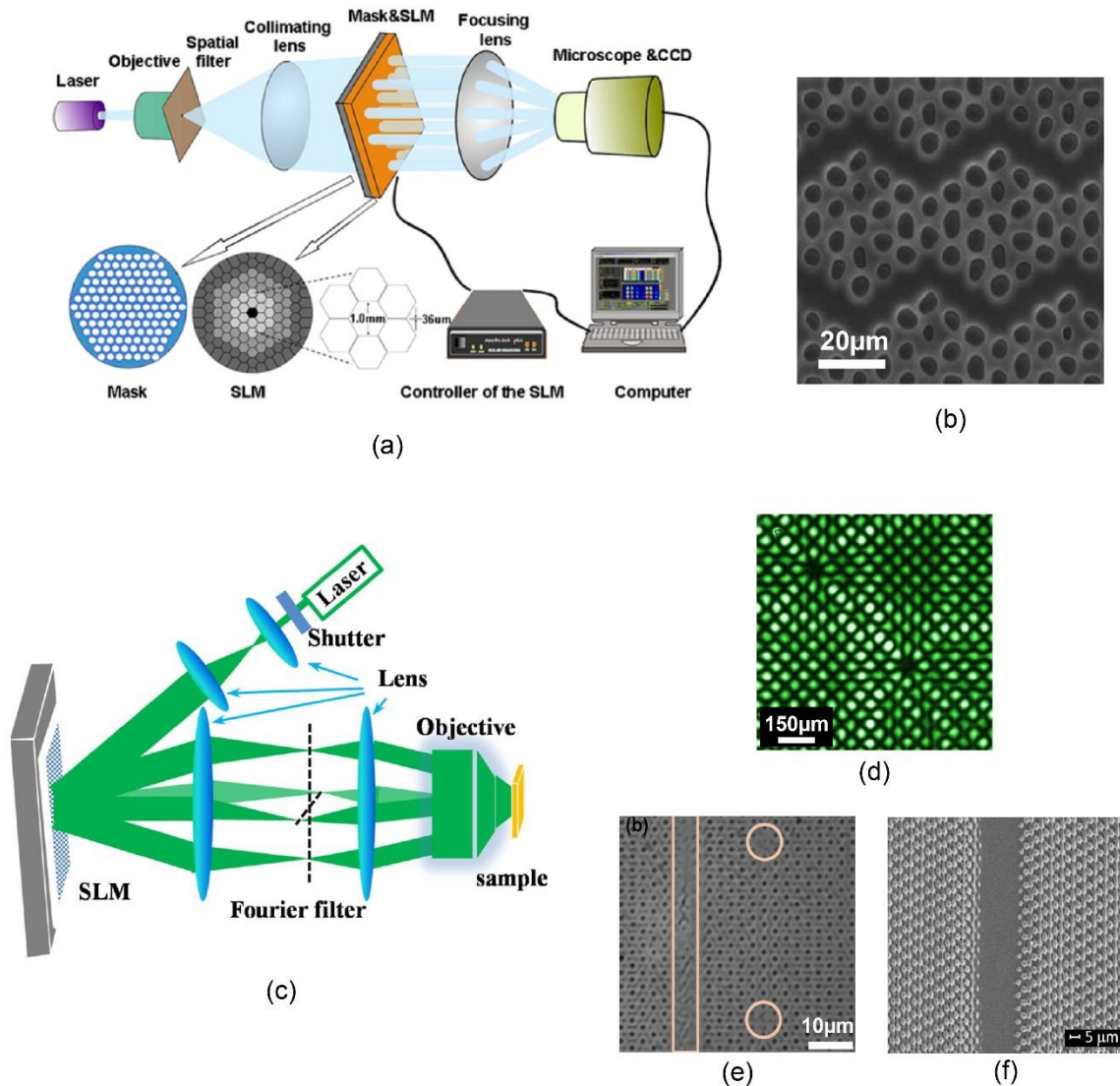


Figure 1.5: (a) Implementation of phase-controlled MBIL and (b) SEM image of a resulting 2D PLB microstructure [54]. (c) DEMPI system [59]. (d) Bessel-Beam-Assisted MBIL CCD image. (e) 2D line- and cavity integrated periodic microstructure obtained by DEMPI [59]. (e) SEM image a line-integrated periodic microstructure produced by displaying a graded phase pattern on the SLM in (c) [87].

illustrated in Figure 1.5(c). The beams eventually overlap at the image plane of the system and interfere to produce a custom-modified interference pattern. A first approach consists in using Bessel beams as some of the interfering beams to create intrinsic cavities by destructive interference as shown in Figure 1.5(d) [56-58]. The cavities are not repeated periodically within the interference pattern and the exposure area can be larger. However, the interference pattern is strongly perturbed by ringing effects produced by the Bessel beams. To address these distortions, Xavier *et al.* [59] discarded the Bessel beams and proposed defect-engineered multiple plane-wave interference to produce line- and cavity-integrated periodic microstructures as shown in Figure 1.5(e). Using an identical setup, Lutkenhaus *et al.* [87] proposed to display a graded phase pattern on the phase SLM and assign a constant zero phase to certain pixels that define the integrated functional elements. With this approach, line-integrated 2D periodic structures were produced as shown in Figure 1.5(f).

In spite of their promise, SLM-assisted MBIL techniques have numerous drawbacks. The SLM pixel array, size, and edge are responsible for blurring effects, lattice distortions, poor lattice quality, and large periodicity. The size of the SLM active area also restricts the exposure area. The lack of control over the amplitude and polarization of the interfering beams limits the range of feasible 2D and 3D lattices as well. Finally, troublesome Fourier filters are typically required at the Fourier plane of the confocal lens system to eliminate higher-order diffraction terms produced by the SLM.

1.3 Pattern-Integrated Interference Lithography

From Table 1.1, a rapid microfabrication technique for large-format 2D and 3D PLB microstructures is missing. To address this need, pattern-integrated interference

lithography (PIIL) was introduced from the Optics Laboratory at Georgia Tech as a novel intrinsically-modified MBIL technique [88]. PIIL combines simultaneously MBIL and photomask imaging, two areas that are traditionally considered exclusive. In PIIL, multiple images of a photomask are produced using multiple intensity-, polarization-, and direction controlled laser beams. The multiple images are then combined using projection optics. As the photomask images overlap, they interfere and produce a 2D or 3D photomask-integrated interference pattern in a single-exposure step. Therefore, PIIL enables the rapid, single-exposure step fabrication of large-format 2D and 3D PLB microstructures.

1.4 Research Objectives and Contributions

Although Burrow *et al.* reported PIIL's theoretical basics and initial proof-of-concept results [88, 89], the mathematical and physical underpinnings of PIIL remain unexplored. A comprehensive understanding of PIIL fundamentals and more definitive experimental results are necessary. The objective of this thesis is therefore to quantify PIIL's fundamental capabilities and limitations in the fabrication of 2D and 3D PLB microstructures through modeling, simulations, system implementation, and experimental demonstration. The results presented in this thesis resulted in the following accomplishments and contributions:

1. The description of PIIL as a successor of optical interference and holography [90].
2. The introduction of a comprehensive multi-beam high-numerical-aperture volume interference/image vector model for PIIL and the derivation of an expression for the optical intensity distribution within a photoresist film produced by a PIIL exposure [91, 92].

3. The development of a simulation software package with a graphical user interface integrating the PIIL exposure model.
4. The introduction of photomask design strategies to reduce lattice distortions in PIIL-produced PLB microstructures [93, 94].
5. The definition of performance metrics and figure of merits to quantify errors in the shape and position of lattice motifs in PIIL-produced PLB microstructures [95, 96].
6. The simulation of PIIL exposures for the fabrication of a *90deg*-bend PhC waveguide, a PhC passband filter, and a PhC stopband filter [93, 95].
7. The calculation and comparison of the transmission spectra of PIIL-produced and idealized *90deg*-bend PhC waveguide, a PhC passband filter, and a PhC stopband filter [95, 96].
8. The simulation of 3D-PIIL exposures for mask-shaped, mask-delimited, and microcavity-integrated 3D PLB microstructures [97-99].
9. The design of a prototype pattern-integrated interference exposure system (PIIES) to implement experimentally PIIL [89, 100].
10. The study of the prototype PIIES performance in producing 2D and 3D periodic interference pattern and in imaging the photomask [101].
11. The development of a more stable and repeatable PIIES alignment and sample focusing procedures [102].
12. The experimental fabrication of pattern-integrated 2D square- and hexagonal periodic microstructures [101, 103, 104].
13. The characterization of proof-of-concept results by SEM and atomic force microscopy [104].

1.5 Thesis Overview

The research objectives and accomplishments described previously are presented in detail in the following chapters.

In Chapter 2, PIIL is introduced as a logical progression from optical interference and holography and a conceptual PIIL system is presented. To simulate numerically PIIL exposures, a comprehensive multi-beam high-numerical-aperture (NA) interference/image vector model is introduced. An expression for the optical intensity distribution produced within a photoresist film during a PIIL exposure is derived as well.

In Chapter 3, 2D-PIIL exposures for three representative 2D PhC devices are simulated; the transfer of the photoresist pattern into the substrate is estimated; and transmission spectra of the PIIL-produced PhC devices are calculated. To mitigate lattice distortions due to the integrated photomask pattern, photomask optimization strategies for PIIL are introduced.

In Chapter 4, 3D-PIIL is introduced as the interference of four or more photomask images to generate custom-modified 3D interference patterns. The impact of light refraction at the air/photoresist interface on the formation of the 3D periodic lattice is first reviewed. Simulated 3D-PIIL exposures of photomask-integrated, photomask-shaped, and microcavity-integrated 3D periodic microstructures are also presented to illustrate the unique potential of PIIL.

In Chapter 5, a prototype PIIES is presented and its capabilities and performance are numerically analyzed using geometric optics and the optical design program ZEMAX. The range of feasible interference periods and the sensitivity of the interference pattern to beam decentering are investigated. Then, the imaging performance of the PIIES objective lenses

as a compound objective lens is studied. The analysis results are finally compared to the estimated precision of the manual alignment of the PIIES.

In Chapter 6, the prototype PIIES is used to demonstrate experimentally PIIL and validate the PIIES analysis results. The experimental procedures including the PIIES alignment, sample processing, and focusing procedure are given. Then, PIIL experimental exposures are presented, characterized by SEM and atomic force microscopy (AFM), and compared to simulated exposures.

In Chapter 7, the research results and accomplishments are summarized and discussed. Short- and long-term future research avenues are presented as well.

Included in this thesis are two appendices. In Appendix A, the Zernike polynomials and coefficients describing optical aberrations and calculated with ZEMAX are given. MATLAB scripts implementing the PIIL vector model are given in Appendix B.

CHAPTER 2

THEORY OF PATTERN-INTEGRATED INTERFERENCE LITHOGRAPHY

In this chapter, the background and theory of PIIL are given. PIIL is first introduced as a logical progression starting from the primary precursors of optical interference and holography. To simulate numerically PIIL exposures, a comprehensive *multi-beam high-numerical-aperture volume interference/image vector model* is introduced, and an expression for the optical intensity distribution produced within a photoresist film during a PIIL exposure is derived. This model is finally integrated into a user-friendly software package. The research presented in this chapter has resulted in three journal papers [90, 91, 103] and two conference presentations [92, 100].

2.1 PIIL Precursors

2.1.1 Optical Interference

In 1807, the formation of optical interference fringes due to two interfering cylindrical waves was first demonstrated by Prof. Thomas Young in his famous double-slit experiment [105]. This was a pivotal result in establishing that light could exhibit unambiguous wave behavior. For present purposes, it is simply stated that optical interference is based on the interference between multiple reference waves as depicted in Figure 2.1(a). Only two beams are shown in Figure 2.1(a) but, in general, there may be three, four, or more beams. The reference waves may be monochromatic plane waves, cylindrical waves, spherical waves, etc.

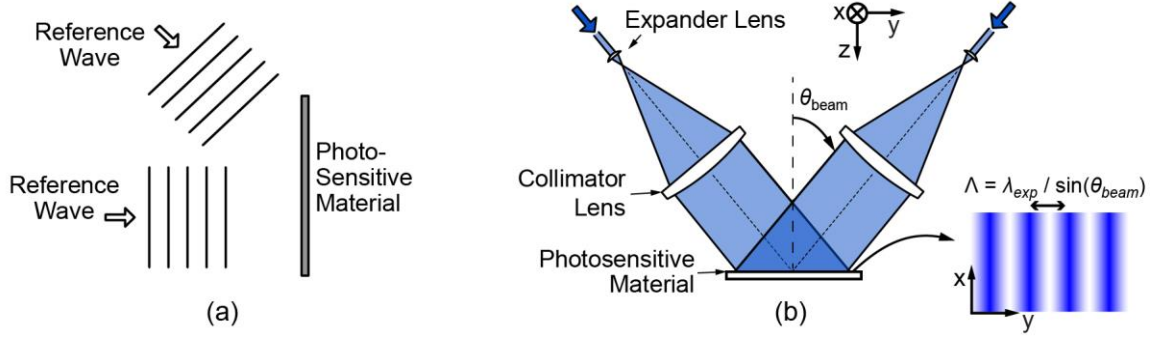


Figure 2.1: (a) Conventional optical interference as the superposition of two reference waves. (b) Canonical interference system configuration.

In the plane of exposure, the multi-beam interference pattern depends on the 1D interference fringes produced by all the possible beam pairs. In the general case of N-beam interference, $N \times (N - 1) / 2$ fringe patterns are generated and superposed. Therefore, the period and the symmetry of the final interference pattern depend on these individual fringe patterns. For the interference of N polarized, monochromatic plane waves, the time-average intensity distribution of the interference pattern may be expressed as [106]

$$I_{MBIL}(\mathbf{r}) = \frac{c_0}{2} \text{Re} \left[\sum_{i=1}^N \mathbf{E}_{pw,i}(\mathbf{r}) \cdot \sum_{i=1}^N \mathbf{E}_{pw,i}^*(\mathbf{r}) \right], \quad (2.1)$$

where c_0 is a unit homogeneity factor term, \mathbf{r} is the spatial coordinate vector, and $\mathbf{E}_{pw,i}$ is the complex electric field vector of the i^{th} plane-wave interfering beam. $\mathbf{E}_{pw,i}$ may be represented in terms of its norm, $E_{pw,i}$, wavevector, \mathbf{k}_i , initial phase, ϕ_i , and normalized field direction, $\hat{\mathbf{e}}_i$, as

$$\mathbf{E}_{pw,i}(\mathbf{r}) = E_{pw,i} \exp[-j(\mathbf{k}_i \cdot \mathbf{r} - \phi_i)] \hat{\mathbf{e}}_i. \quad (2.2)$$

In MBIL, a change in phase of one or more of the interfering beams results simply in a spatial shift of the interference pattern. Hereafter in the thesis, the beam phase, ϕ_i , equals zero.

A canonical interference system is shown in Figure 2.1(b). Experimental research in optical interference benefited dramatically from the development of the laser, which offered an unprecedented temporally coherent source. For high contrast interference fringes, the input beams also need to be mutually coherent and thus, are invariably derived from the same laser source. In Figure 2.1(b), the two beams shown would produce linear fringes equally spaced by a period, Λ_{1D} , expressed as

$$\Lambda_{1D} = \frac{2\pi}{|\mathbf{k}_2 - \mathbf{k}_1|} = \frac{\lambda_{exp}}{2\sin\theta_{beam}}, \quad (2.3)$$

where λ_{exp} is the free-space wavelength and θ_{beam} is the common beam incidence angle defined between the z-axis normal to the substrate surface and the wavevectors. Although the expression of Λ_{1D} depends on the beam configuration, it is always proportional to the inverse of $\sin(\theta_{beam})$ in the plane of the substrate. As discussed in Chapter 1, the optical interference pattern can be recorded in a photoresist film by MBIL for microfabrication purposes.

2.1.2 Holography

While optical interference requires two or more reference waves, holography may be described as the interference of a reference wave with a subject wave as depicted in Figure 2.2(a). The feasibility of holography was first demonstrated in 1948 by Dennis Gabor [107] and later improved by Leith and Upatnieks [108, 109], who introduced an off-axis reference wave configuration as shown in Figure 2.2(a).

In many holographic applications, the subject wave is a 2D Fourier transform of a 2D amplitude transmittance Object A as shown in Figure 2.2(b) [110]. The Fourier transform amplitude is produced in the back focal plane of Lens 1 by placing the Object A in the front

focal plane of that lens and coherently illuminating it. The reference wave is plane-wave-like in nature and overlaps the subject wave at the back focal plane of Lens 1. The interference pattern, typically recorded in a photosensitive material, is the Fourier transform hologram of Object A. By illuminating the hologram with the original reference beam as depicted in Figure 2.2(c), the Fourier transform of Object A is reproduced and Object A can be reconstructed, albeit upside down and left-right reversed, by using a second lens performing a Fourier transform. In addition to the arrangement shown in Figure 2.2(b), a multitude of holographic system configurations have been designed, analyzed, and developed and many of these appear in principal books on the subject [111-113]. Nevertheless, regardless of their complexity, all of these configurations are essentially comprised of a reference wave and a subject wave that interfere at a photosensitive material as represented by Figure 2.2(b).

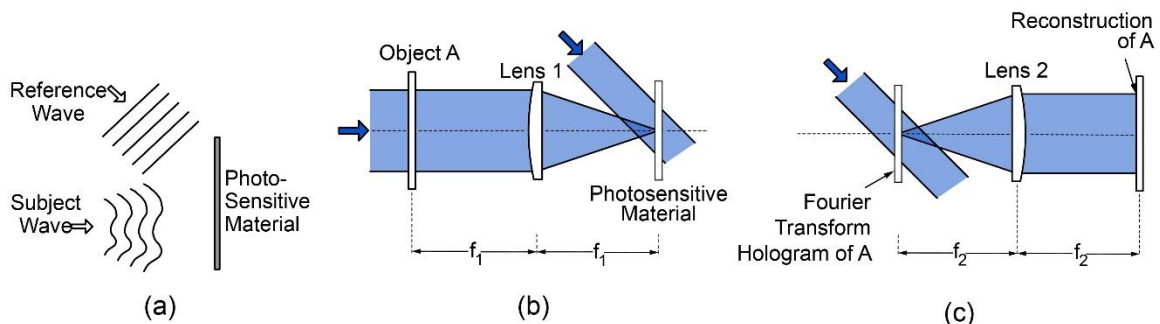


Figure 2.2: (a) Conventional holography as the interference of a subject wave with a reference wave. (b) Recording of the Fourier transform hologram of an Object A. (c) Reconstruction of Object A by illuminating the hologram with the reference wave.

Similar to optical interference, the development of holography came at the same time as the invention of the laser which provided the needed coherent source and thus, enabled the formation of high-contrast interference fringes. Holograms are now widely used, for

example, for security purposes on credit cards, currency, and official documents; as biosensors to detect, for instance, pancreatic disorders [114]; and in the area of data storage with holographic data recording systems that store 500GB on a Blu-ray disk [115].

2.2 PIIL Concept

Considering interference as the combination of two or more reference waves and holography as the combination of a reference wave and a subject wave, conceptually leads to other possibilities including incorporating waves that have joint reference and subject roles. The terminology pattern-integrated interference (PII) has been put forward as an appropriate description of an example of this case [103]. For present purposes, it is simply stated that pattern-integrated interference systems are based on the interference between two, three, or more reference/subject waves. In PII, each wave has a dual role as both a reference wave and as a subject wave as depicted in Figure 2.3. The multiple reference/subject waves can be identical to each other or may differ from one another. The exposure, formation, and processing of the resulting patterns in a photoresist is therefore called pattern-integrated interference lithography (PIIL).

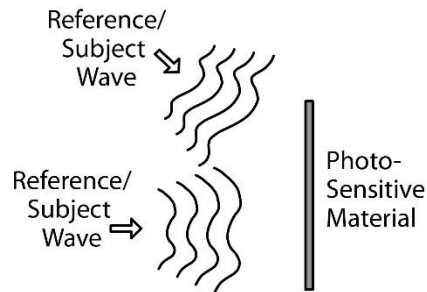


Figure 2.3: PII as the superposition of two, three, or more reference/subject waves. The resulting interference patterns may be recorded in a photosensitive material.

The PIIL technique is illustrated in the conceptual optical system depicted in Figure 2.4(a). Using expander lenses (ELs), a condenser lens (CL), and two objective lenses (OL1 and OL2) arranged in an $8f$ confocal lens configuration, multiple laser beams with free-space exposure wavelength λ_{exp} are sequentially focused, collimated, focused, and collimated. For clarity, only two beams are shown in Figure 2.4(a), but more beams propagating through the system can be arranged around the z -axis. At the back focal plane of OL2, the collimated beams overlap and interfere. Although not shown in Figure 2.4(a), the multiple beams are generated from a single laser beam and are individually controlled in amplitude and polarization using a combination of half-wave plates and polarizing beam-splitter cubes [81]. In addition, the lateral displacement from the z -axis, d_{beam} , can be adjusted for each beam to control the common beam incidence angle at the back focal plane of OL2, θ_{beam} . Since the amplitude, polarization, and direction of the beams are individually controlled, 2D and 3D interference patterns with a broad range of lattice symmetries and lattice constants can be generated. With appropriate beam polarizations and amplitudes, the three- and four-beam umbrella configurations depicted in Figure 2.4(b) produce a 2D interference pattern with square lattice symmetry and a 3D face-centered rhombohedral lattice, respectively.

In addition, the two objective lenses OL1 and OL2 are arranged in a Fourier transform configuration and thus, form a confocal projection lens with an object plane (OL1 front focal plane) and an image plane (OL2 back focal plane). When a photomask object is placed at the OL1 front focal plane, Fourier transforms of the photomask amplitude transmittance are produced by the off-axis beams. OL2 then performs an inverse Fourier

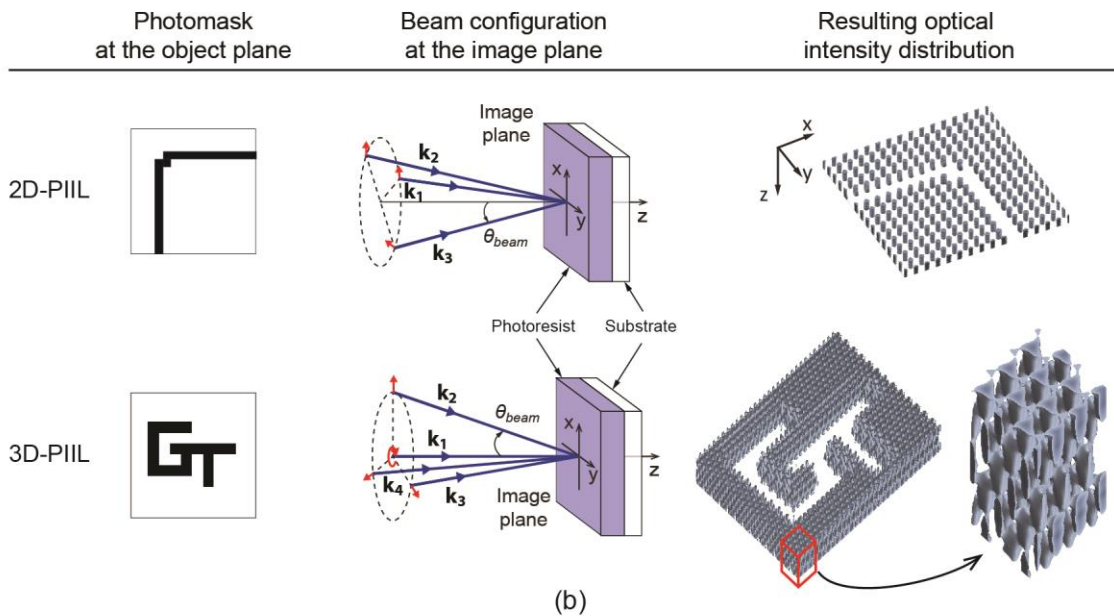
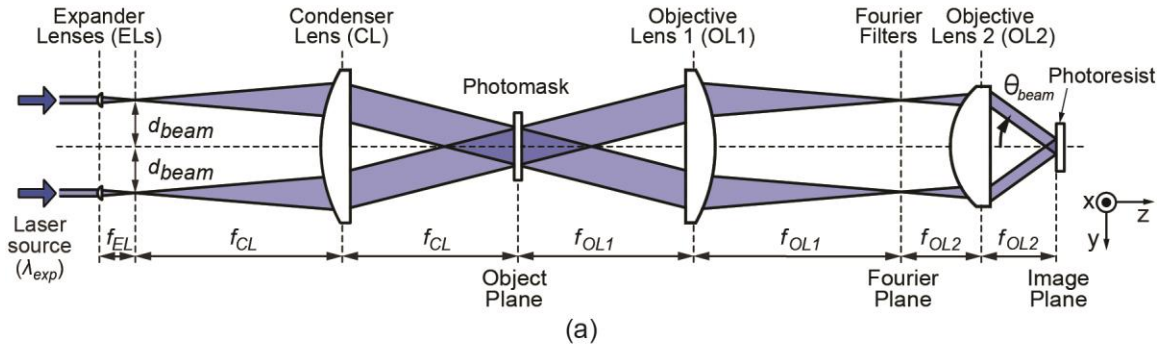


Figure 2.4: (a) A conceptual PIIL system consists of an $8f$ optical system, where multiple polarization- and amplitude-controlled laser beams project demagnified images of a photomask, which overlap and interfere at the image plane of the system. Only two beams are shown for clarity but, there may be three, or more beams. (b) By carefully adjusting the beam amplitudes, polarizations, and directions, 2D and 3D interference patterns that integrate the photomask pattern can be produced in a single exposure.

transform and projects images of the photomask at the OL2 image plane, albeit upside down, left-right reversed, and demagnified by the ratio of the objective lens focal lengths, $M = f_{OL2} / f_{OL1}$. Once they overlap, the photomask images interfere and produce a custom-modified interference pattern that integrates the photomask pattern. The PIIL technique consists in recording this custom-modified interference pattern within a photoresist film for microfabrication purposes. Therefore, PIIL enables the rapid, single-exposure step fabrication of a wide variety of large-format 2D and 3D periodic-lattice-based microstructures. Example photomasks and representative 2D and 3D PIIL exposures are shown in Figure 2.4(b) to illustrate typical results.

2.3 PIIL Model

For the past 50 years, optical lithography simulators have driven the development of increasingly complex photolithographic systems that are used in micro- and nanotechnologies [116]. Therefore, quantifying the fundamental capabilities and limitations of PIIL requires the development of a new comprehensive model describing the formation of custom-modified interference patterns by PIIL. Commercial ray tracing and conventional photolithography simulators were initially tested to simulate PIIL [117-119]. These software packages, however, have proved to be unsatisfactory in simulating both multi-beam imaging and multi-beam interference lithography simultaneously. Therefore, a comprehensive model has been developed to simulate PIIL exposures.

2.3.1 High-NA Optics Considerations

The numerical aperture (NA) of a lens is expressed as

$$NA = n_{imm} \sin\theta_{max}, \quad (2.4)$$

where n_{imm} is the real part of the refractive index of the immersion medium surrounding the lens and θ_{max} is the maximum half-angle of diffracted light that can propagate through the lens as shown in Figure 2.5. The NA describes the light acceptance cone of the lens. The quantity n_{imm} is generally equal to one for a “dry” system, but immersion fluids can be used to increase artificially the NA without increasing the size of the lens [120, 121].

In the conceptual PIIL system of Figure 2.4(a), an OL2 with high NA is desirable for both the formation of the multi-beam interference pattern and the photomask imaging. For the interference pattern, a high-NA OL2 enables larger θ_{beam} and thus, smaller interference periodicity, which decreases with increasing θ_{beam} . For the photomask imaging, the critical dimension, which is the smallest photomask feature that the objective lens can image, is given by the well-known variation of the Rayleigh’s formula,

$$R = \frac{k_p \lambda_{exp}}{NA}, \quad (2.5)$$

where k_p is a process-dependent quantity. To decrease the critical dimension, k_p has been continuously reduced through photoresist improvements and resolution enhancement techniques [122], exposure wavelengths have been progressively reduced from visible to extreme ultra-violet wavelengths [123-126], and the NA has been increased using immersion fluids [120, 121]. Therefore, using a high-NA OL2 in PIIL enables the projection and integration of smaller photomask patterns within interference-based periodic lattices.

2.3.2 Vector Model of High-NA Imaging in Thin Films

For low-NA optical system, imaging can be modeled using a scalar model based on the Fresnel approximation [110]. However, as light propagates through a lens with a NA larger than 0.6, the direction of the electric field begins to be affected [127]. Specifically, a field lying in the xy -plane prior to a high-NA lens will be rotated after the lens and have different vector components along the x -, y -, and z -direction as illustrated in Figure 2.5. In PIIL, such field direction changes impact both the photomask imaging and the formation of the interference pattern, whose absolute contrast, contrast uniformity, and lattice symmetry depend on the interfering electric fields [128, 129]. Since field direction changes cannot be neglected, a scalar modeling is inadequate under high-NA conditions and thus, the PIIL model must account for the vector nature of each interfering/imaging beam.

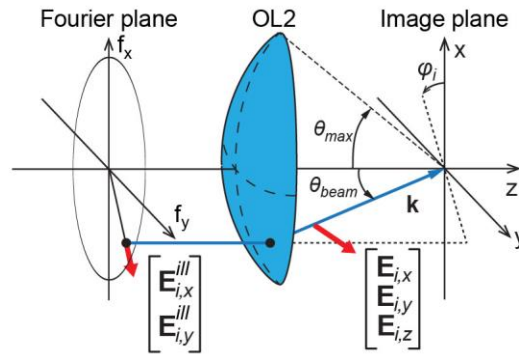


Figure 2.5: Illustration of light propagation and polarization rotation through a high-NA lens.

Yeung [130] first developed a vector model to calculate the aerial image produced by a high-NA imaging system, although along one spatial dimension only. Yeung's method was significantly improved by Flagello *et al.* [127], who proposed a 3D vector model of high-NA imaging including effects of stacked thin films on a substrate in a computer-

friendly matrix format. According to Flagello's formalism, the 3×1 vector image electric field \mathbf{E}_i produced within the volume of the first film of a stack of thin films by the i^{th} interfering beam may be expressed as [127]:

$$\begin{aligned} \mathbf{E}_i(x,y,z) = \mathcal{F}^{-1} & [\mathbf{M}_F^{3 \times 5}(\alpha, \beta, z) \mathbf{M}_P^{5 \times 2}(\alpha, \beta) \mathbf{E}_i^{ill} O(\alpha, \beta) \\ & \times P(\alpha, \beta) S(\theta_{beam}, \varphi_i) \exp(-j2\pi\gamma z_0) \\ & \times \exp(-j2\pi W(\alpha, \beta)) C(\alpha, \beta)], \end{aligned} \quad (2.6)$$

where (x, y, z) are the Cartesian coordinates in the image space; \mathcal{F}^{-1} is the inverse Fourier transform; α , β , and γ are the direction cosines in the Fourier space normalized with respect to the image-side NA; $\mathbf{M}_F^{3 \times 5}(\alpha, \beta, z)$ is a 3×5 film function matrix that is a function of the complex refractive indices of the stacked thin films (including the photoresist) and accounts for the electric-field-dependent reflections, transmission, and absorption of the downward- and upward-traveling waves at the interfaces between the stacked thin films; $\mathbf{M}_P^{5 \times 2}(\alpha, \beta)$ is a 5×2 electric field correction matrix that accounts for high-NA-based polarization changes produced by OL2; \mathbf{E}_i^{ill} is the input 2×1 vector electric field defined in the xy -plane of the i^{th} beam illuminating the photomask; $O(\alpha, \beta)$ is the Fourier transform of the photomask object assuming a thin-mask approximation; $P(\alpha, \beta)$ is a top-hat transmission function accounting for the limited size of the optics ($P(\alpha, \beta) = 1$ for $\sqrt{\alpha^2 + \beta^2} \leq 1$, 0 otherwise); φ_i is the beam azimuthal angle at the image plane; $S(\theta_{beam}, \varphi_i)$ describes the off-axis propagation of the beam; z_0 is the distance between the image focal plane and the surface of the photoresist film and represents a defocus term; $W(\alpha, \beta)$ is the optical path difference function due to lens aberrations; and $C(\alpha, \beta)$ is an energy conservation factor due to the differential areas on the OL1 entrance and OL2 exit pupil surfaces. The detailed

equations for $\mathbf{M}_F^{3 \times 5}$, $\mathbf{M}_P^{5 \times 2}$, $C(\alpha, \beta)$ can be found in Flagello's seminal publication [127].

The $W(\alpha, \beta)$ function is discussed in Appendix A.

To illustrate the comprehensive nature of this model, simulation results for an example photomask imaged by a single off-axis propagating beam are shown in Figure 2.6. Simulation parameters including the photoresist thickness, t_{PR} , photoresist complex refractive index, \mathbf{n}_{PR} , and substrate complex refractive index, \mathbf{n}_{sub} , are listed in Table 2.1.

Table 2.1: Simulation parameters used for the simulation results of Figure 2.6.

$\theta_{beam} (deg)$	NA	M	$\lambda_{exp} (nm)$	\mathbf{E}_i^{ill}	$\varphi_i (deg)$	\mathbf{n}_{PR}	$t_{PR} (\mu m)$	\mathbf{n}_{sub}	$z_0 (\mu m)$
25.4	0.8	0.25	363.8	[0 1]	-45	1.73- j0.003	5	1.47	0

The magnitudes of the quantity inside the inverse Fourier transform transformation in Equation (2.6) along the x-, y-, and z-axis are shown in Figure 2.6(b). The circular shapes are due to the $P(\alpha, \beta)$ function that accounts for the OL2 clear aperture and truncates spatial frequencies beyond the NA of OL2. The center of the photomask diffraction pattern is not centered on the origin (0, 0), but shifted by $(\sin\theta_{beam} \times \cos\varphi_i, \sin\theta_{beam} \times \sin\varphi_i)$ from the origin due to the off-axis propagation of the beam represented by the $S(\theta_{beam}, \varphi_i)$ term. The energy conservation term $C(\alpha, \beta)$ is a circularly symmetric function that produces the rings visible in the projection along the x-direction. These rings are also present in the two other projections, but not distinguishable due to the color bar scale. Finally, although the illuminating electric field \mathbf{E}_i^{ill} is y-polarized, projections along the x- and z-axis are present due to the polarization changes accounted for in the $\mathbf{M}_P^{5 \times 2}(\alpha, \beta, z)$ term. The magnitude of

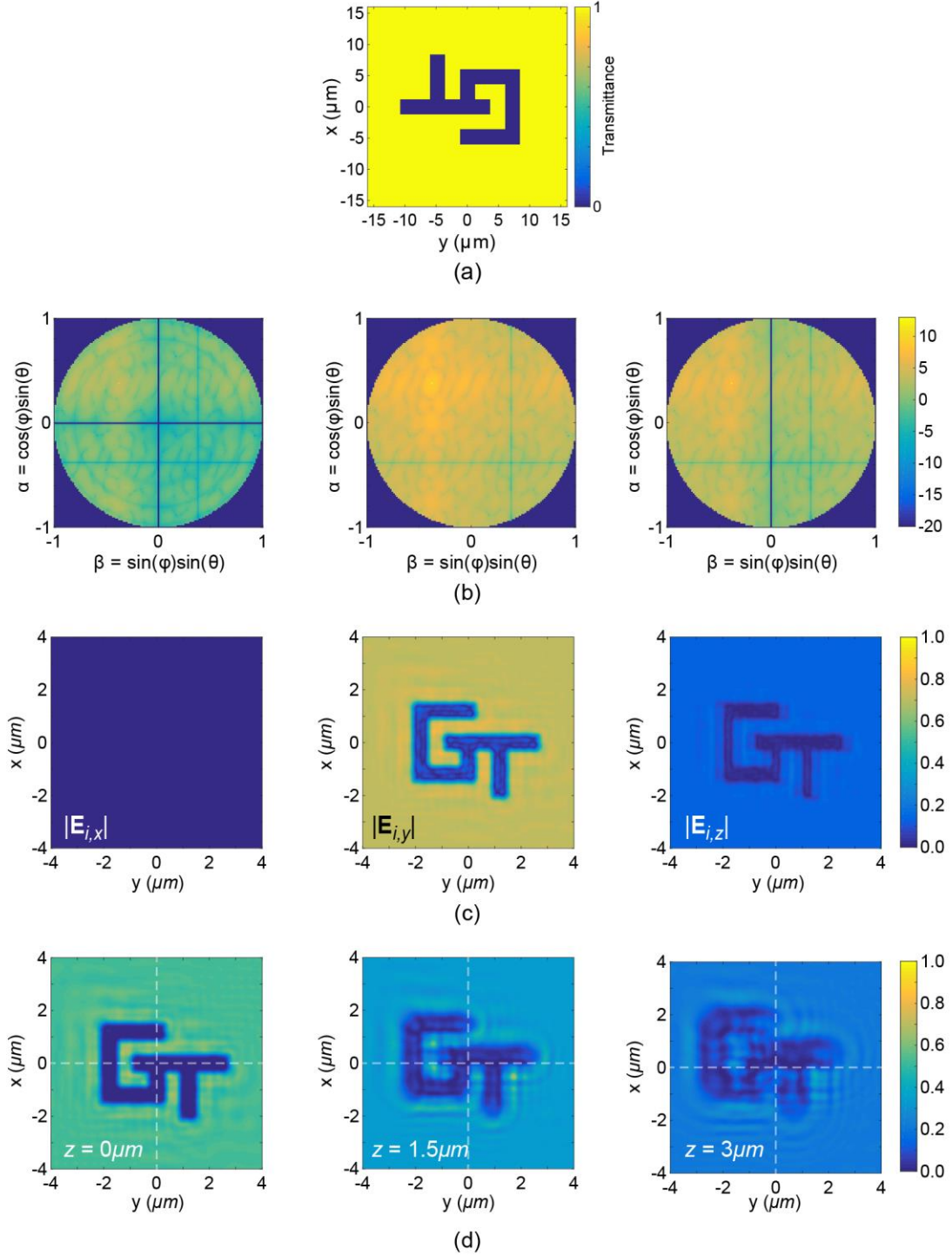


Figure 2.6: (a) Example photomask transmittance. (b) Magnitude of the complex projection of the diffraction pattern along the x -, y -, and z -axis. (c) Magnitude of the x -, y -, and z -component of \mathbf{E}_i at the photoresist surface ($z = 0 \mu\text{m}$). (d) $|\mathbf{E}_i|^2$ at depths $z = 0 \mu\text{m}$, $z = 1.5 \mu\text{m}$, and $z = 3 \mu\text{m}$ illustrating defocus, off-axis imaging, and photoresist absorption effects.

the x-, y-, and z-components of the vector electric field $\mathbf{E}_i(x,y,z)$ at the plane of focus are shown in Figure 2.6(c). Although initially y-polarized, the electric field at the image plane has a non-negligible component along the z-axis. Finally, $|\mathbf{E}_i|^2$ calculated at $z = 0\mu m$, $z = 1.5\mu m$, and $z = 3\mu m$ from the photoresist surface are shown in Figure 2.6(d). Defocus effects, position shift due to off-axis beam propagation, and photoresist absorption are noticeable.

2.3.3 MBIL Model

Since multiple beams are producing multiple images of the photomask in PIIL, the vector model of high-NA imaging can be used to simulate the complex electric field distribution within the volume of the photoresist of each imaging/interfering beam, $\mathbf{E}_i(\mathbf{r})$. To model the final PIIL exposure, the N simulated volume images $\mathbf{E}_i(\mathbf{r})$ are then combined using the expression of the time-average intensity distribution for the interference of N polarized, monochromatic waves expressed in Equation (2.1). The PIIL exposure intensity distribution, $I_{PIIL}(\mathbf{r})$, is expressed as

$$I_{PIIL}(\mathbf{r}) = \frac{c_0}{2} \operatorname{Re} \left[\sum_{i=1}^N \mathbf{E}_i(\mathbf{r}) \cdot \sum_{i=1}^N \mathbf{E}_i^*(\mathbf{r}) \right]. \quad (2.7)$$

The interference between the multiple photomask images produces a photomask-integrated interference-based periodic lattice. Away from the integrated photomask pattern, the symmetry, periodicity, motif size and shape, and contrast of the interference pattern depend on the amplitudes, polarizations, and wavevectors of the interfering/imaging beams [106]. A flow chart describing the calculation of the PIIL exposure is shown in Figure 2.7.

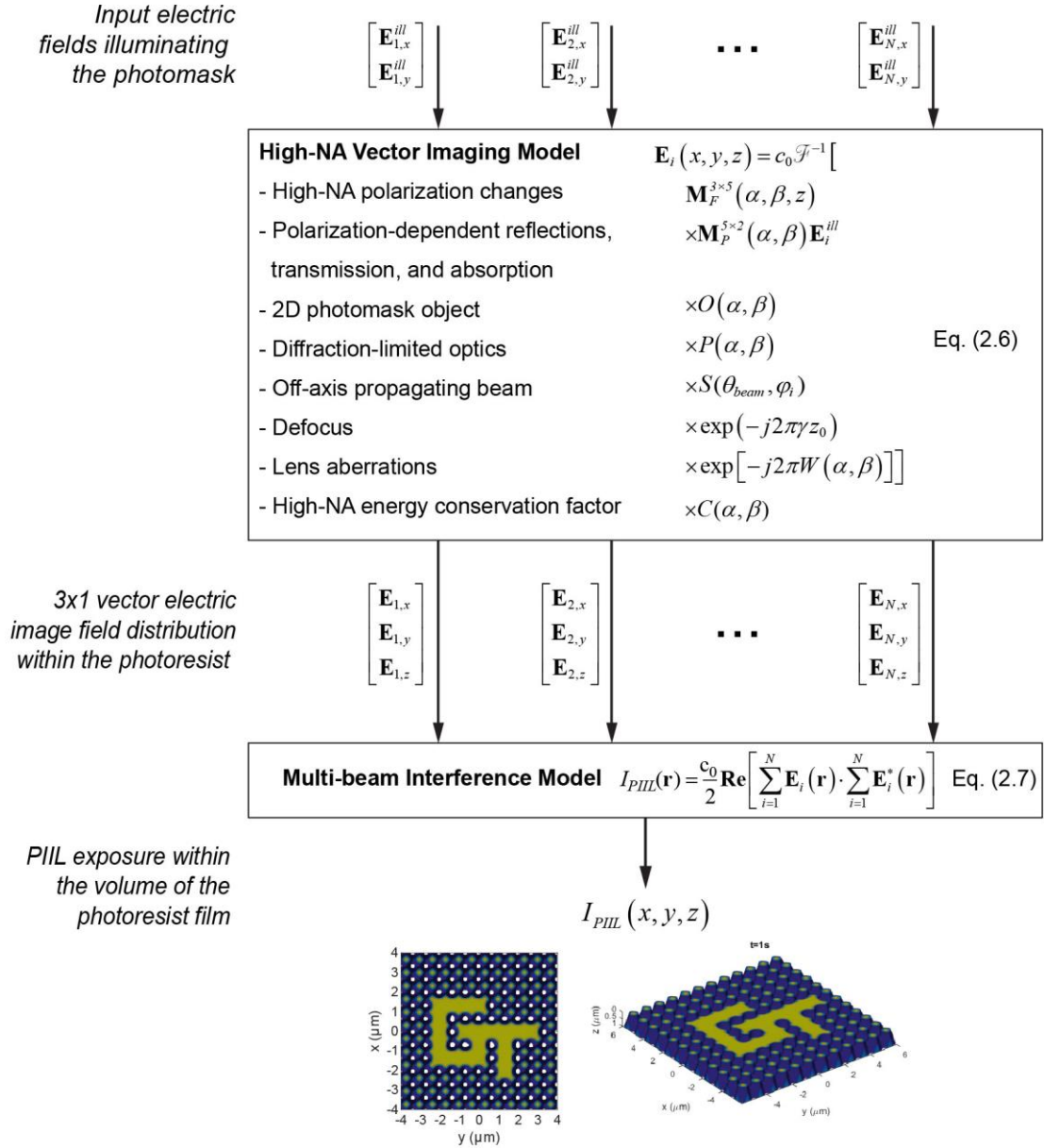


Figure 2.7: Flow chart of the calculation of the optical intensity distribution within the photoresist film produced by the PIIL exposure. The vector electric field distribution produced by each beam in the volume of the photoresist are first calculated with Equation (2.6) before being combined using the multi-beam interference model with Equation (2.7).

The novel multi-beam high-NA vector interference/image model has been implemented using the MATLAB numerical computing environment, which is well suited for image processing, matrix manipulations, and algorithm implementation. MATLAB scripts and custom function are given in Appendix B. The MATLAB script has further been integrated into a PIIL simulator software package with a graphical user interface (GUI) to facilitate its utilization and the simulation of 2D and 3D PIIL exposures. A screen capture of the PIIL simulator GUI is shown in Figure 2.8.

2.4 Time-Dependent Exposure Simulations

Generally, the topology of the patterned photoresist can be approximated by considering the calculated optical intensity distribution below or above a constant intensity threshold. By varying the intensity threshold, different energy doses received by the photoresist can be simulated. However, the PIIL model presented in Section 2.3 does not account for the exposure kinetics and photoresist bleaching effects. Photoresist bleaching during the exposure is a decrease in photoresist absorption, α_{PR} , that may be expressed for positive-tone photoresist as [131]

$$\alpha_{PR}(\mathbf{r}, t) = A_D \times c_{PAC}(\mathbf{r}, t) + B_D, \quad (2.8)$$

where A_D and B_D are the first and second Dill's parameters, which represent bleachable and non-bleachable absorption coefficients, respectively, and $c_{PAC}(\mathbf{r}, t)$ is the relative concentration of photoactive compound (PAC) that modify the photoresist solubility when exposed. At $t = 0 \text{ sec}$, no PAC has been exposed, $c_{PAC}(t = 0) = 1$, and $\alpha_{PR}(t = 0) = A_D + B_D$. Ultimately, the photoresist will be totally exposed leading to $c_{PAC}(t = \infty) = 0$, $\alpha_{PR}(t = \infty) = B_D$, and $\alpha_{PR}(t = \infty) < \alpha_{PR}(t = 0)$, hence the reduction in absorption coefficient.



Georgia Tech Optics Lab

Pattern Integrated Interference Lithography Simulator v1.0

Photomask Design

Function element:

Blocking cell shape:

Blocking cell aspect ratio:

Physical Parameters

Number of lattice constant across the image (even integer):

Magnification:

Numerical aperture, NA:

Defocus, z0 (in microns):

Photoresist Properties

Photoresist Type: Positive photoresist Negative photoresist

Photoresist thickness (microns): Incremental layers:

Photoresist Type:

- Air/No photoresist
- S1813 on glass
- SU8 on Si
- SU8 on Glass
- User defined photoresist

User Defined Values			
A	<input type="text" value="0"/>	k_PR	<input type="text" value="0"/>
B	<input type="text" value="0"/>	n_sub	<input type="text" value="0"/>
C	<input type="text" value="0"/>	n_BARC	<input type="text" value="0"/>
n_PR	<input type="text" value="0"/>	BARC_depth	<input type="text" value="0"/>

Beam Parameters

Beam Configuration

- 3 Beams / 2D Square Lattice
- 3 Beams / 2D Hexagonal Lattice
- 4 Beams / 2D Square Lattice
- 4 Beams / 3D Face-Centered Cubic Lattice
- 5 Beams / 3D Woodpile Lattice (Diamond)
- User defined beam configuration

User Defined Values

N_unit_scaled_x	N_unit_scaled_y	Beam 1	Beam 2	Beam 3	Beam 4	Beam 5
<input type="text" value="0"/>	<input type="text" value="0"/>	<input type="text" value="0"/>	<input type="text" value="0"/>	<input type="text" value="0"/>	<input type="text" value="0"/>	<input type="text" value="0"/>
Azimuthal angle phi (deg)		<input type="text" value="0"/>				
Angle of incidence theta (deg)		<input type="text" value="0"/>				
Normalized xy-plane coordinates of the polarization		<input type="text" value="0"/>				

Wavelength, λ (nm)

- 193
- 248
- 363.8
- User defined wavelength

Lattice constant, Λ (in nm):

Pixels / Λ (odd integer):

Save/Load

Name of save file:

Name of load file:

Plotting Parameters

Side length of the plotted area (in periods):

[3D Plot] View angle elevation:

[3D Plot] View angle rotation:

[3D Plot] Normalized intensity threshold (between 0 and 1):

[2D Plot] Specific layer to graph (between 0 and "incremental layers"):

Figure 2.8: Screen capture of the PIIL simulator GUI.

Introducing the optical sensitivity parameter or third Dill's parameter, C_D , $c_{PAC}(\mathbf{r}, t)$ may be expressed as a function of I_{PILL} as [131]

$$c_{PAC}(\mathbf{r}, t + \Delta t) = c_{PAC}(\mathbf{r}, t) \times \exp[-C_D \times I_{PILL}(\mathbf{r}, t) \times \Delta t], \quad (2.9)$$

where Δt is a small time increment such that $|c_{PAC}(\mathbf{r}, t + \Delta t) - c_{PAC}(\mathbf{r}, t)| < 0.2$ [131]. Equation (2.9) represents the conversion of the optical intensity distribution into a latent image of chemical reaction products from the exposure of the PAC. Equation (2.9) further reflects the decrease of the PAC concentration with the energy dose $I_{PILL}(\mathbf{r}, t) \times \Delta t$. The new PAC distribution at $t + \Delta t$ can then be used to update the imaginary part of the photoresist complex refractive index as [131]

$$\begin{aligned} \mathbf{n}_{PR}(\mathbf{r}, t + \Delta t) &= n_{PR} - j \frac{\lambda_{exp} \alpha_{PR}(\mathbf{r}, t + \Delta t)}{4\pi} \\ &= n_{PR} - j \frac{\lambda_{exp} (A_D \times c_{PAC}(\mathbf{r}, t + \Delta t) + B_D)}{4\pi}. \end{aligned} \quad (2.10)$$

With this new refractive index value, the new optical intensity distribution at the next time step, $I_{PILL}(\mathbf{r}, t + \Delta t)$, can be calculated. Calculations end when the exposure time, t_{exp} , is reached. A flow chart describing the iterative calculation of c_{PAC} and I_{PILL} is depicted in Figure 2.9.

To illustrate the time-dependent model for PILL exposure, simulation results are shown in Figure 2.10. The photoresist parameters are those of Microchem's S1813 positive-tone photoresist for which $A_D = 1.07 \mu m^{-1}$, $B_D = 0.31 \mu m^{-1}$, $C_D = 0.015 cm^2/mJ$. To simulate a $100 mJ/cm^2$ exposure dose, which is the nominal dose for Microchem's S1813, the optical intensity distribution is normalized and multiplied by a $100 mW/cm^2$ factor and the exposure time, t_{exp} , is $1 sec$. As shown in the last exposure simulation in Figure 2.10, the photoresist film starts to be exposed through and reveal the substrate in white for $t = 1 sec$.

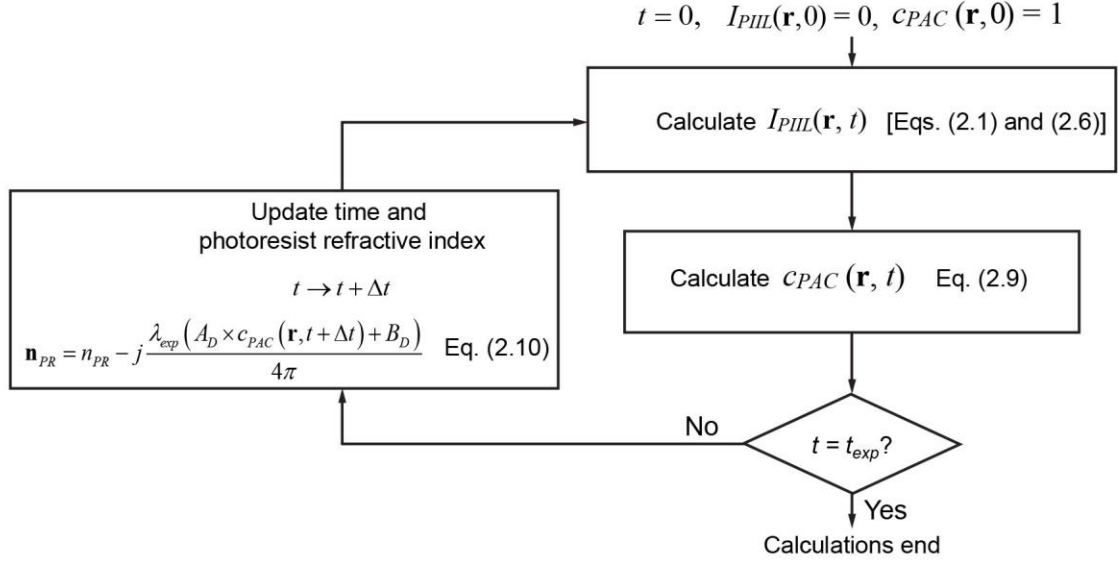


Figure 2.9: Flow chart of the calculation of c_{PAC} and I_{PIL} as a function of time.

2.5 Summary

As a logical progression from optical interference and holography, PII introduces the concept of interference between multiple reference/subject waves. For microfabrication purposes, the novel area of PIIL consists in recording the custom-modified interference pattern produced by PII in a photoresist. The patterned photoresist can subsequently serve as an etching or lift-off mask, or as an infiltration/inversion 3D bicontinuous template.

To simulate PIIL exposures of 2D and 3D PLB microstructures, a comprehensive multi-beam high-NA interference/image vector model was formulated by coupling a high-NA imaging vector model and the multi-beam interference model. This comprehensive model accounts for the off-axis propagation of the beams, the diffraction limit of the projection lenses, polarization changes due to high-NA optics, an energy conservation factor, Fresnel's equations, standing wave effects within the photoresist, photoresist absorption, defocus effects, and possible optical aberrations.

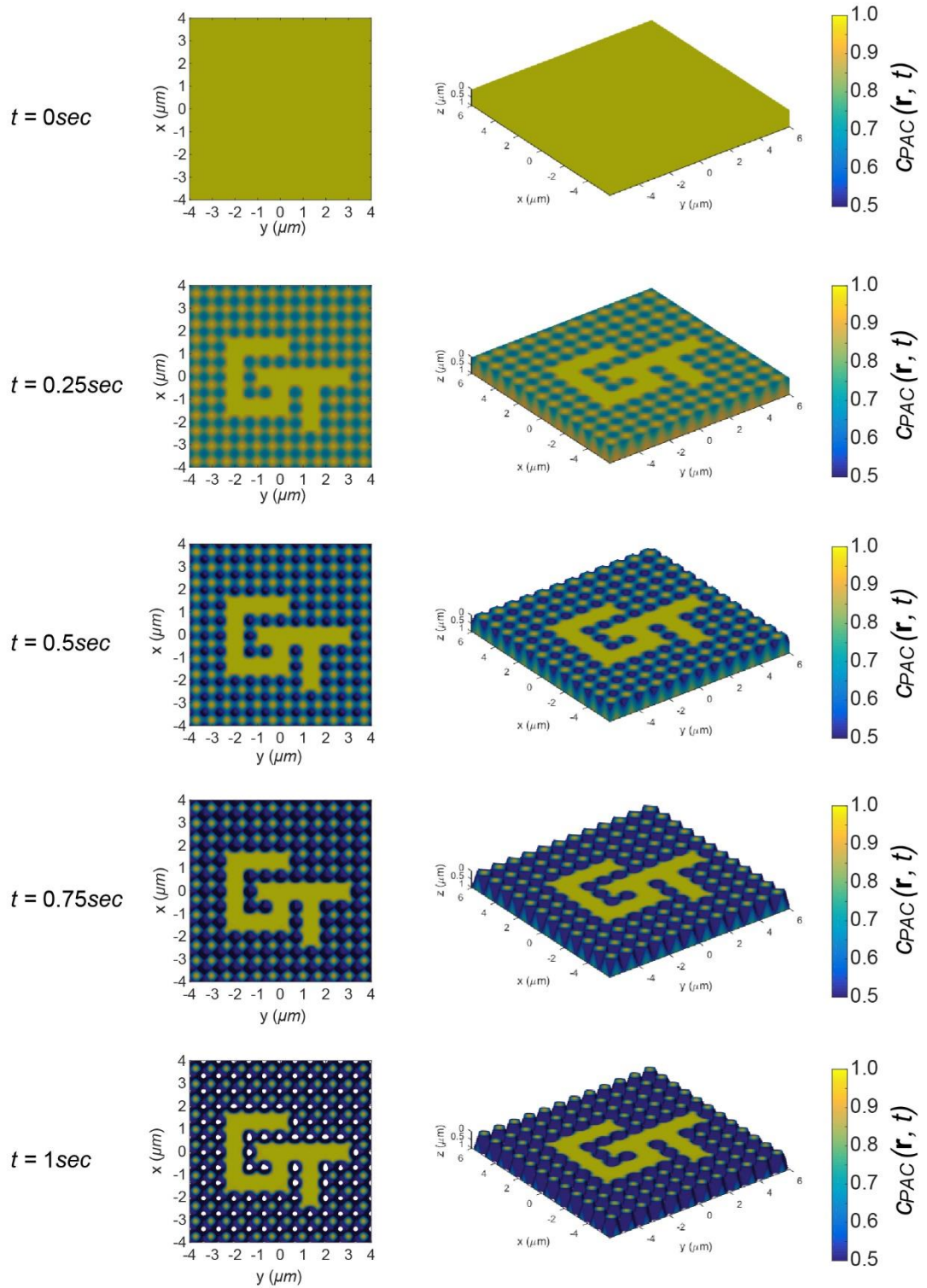


Figure 2.10: Top and isometric views of simulated relative PAC concentration $CPAC(\mathbf{r}, t)$ for a bottom threshold of 50% from $t = 0 \text{ sec}$ to $t_{end} = 1 \text{ sec}$.

To model photoresist exposure kinetics and photoresist bleaching, this formulation can further account for the time-dependent PAC concentration. This PIIL model was finally integrated into a user-friendly software package with a GUI to facilitate PIIL exposure simulations and research.

CHAPTER 3

PATTERN-INTEGRATED INTERFERENCE LITHOGRAPHY FOR TWO-DIMENSIONAL PERIODIC-LATTICE-BASED MICROSTRUCTURES

Perhaps the most documented and studied periodic-lattice-based (PLB) microstructures are photonic-crystal (PhC) devices. As such, they represent an important potential application for PIIL. Using the PIIL vector model derived in Chapter 2, 2D-PIIL exposures for three representative 2D PhC devices are simulated. Realistic lithographic conditions are used; the transfer of the photoresist pattern into the substrate is estimated; and transmission spectra of the PIIL-produced PhC devices are calculated. To mitigate lattice distortions due to the integration of the photomask pattern, the field of photomask optimization for PIIL is introduced and investigated. This research has resulted in two journal papers [94, 95] and a conference presentation [93].

3.1 Photonic-Crystal Devices Design and Simulation Parameters

PhC devices are PLB microstructures made of dielectric materials with different refractive indices that exhibit photonic bandgaps and allow the control of light propagation and light-matter interaction at the wavelength scale [3, 4]. As such, they represent one of the most documented examples of PLB microstructures and a promising application for PIIL. In this Chapter, three representative PhC devices are studied and are depicted in Figure 3.1: a *90deg*-bend waveguide [132], a passband filter [133], and a stopband filter [134]. Although not necessary optimal, the three PhC devices have the same design for consistency: a 2D square-lattice of silicon pillars with a common period of $580nm$ and

pillar radius $r_p = 104nm$. In the near infrared, silicon has a refractive index $n_{Si}(1.5\mu m) = 3.4$ and the PhC exhibits a photonic bandgap for a TM mode, *i.e.* an electric field parallel to the pillars [132]. Removing a single row of pillars from the PhC enables a guided mode for wavelengths ranging from $1.31\mu m$ to $1.86\mu m$.

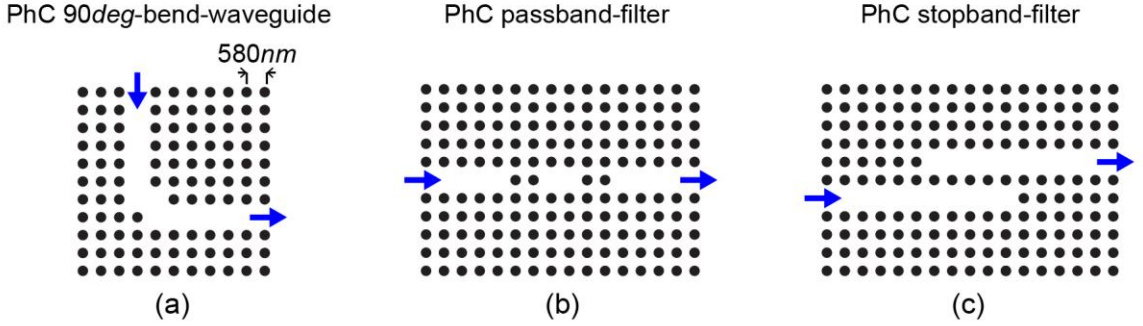


Figure 3.1: Schematic representations of the PhC (a) 90deg-bend waveguide, (b) passband filter, and (c) stopband filter.

The fabrication of the three PhC devices by PIIL is simulated using the PIIL vector model presented in Chapter 2. To produce a 2D square lattice with $p4m$ plane-group symmetry, a three-beam configuration is employed. The arrangement of the interfering beams at the image plane is illustrated in Figure 3.2(a) and a unit cell of the interference pattern is represented in Figure 3.2(b). The beams azimuthal angles are $\varphi_1 = -135deg$, $\varphi_2 = 135deg$, and $\varphi_3 = -45deg$. At the object plane, the linearly-polarized beams illuminating the photomask are $\mathbf{E}_1^{ill} = [\sqrt{2}/2, -\sqrt{2}/2]$, $\mathbf{E}_2^{ill} = [\sqrt{2}/2, 0]$, and $\mathbf{E}_3^{ill} = [0, -\sqrt{2}/2]$. Of note, the intensity of the first beam is twice that of the two other beams. With these beam parameters, the interference pattern has a near-unity absolute contrast, which is lithographically useful, as well as equal contrast along the lattice-vector directions [128]. The free-space exposure wavelength, λ_{exp} , is $248nm$ and the common

beam incidence angle at the image plane, θ_{beam} , is $17.6deg$. The resulting interference period, Λ_{sq} , expressed as

$$\Lambda_{sq} = \frac{\lambda_{exp}}{\sqrt{2} \sin\theta_{beam}} \quad (3.1)$$

equals $580nm$. The image-side numerical aperture, NA, defined in Chapter 2 is 0.8 and the magnification of the compound objective lens, M , is 0.25. The optical system is assumed free of optical aberrations and thus, wavefront phase errors are not included in the present simulation results.

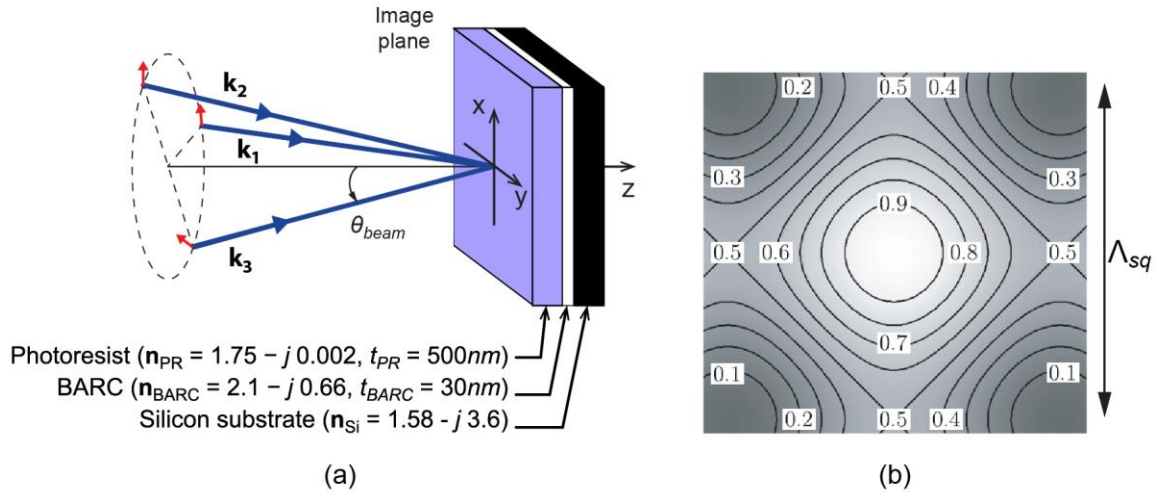


Figure 3.2: (a) Configuration of the three interfering beams at the image plane where the photoresist, BARC, and substrate arrangement is located. (b) Normalized intensity contour for the unit cell of a square-lattice interference pattern with $p4m$ plane group symmetry [128].

The photosensitive material is a $500nm$ -thick film of negative-tone photoresist with a complex refractive index $\mathbf{n}_{PR}(\lambda_{exp}) = 1.75 - j0.002$. A hard intensity threshold is adopted for the photoresist response. A 0.845 normalized intensity threshold is used to produce interference motif with $\sim 104nm$ radius, although the interference motif are not perfectly

circular. It is also assumed that the surface of the photoresist film lies at the plane of best focus and thus, the quantity z_0 equals $0\mu\text{m}$. Silicon with complex refractive index $\mathbf{n}_{\text{Si}}(\lambda_{\text{exp}}) = 1.58 - j3.6$ at the exposure wavelength is chosen as substrate. In the absence of an antireflective coating, the beams are partially back-reflected from the substrate due to the mismatch between the photoresist and the substrate refractive indices. Forward- and backward-propagating waves interference, resulting in detrimental standing waves within the photoresist film. The amplitude of these standing waves can be strongly mitigated with a 30nm -thick bottom antireflective coating (BARC) of hydrogenated silicon oxynitride ($\mathbf{n}_{\text{BARC}}(\lambda_{\text{exp}}) = 2.1 - j0.66$) between the photoresist and substrate [116, 135]. Finally, photomasks with Λ_{sq}/M -wide patterns, hereafter referred to as elementary photomasks, are used as object to be projected. Due to the system demagnification, the photomask pattern width is reduced to Λ_{sq} at the image plane to match the interference period. The elementary photomask for the 90deg -bend waveguide is shown in Figure 3.3(a).

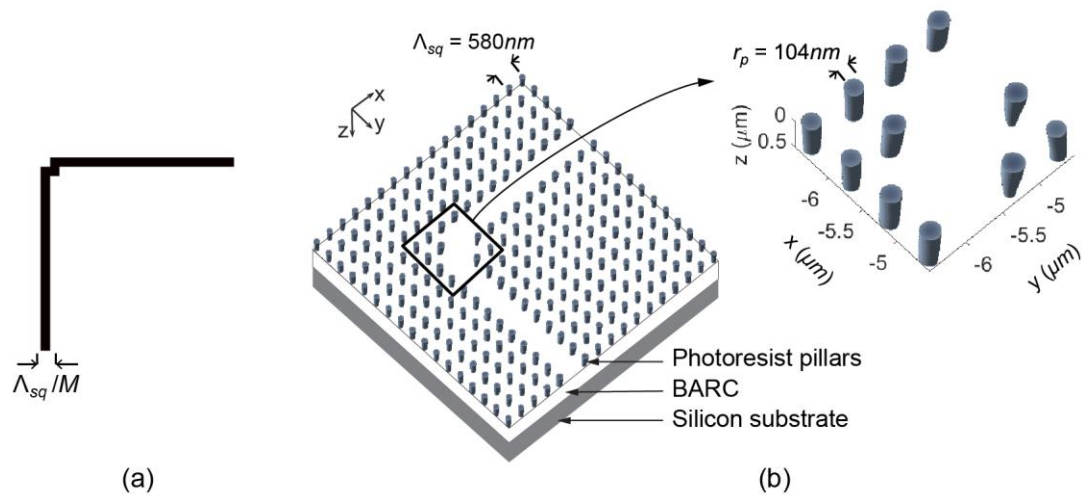


Figure 3.3: (a) Elementary photomask for the 90deg -bend waveguide. Once projected, the waveguide width is Λ_{sq} . (b) Simulated PIIL exposure. The close-up view shows pillar distortions near the integrated waveguide.

A 3D view of the simulated PIII exposure for the $90deg$ -bend waveguide shown in Figure 3.3(b) demonstrate a satisfactory integration of the photomask features within the interference pattern. The pixel resolution in the simulation is $5.74nm/px$ and a single period is $101px$ -long, providing both accurate results and acceptable computational time. While the pillars are essentially unperturbed, a close-up view of the lattice shows that the pillars located next to the waveguide are visibly distorted. These distortions are due to a combination of edge diffraction from the photomask pattern, defocus through the photoresist film, and off-axis imaging effects. Although not completely eliminated, standing waves are strongly mitigated.

In photolithography, the patterned photoresist film is typically used as a mask to transfer a pattern into the substrate through, for example, an anisotropic etching step. To estimate the transferred pattern into the silicon substrate, the union of the 2D pillar profiles in the xy -plane is calculated along the z -axis. The result is a 2D binary structure of the estimated silicon pillar that accounts for the structural variations of the pillars along the x -, y -, and z -direction and thus, shadowing effects during the etching process. A top-view of the resulting binary pattern is shown in Figure 3.4(a), where the black spots correspond to the estimated fabricated silicon pillars. Figure 3.4(b) is obtained by subtracting the estimated silicon pillars from their defect-free equivalents obtained with a blank mask, and hereafter referred to as reference pillars. In Figure 3.4(b), the white (black) pixels have a $+1$ (-1) value and represent pixels that are present (absent) in the estimated pillars, but absent (present) in the reference pillars. As previously noted, pillars next to the waveguide are visibly larger and distorted compared to the reference pillars. Moreover, the larger pillars reduce the effective width of the waveguide by 5.6%. Lattice disorder and structural

variations are known to impact the resonant properties of the PhC and to be responsible for light scattering and radiation losses [136-138]. In particular, Lima *et al.* [139] showed that transmission spectra of a PhC straight waveguide is strongly deteriorated when the borders of the waveguide are affected by disorder. The transmission spectrum may also hop and experience mode shifts when the waveguide width varies [140].

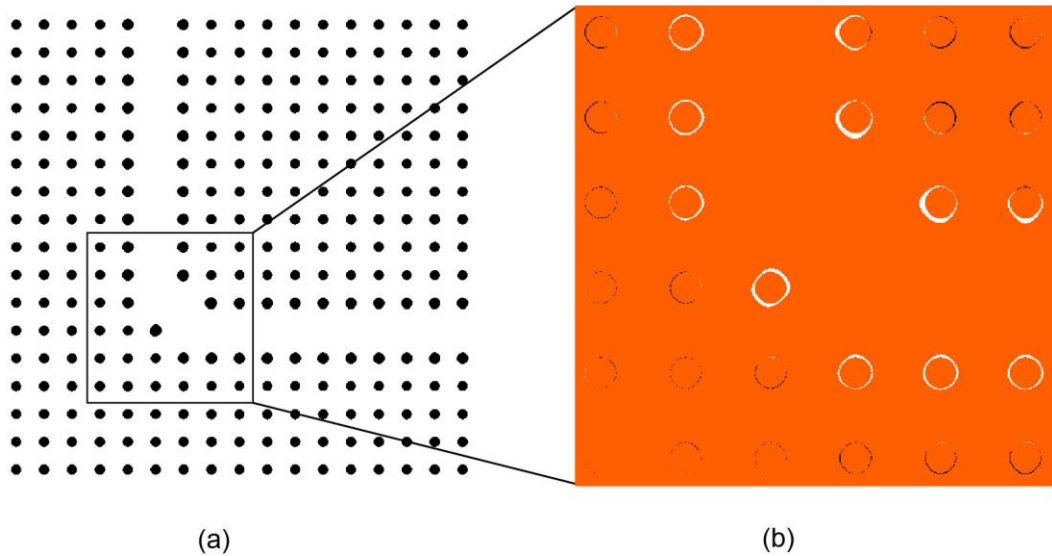


Figure 3.4: (a) Estimated etched structure in the silicon substrate accounting for the 3D structural variations of the pillars. (b) Comparison between the estimated and reference pillars. White (black) pixels represent pixels that are present (absent) in the estimated pillars, but absent (present) in the reference pillars.

3.2 Photomask Improvement

A possible approach to mitigate pillar distortions consists in designing a photomask pattern that would pre-compensate these imperfections. In photolithography, photomask optimization plays a fundamental role in keeping pace with Moore's law and the need for ever smaller photolithographic resolution. To reduce irregularities in projected images, resolution enhancement techniques emerged including optical proximity correction (OPC)

[141], sub-resolution assist features [142], source-mask optimization [143], as well as alternating and attenuated phase-shifting masks [144-146]. Rather than the perfect imaging of a target pattern, the present objective is more the reduction of undesired lattice distortions during the PIIL exposure. To investigate the unexplored area of photomask optimization in PIIL, the problem is reduced to the design of a photomask pattern for a single missing pillar within a 2D square-lattice as depicted in Figure 3.5(a). For this case, the objective is to determine a single-motif-blocking pattern that mitigates distortions on its eight closest pillar neighbors. To determine this pattern, five geometric shapes and nine widths, w , are considered as illustrated in Figure 3.5(b). The shapes include a square, a $90deg$ -rotated square, a hexagon, a $30deg$ -rotated hexagon, and a disc. The widths range from $0.5 \Lambda_{sq}/M$ to $1.3 \Lambda_{sq}/M$. To quantify the distortions, a pillar-area error, e_{area} , defined as

$$e_{area} = \frac{\sum_{m,n} |v(m,n) - \tau(m,n)|}{\sum_{m,n} \tau(m,n)}, \quad (3.2)$$

and a pillar-displacement error, e_{disp} , defined as

$$e_{disp} = \frac{d}{\Lambda_{sq}} \quad (3.3)$$

are defined, where (m,n) are pixel indices within the $101px \times 101px$ area corresponding to the pillar, $v(m,n)$ and $\tau(m,n)$ are the binary pixel values (0 or 1) of the estimated and reference pillar, respectively, and d is the distance between the center of mass of the estimated pillar and its expected location in the lattice. For clarification, the symbols of Equations (3.2) and (3.3) are illustrated in Figure 3.5(c).

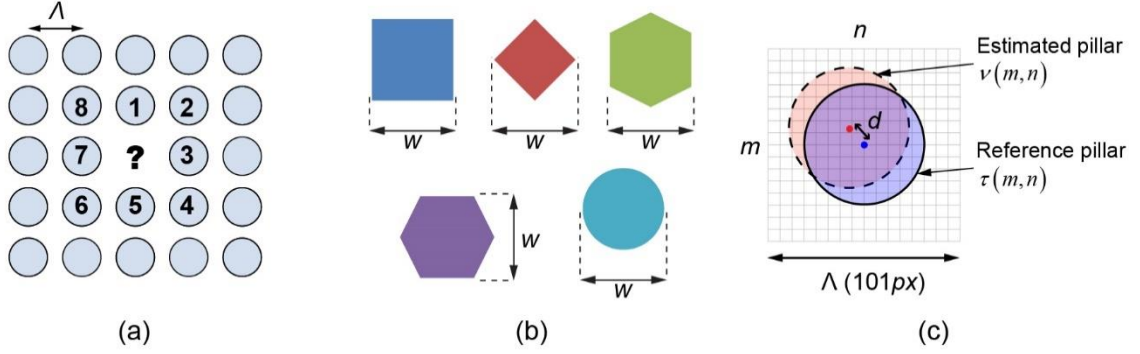


Figure 3.5: (a) Schematic representation of the photomask design problem in PIIL. (b) Five possible geometric shapes for the single-motif-blocking photomask. (c) Illustration of the symbols used in Equations (3.2) and (3.3).

For the five shapes and nine widths, 45 PIIL exposures and corresponding estimated etched pillars are simulated using the beam configuration and materials described previously. For each simulation, the pillar-area and pillar-displacement error of the eight neighbors pillars are calculated and the eight values are averaged. For the five shapes, the average pillar-area error, \bar{e}_{area} , and average pillar-displacement error, \bar{e}_{disp} , are plotted as functions of the element width, w , in Figures 3.6(a) and (b), respectively. The geometric mean $(\bar{e}_{area} \bar{e}_{disp})^{1/2}$ is also calculated as a figure of merit and plotted in Figure 3.6(c) to determine the best pattern. Undersized ($w < \Lambda_{sq}/M$) and oversized elements ($w > \Lambda_{sq}/M$) generate larger pillar distortions due to stronger diffraction effects and overlapping with the interference pattern, respectively. The shape of the pillars is significantly more changed than their relative positions, suggesting that the interference motifs are more impacted than the norm and direction of the lattice vectors. Out of the 45 possible elements, the best candidate to mitigate distortions among the closest pillars is the $0.9\Lambda_{sq}/M$ -wide $45deg$ -rotated square. Noteworthy, the Λ_{sq}/M -wide square initially used as the building block to create the elementary photomask in Figure 3.3(a) represents one of the worst

possibilities. Its figure of merit is three times larger than that of the $0.9\Lambda_{sq}/M$ -wide 45deg-rotated square.

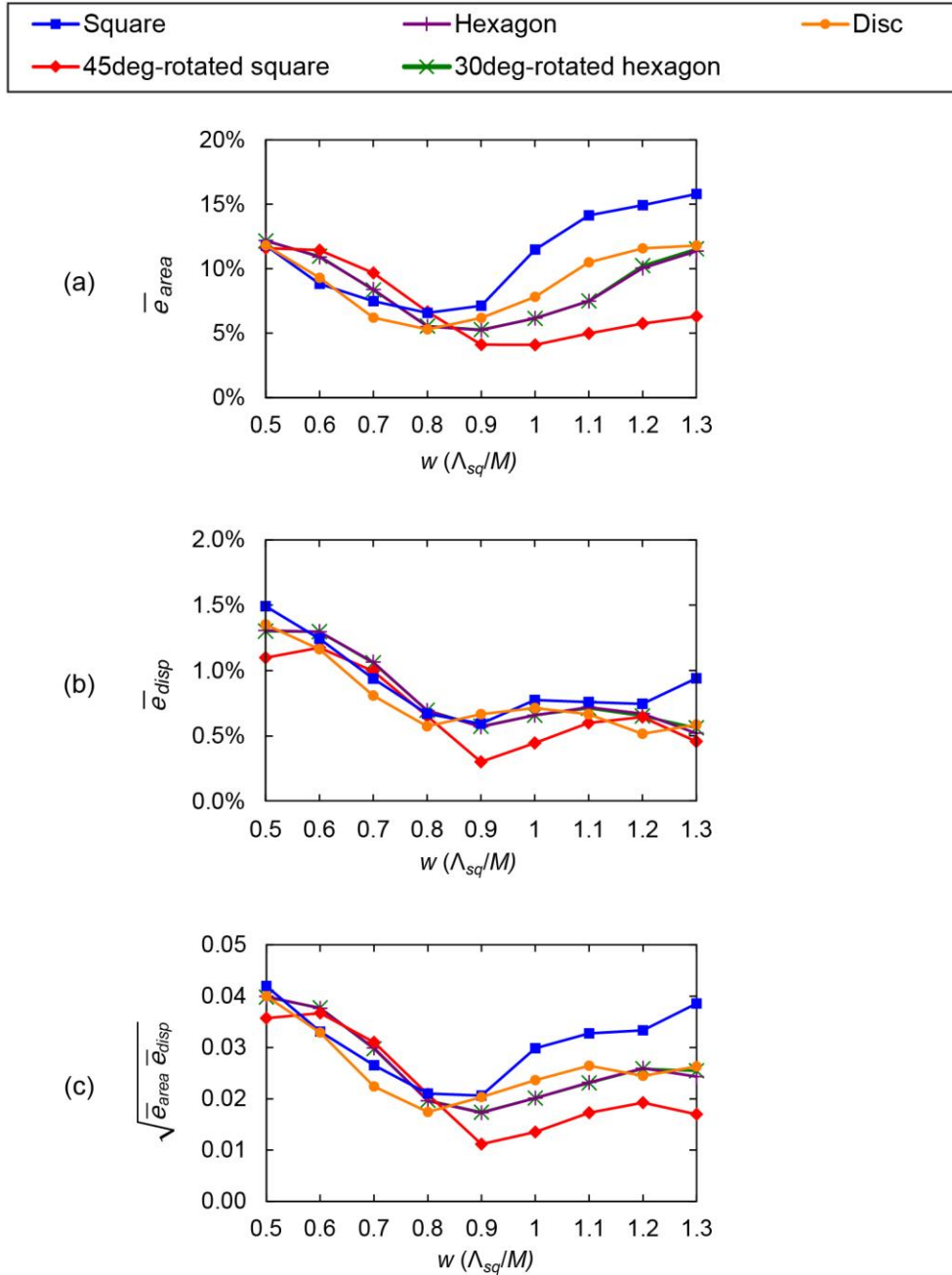


Figure 3.6: (a) Average pillar-area error, \bar{e}_{area} . (b) Average pillar-displacement error, \bar{e}_{disp} . (c) Geometric mean of \bar{e}_{area} and \bar{e}_{disp} as figure of merit. The $0.9\Lambda_{sq}/M$ -wide 45deg-rotated square mitigates pillar distortions the most. Counter-intuitively, the elementary Λ_{sq}/M -wide square exhibits poor performance.

3.3 Simulated PIIL Exposures and Estimated Fabrication

The study on photomask improvement determined that the $0.9\Lambda/m$ -wide $45deg$ -rotated square generates the least pillar distortions. This element is therefore used as a building block to create the complete photomasks of the PhC devices as shown in Figures 3.7(a)-(c). The corresponding simulated PIIL exposures in Figures 3.7(d)-(f) show the successful integration of the photomask within the interference patterns. As shown in the top close-up views of Figures 3.7(d)-(f), the pillars next to the functional elements are significantly less distorted. A couple of periods away from the functional elements, the pillars become undistorted. The conic shapes of the pillars are due to photoresist optical absorption. Residual faint standing waves are indicated by the seven black arrows in Figure 3.7(f). The number of standing waves matches the theoretical value of $t_{PR} / (\lambda_{exp} / 2n_{PR}) \approx 7$.

The estimated pillar structures etched in the silicon substrate are shown in Figures 3.8(a)-(c). The insets are obtained by subtracting the estimated pillars and the reference pillars. For the $90deg$ -bend waveguide, e_{area} and e_{disp} are calculated and averaged for pillars located Λ_{sq} , $2\Lambda_{sq}$, and $3\Lambda_{sq}$ away from the functional element (yellow, blue, and red areas in Figure 3.9(a), respectively). The quantities \bar{e}_{area} and \bar{e}_{disp} are plotted in Figure 3.9(b) for the elementary photomask made of Λ_{sq}/M -wide squares and for the improved photomask made of $0.9\Lambda_{sq}/M$ -wide $45deg$ -rotated squares. With the improved photomask, \bar{e}_{area} and \bar{e}_{disp} are divided by 3.3 and 2.7, respectively, for the pillars closest to the waveguide. Those values are similar for the PhC passband and stopband filters. The effective waveguide width is still slightly reduced, but by 1.9% only (compared to 5.6%).

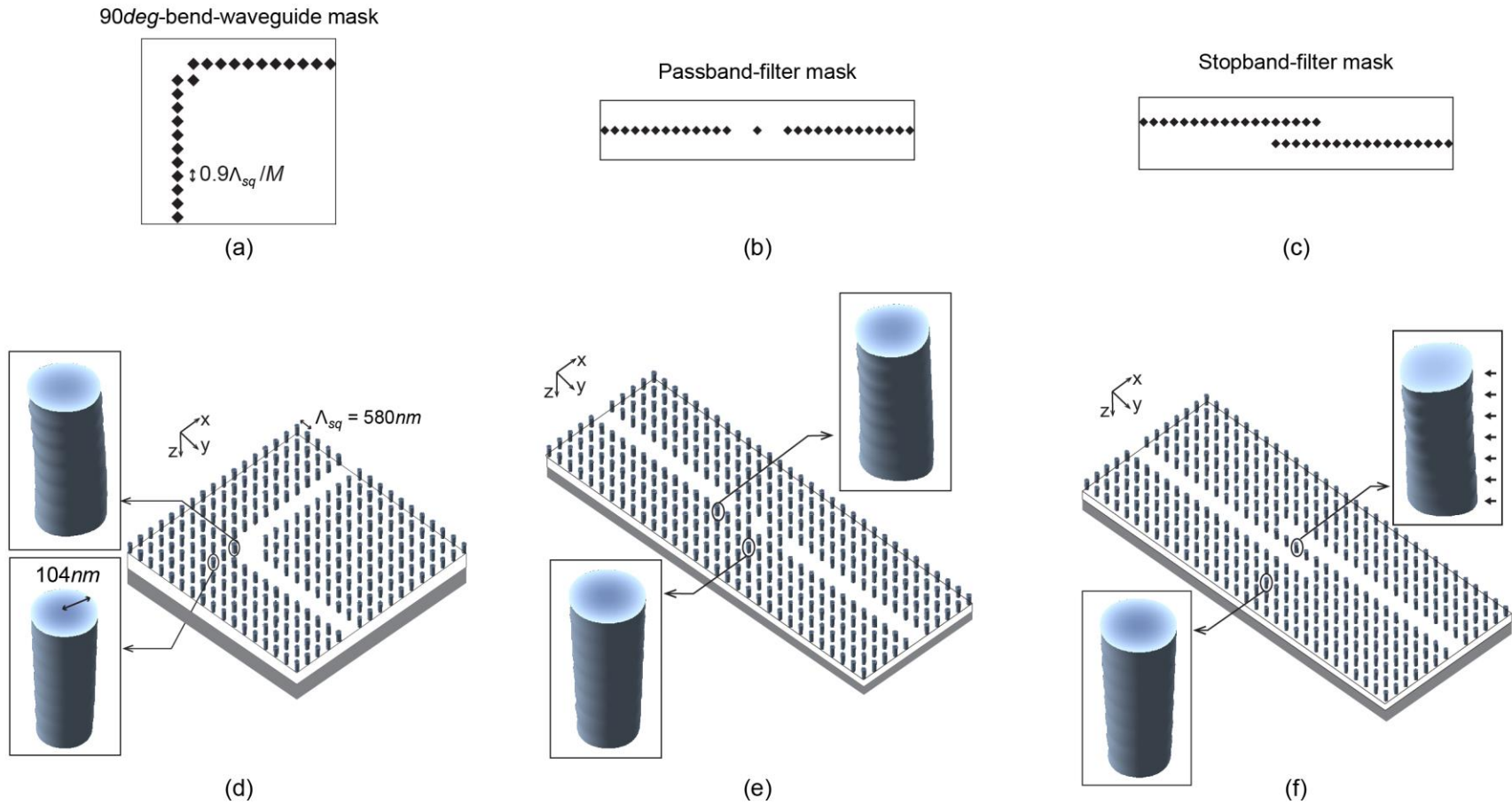


Figure 3.7: Improved photomasks designed with $0.9\Lambda_{sq}/M$ -wide 45deg -rotated squares as building blocks for the (a) PhC 90deg -bend waveguide, (b) passband filter, and (c) stopband filter. (d), (e), and (f) Corresponding simulated PIIL exposures with close-up views on selected pillars.

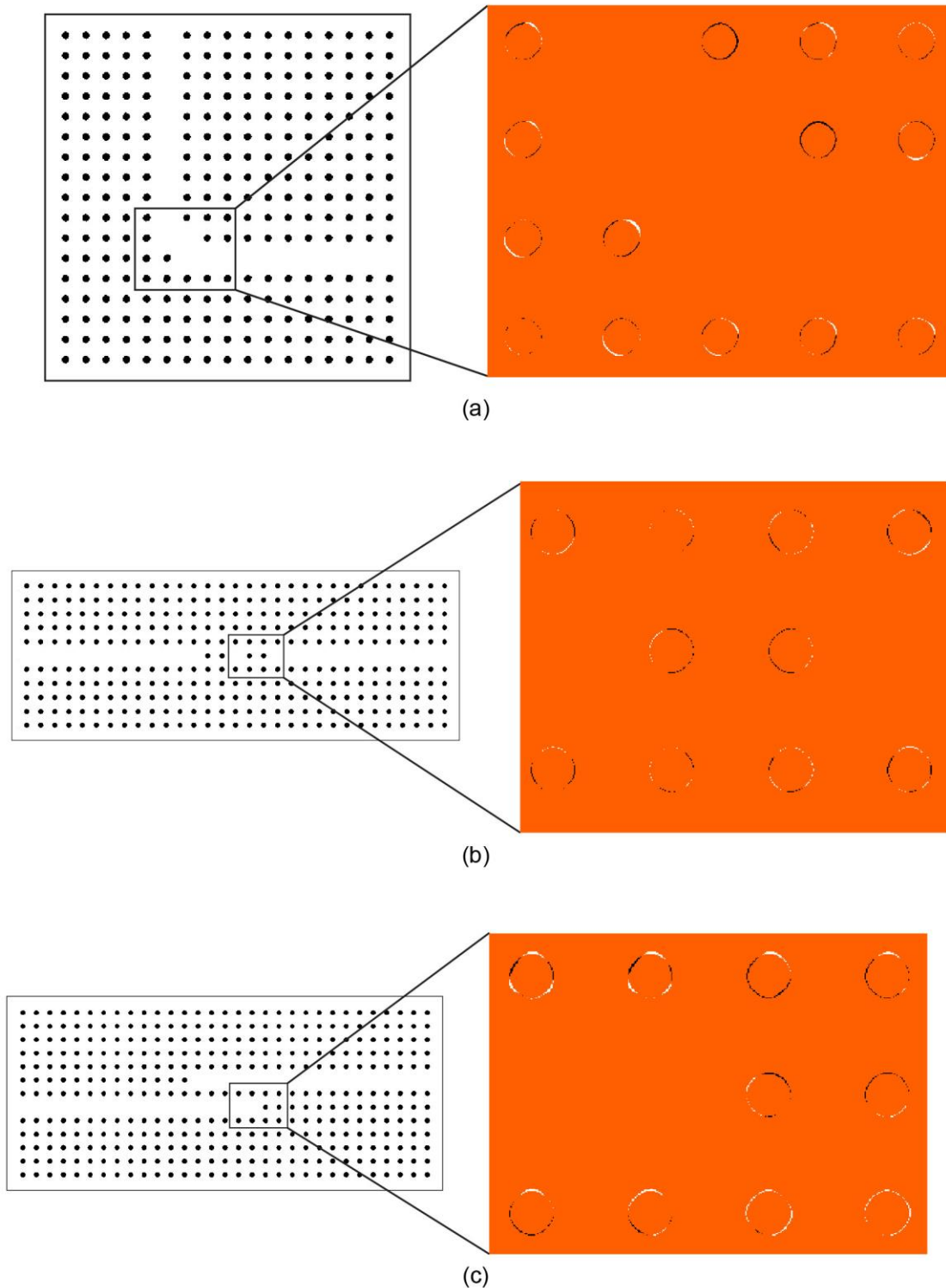


Figure 3.8: (a), (b), and (c) Estimated silicon pillar structures for the PhC $90deg$ -bend waveguide, passband filter, and stopband filter, respectively. In the insets, white (black) pixels represent pixels that are present (absent) in the estimated pillars, but absent (present) in the reference pillars. Pillar distortions are significantly reduced with the improved photomask design.

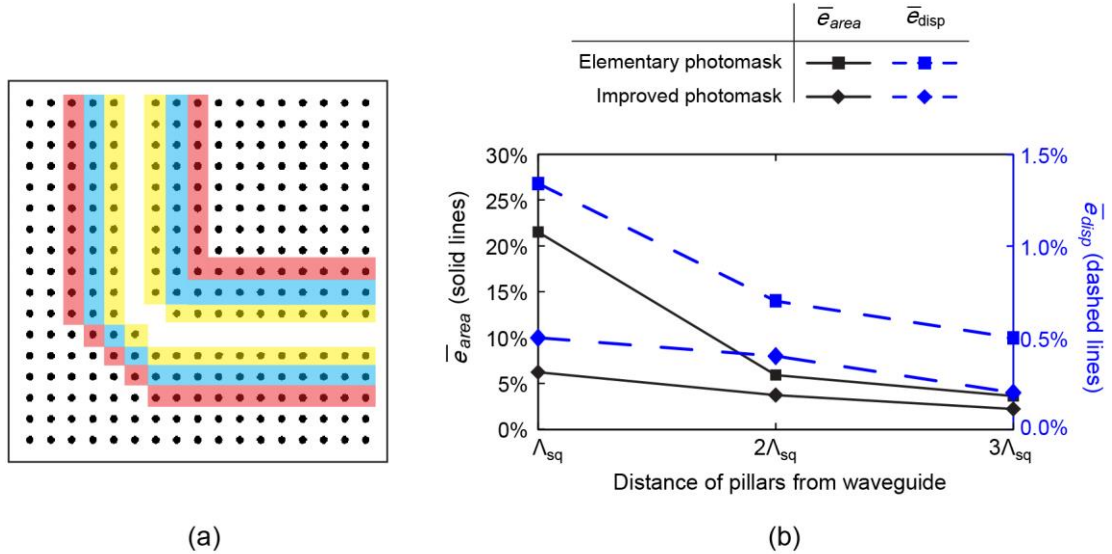


Figure 3.9: (a) Location of the pillars Λ_{sq} (yellow), $2\Lambda_{sq}$ (blue), and $3\Lambda_{sq}$ (red) from the waveguide. (b) Comparison of the averaged errors \bar{e}_{area} and \bar{e}_{disp} between the elementary and improved photomask. The averaged errors are calculated for pillars located at different distances from the waveguide.

In addition, the errors keep decreasing away from the integrated photomask pattern, confirming that distortions are confined close to the functional element and that the rest of the lattice is comparable to an undistorted periodic lattice.

To explain the distortion reduction observed with the $45deg$ -rotated squares, the concepts of *photomask-edge-facing* and *photomask-vertex-facing* interference motifs are next presented. In the case of the elementary photomask (Figure 3.3(a)), interference motifs next to the integrated photomask pattern are facing the *edges* of the photomask pattern and thus, are referred to as photomask-edge-facing interference motifs. Conversely with the improved photomask (Figure 3.7), the interference motifs are facing the *vertices* of the $45deg$ -rotated squares that form the photomask and thus, are referred to as photomask-vertex-facing interference motifs. This subtle difference has important

consequences illustrated in Figure 3.10. Due to edge diffraction, defocus, and off-axis imaging, unavoidable optical amplitude fluctuations are created around the integrated photomask pattern. These fluctuations impact the optical intensity distribution in the interference pattern, resulting in distorted interference motifs and thus, distorted pillars. However, the fluctuations are more pronounced near the photomask edges. Therefore, photomask-edge-facing interference motifs are more subject to distortions than photomask-vertex-facing interference motifs. To illustrate this result, amplitudes of Beam 1 at the surface of the photoresist are shown in Figures 3.10(a) and (b) for both the elementary photomask and the improved photomask of the $90deg$ -bend waveguide, respectively.

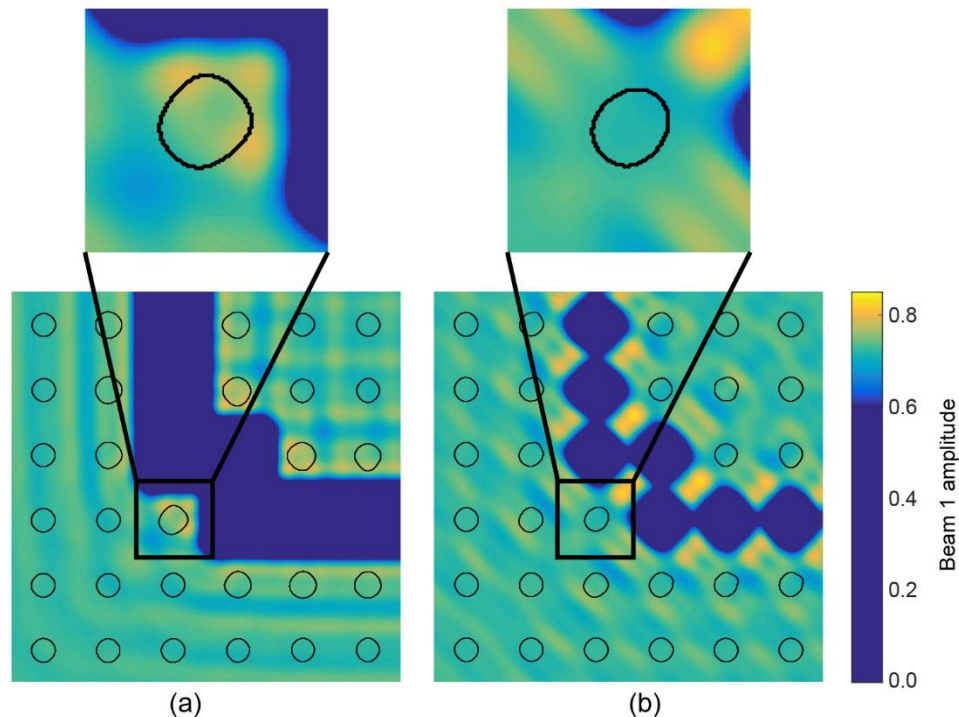


Figure 3.10: Amplitude of Beam 1 at the surface of the photoresist produced with (a) the elementary and (b) improved photomask of the $90deg$ -bend waveguide. With $45deg$ -rotated squares, amplitude fluctuations interfere less with the formation of the interference motifs.

In both Figures 3.10(a) and (b), contour plots corresponding to the estimated pillars have been superposed. Both figures have the same colorbar scale, which has been adjusted to improve contrast. In Figure 3.10(a), amplitude fluctuations are located near the pillar location and clearly distort the shape of the pillars. Conversely, photomask-vertex-facing pillars in Figure 3.10(b) are located in areas of relatively constant amplitude and thus, are less distorted. Similar observations are made with Beam 2 and Beam 3.

3.4 Photonic-Crystal Device Performance

To evaluate the performance of the three PIIL-produced PhC devices, their transmission spectra are calculated using the finite element modeling software COMSOL Multiphysics. The pillars are assumed to be infinitely long. A TM electric field is created at Port 1 and scattering boundary conditions are set at the edges of the simulation areas. The time-average power transmission is calculated as $|S_{21}|^2$, where S_{21} is the scattering parameter from Port 1 to Port 2. The transmission spectra are shown in Figure 3.11. For reference, the transmission spectra of idealized equivalent PhC devices made of defect-free circular pillars are calculated under the same conditions and are plotted in dashed lines. Transmission characteristics are listed and compared in Table 3.1. In spite of pillar distortions, the PIIL-produced PhC devices exhibit performance almost as good as that of the idealized devices. The transmission window of the *90deg*-bend waveguide produced by PIIL is only *3nm* shorter. For the PhC passband filter, the transmission maxima difference is 0.3 percentage point and the full width at half maxima (FWHM) difference is 1.1%. For the PhC stopband filter, the transmission minima difference is 0.06 percentage point and the FWHM difference is -3.8% .

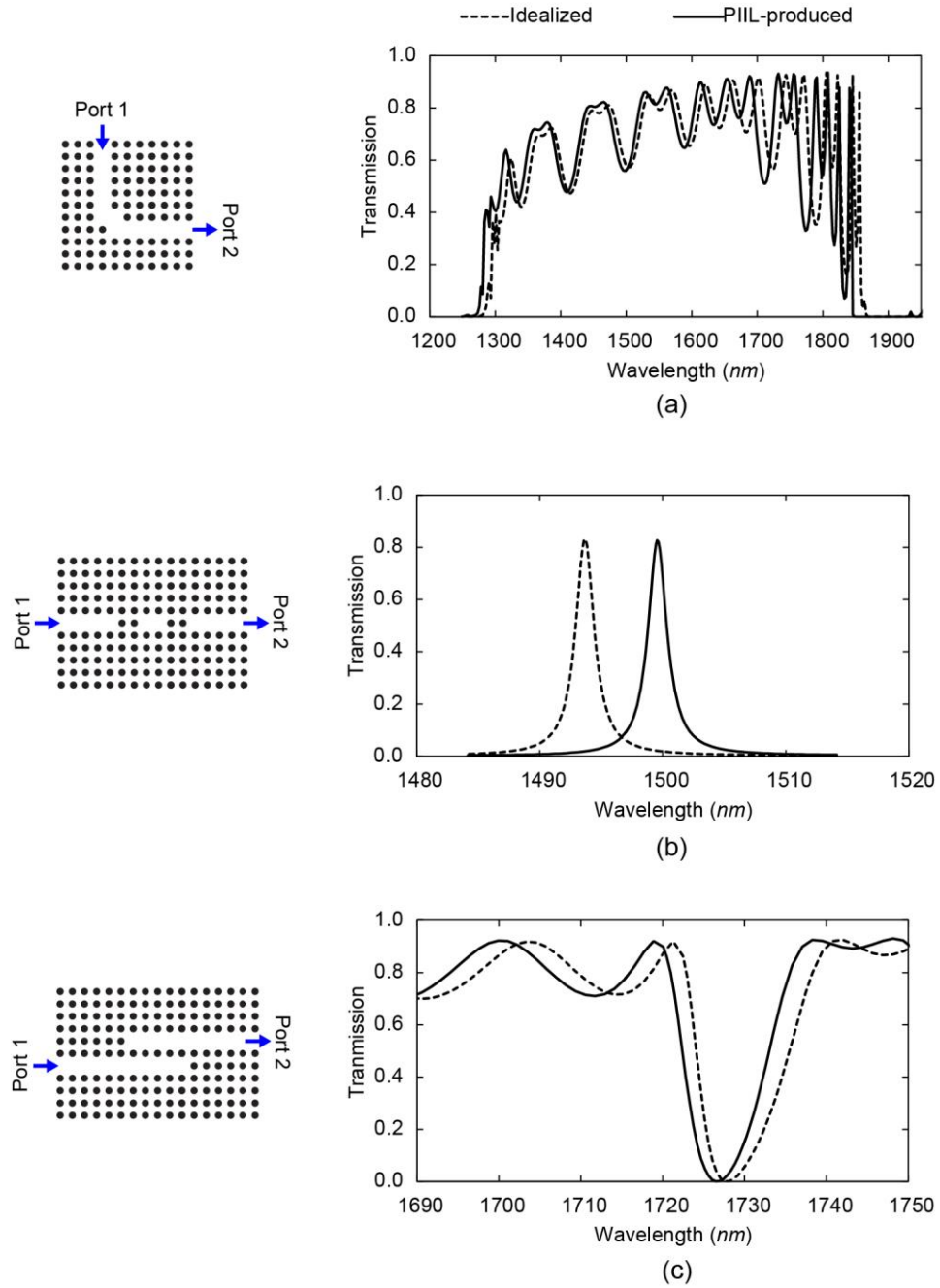


Figure 3.11: Transmission spectra between Port 1 and Port 2 of the PILL-produced and idealized PhC (a) $90deg$ -bend waveguide, (b) passband filter, and (c) stopband filter.

Table 3.1: Comparison of transmission spectrum characteristics between the PIIL-produced and idealized PhC devices

	Bend Waveguide	Passband Filter		Stopband Filter	
	Transmission Window	Maximum Transmission	FWHM	Minimum Transmission	FWHM
PIIL Produced	565nm	82.8%	1.86nm	0.1%	10.2nm
Idealized	568nm	83.1%	1.84nm	0.04%	10.6nm
Blue Shift	12nm	6nm		1nm	

The noticeable difference in the spectra, however, is a blue shift towards shorter wavelengths. The shifts are 12nm for the 90deg-bend waveguide, 6nm for the passband filter, and 1nm for the stopband filter. Similar blue shifts have been reported in PhC slab waveguides when the effective width of the PhC waveguide is reduced [140]. Even with the improved photomasks, the pillars adjacent to the functional elements are slightly deformed toward the functional element as illustrated in the insets of Figure 3.8. As a result, the effective waveguide width is slightly reduced by 1.9% and the transmission spectra are shifted toward shorter wavelengths. Worth mentioning, Fabry-Pérot oscillations due to the finite size of the devices also appear in the spectra. The Fabry-Pérot oscillation period, which is not constant, suggests a strongly dispersive character of the PhC. At larger wavelengths close to the Brillouin zone boundary, the group velocity decreases and thus, the group index n_g increases, resulting in a shorter wavelength separation $\Delta\lambda \propto 1/n_g$ [132]. In addition, intensity transmissions are not 100% because of imperfect light coupling at Port 1.

3.5 Summary

To assess PIIL capabilities in producing functional 2D PLB microstructures, the fabrication and transmission spectra of three representative 2D PhC devices including a $90deg$ -bend waveguide, a passband filter, and a stopband filter were simulated. The comprehensive PIIL vector model presented in Chapter 2 and realistic photolithographic conditions were employed, thereby emphasizing the feasibility and practicality of PIIL. Initial PIIL exposure simulations show detrimental structure distortions in the vicinity of the integrated photomask pattern when elementary photomasks are employed. Yet, the photomasks can be designed to pre-compensate lattice distortions during PIIL exposures. Similar to OPC developed in photolithography, the new field of photomask optimization for PIIL was introduced and investigated. A brute-force search approach was presented and single-motif-blocking patterns with various shapes and widths were studied. For the present PhC devices, a $0.9\Lambda_{sq}/M$ -wide $45deg$ -rotated square element yields the smallest figure of merit, which combines pillar-area and pillar-displacement errors. Noteworthy, the intuitive Λ_{sq}/M -wide square is actually inadequate and yields large lattice distortions, thereby highlighting the need for appropriate photomask design in PIIL.

The $0.9\Lambda_{sq}/M$ -wide $45deg$ -rotated square was then used as a building block to create the photomask patterns for the PhC devices. With these improved photomasks, pillar-area and pillar-displacement errors were reduced to less than 6.5% and 0.5%, respectively, and rapidly decrease away from the functional element. As a result, the transmission spectra of the PIIL-produced PhC devices are as good as those of their idealized equivalents, except for a slight blue shift due to a small reduction of the waveguide width.

CHAPTER 4

PATTERN-INTEGRATED INTERFERENCE LITHOGRAPHY FOR THREE-DIMENSIONAL PERIODIC-LATTICE-BASED MICROSTRUCTURES

The promising simulations of 2D-PIIL exposures lead to considering the more complex case of 3D-PIIL, where the interference of four or more photomask images produces custom-modified 3D interference patterns. 3D-PIIL is introduced and simulated using realistic lithographic conditions and the PIIL vector model derived in Chapter 2. Simulated exposures of photomask-integrated, photomask-shaped, and microcavity-integrated 3D periodic microstructures are presented and illustrate the capabilities of 3D-PIIL. This research has resulted in two journal papers [91, 98] and two conference presentations [97, 99].

4.1 Beam Configurations for 3D-PIIL

Similar to 2D-PIIL, the periodicity and lattice symmetry of a multi-beam 3D interference pattern are determined by the amplitude, polarization, and wavevector configuration of the interfering beams [128]. With four or more interfering beams, 3D interference patterns including all fourteen 3D Bravais lattices can be generated [63]. The interfering beams typically form an umbrella configuration, where multiple side beams are symmetrically arranged around a central beam propagating perpendicular to the photoresist film. Two representative beam configurations are depicted in Figures 4.1(a) and (c). For the (3+1)-beam configuration in Figure 4.1(a), the central beam is circularly polarized and the side beams are radially polarized, *i.e.* the beam polarization is linear and lies in the plane of

incidence of the beam. With an appropriate common beam incidence angle, θ_{beam} , this beam configuration produces a 3D interference pattern with a face-centered-cubic (FCC) unit cell shown in Figure 4.1(b) [147, 148]. For the (4+1)-beam configuration in Figure 4.1(c), four radially polarized side beams are symmetrically arranged around a circularly polarized central beam to produce a 3D interference pattern with a diamond cubic (DC) unit cell shown in Figure 4.1(d) [149]. The 2×1 field direction vectors of the beams illuminating the photomask, \mathbf{E}_i^{ill} , are listed in Table 4.1.

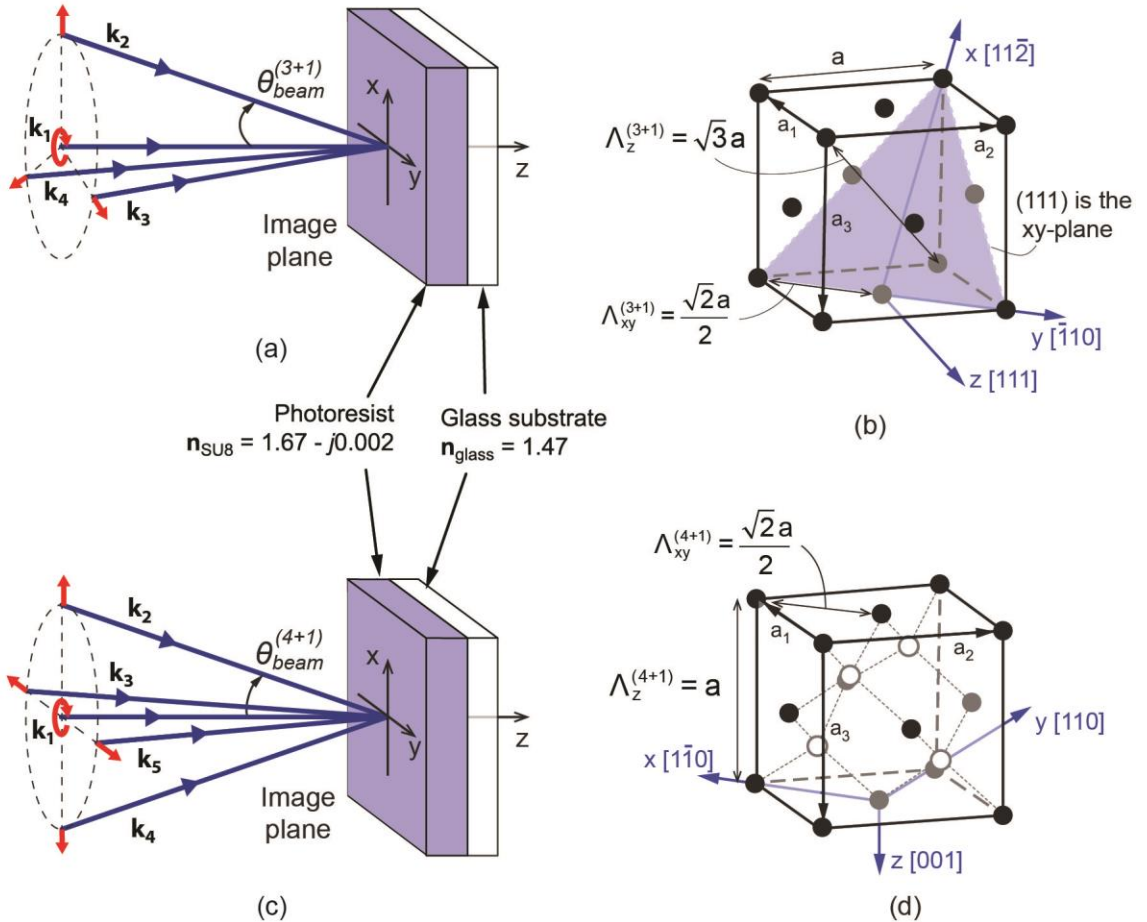


Figure 4.1: (a) (3+1)-beam configuration and (b) resulting FCC unit cell. (c) (4+1)-beam configuration and (d) corresponding DC unit cell of the interference pattern. SU8 is used as photoresist and is coated on glass to minimize back reflections.

Table 4.1: Field directions of the beams illuminating the photomask

	(3+1)-beam (see Figure 4.1(a))	(4+1)-beam (see Figure 4.1(c))
\mathbf{E}_1^{ill}	$[1 \ j]^T$	$[1 \ j]^T$
\mathbf{E}_2^{ill}	$[1 \ 0]^T$	$[1 \ 0]^T$
\mathbf{E}_3^{ill}	$[-1/2 \ \sqrt{3}/2]^T$	$[0 \ -1]^T$
\mathbf{E}_4^{ill}	$[-1/2 \ -\sqrt{3}/2]^T$	$[-1 \ 0]^T$
\mathbf{E}_5^{ill}	NA	$[0 \ 1]^T$

Of note, the edges of the unit cell in Figures 4.1(b) and (c) are not necessary collinear with the x-, y-, and z-axis. For convenience, the interference period in the xy-plane, $\Lambda_{xy}^{(q+1)}$, and period along the z-axis, $\Lambda_z^{(q+1)}$ are defined where q equals 3 or 4, for the (3+1)- or (4+1)-beam configuration, respectively. $\Lambda_{xy}^{(q+1)}$ and $\Lambda_z^{(q+1)}$ may be expressed as functions of the unit cell lattice constant, a . For the (3+1)-beam configuration (FCC lattice),

$$\Lambda_{xy}^{(3+1)} = \frac{\sqrt{2}a}{2} \quad (4.1)$$

and

$$\Lambda_z^{(3+1)} = \sqrt{3}a. \quad (4.2)$$

Combining Equations (4.1) and (4.2), the face-centered unit cell is cubic when

$$\Lambda_z^{(3+1)} / \Lambda_{xy}^{(3+1)} = \sqrt{6} \quad (4.3)$$

For the (4+1)-beam configuration,

$$\Lambda_{xy}^{(4+1)} = \frac{\sqrt{2}a}{2} \quad (4.4)$$

and

$$\Lambda_z^{(4+1)} = a. \quad (4.5)$$

Combining Equations (4.4) and (4.5), the diamond unit cell is cubic when

$$\Lambda_z^{(3+1)} / \Lambda_{xy}^{(3+1)} = \sqrt{2} \quad (4.6)$$

Alternatively, $\Lambda_{xy}^{(q+1)}$ and $\Lambda_z^{(q+1)}$ can be expressed as functions of the exposure wavelength, λ_{exp} , and common beam incidence angle, $\theta_{beam}^{(q+1)}$. For the (3+1)-beam configuration,

$$\Lambda_{xy}^{(3+1)} = \frac{2\lambda_{exp}}{\sqrt{3} \sin\theta_{beam}^{(3+1)}}, \quad (4.7)$$

and for the (4+1)-beam configuration,

$$\Lambda_{xy}^{(4+1)} = \frac{\lambda_{exp}}{\sin\theta_{beam}^{(4+1)}}. \quad (4.8)$$

In the xy-plane parallel to the photoresist surface, the period is the same in air and in SU8. However, due to refraction, the period along the z-axis depends on the real part of the photoresist refractive index, n_{PR} . For both beam configurations, $\Lambda_z^{(q+1)}$ may be expressed as

$$\Lambda_z^{(q+1)} = \frac{\lambda_{exp}/n_{PR}}{2\sin^2(\sin^{-1}(\sin\theta_{beam}^{(q+1)}/n_{PR})/2)}. \quad (4.9)$$

Therefore, the conditions for cubic unit cell given in Equations (4.3) and (4.6) may not be met due to refraction and are only valid for a certain combination of n_{PR} and $\theta_{beam}^{(q+1)}$. For a photoresist with a refractive $n_{PR} = 1.67$, the $\Lambda_z^{(q+1)}/\Lambda_{xy}^{(q+1)}$ ratios, which are independent of λ_{exp} , are plotted as functions of $\theta_{beam}^{(q+1)}$ in Figure 4.2. Horizontal lines corresponding to $\Lambda_z^{(3+1)}/\Lambda_{xy}^{(3+1)} = \sqrt{6}$ and $\Lambda_z^{(3+1)}/\Lambda_{xy}^{(3+1)} = \sqrt{2}$ are added, but are not intersected by the plots. Therefore, the equalities in Equations (4.3) and (4.6) cannot be met with this photoresist and the unit cell cannot be cubic.

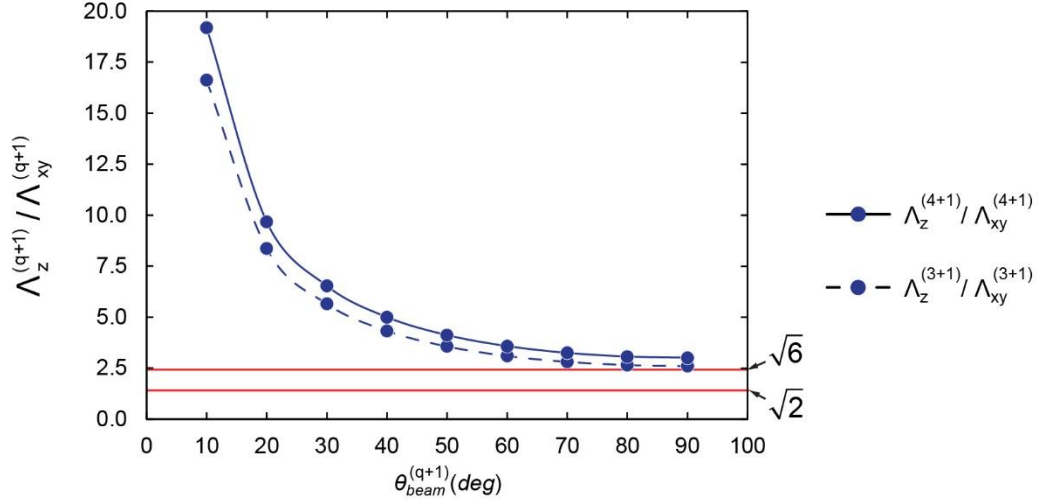


Figure 4.2: $\Lambda_z^{(3+1)} / \Lambda_{xy}^{(3+1)}$ ratios as functions of $\theta_{beam}^{(q+1)}$. Conditions for cubic unit cell are not be met due to refraction at the air/photoresist interface.

Refraction issues at the air/photoresist interface in multi-beam interference lithography may be addressed by using a prism whose refractive index matches that of the photoresist [78, 150]. In that index matching (IM) case, Equation (4.9) may be simplified to

$$\Lambda_z^{(q+1),IM} = \frac{\lambda_{exp}}{2\sin^2(\theta_{beam}^{(q+1)}/2)}. \quad (4.10)$$

The $\Lambda_z^{(q+1),IM} / \Lambda_{xy}^{(3+1)}$ ratios for the two beam configurations are plotted as functions of $\theta_{beam}^{(q+1)}$ in Figure 4.3. With an index matching material, the conditions for cubic unit cell are satisfied for $\theta_{beam}^{(3+1),FCC} = 38.9deg$ and $\theta_{beam}^{(4+1),DC} = 70.5deg$. At those angle values, the curves intersect the $\sqrt{6}$ and $\sqrt{2}$ constant lines. Similar to immersion photolithography, a refractive-index-matching immersion fluid may be used in 3D-PIIL instead of a prism to address refraction issues at the air/photoresist interface. Yet, in 3D-PIIL, $\theta_{beam}^{(q+1)}$ is typically limited by the image-side NA and may not be as large as desired. In theory, $\theta_{beam}^{(q+1)}$ with

values larger than $40deg$ are feasible using a NA larger than 0.65, but an even larger NA would be more appropriate to ensure a propagation of the beams closer to the optical axis, reduce optical aberrations, and enable larger exposure spots.

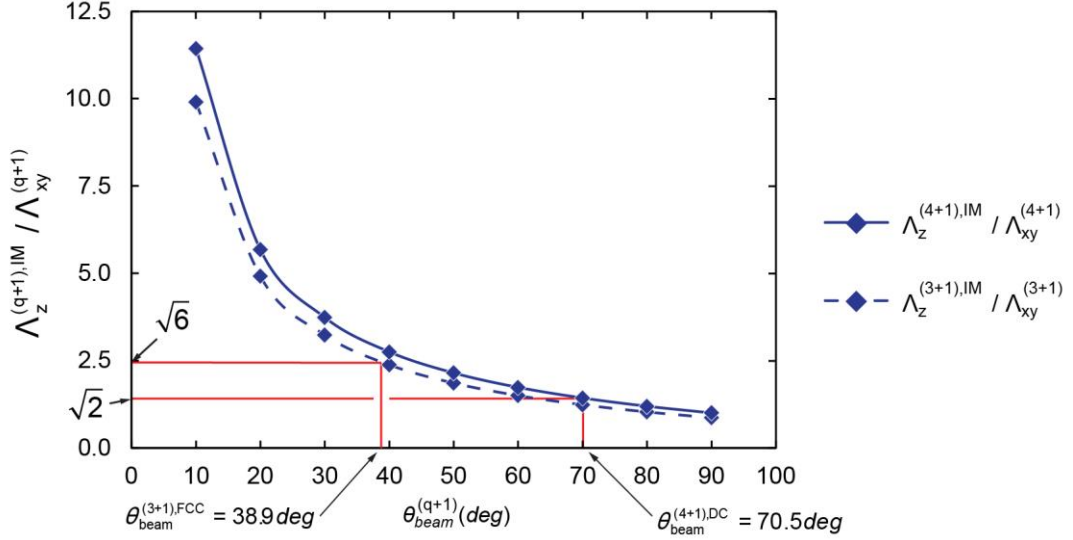


Figure 4.3: $\Lambda_z^{(q+1),IM} / \Lambda_{xy}^{(q+1)}$ ratios as functions of $\theta_{beam}^{(q+1)}$. With an index-matching material, conditions for cubic unit cell are met for $\theta_{beam}^{(3+1),FCC} = 38.9deg$ and $\theta_{beam}^{(4+1),DC} = 70.5deg$.

4.2 3D-PIIL Exposure Simulation Parameters

In the following 3D-PIIL exposure simulations, realistic photolithographic conditions are considered to illustrate the practical capabilities of 3D-PIIL. As in Chapter 3, the NA is 0.8 and magnification of the compound objective lens, M , is 0.25. By their nature, 3D-PIIL exposures typically require a photoresist film thicker than that for 2D-PIIL. Due to its low absorption at $363.8nm$, sub-100nm resolution capability, and suitability for the fabrication of thick and high aspect ratio microstructures [151], the negative-tone SU8 photoresist has been widely used in 3D MBIL [32, 69, 78, 152]. Therefore, the exposure wavelength, λ_{exp} , is $363.8nm$ and SU8 with a complex refractive index $\mathbf{n}_{SU8}(\lambda_{exp}) = 1.67 - j6 \times 10^{-5}$ is used as

photoresist. Back reflections and standing waves within the photoresist are mitigated by coating the SU8 on a glass substrate with a refractive index $n_{\text{glass}}(\lambda_{\text{exp}}) = 1.47$.

To generate a common $1\mu\text{m}$ period in the xy -plane for both interference patterns, the beam angles are set as $\theta_{\text{beam}}^{(3+1)} = 24.8\text{deg}$ and $\theta_{\text{beam}}^{(4+1)} = 21.3\text{deg}$. With these angles, the periods along the z -axis are $\Lambda_z^{(3+1)} = 6.78\mu\text{m}$ and $\Lambda_z^{(4+1)} = 9.07\mu\text{m}$. Since no index-matching immersion fluid is considered, the conditions for cubic unit cell in Equations (4.3) and (4.6) are not met. The unit cells are not cubic, but elongated along the z -axis to become face-centered rhombohedral (FCR) and woodpile (diamond rhombohedral) for the (3+1)- and (4+1)-beam configurations, respectively. The interference patterns produced by the two beam configurations are shown in Figure 4.4. For comparison with the cubic unit cells, selected lattice motifs (matching both lattices are superposed to the interference patterns.

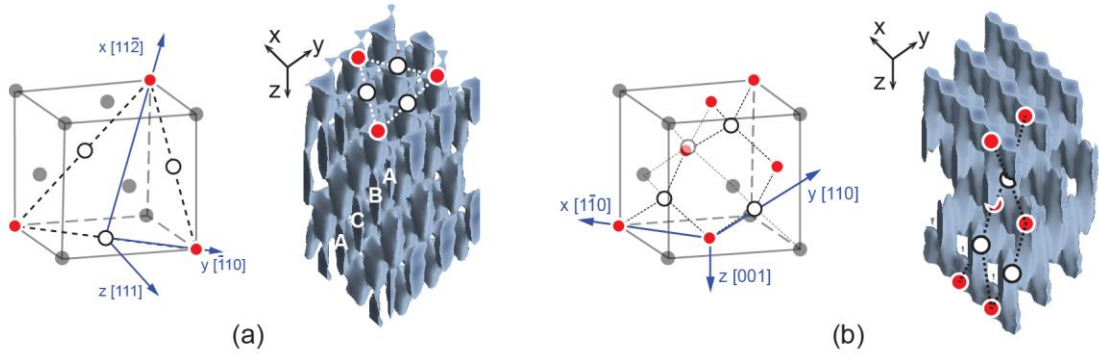


Figure 4.4: (a) FCC lattice and simulated interference pattern with FCR lattice generated by the (3+1)-beam configuration. The ABC layer sequence is visible in the xz -plane. (b) DC lattice and simulated interference pattern with woodpile lattice generated by the (4+1)-beam configuration. Matching lattice motifs are superposed to the interference patterns.

In spite of the lattice stretch along the z -axis, the interference patterns remain bicontinuous over a certain range of intensity thresholds as shown in Figure 4.5 and

Figure 4.6. The interference pattern is bicontinuous when the optical intensity distribution above and below the intensity threshold form two distinct regions, “each of which being completely connected within itself” [153]. When exposed, the 3D periodic structure becomes a self-standing open network of pores with important potential applications in bioengineering or microfluidics. For the (3+1)-beam configuration, the lattice is bicontinuous for a normalized intensity threshold ranging from 24% to 59%. For this range, the filling factor decreases from 74% to 21%. For the (4+1)-beam configuration, the lattice is bicontinuous for a normalized intensity threshold ranging from 16% to 60%. For this range, the filling factor decreases from 84% to 17%. The absolute contrasts, defined as $(I_{PIIL,max} - I_{PIIL,min}) / (I_{PIIL,max} + I_{PIIL,min})$, are close to unity and are 0.95 and 0.90 for the (3+1)- and (4+1)-beam configuration, respectively.

4.3 Simulated 3D-PIIL Exposures

By combining 3D-MBIL and photomask imaging simultaneously, 3D-PIIL enables the fabrication of bicontinuous PLB microstructures in a single-exposure step. The capabilities of the new field of 3D-PIIL are explored and analyzed in this Section.

4.3.1 Photomask-Integrated 3D Periodic Microstructure

A first case illustrating 3D-PIIL capabilities is the fabrication of photomask-integrated 3D periodic microstructures. A clear-field photomask, which is transparent to light except for certain opaque features, is used in this example. The photomask pattern can be arbitrary and to illustrate this versatility, a clear-field photomask representing a simplified version of the Georgia Institute of Technology (GT) logo depicted in Figure 4.7(a) is used in the

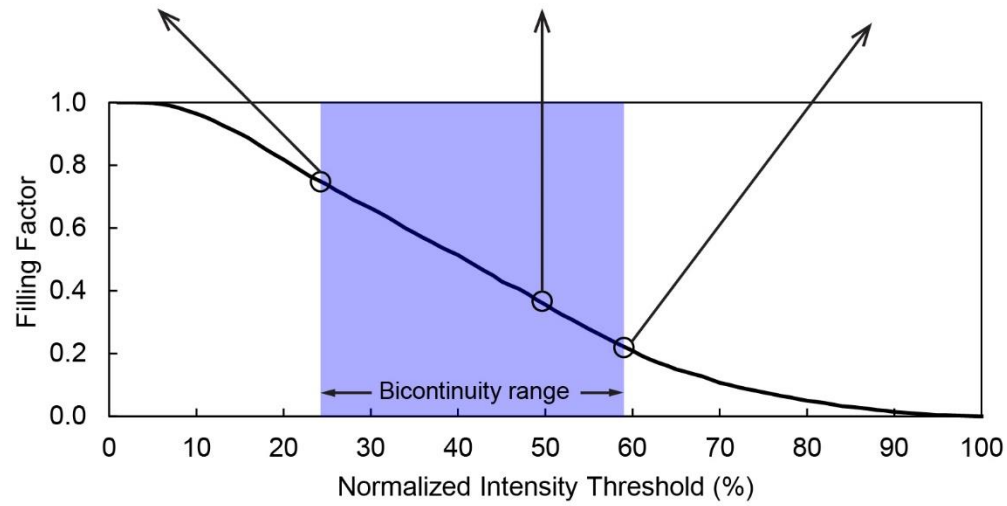
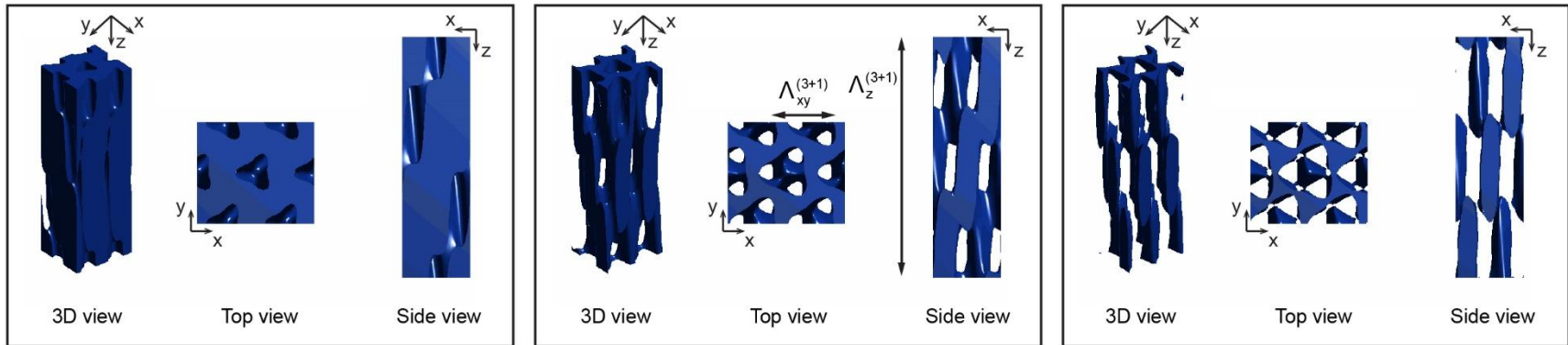


Figure 4.5: Filling factor of the 3D interference pattern with FCR lattice as a function of the normalized intensity threshold. The interference pattern is bicontinuous for normalized intensity threshold ranging from 24% to 59%.

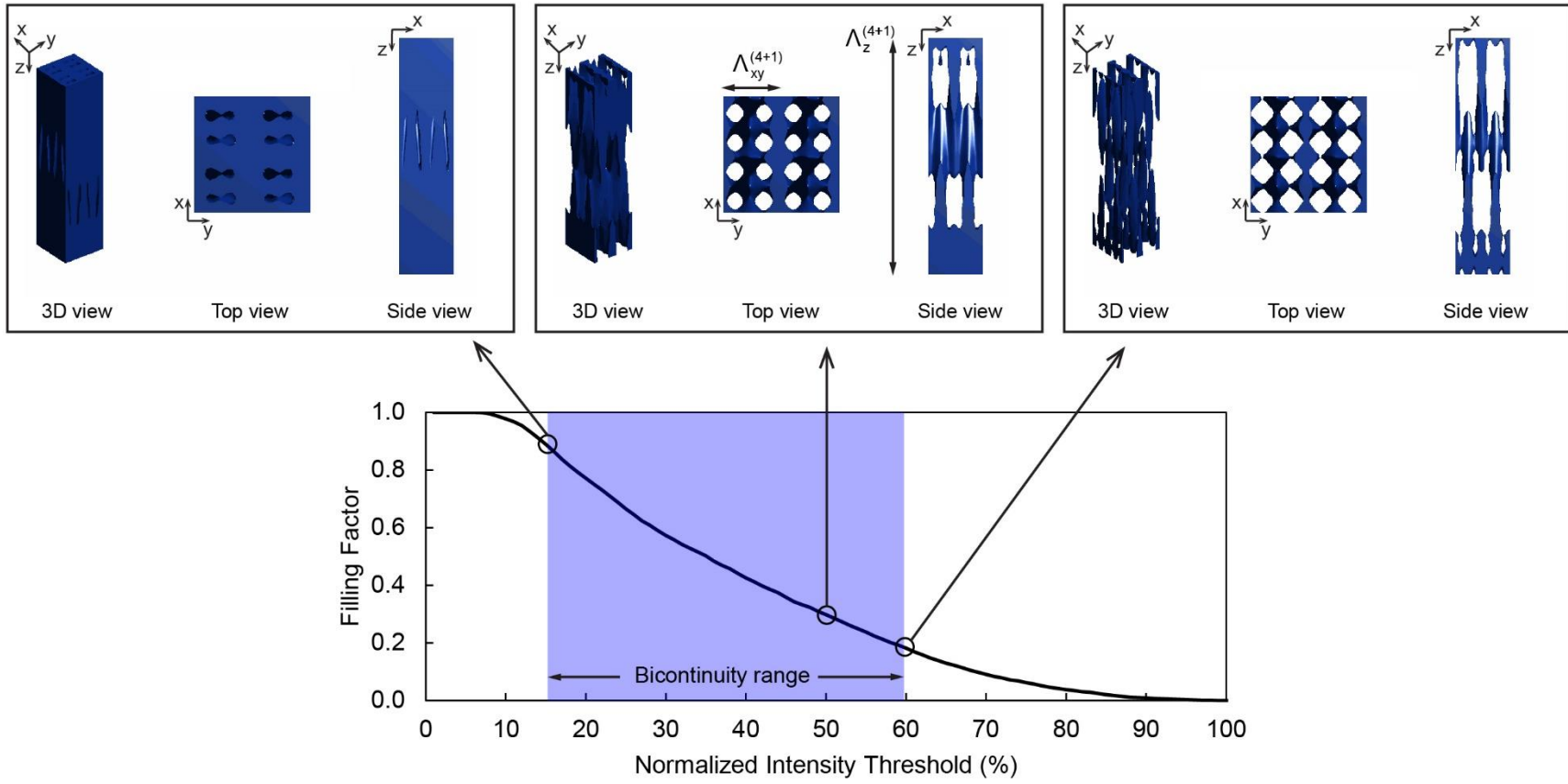
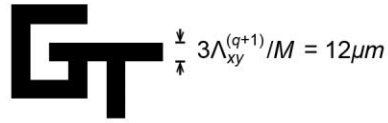


Figure 4.6: Filling factor of the 3D interference pattern with woodpile lattice as a function of the normalized intensity threshold. The interference pattern is bicontinuous for normalized intensity threshold ranging from 16% to 60%.

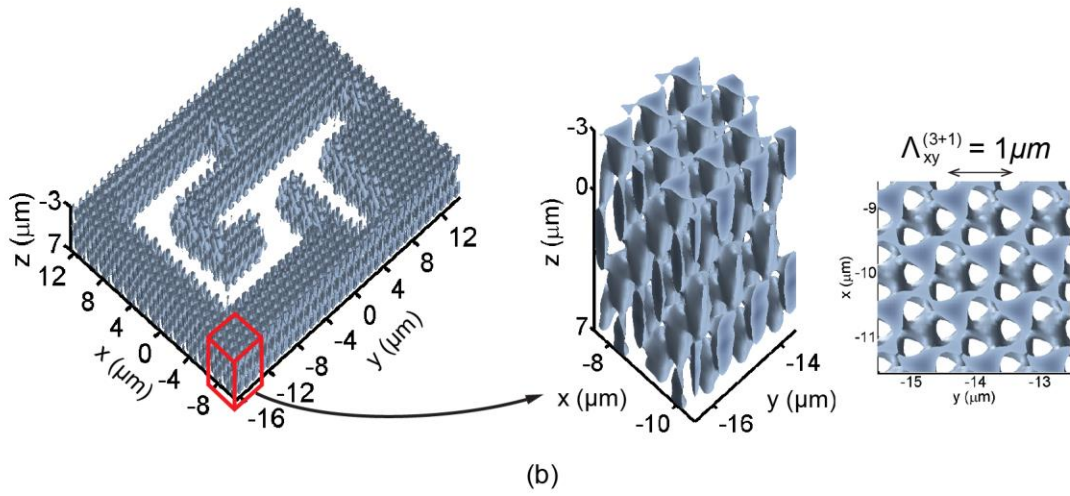
present simulations. The width of the GT logo letters is $3\Lambda_{xy}^{(q+1)}/M = 12\mu\text{m}$ and cover three interference periods in the xy-plane. The SU8 film thickness, t_{SU8} , is $10\mu\text{m}$ and corresponds to $1.48\Lambda_z^{(3+1)}$ and $1.1\Lambda_z^{(4+1)}$. The surface of the SU8 film is also displaced such that the image focal plane lies in the center of the photoresist. Due to refraction, the common beam angle of propagation inside the photoresist, $\theta_{\text{SU8}}^{(q+1)}$, defined as

$$\theta_{\text{SU8}}^{(q+1)} = \sin^{-1} \left(\sin \theta_{\text{beam}}^{(q+1)} / n_{\text{SU8}} \right) \quad (4.11)$$

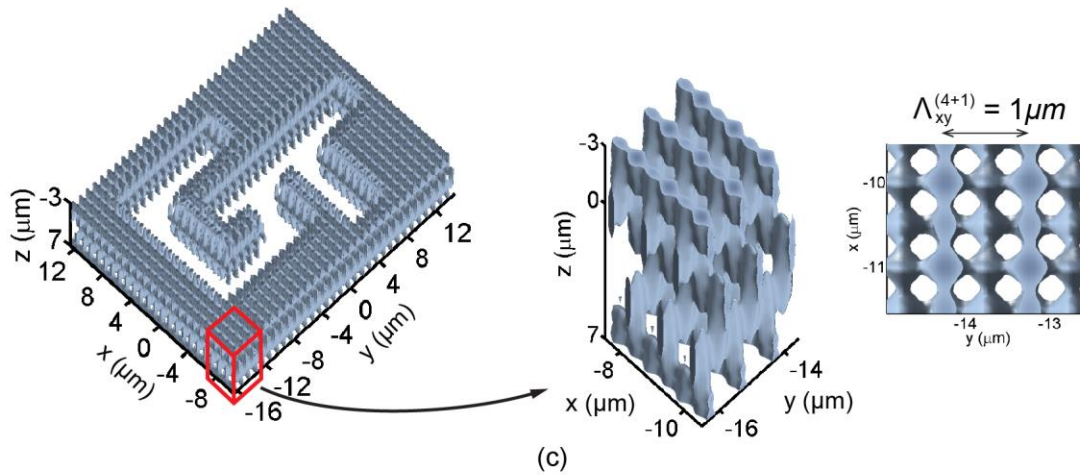
is smaller than $\theta_{\text{beam}}^{(q+1)}$. Therefore, the position of the image focal plane along the z-axis is different in air and in the photoresist. The surface of the photoresist film must be shifted by $z_0 = -(t_{\text{SU8}} / 2) / n_{\text{SU8}} = -3\mu\text{m}$. With this shift, the image focal plane lies in the center of the photoresist film at $z = 2\mu\text{m}, 5\mu\text{m}$ below the photoresist surface. The resulting simulated 3D-PIIL exposures are shown for a normalized intensity threshold of 50% in Figures 4.7(a) and (b) for the (3+1)- and (4+1)-beam configurations, respectively. The simulated exposures exhibit an excellent integration of the photomask within the 3D interference patterns through the complete thickness of the photoresist. In the vicinity of the integrated GT logo, the interference pattern is slightly perturbed due to edge diffraction, defocus, and off-axis imaging effects. However, similar to 2D-PIIL results, the distortions are confined close to the integrated pattern and the 3D lattice becomes remarkably unperturbed only a few periods away from the GT logo. 3D and top views of portions of the undistorted lattice are shown in Figures 4.7(a) and (b). For practical applications, the integrated photomask pattern could be a network of microfluidic channels within a 3D bioscaffold or a waveguide within a 3D photonic crystal.



(a)



(b)

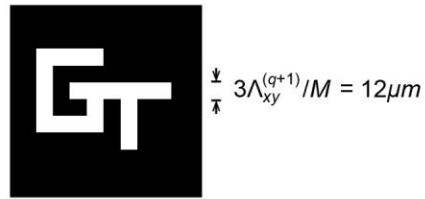


(c)

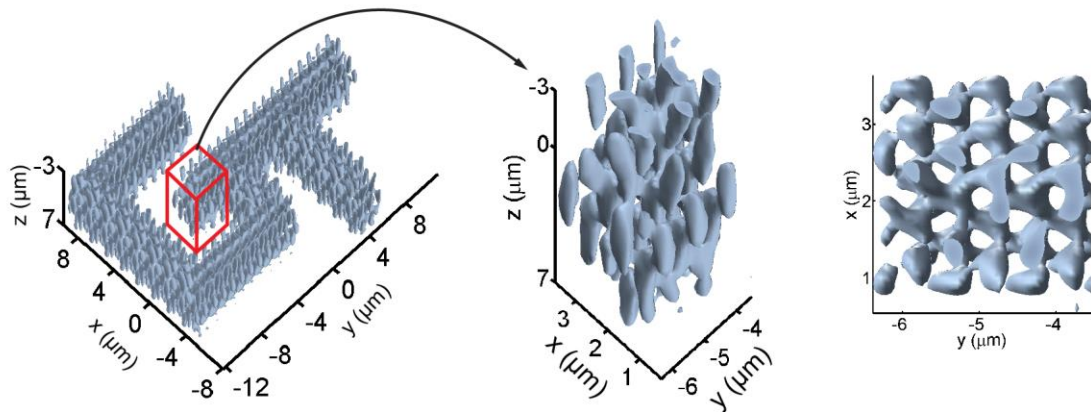
Figure 4.7: (a) Clear-field photomask with opaque GT logo. 3D and top views of the simulated 3D-PIIL exposures for the (b) (3+1)- and (c) (4+1)-beam configuration.

4.3.2 Photomask-Shaped 3D Periodic Microstructure

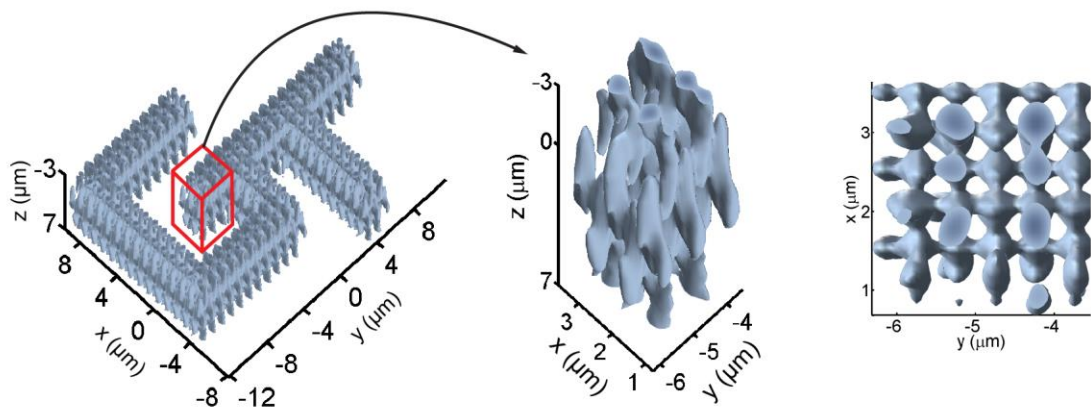
Alternatively, a dark-field version of the GT logo photomask depicted in Figure 4.8(a) can be used to produce photomask-shaped 3D periodic microstructures by 3D-PIIL. A dark-field photomask is opaque to light except for certain transparent portions. The exposure parameters are identical to those of Section 4.3.1. Simulated PIIL exposures for the (3+1)- and (4+1)-beam configurations are shown in Figures 4.8(b) and (c), respectively. With the dark-field photomask, 3D bicontinuous microstructures shaped like the photomask pattern can be produced. While lattice distortions are small at the focal plane ($z = 2\mu\text{m}$), edge diffraction effects are stronger and exacerbated by defocus and off-axis imaging near the top ($z = -3\mu\text{m}$) and bottom ($z = 7\mu\text{m}$) of the photoresist film. In addition, these perturbations are confined within the small areas of the GT logo. As a result, the 3D interference pattern becomes strongly perturbed and the lattice lacks periodicity at the bottom and surface of the photoresist film. With thicker transparent photomask patterns, distortions would be confined near the photomask edges and the interference pattern would be better reconstructed in the center of the photomask pattern. The distortions would also be reduced using a smaller exposure wavelength. Yet, without being periodic, the FCR-like and woodpile-like structures are still bicontinuous and thus, self-standing. Potential applications for these photomask-shaped 3D lattices include complex microfluidic structures for particle filtering, diagnostics, and passive mixing.



(a)



(b)



(c)

Figure 4.8: (a) Dark-field photomask with transparent GT logo. 3D and top views of the simulated 3D-PIIL exposures for the (b) (3+1)- and (c) (4+1)-beam configuration.

4.3.3 Microcavity Integrated at the Top of a 3D Periodic Structure

A third case illustrating 3D-PIIL capabilities is the fabrication of a 3D periodic microstructure with microcavities integrated at the surface. Here, the photomask is an opaque disc with radius $\Lambda_{xy}^{(q+1)}/M = 4\mu\text{m}$ needed to create the microcavity. The thickness of the SU8 film is increased to $t_{\text{SU8}} = 20\mu\text{m}$. Also, the image focal plane lies at the surface of the photoresist film ($z_0 = 0\mu\text{m}$). Simulated 3D-PIIL exposures for an intensity threshold of 35% are shown in Figures 4.9(b) and (c) for the (3+1)- and (4+1)-beam configurations, respectively. At the photoresist surface, the projected images of the disc are overlapping and focused and thus, create a microcavity-integrated interference pattern similar to the results presented in Section 4.3.1. However, since the beams are propagating obliquely, the images of the disc are progressively separating and becoming defocused deeper in the photoresist. If the photoresist film is thick enough, the 3D interference pattern starts to reconstruct below the microcavity by superposition of the out-of-focus and non-overlapping images of the disc. Exploded 3D views and side views of the central slice in Figures 4.9(b) and (c) show the 3D interference pattern reconstructed below the microcavity. Although perturbed immediately below the microcavity, interference pattern distortions weaken for distances deeper in the SU8 film.

The microcavity radius depends on the photomask disc radius and the system demagnification, M . Here, the microcavity radius, r_{cav} , is about $4\mu\text{m} \times M = 1\mu\text{m}$. The microcavity depth, d_{cav} , not only depends on r_{cav} , but also on the beam propagation angle in the photoresist, $\theta_{\text{SU8}}^{(q+1)}$, defined in Equation (4.11). Using simple geometric optics, d_{cav} can be estimated in good approximation by calculating the distance from the surface

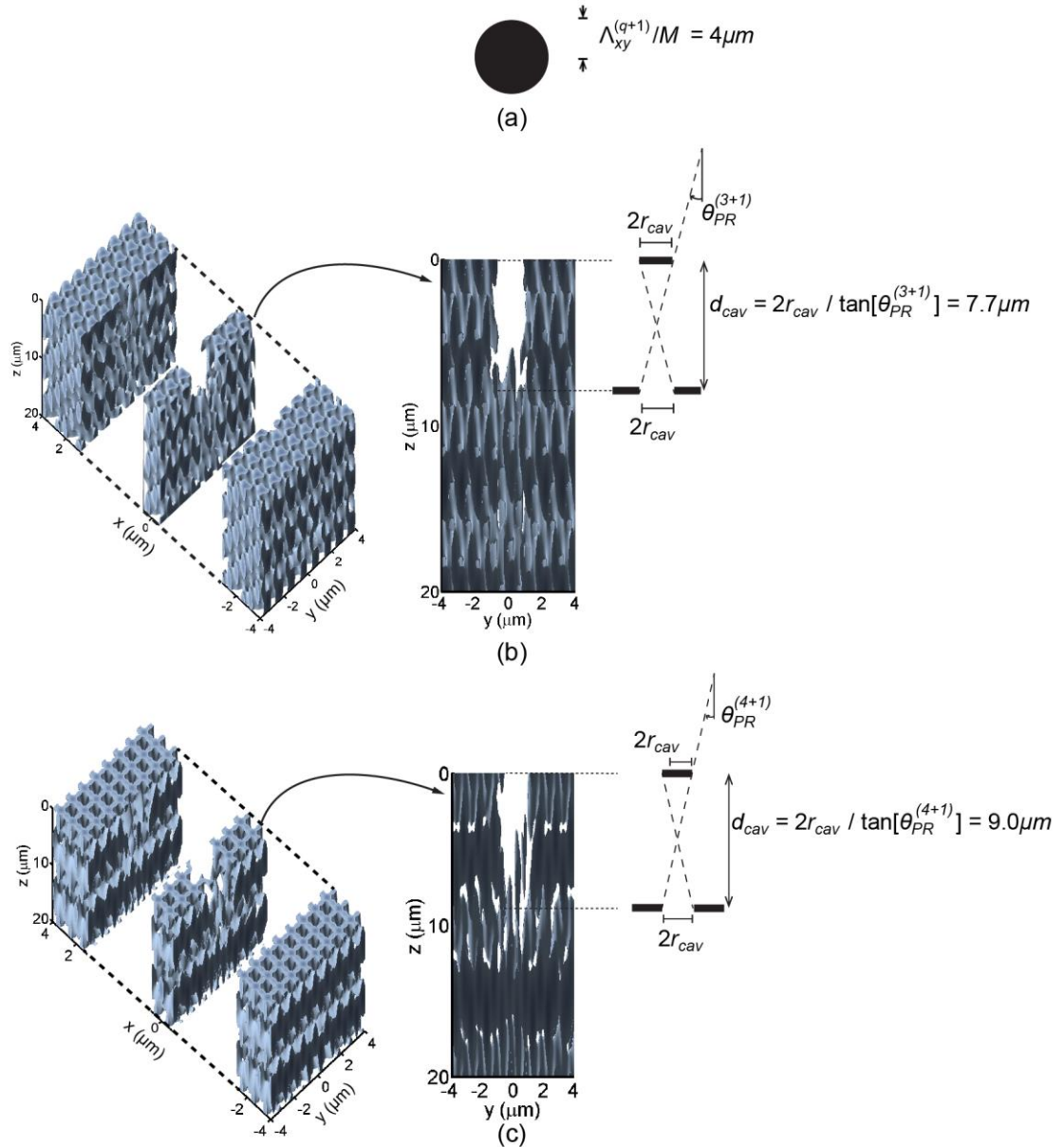


Figure 4.9: (a) Photomask with an opaque disc to create the cavity within the interference pattern. Exploded views of the simulated 3D-PIIL exposures for the (b) (3+1)- and (c) (4+1)-beam configuration. A microcavity is created at the surface of the 3D interference pattern. Side views of the central slice ($x = 0 \mu\text{m}$) depict the interference pattern being reproduced below the microcavity. The intensity threshold is 35% of the maximum intensity produced with a blank mask.

at which the images become separated by $2r_{cav}$ as illustrated in Figures 4.9(b) and (c). The estimated microcavity depths are $7.7\mu m$ and $9.0\mu m$ for the (3+1)- and (4+1)-beam configurations, respectively, and match well with measurements from the simulated exposures. Analogous to the relationship between $\theta_{beam}^{(q+1)}$ and the cubic nature of the unit cell discussed previously, the aspect ratio of the microcavity, r_{cav} / d_{cav} , depends on the tangent of $\theta_{SU8}^{(q+1)}$. With larger $\theta_{beam}^{(q+1)}$ (and thus $\theta_{SU8}^{(q+1)}$), the cavity is more spherical and unit cell is more cubical. With smaller $\theta_{beam}^{(q+1)}$, the cavity and the unit cell are more elongated along the z-axis.

Although not simulated here, it is possible to displace the sample such that the image focal plane lies at the bottom of the photoresist film. In that case, the images of the disc would start to overlap and create the microcavity deeper in the photoresist and the microcavity would be connected to the substrate. The result would be a microcavity integrated at the bottom of the lattice.

4.3.4 Microcavity-Integrated 3D Periodic Microstructure

A fourth case illustrating 3D-PIIL capabilities is the complete embedding of a microcavity within a 3D periodic microstructure. The principle of this unique result is similar to that of Section 4.3.3, yet an even thicker photoresist film is employed and the image focal plane is located at the center of the photoresist film to allow the interference pattern to reconstruct above and below the microcavity. The SU8 film thickness is therefore increased to $t_{SU8} = 50\mu m$ and its surface is shifted by $z_0 = -(t_{SU8} / 2) / n_{SU8} = -15\mu m$. The photomask used in both simulations is identical to that of Figure 4.9(a). Simulation results for the

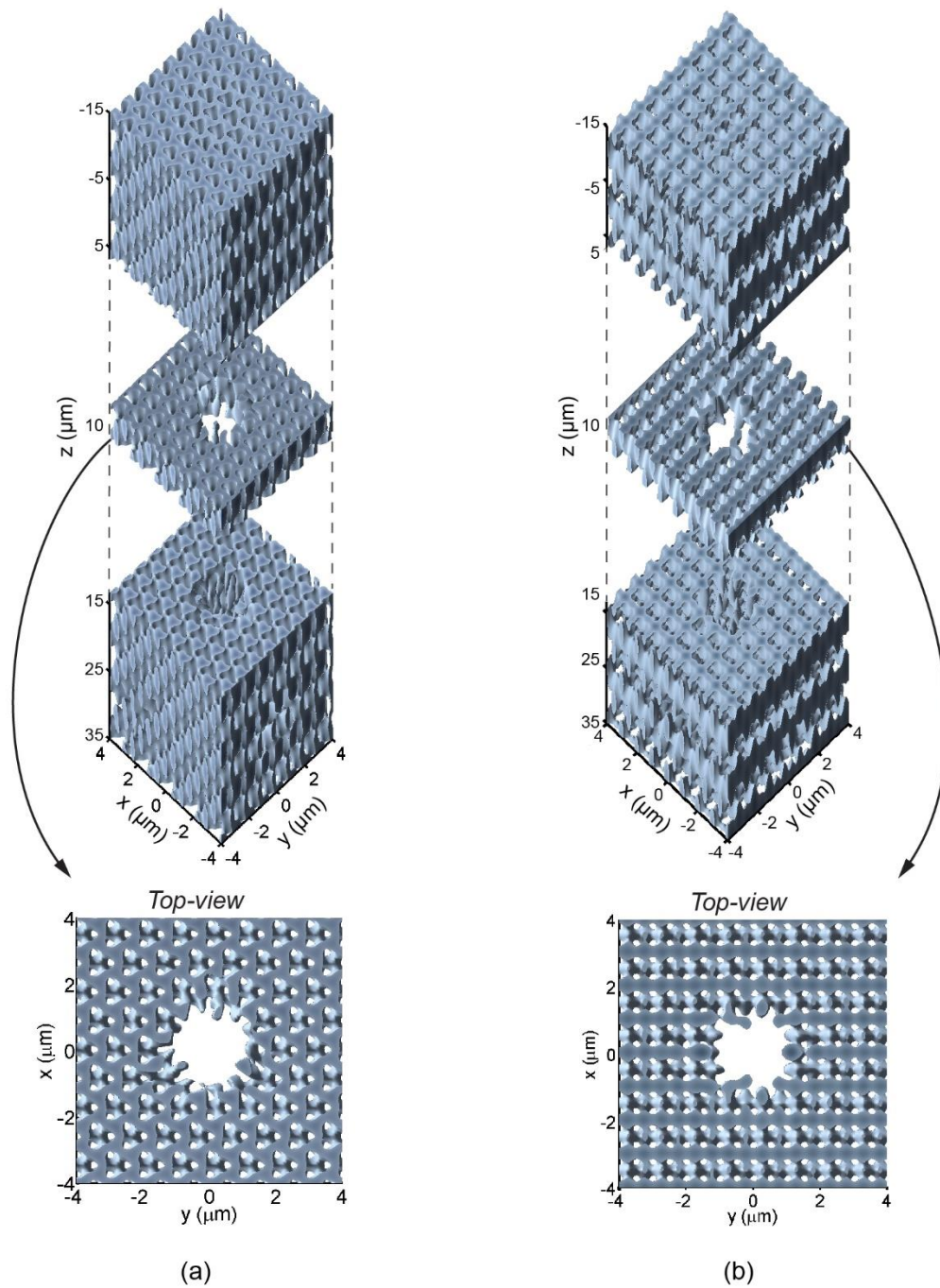


Figure 4.10: Exploded views of the simulated 3D-PIIL exposures for the (a) (3+1)- and (b) (4+1)-beam configuration. A microcavity is successfully embedded within the 3D interference pattern. Above and below the image focal plane ($z = 10\mu\text{m}$), the 3D interference pattern is progressively reproduced by interference of the out-of-focus and non-overlapping images of the disc photomask. The intensity threshold is 35% of the maximum intensity produced with a blank mask.

(3+1)- and (4+1)-beam configurations are shown in Figures 4.10(a) and (b), respectively. At the image focal plane ($z = 10\mu\text{m}$), the images of the disc create a cavity within the interference pattern as illustrated in the close-up views of slices. Close to the surface ($z = -15\mu\text{m}$) and the bottom ($z = 35\mu\text{m}$) of the SU8 film, however, the defocused and non-overlapping images of the disc interfere, leading to a reconstruction of the 3D interference pattern. Similar to Section 4.3.3 results, the dimensions of the integrated microcavity depend on r_{cav} and $\theta_{\text{SU8}}^{(q+1)}$. In Figure 4.10, the microcavity dimensions for the (3+1)- and (4+1)-beam configurations are about $2\mu\text{m} \times 15\mu\text{m}$ and $2\mu\text{m} \times 18\mu\text{m}$, respectively. These dimensions are twice those of the microcavities in Section 4.3.3, which is logical given the symmetry of the result. Such a microcavity could be used, for example, for particle encapsulation or a high-Q optical resonator. In the literature, there is no existing microfabrication technique capable of producing such microcavity-integrated 3D periodic microstructures in a rapid, single-exposure step. As such, 3D-PIIL has been highlighted in a "Spotlight on Optics" article by the Optical Society of America as *"the only method that can both create and pattern 3D periodic structures in a single step"* [154].

4.4 Summary

By enabling the rapid, single-exposure step fabrication of large-format 3D PLB microstructures, 3D-PIIL addresses the rapidity issue of current 3D microfabrication techniques. Through thoughtful positioning of the surface of the photoresist film relative to the image plane, photomask-integrated, photomask-shaped 3D periodic microstructures as well as microcavities integrated on top of, or fully embedded within 3D periodic microstructures were presented to illustrate 3D-PIIL capabilities.

Refraction effects at the interface between the air and the photoresist are discussed as well. Due to the change of beam angle of propagation within the photoresist, the 3D periodic lattices are stretched along the normal of the photoresist surface and 3D cubic lattices may not be feasible. Similar to immersion photolithography, immersion PIIL could address this issue by employing an immersion fluid, whose refractive index matches that of the photoresist, to impede refraction effects.

CHAPTER 5

PATTERN-INTEGRATED INTERFERENCE EXPOSURE SYSTEM DESIGN AND ANALYSIS

To demonstrate PIIL experimentally and to confirm PIIL exposure simulations, a pattern-integrated interference exposure system (PIIES) prototype is designed and implemented. The PIIES capabilities and performance are also numerically analyzed using geometric optics and the ray-tracing software ZEMAX. First, the range of feasible interference periods and the sensitivity of the interference pattern to beam decentering are investigated. Then, the imaging performance of the PIIES objective lenses as a compound objective lens is studied. The analysis results are finally compared to the estimated precision of the manual alignment of the PIIES. This research has resulted in two journal papers [89, 101].

5.1 PIIES Implementation

A top view of the complete PIIES is depicted in Figure 5.1(a) and a picture of the prototype system in the laboratory is shown in Figure 5.1(b). The PIIES is installed on a vibration-isolated optical table defining the yz -plane. A Spectra-Physics argon-ion UV laser operating at a single-line exposure wavelength, λ_{exp} , of $363.8nm$ is used as the laser source. The laser beam is divided and redirected using zero-order half-wave plates (HWPs), broadband polarizing beam-splitter cubes (PBSCs), and mirrors (M1 to M8). By rotating a HWP positioned before (after) a PBSC, the intensity (polarization) of the beams exiting the PBSC can be controlled. As a result, the multiple beams are individually controlled in intensity and polarization [81].

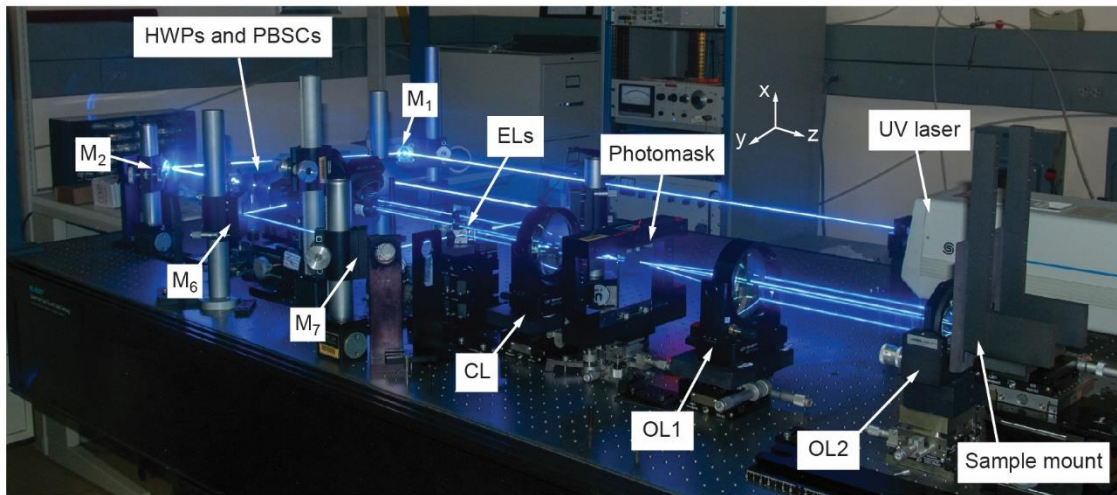
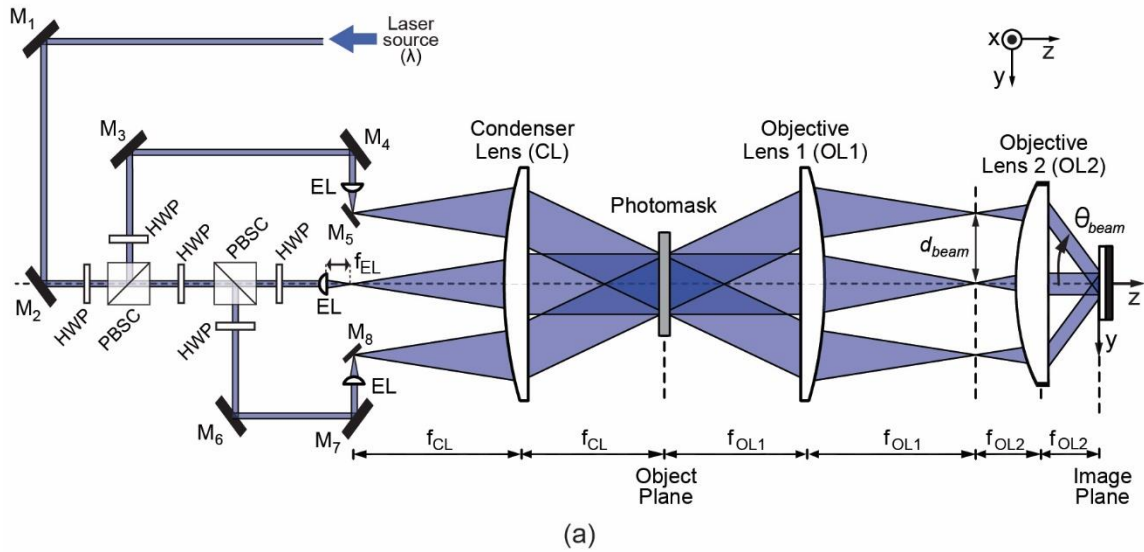


Figure 5.1: (a) Schematic representation of the PIIES. (b) Picture of the prototype PIIES in the laboratory. Selected components from (a) are labeled.

As explained in Section 2.3.1, an image-side high numerical aperture (NA) is desirable in PIIL to allow for both higher resolution and a smaller interference period. In addition, large-diameter lenses are necessary to expand the cross-section of the interfering beams and thus, increase the exposure area at the image plane. The only commercially-available lens that meets these criterion is a Thorlabs large-diameter aspheric lens (Thorlabs

AL7560-A) with $NA = 0.62$ at a lens design wavelength, λ_{des} , of $780nm$. This lens is chosen as the objective lens 2 (OL2) and has a focal length $f_{OL2} = 60mm$. For the objective lens 1 (OL1), another large-diameter aspheric lens (Thorlabs AL100200-A) is employed, but with focal length $f_{OL1} = 200mm$. Therefore, the compound objective lens magnification, $M = f_{OL2} / f_{OL1}$, is 0.3. For beam propagation symmetry and to facilitate system alignment, the condenser lens (CL) is identical to OL1. The expander lenses (ELs) are $0.5in$ -diameter mounted aspheric lenses (Thorlabs A220TM-A) with focal length $f_{EL} = 11mm$. The M5 and M8 mirrors are $0.5in$ -diameter mirrors. The small diameters of the ELs and the mirrors ensure a minimized form factor and allow the beams to be aligned as close as possible prior to the CL.

To maintain a reduced form factor, M5 and M8 are mounted in miniature corner mounts (Newport 9871-K); the ELs are secured in $0.5in$ -diameter lens mounts (Thorlabs LMR05S); and the ELs, M5, and M8 are all placed on $1.5in$ -wide compact three-axis linear stages (Newport DS40-XYZ). The positioning of the other optics is less constraining. The CL, OL1, and OL2 are secured in robust two-rotation-axis gimbal lens mounts (Newport 605-4 and Aerotech AOM110). For positioning in the yz -plane, the mounted CL and OL1 are placed on two linear stages (Newport 426) staked at $90deg$, while the mounted OL2 is positioned on a three-axis linear stage (Newport ULTRAlign XYZ).

For the photomask and sample, robust custom mounts were designed and fabricated. The photomask mount placed at the object plane (OP) is stacked on a two-axis linear stage (Thorlabs XYT1) for alignment in the yz -plane, a platform (Thorlabs PY004) for both pitch (rotation around the y -axis) and yaw (rotation around the z -axis) correction, and a lab jack (Thorlabs L490) for translation along the x -axis (normal to the table). For the sample

mount located at the image plane (IP), a tilt/yaw platform and a lab jack identical to those for the photomask mount are employed as well. The positioning of the sample mount in the yz-plane is done with two linear stages stacked at $90deg$. The actuator of the linear stage oriented along the z-axis is a high-precision differential micrometer with sub-micron sensitivity (Newport DM-25L), which is needed position precisely the sample at the image focal plane.

5.2 Interference Pattern Formation Capability

5.2.1 Range of Feasible Angles of Incidence

To assess the capabilities of the PIIES in producing useful interference patterns, the range of feasible common beam incidence angles at the image plane, θ_{beam} , is first determined using ZEMAX [155]. The lenses are modeled in ZEMAX using the lens characteristics given in Table 5.1, which are provided by the lens manufacturer. The ZEMAX-simulated ray trace for a single beam through the modeled PIIES is shown in Figure 5.2.

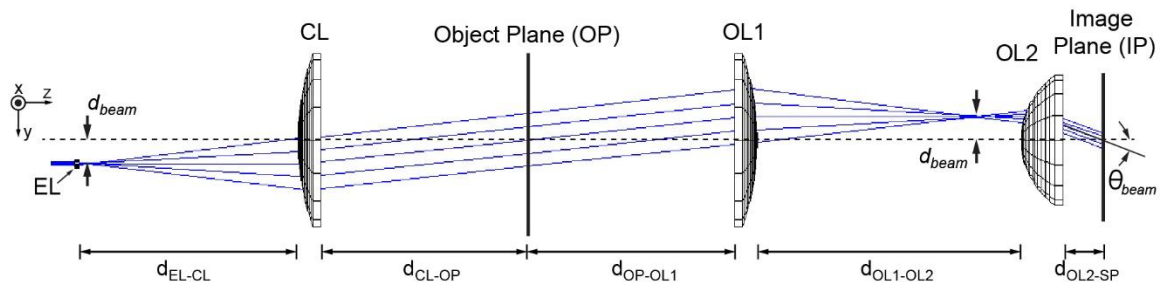


Figure 5.2: Ray tracing of a single beam through the ZEMAX-modeled PIIES.

Table 5.1: Lens parameters of EL, CL, OL1, and OL2 as given in the datasheets.

Lens Parameter	EL	CL and OL1*	OL2*
Thorlabs Part Number	A220TM-A	AL100200-A	AL7560-A
Design Wavelength, λ_{des} (nm)	633	780	780
Focal Length (mm)	11	200	60
Working Distance (mm)	6.91	187.4	36.5
Clear Aperture (mm)	5.5	92	58
NA	0.26	0.23	0.62
<i>Aspheric Coefficients</i>			
Radius (mm)	72.47 / -5.97	102.24 / ∞	43.84 / ∞
Conic	–	-1.318	-0.751
2 nd order (mm^{-2})	–	–	0.005
4 th order (mm^{-4})	3.384×10^{-4}	8.682×10^{-8}	1.616×10^{-6}
6 th order (mm^{-6})	1.305×10^{-5}	1.773×10^{-13}	3.726×10^{-10}
8 th order (mm^{-8})	-1.098×10^{-6}	1.903×10^{-17}	9.893×10^{-14}
10 th order (mm^{-10})	1.374×10^{-7}	–	1.099×10^{-17}
12 th order (mm^{-12})	-5.496×10^{-9}	–	–

*Note: Since their purchase, the AL100200-A and AL7560-A lenses have been redesigned by Thorlabs. The lens characteristics now available from Thorlabs is different from the lens characteristics in the table.

The propagation of the beams within the PIIES must meet the following conditions:

- 1) Collimation of the beam at the object plane,
- 2) Centering of the beam on the origin at the object plane,
- 3) Beam propagation parallel to the z-axis between OL1 and OL2,
- 4) Collimation of the beam at the image plane,
- 5) Centering of the beam on the origin at the image plane, and
- 6) Achieving the specified value of θ_{beam} at the image plane.

Meeting those constraints for a specific value of θ_{beam} requires a particular positioning of the various optical elements within the PIIES configuration. Using the ZEMAX optimization algorithm, the lateral beam displacement, d_{beam} , and the distances d_{EL-CL} ,

d_{CL-OP} , d_{OP-OL1} , $d_{OL1-OL2}$, and d_{OL2-IP} , defined in Figure 5.2 are set as variable parameters in the optimization of the above constraints.

Physical constraints of the opto-mechanical system limit the feasible values of d_{beam} and θ_{beam} . The M5 and M8 mirror mounts in Figure 5.1(a) come into contact for $d_{beam} \approx 5mm$, corresponding to a minimum value of θ_{beam} of about $5deg$. For θ_{beam} larger than $30deg$, the beam becomes vignetted due to the limited clear aperture of OL2. This vignetting reduces the diameter of the overlapping beams at the sample plane and thus, the exposure area. Therefore, θ_{beam} ranges from $5deg$ to $30deg$. The ZEMAX optimization indicates that experimentally feasible values of d_{beam} and inter-plane distances were found that satisfy the above constraints. Of note, d_{EL-CL} , $d_{OL1-OL2}$, and the PIIES total length, d_{total} , measured from the EL to the sample plane, were found to vary with θ_{beam} . The corresponding change in axial length Δd_{EL-CL} , $\Delta d_{OL1-OL2}$, and Δd_{total} are plotted as a function of θ_{beam} in Figure 5.3. d_{EL-CL} , $d_{OL1-OL2}$, and d_{total} decreases by about 12%, 12%, and 6%, respectively, for θ_{beam} increasing from $5deg$ to $30deg$. These results suggest that ELs, OL2, and the sample mount must be repositioned for a new values of d_{beam} and θ_{beam} , while the CL, photomask, and OL1 remain relatively fixed.

5.2.2 Range of Feasible Interference Periods

From an experimental perspective, monitoring and adjusting d_{beam} during the PIIES alignment is significantly more practical and less prone to errors than measuring θ_{beam} once the complete PIIES has been aligned. Therefore, a relationship between d_{beam} and the desired interference period produced at the image plane is valuable. This relationship is

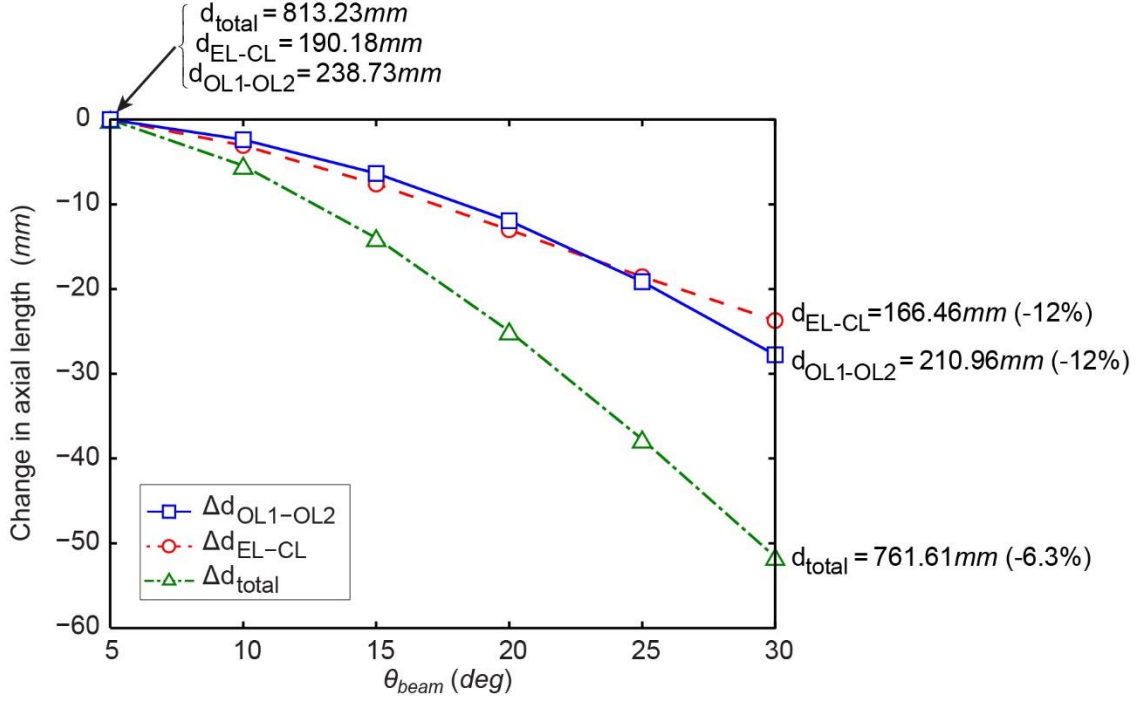


Figure 5.3: The EL, CL, OL1, and OL2 can be positioned to satisfy the beam propagation constraints for the full range of feasible θ_{beam} . However, the distances d_{EL-CL} , $d_{OL1-OL2}$, and thus, d_{total} decrease as θ_{beam} increases.

evaluated for four typical lattice symmetries of multi-beam interference patterns: a 2D hexagonal and square lattices produced with three beams, a 3D face-centered-rhombohedral (FCR) lattice produced with four beams, and a 3D woodpile lattice produced with five beams. A 2D hexagonal-lattice interference pattern is typically generated with three interfering beams symmetrically distributed around the z-axis. The resulting interference period in the xy-plane, Λ_{hex} , is expressed as

$$\Lambda_{hex} = \frac{2\lambda_{exp}}{3\sin\theta_{beam}}. \quad (5.1)$$

The periods in the xy-plane for the 2D square-lattice (Λ_{sq}), 3D FCR- lattice ($\Lambda_{xy}^{(3+1)}$), and 3D woodpile-lattice ($\Lambda_{xy}^{(4+1)}$) interference patterns are given in Equations (3.1), (4.7) and

(4.8), respectively. The period along the z-axis for 3D interference patterns, $\Lambda_z^{(q+1)}$, where q equals 3 or 4 for the (3+1)- or (4+1)-beam configuration, respectively, is given in Equation (4.9). Using the ZEMAX optimization results from the previous section, d_{beam} can be calculated for each simulated θ_{beam} . For θ_{beam} ranging from $5deg$ to $30deg$, d_{beam} ranges from $4.95mm$ to $27.19mm$. From this relationship, feasible values of Λ_{sq} and Λ_{hex} are calculated for the 2D interference patterns and plotted as functions of d_{beam} in Figure 5.4(a). Likewise for the 3D interference patterns, feasible values of $\Lambda_{xy}^{(3+1)}$, $\Lambda_{xy}^{(4+1)}$, and $\Lambda_z^{(q+1)}$ are calculated and plotted as functions of d_{beam} in Figure 5.4(b). Numerical values of d_{beam} and the interference periods for $\theta_{beam} = 5deg$ and $\theta_{beam} = 30deg$ are given in Table 5.2.

Table 5.2: Numerical values of d_{beam} and the interference periods for the extreme values $\theta_{beam} = 5deg$ and $\theta_{beam} = 30deg$.

	d_{beam} (mm)	Λ_{sq} (μm)	Λ_{hex} (μm)	$\Lambda_{xy}^{(3+1)}$ (μm)	$\Lambda_{xy}^{(4+1)}$ (μm)	Λ_z (μm)
$\theta_{beam} = 5deg$	4.95	2.95	2.78	4.82	3.99	160
$\theta_{beam} = 30deg$	27.19	0.51	0.49	0.84	0.70	1.1

The feasible periods in the xy-plane range from sub-micron to a few microns. However, the feasible periods along the z-axis for 3D-PIIL exposures range from $\sim 10\mu m$ to more than $150\mu m$. Since no immersion fluid is used in the present prototype PIIES, the 3D interference patterns are stretched along the z-axis. As discussed in Chapter 4, a photoresist-index-matching fluid would be needed to produce 3D cubic-lattice interference patterns. The data points in Figures 5.4(a) and (b) are fitted to power functions with R^2 larger than 0.999 for the five fitting equations. These empirical equations provide a

practical means to adjust d_{beam} and align the PIIES for a targeted interference period and will be used for the PIIL experimental demonstration.

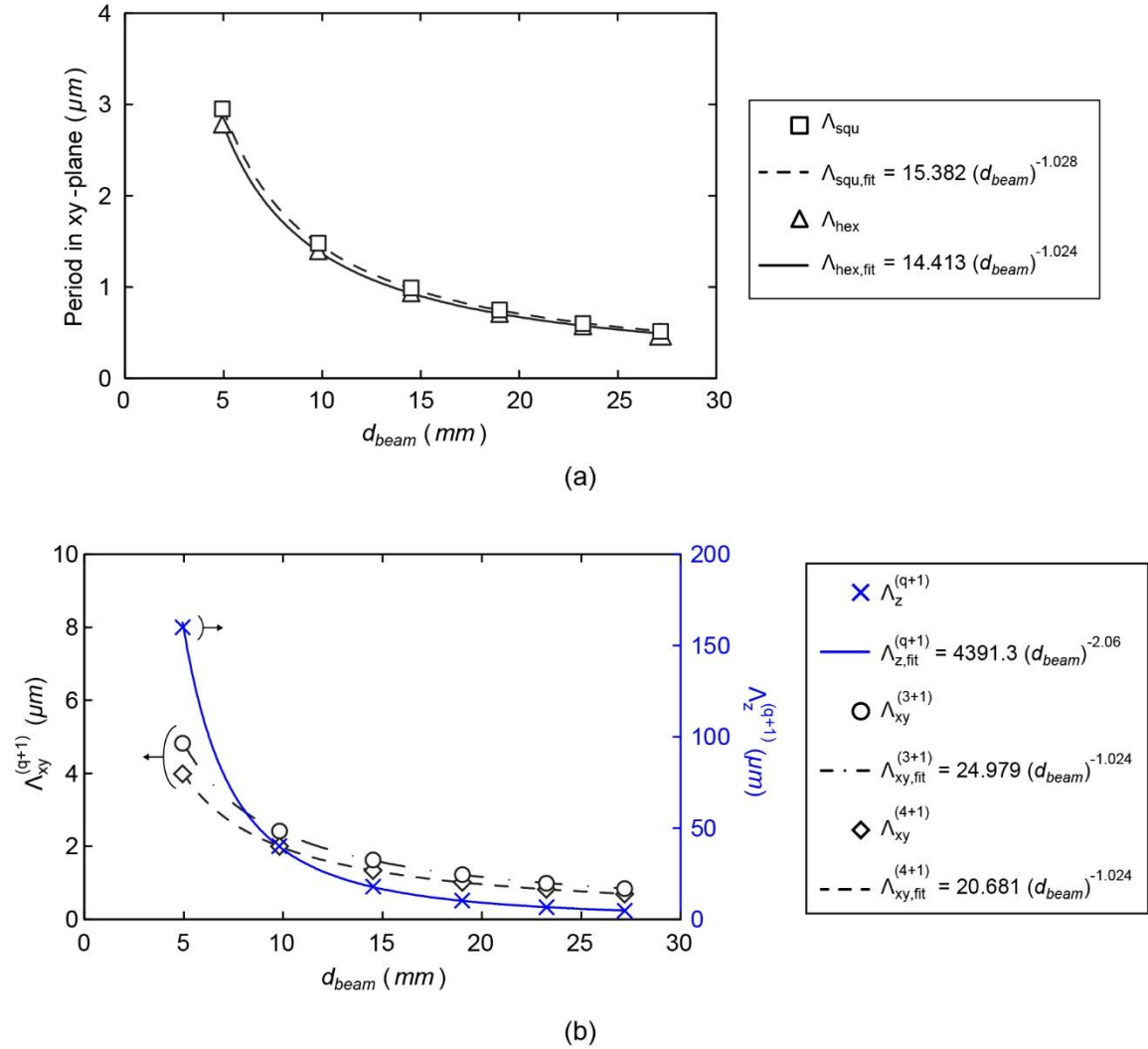


Figure 5.4: Feasible periods for (a) 2D square- and hexagonal-lattice and (b) 3D FCR- and woodpile-lattice interference patterns. Equations fitting the data points are given as well and are practical in aligning the prototype PIIES to target a particular interference period.

5.2.3 Interference Pattern Sensitivity to Beam Misalignment

At the PIIES image plane, the interference pattern depends on the 1D interference fringes produced by all of the possible beam pairs. In the general case of N-beam interference, $N \times (N - 1) / 2$ fringe patterns are generated and contribute to the formation of the multi-beam interference pattern. Therefore, the period and the symmetry of the final interference pattern depend on these individual fringe patterns. Due to possible lens or beam misalignment, the interfering beams may be subject to positioning errors such as decentering and tilting. The objective of this section is to quantify the error in the period and the orientation of the interference fringes produced by a single beam pair when one of the interfering beams is decentered with respect to the z-axis. The impact of beam tilting on imaging is discussed later.

5.2.3.1 Perfect Beam Alignment

The two-beam interference case at the PIIES image plane in the *absence* of beam misalignment is first reviewed. The period between the bright and dark fringes and their orientation produced by the interference of two coherent, monochromatic beams depend on the beam wavevectors. In the PIIES, the direction of the i^{th} interfering beam at the image focal plane may be expressed as $[d_{beam}\cos\varphi_i \quad d_{beam}\sin\varphi_i \quad f_{OL2}]$, where φ_i is the azimuthal angle of the i^{th} beam with respect to the x-axis. This vector can be normalized as

$$\mathbf{k}_i = \frac{2\pi}{\lambda_{exp}} \begin{bmatrix} \cos\varphi_i \sin\theta_{beam} \\ \sin\varphi_i \sin\theta_{beam} \\ \cos\theta_{beam} \end{bmatrix}, \quad (5.2)$$

which is the beam wavevector. The interference fringes produced by the two beams are characterized by the grating vector expressed as

$$\Delta \mathbf{k} = \mathbf{k}_2 - \mathbf{k}_1 = \frac{2\pi}{\lambda_{exp}} \begin{bmatrix} (\cos\varphi_2 - \cos\varphi_1)\sin\theta_{beam} \\ (\sin\varphi_2 - \sin\varphi_1)\sin\theta_{beam} \\ 0 \end{bmatrix}. \quad (5.3)$$

Noteworthy, the component along the z-axis of the grating vector is 0 and thus, there is no periodicity along the z-direction. From Equation (5.3), the period in the xy-plane between two fringes may be expressed as

$$\Lambda_{1D} = \frac{2\pi}{|\Delta \mathbf{k}|} = \frac{\lambda_{exp}}{\sin\theta_{beam} \sqrt{(\cos\varphi_2 - \cos\varphi_1)^2 + (\sin\varphi_2 - \sin\varphi_1)^2}} \quad (5.4)$$

and the orientation of the grating vector relative to the x-axis as

$$\Theta = \tan^{-1} \left(\frac{\Delta k_y}{\Delta k_x} \right) = \tan^{-1} \left(\frac{\sin\varphi_2 - \sin\varphi_1}{\cos\varphi_2 - \cos\varphi_1} \right). \quad (5.5)$$

The quantities $\Delta \mathbf{k}$, Λ_{1D} , and Θ are illustrated in Figure 5.5. With azimuthal angles $\varphi_1 = 180deg$ and $\varphi_2 = -90deg$ for the two beams, the period of the fringe pattern is $\Lambda_{1D} = \lambda_{exp}/2\sin\theta_{beam}$ and the orientation is $\Theta = -45deg$ with respect to the x-axis.

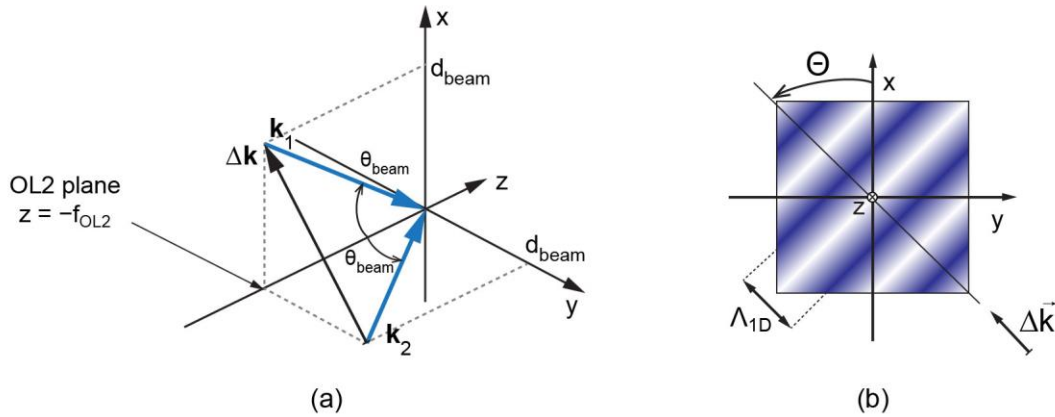


Figure 5.5: (a) Example two-beam configuration propagating after OL2. (b) Corresponding fringe interference pattern in the xy-plane.

5.2.3.2 Imperfect Beam Alignment

A beam decentering is now assumed for the second beam and corresponds to a change in the intersect point between \mathbf{k}_2 and the $z = -f_{OL2}$ plane. Physically, it corresponds to a change in d_{beam} and φ_2 for the second beam, but the beam still propagates parallel to the z -axis between OL1 and OL2. Due to the decentering, the second beam has a different lateral beam displacement, d_{beam}^* , different angle of incidence, θ_{beam}^* , and a different azimuthal angle, φ_i^* which are illustrated in Figure 5.6(a). These new beam parameters modify the grating vector and thus, both the fringe period and fringe orientation. The beam decentering may be expressed as a function of two parameters: a radial distance error from the ideal intersection between \mathbf{k}_2 and the $z = -f_{OL2}$ plane, ρ , and an azimuthal angle error, η . The propagation vector of the decentered beam is now expressed as

$$\mathbf{k}_2^* = \begin{bmatrix} d_{beam} \cos \varphi_2 - \rho \cos \eta \\ d_{beam} \sin \varphi_2 - \rho \sin \eta \\ f_{OL2} \end{bmatrix}, \quad (5.6)$$

and the modified grating vector is expressed as

$$\Delta \mathbf{k}^* = \frac{2\pi}{\lambda_{exp}} \frac{\mathbf{k}_2^*}{|\mathbf{k}_2^*|} - \mathbf{k}_1. \quad (5.7)$$

The expressions for the modified fringe period and orientation are

$$\Lambda_{1D}^* = \frac{2\pi}{|\Delta \mathbf{k}^*|} \quad (5.8)$$

and

$$\Theta^* = \tan^{-1} \left(\frac{\Delta k_y^*}{\Delta k_x^*} \right), \quad (5.9)$$

respectively.

Typical values of Λ_{1D} , and Θ given in Table 5.3 are used to calculate changes in fringe period and orientation. The relative fringe period error, $e_\Lambda = (\Lambda_{1D}^* - \Lambda_{1D}) / \Lambda_{1D}$, and the fringe orientation error, $e_\Theta = \Theta^* - \Theta$, at the image plane are calculated with Equations (5.8) and (5.9). The maximum radial distance error, ρ_{max} , is $0.5mm$, which represents the maximum beam decentering. The quantities e_Λ and e_Θ are plotted in Figures 5.6(b) and (c), respectively, as functions of the coordinates of the intersect point between \mathbf{k}_2^* and the $z = -f_{OL2}$ plane.

Table 5.3: Beam parameters for the calculations of e_Λ and e_Θ

λ_{exp} (nm)	d_{beam} (mm)	θ_{beam} (deg)	Λ (μm)	Θ (deg)	f_{OL2} (mm)	ρ_{max} (mm)	φ_1 (deg)	φ_2 (deg)
363.8	13.97	14.62	0.95	-45	53.17	0.5	180	-90

The direction of the horizontal and vertical axes of the plots in Figures 5.6(b) and (c) are identical to those of the x- and y-axis in Figures 5.6(a). Along the x-axis, the decentering ranges from $-\rho_{max}$ to ρ_{max} . Along the y-axis, the decentering ranges from $d_{beam} - \rho_{max}$ to $d_{beam} + \rho_{max}$. The $(0, d_{beam})$ point (center of the plots) corresponds to an absence of decentering since the second beam propagates along its ideal path. The top-left corner point $(\rho_{max}, d_{beam} - \rho_{max})$, however, corresponds to a decentering with $\rho = \sqrt{2}\rho_{max} = 0.71mm$ and $\eta = -45deg$ with respect to the x-axis. From the calculations, e_Λ ranges from -3.34% to 3.6% and e_Θ ranges from $-1.98deg$ to $1.99deg$.

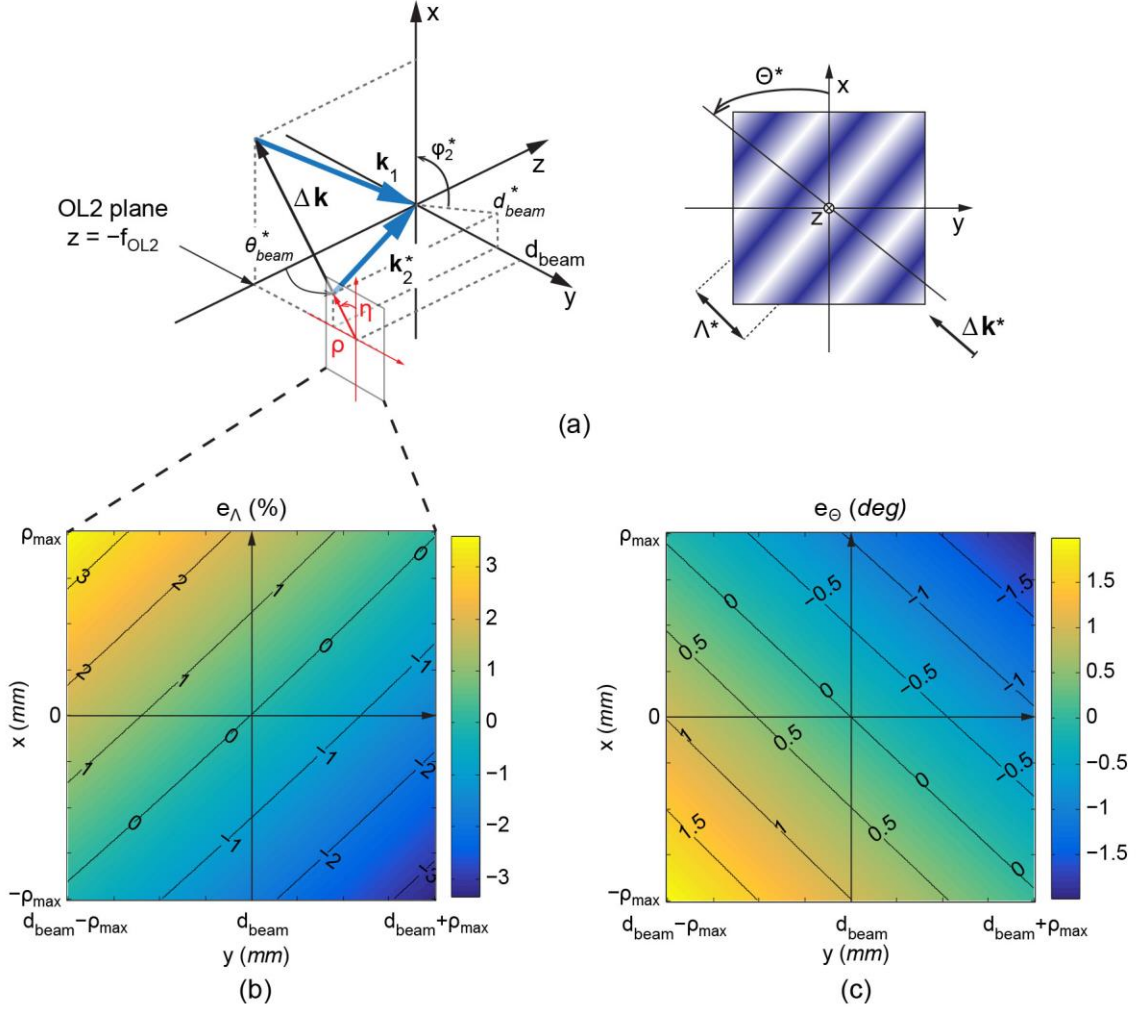


Figure 5.6: (a) Example two-beam configuration propagating after OL2, where the second beam is decentered relative to the z-axis. As a result, the period and orientation of the interference fringes are modified. (b) and (c) Relative fringe period error and fringe orientation error, respectively, as functions of the beam decentering in the xy-plane.

Due to their relative symmetry, it is interesting to analyze the plots by quadrants. A beam decentering in the top-left (bottom-right) quadrant in both plots results in a slightly decreased (increased) length of $\Delta \mathbf{k}^*$, resulting in an increased (decreased) Λ^* according to Equation (5.8). However, the direction of $\Delta \mathbf{k}^*$ is not significantly changed and thus, e_θ is small. Conversely, a beam decentering in the top-right (bottom-left) quadrant of both plots results in a slightly clockwise (counter-clockwise) rotation of $\Delta \mathbf{k}^*$, and thus a clockwise

(counter-clockwise) rotation of the fringes. Here, $\Theta = -45\text{deg}$, so a clockwise rotation results in a negative e_Θ since $\Theta^* < \Theta$. However, the length of $\Delta\mathbf{k}^*$ does not change significantly and thus, e_Λ is small.

Noteworthy, the plots are not exactly symmetrical with respect to the $x=y$ -axis. The contour lines are not straight lines, but arcs due to the beam arrangement. Also, the period and orientation errors are not coupled. With a beam decentering of $(\rho_{max}, d_{beam} + \rho_{max})$, it is possible to obtain a small period error, but a large orientation error, and *vice-versa*. Also, since $\theta_{beam}^* \neq \theta_{beam}$, $\Delta\mathbf{k}_z^* \neq 0$ and thus, a periodicity along the z -direction is expected. Yet, $\Delta\mathbf{k}_z^*$ remains very small compared to $\Delta\mathbf{k}_x^*$ and $\Delta\mathbf{k}_y^*$ and as a result, the grating vector lies essentially in the xy -plane.

5.3 Photomask Imaging with the Prototype PIIES

In the PIIES, the OL1 and OL2 form a confocal compound objective lens (COL) that projects images of the photomask placed at the object plane (OL1 front focal plane) to the image plane (OL2 back focal plane). In this Section, the imaging performance of the COL is analyzed with the ZEMAX software at both $\lambda_{exp} = 363.8\text{nm}$ and at $\lambda_{des} = 780\text{nm}$ wavelengths to evaluate the impact of using an exposure wavelength that differs from the lens design wavelength. The performance of a diffraction-limited lens system is generally considered acceptable when it produces no more than one quarter-wavelength (0.25waves) wavefront optical path difference (OPD) [116]. The root-mean square (RMS) OPD of the COL is derived from the 37 first Zernike coefficients describing a map of phase errors across the exit pupil that can be calculated with ZEMAX. More details about the Zernike polynomials and coefficients are given Appendix A. First, OL1, OL2, and COL are studied

individually for the case of a perfect alignment with the z-axis. Then, the impact of lens decentering and tilting on the COL imaging performance is investigated. Finally, image shifting due to beam tilting and the image distortion field are investigated.

5.3.1 COL Imaging Performance with Perfectly Aligned Lenses

To calculate the RMS OPD of OL1 and OL2, the lens working distance defined from the lens back face to the back focal plane as depicted in Figures 5.7(a) and (b), is optimized to minimize the RMS OPD. The RMS OPD values for OL1 and OL2 at λ_{des} and λ_{exp} are given in Table 5.4. As expected, the RMS OPD is almost zero for OL1 and OL2 at the lens design wavelength. The optimized working distances for OL1 and OL2 are $187.4mm$ and $36.6mm$, respectively. Those values are in excellent agreement with the lens working distances listed in Table 5.1. When the wavelength is changed to λ_{exp} , the RMS OPDs increase and the working distances decrease. The RMS OPD of OL1 and OL2 are $0.23waves$ and $0.69waves$, respectively. This increase in OPD is essentially due to spherical aberrations. The Z1 (piston), Z9, Z16, Z25, Z36, and Z37 (3rd, 5th, 7th, 9th, and 11th order spherical aberrations, respectively) Zernike coefficients contribute to the increased OPD. The Zernike coefficient values are given in Appendix A. Also, the OL1 and OL2 working distances are reduced to $178.2mm$ and $33.9mm$, respectively. The reduction in working distance expected since $\lambda_{exp} < \lambda_{des}$.

OL1 and OL2 are next combined to be analyzed as a COL. The distance between OL1 and OL2 is fixed to a typical distance of $230mm$. This is due to the fact that if the OL1-OL2 distance is set as a variable, the optimization diverges and no realistic solution is found. However, the distance from the object plane to the front face of OL1 and the distance from the back face of OL2 to the image plane illustrated in Figure 5.7(c) are set

as variables. The RMS OPDs for the COL are given in Table 5.4. At λ_{des} , the RMS OPD of the COL is almost zero as expected. At λ_{exp} , however, the RMS OPD of the COL is 0.46 waves, which is almost twice the quarter wavelength limit. Therefore, using an exposure wavelength different from the lens design wavelength results in spherical aberrations that deteriorate the imaging of the photomask.

Table 5.4: RMS OPD for OL1, OL2, and COL at the design and exposure wavelengths.

	RMS OPD (waves)		
	OL1	OL2	COL
$\lambda_{des} = 780nm$	0.000	0.002	0.003
$\lambda_{exp} = 363.8nm$	0.232	0.687	0.461

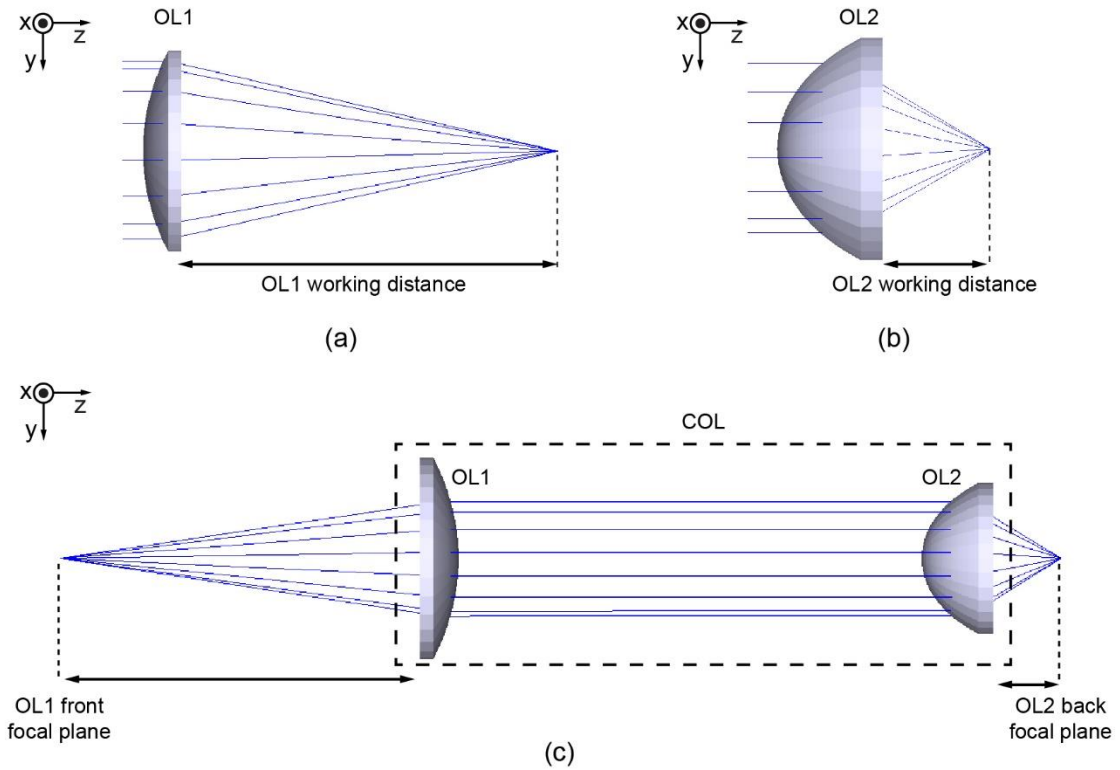


Figure 5.7: ZEMAX modeling of (a) OL1, (b) OL2, and (c) COL.

5.3.2 Imaging Performance with Decentered or Tilted Lenses

The impact of lens decentering and tilting on the imaging performance of the COL is next studied. Lens decentering is defined as a lateral shift of the lens within the xy-plane and thus, a lens misalignment relative to the z-axis. Lens tilting is defined as yaw (rotation around the x-axis) or pitch (rotation around the y-axis).

To study the impact of lens decentering on the RMS OPD of the COL, OL1 and OL2 are decentered separately. First OL1 is decentered while OL2 is maintained perfectly aligned. Then OL2 is decentered while OL1 is maintained perfectly aligned. Also, the decentering is applied along the $y=x$ axis. The RMS OPDs of the COL are plotted as functions of OL1 and OL2 decentering in Figure 5.8(b) and (c), respectively. The dashed and solid lines correspond to RMS OPD calculations at λ_{des} and λ_{exp} , respectively. OL1 appears to be significantly more sensitive to decentering than OL2. At λ_{des} , a decentering smaller than $50\mu m$ remains acceptable as the RMS OPD is still smaller than $0.25waves$. At λ_{exp} , a decentering smaller than $25\mu m$ does not increase noticeably the RMS OPD above its starting value of $0.46waves$. $25\mu m$ may be considered as an acceptable decenter error during the PIIES alignment. Of note, even if OL2 is less sensitive to decentering than OL1, large decentering of OL2 will result in a detrimental lateral shift of the projected images that should be prevented.

Similar to the decentering study, OL1 and OL2 are not tilted simultaneously, but separately to study the influence of lens tilting. Also, the tilt angle is applied as yaw and pitch simultaneously. The RMS OPDs of the COL are plotted as functions of tilt angles applied on OL1 and OL2 in Figure 5.9(b) and (c), respectively. The dashed and solid lines

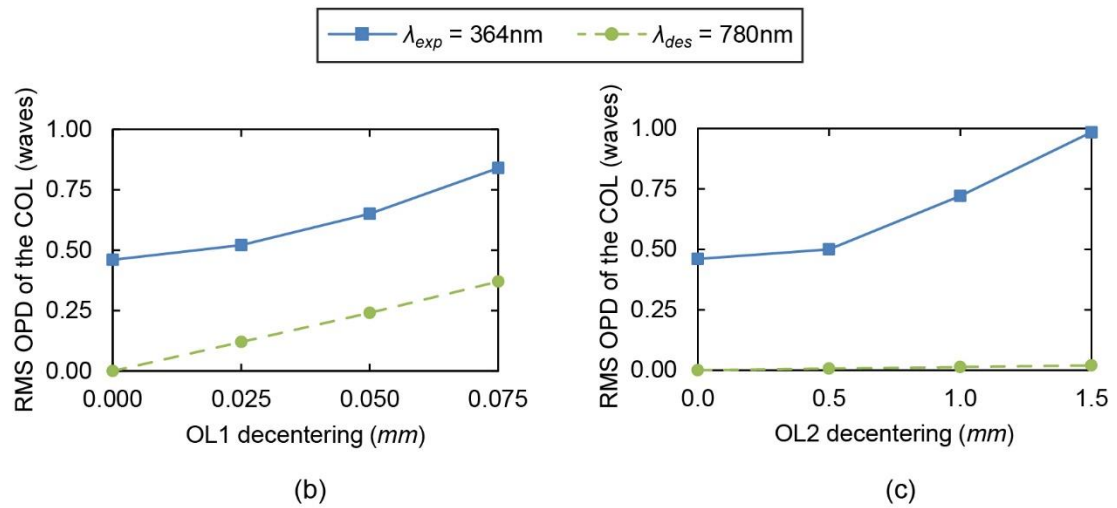
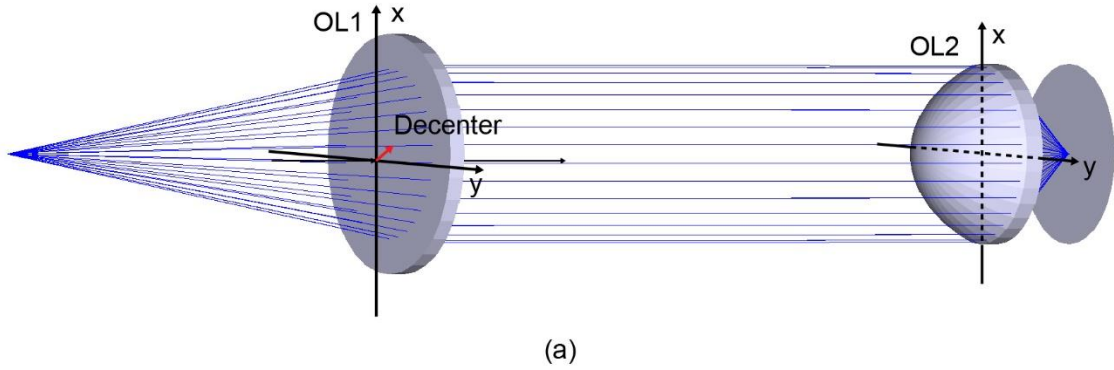


Figure 5.8: (a) Illustration of lens decentering applied on OL1 in the COL. (b) and (c) Calculated RMS OPDs as functions of OL1 and OL2 decentering at λ_{des} and λ_{exp} wavelengths.

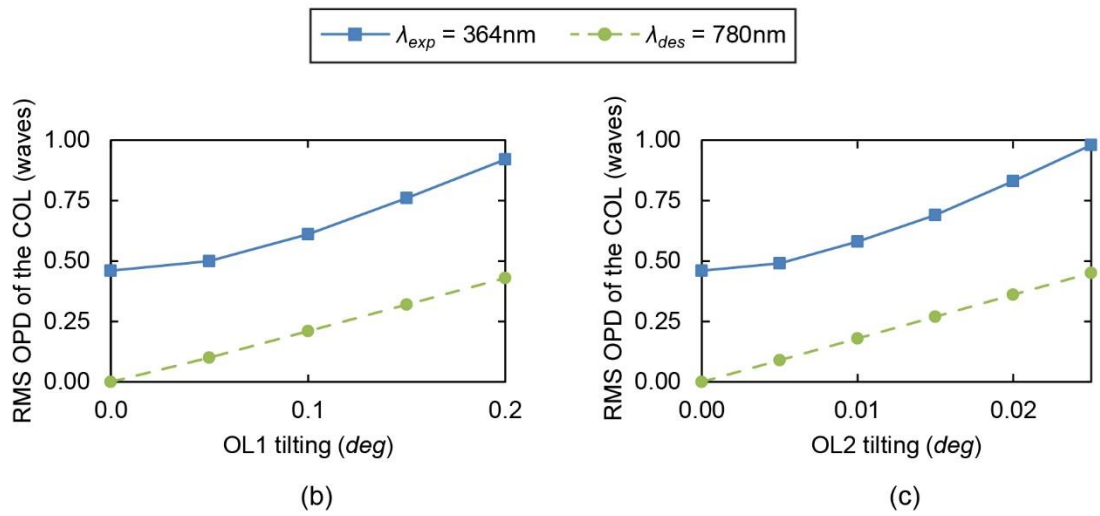
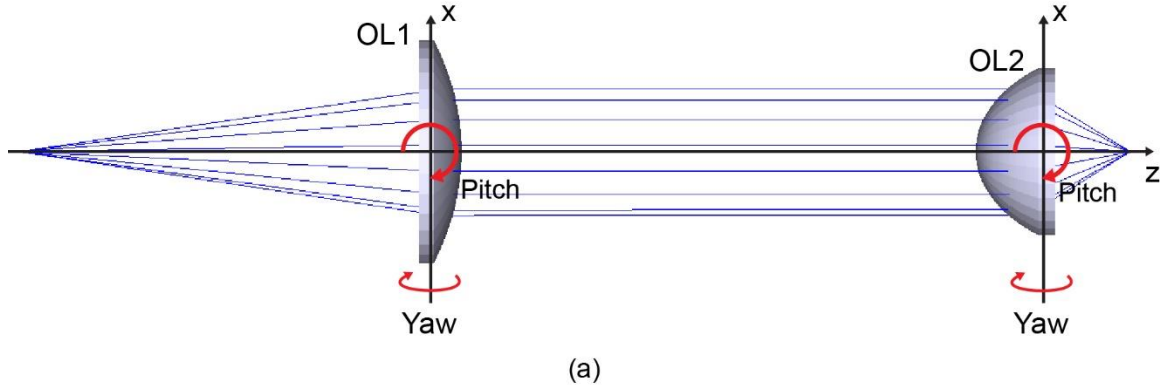


Figure 5.9: (a) Illustration of lens tilting in the COL. (b) and (c) Calculated RMS OPDs as functions of OL1 and OL2 tilt angles at λ_{des} and λ_{exp} wavelengths.

correspond to RMS OPD calculated at λ_{des} and λ_{exp} , respectively. Unlike decentering, OL2 is significantly more sensitive to tilting than OL1. To produce an identical RMS OPD, OL1 has to be tilted almost ten times more than OL2. At λ_{des} , tilt angles smaller than $0.1deg$ for OL1 and $0.015deg$ for OL2 result in RMS OPD smaller than $0.25waves$. At λ_{exp} , a tilt error smaller than $5 \times 10^{-3}deg$ remains acceptable as it does not increase the RMS OPD above $0.46waves$ significantly.

5.3.3 Exposure Field Distortions

Image distortions across the field of exposure at the COL image plane are next analyzed. The ZEMAX distortion grid analysis tool was used to calculate the image-plane coordinates of a grid of points located at the object plane. The coordinates of the imaged grid points can be compared to the reference coordinates of the undistorted image of the grid. From these grid point coordinates, a distortion error is calculated as the difference between the radial coordinates of an actual grid point and the radial coordinates of the reference grid point. For the present calculation, λ_{exp} is used as the exposure wavelength and d_{beam} and θ_{beam} are equal to the typical values listed in Table 5.3. The COL is assumed to be perfectly aligned. Interfering beams with these parameters generate interference patterns with a $\sim 1\mu m$ -period. The width of the simulated grid is $8.6mm$ at the object plane. At the image plane, the width of the projected grid is about $2.5mm$. The ratio of the widths is 0.29 and is consistent with the estimated magnification $M = 0.3$ of the COL. Two beam configurations are considered and shown in Figure 5.10(a) and Figure 5.11(a), respectively.

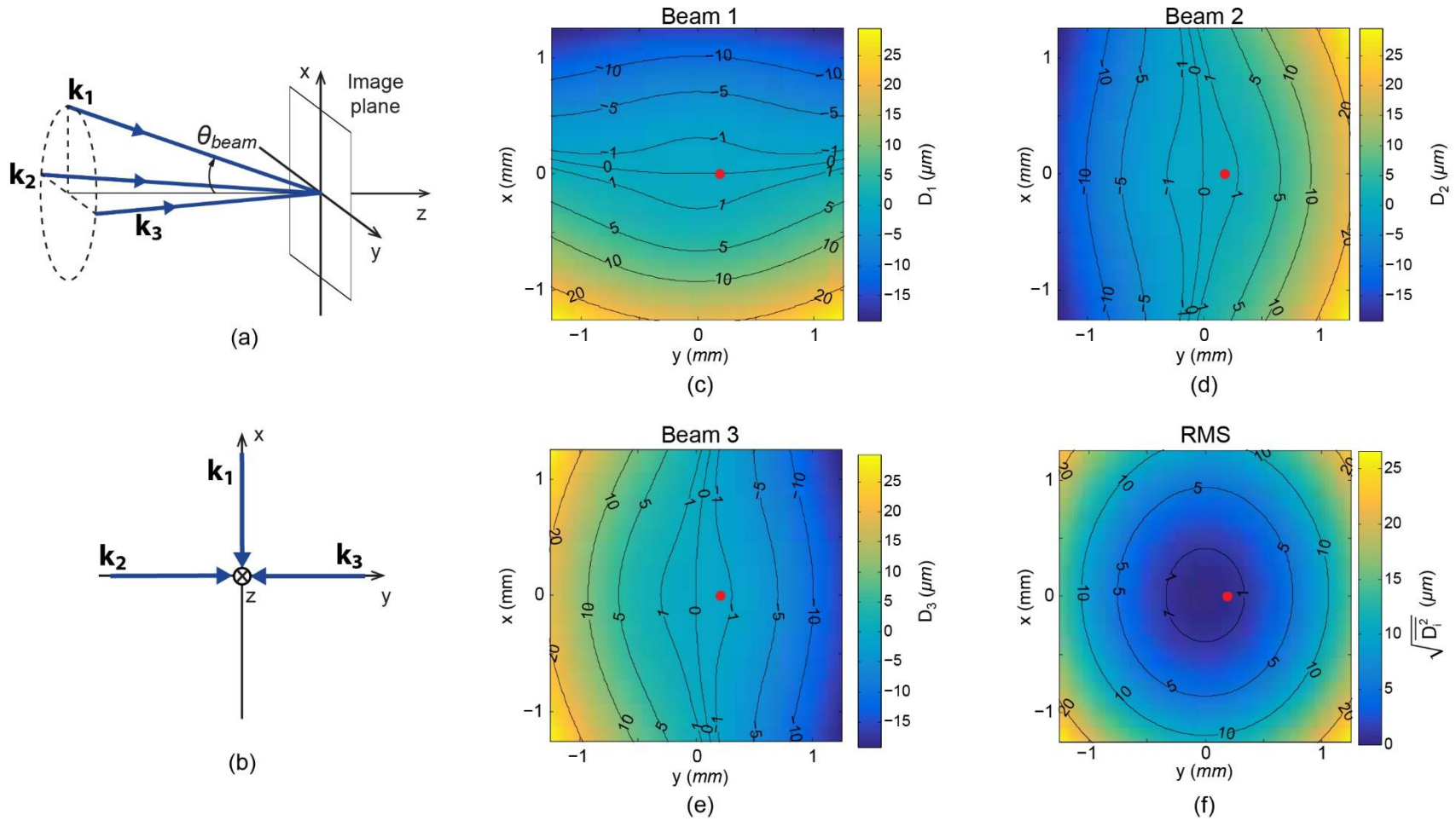


Figure 5.10: (a) 3D and (b) 2D representations of an example three-beam configuration at the COL image plane. (c), (d), and (e) Distortion error across the image plane for the first, second, and third beam, respectively. The three red dots correspond to the discussed example points. (f) RMS of the three distortion error maps. The exposure field area with $\text{RMS} < 0.5\mu\text{m}$ is smaller than 0.2mm^2 and centered on the optical axis.

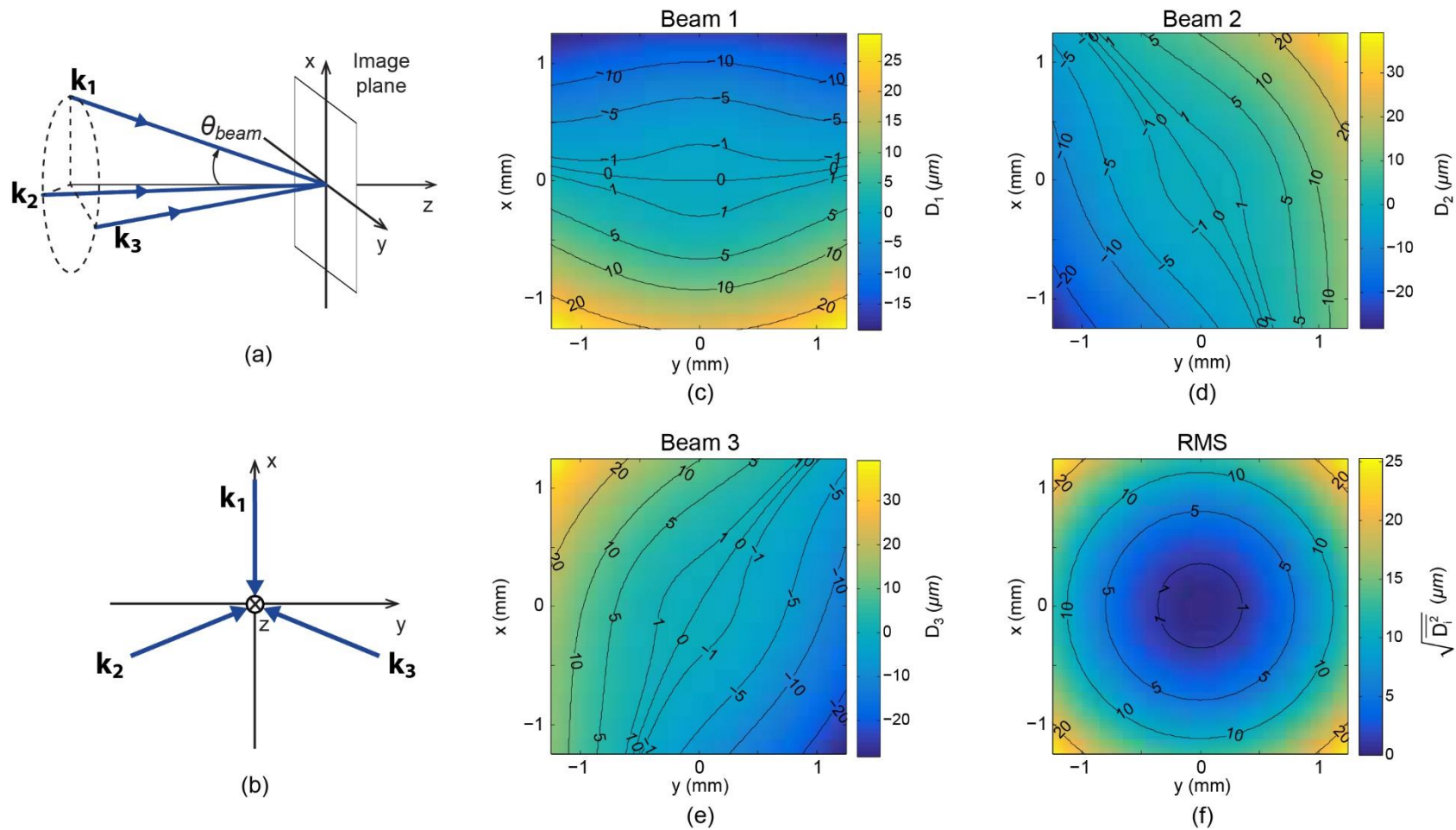


Figure 5.11: (a) 3D and (b) 2D representations of an example three-beam configuration at the COL image plane. (c), (d), and (e) Distortion error across the image plane for the first, second, and third beam, respectively. (f) RMS of the three distortion error maps. The exposure field area with RMS distortion errors $< 0.5 \mu\text{m}$ is smaller than 0.2mm^2 and centered on the optical axis.

For the first beam configuration, the distortion errors at the image plane generated by each of the three beams, D_1 , D_2 , and D_3 , are plotted in Figures 5.10(c)-(e), respectively. A pixel with a negative (positive) error correspond to a projected grid point that is closer to (further from) the origin than the reference projected grid point. Of note, the distortion errors exhibit a symmetry along the projections in the xy -plane of their corresponding beams, which are depicted in Figure 5.10(b). Yet, the grids are distorted differently depending on the beam. For example, for a reference point projected at $(x, y) = (0, 250\mu\text{m})$, the actual grid point is located at $(0, 250\mu\text{m})$ with the first beam ($0.0\mu\text{m}$ error), $(0, 250.7\mu\text{m})$ with the second beam ($0.7\mu\text{m}$ error), and $(0, 249.3\mu\text{m})$ with the third beam ($-0.7\mu\text{m}$ error). The corresponding points are marked with red dots in the distortion errors maps in Figures 5.10(c)-(e). Therefore, the RMS distortion error for this particular point only $250\mu\text{m}$ from the optical axis is $0.56\mu\text{m}$, which is already half the targeted interference period of $1\mu\text{m}$. Such a misalignment of the images is therefore extremely detrimental when attempting to integrate the superposed photomask features within the interference pattern. The field of exposure with $\text{RMS} < 0.5\mu\text{m}$ is expected to be smaller than 0.2mm^2 around the optical axis. The RMS distortion error is plotted in Figure 5.10(f). It is stretched along the x -axis, which is the axis of symmetry of the projection of the three-beam configuration in the xy -plane. The maximum RMS distortion error in the $2.5\text{mm} \times 2.5\text{mm}$ image field is $26.6\mu\text{m}$.

Similar results for the second beam configuration shown in Figure 5.11(a) are calculated and plotted in Figures 5.11(c)-(f). The distortion errors also exhibit symmetries along axes that are matching the projections of their respective beams in the xy -plane depicted in Figure 5.11(b). The RMS distortion error is circularly symmetrical due to the

symmetry of the beam configuration. Similar to the previous results, the exposure field around the optical axis is smaller than $0.2mm^2$ for RMS distortion errors smaller than $0.5\mu m$. The maximum RMS distortion error is $25.34\mu m$ and is slightly smaller than that for the first beam configuration due to the more symmetrical beam configuration.

Interestingly, the calculated distortion errors at the $\lambda_{des} = 780nm$ lens design wavelength are very similar. For example, the maximum RMS distortion errors calculated at λ_{des} are $24.92\mu m$ and $23.78\mu m$ for the two beam configurations, respectively. These values are only 6% smaller than those obtained with λ_{exp} . Although the on-axis imaging is significantly better at λ_{des} as shown in Section 5.3.1, the field of exposure remains significantly limited around the optical axis with both wavelengths. This result is actually not entirely surprising knowing that state-of-the-art photolithographic lenses contain tens of simple lens elements to correct for optical aberrations over field of view larger than $500mm^2$. The simple design of the COL in the prototype PIIES appears to be too rudimentary to align correctly multiple images over large exposure fields. A photolithographic-grade COL would therefore be needed in the PIIES to enable the precise superposition of photomask images over large areas.

5.3.4 Image Shifting with Beam Tilting

In addition to beam decentering, one or more of the interfering beams may be tilted between OL1 and OL2, *i.e.* the beam is not propagating parallel to the z-axis. The consequence of a tilted beam between OL1 and OL2 is a lateral shift of the photomask image at the image plane, which is detrimental to the accurate superposition of the photomask images and their integration within the interference pattern.

To study the impact of beam tilt, the problem is simplified by assuming that the beam is at the correct d_{beam} distance from the z -axis at the front focal plane of OL2, but is tilted by an angle ψ . In the paraxial approximation, the tilted and non-tilted beams propagate parallel after OL2 and thus, have the same angle of incidence θ_{beam} as illustrated in Figure 5.12(a). Yet, the tilted beam is shifted upward in the present example and does not intersect the image plane on the optical axis. From geometrical optics, the shift, σ , can be estimated as $\sigma = f_{OL2} \sin \psi$. With $f_{OL2} = 53.17mm$ (Table 5.3), σ is plotted as a function of ψ in Figure 5.12(a). A beam tilt as small as $10^{-3}deg$ is sufficient to produce a $1\mu m$ shift at the image plane. Since the feasible periods calculated in Section 5.2.2 are close to $1\mu m$, it means that the beams must be aligned with less than $10^{-3}deg$ tilt error to insure a correct superposition of the images during the PIIL exposures. The shift can also be calculated using the ZEMAX software, which provides a more rigorous simulation of the beam propagation through the lens. The ZEMAX-calculated shifts are plotted as a function of ψ in Figure 5.12(b) and show a very good agreement with the paraxial model.

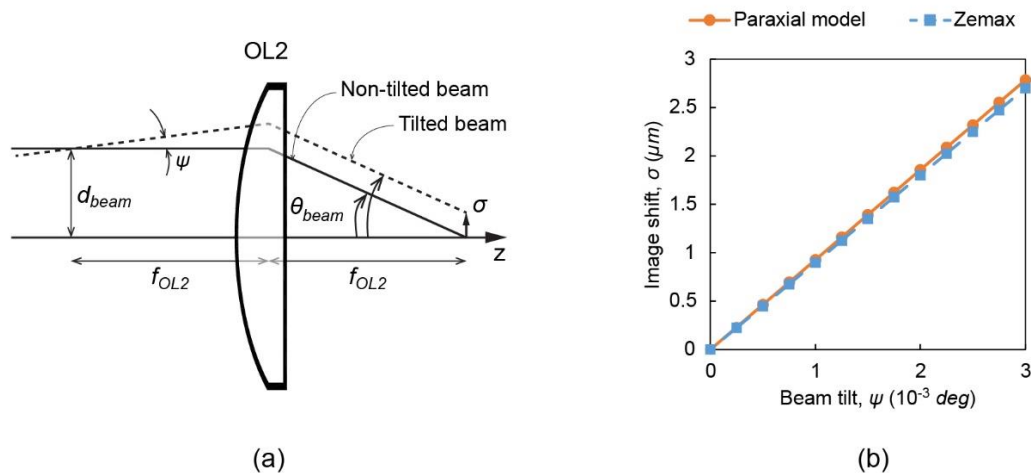


Figure 5.12: (a) Schematic representation of the propagation of a non-tilted (solid line) and tilted (dotted line) beam chief ray through OL2. The tilted ray is shifted upward at the image plane. (b) Image shift as a function of the beam tilt. Tilt error as low as $10^{-3}deg$ can introduce a detrimental $1\mu m$ shift.

5.4 Summary

A prototype PIIES implementing the PIIL technique was implemented with commercially-available lens components and opto-mechanical parts. The prototype PIIES was further analyzed using ZEMAX and geometrical optics. The analysis results are summarized in Table 5.5 and in Table 5.6.

Table 5.5: Summary of PIIES capabilities

Range of θ_{beam}	<i>5deg to 30deg</i>
Range of interference period in the xy-plane	<i>~ 0.5μm to ~5μm</i>
Range of interference period along the z-axis (for 3D interference patterns)	<i>~ 1μm to ~160μm</i>
Minimum on-axis RMS OPD	<i>0.46waves</i>
Exposure field area with RMS distortion errors <0.5 μm	<i>~ 250μm \times 250μm</i>

The prototype PIIES allows for a relatively large range of beam incidence angles at the image plane. Of note, beam vignetting begins to occur for beam angles close to *30deg* and may result in reduced exposure areas and beam aberrations. With an exposure wavelength of *363.8nm*, the range of beam incidence angles enables interference periods ranging from sub-micron to a few microns in the xy-plane and from microns to tens of microns along the z-axis for 3D interference patterns. Empirical fitting equations between the interference period and the lateral beam displacement were derived. From an experimental perspective, these relationships are practical and facilitate the PIIES alignment in targeting a desired lattice period. In case of beam decentering, the period and orientation of the interference fringe that form the complete interference pattern may be

modified. For $\pm 0.25mm$ decentering, the relative fringe period errors is about $\pm 2\%$ and the fringe orientation error is about $\pm 1deg$.

The capabilities of the PIIES COL in projecting the multiple images of the photomask have been studied as well. The use of an exposure wavelength different from the lens design wavelength results in a large $0.46waves$ RMS OPD, essentially due to spherical aberrations. Imperfect imaging of the photomask pattern is therefore expected. The RMS OPD is further worsened with lens decentering and tilting. Yet, $25\mu m$ lens decentering and $5mdeg$ lens tilting remain acceptable as to not increase significantly the RMS OPD above $0.46waves$. Photomask image superposition is also impeded due to field distortions at the image plane. Overlay errors smaller than $0.5\mu m$ are achieved in an exposure area of $250\mu m \times 250\mu m$ only. Finally, $1\mu m$ overlay errors are also possible with beam tilting as small as $1mdeg$.

Table 5.6: Summary of PIIES sensitivity analysis compared to estimated experimental precision.

Numerical Analysis Results		Estimated Alignment Precision
Maximum beam decentering for $e_{\Lambda} < 2\%$ and $e_{\Theta} < 1deg$	$\pm 0.25mm$	$\pm 0.25mm$
Maximum acceptable lens decentering	$25\mu m$	$\pm 33\mu m$
Maximum acceptable lens tilting	$5mdeg$	$\pm 9mdeg$
Maximum beam tilt for image shift $< 1\mu m$	$1mdeg$	$\pm 7mdeg$

These results must be compared with the estimated alignment precisions of the PIIES as listed in Table 5.6. For example, the laser beams are experimentally aligned on the target with an estimated precision of $\pm 0.25mm$, which can be considered as the maximum

experimental beam decentering error. Since the beam are aligned over a $\sim 2m$ distance (half the length of the optical table), the maximum experimental beam tilting error is estimated at $\pm \tan^{-1}(0.25 / 2000) \approx \pm 7mdeg$. When the lenses are positioned, the distance available to align the beams is reduced to $\sim 1.5m$. Using geometrical optics, the maximum experimental lens decentering and tilting errors are estimated as $\pm f_{OLI} \times 0.25 / 1500 \approx \pm 33\mu m$ and $\tan^{-1}(0.25 / 1500) \approx \pm 9mdeg$, respectively.

CHAPTER 6

PIIL EXPERIMENTAL DEMONSTRATION

In this Chapter, the prototype PIIES presented in Chapter 5 is used to demonstrate PIIL experimentally and validate the PIIES analysis results. The experimental procedures including the PIIES alignment, sample processing, and focusing procedure are first given. Then, PIIL experimental exposures are presented, characterized by scanning-electron microscopy (SEM) and atomic force microscopy (AFM), and compared to simulated PIIL exposures. This research has resulted in two journal papers [102, 104].

6.1 Experimental Procedure

6.1.1 PIIES Alignment Procedure

The alignment procedure for the prototype PIIES initially reported in [89] proved to lack precision and repeatability given the requirements discussed in Chapter 5 and thus, had to be reexamined. A new alignment procedure was established and is presented in this Section. Four schematic representations of the prototype PIIES at different stages of its alignment are depicted in Figures 6.1 to 6.4. Although more beams can be aligned with this procedure, only the central beam and two side beams, all contained in the yz -plane, are represented for clarity. In this new alignment procedure, the central beam represents the PIIES optical axis and thus, plays a crucial role in the system alignment. For 2D-PIIL, the central beam is blocked, but it is typically used as one of the interfering beams for 3D-PIIL exposures.

The first alignment steps consist in positioning the two mirrors M1 and M2 so that the laser beam is redirected along the z-axis and propagates along the length of the optical table (Figure 6.1). Using the longest available optical path is counter-intuitive for an interference-based system, but in the absence of high-resolution alignment tools, aligning the laser beams over long distances helps minimizing beam tilt errors. A more advanced PIIES with automatic alignment system could be more compact. After the positioning of the M1 and M2 mirrors, the half-wave plates (HWPs) and polarizing beam-splitter cubes (PBSCs) are added to divide the initial laser beam into multiple polarization- and intensity-controlled beams. Although not represented in Figure 6.1, additional HWP and PBSC are used right after the M2 mirror to control the beam intensity in the PIIES. Since the HWPs and PBSCs may modify beam propagation, the alignment of the central beam has to be verified. The precise alignment of the central beam is crucial since it represents the PIIES optical axis and as such, it is later used to align the condenser lens (CL), objective lens 1 (OL1), objective lens 2 (OL2), photomask, and the sample.

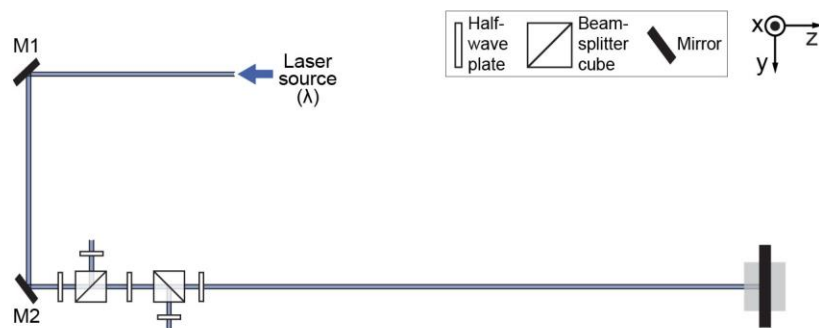


Figure 6.1: Alignment of the HWPs, PBSCs, and central beam.

The next major steps involve the positioning of the M3 to M8 mirrors as depicted in Figure 6.2. The M3, M4, M6, and M7 mirrors must first be carefully aligned such that the two side beams propagate parallel to the y-axis. Then, the M5 and M8 mirrors are positioned to redirect the side beams parallel to the z-axis and at the correct lateral beam displacement, d_{beam} . The expander lenses (ELs) are also temporarily positioned such that the chief rays of the expanded beams propagate along the z-direction as well.

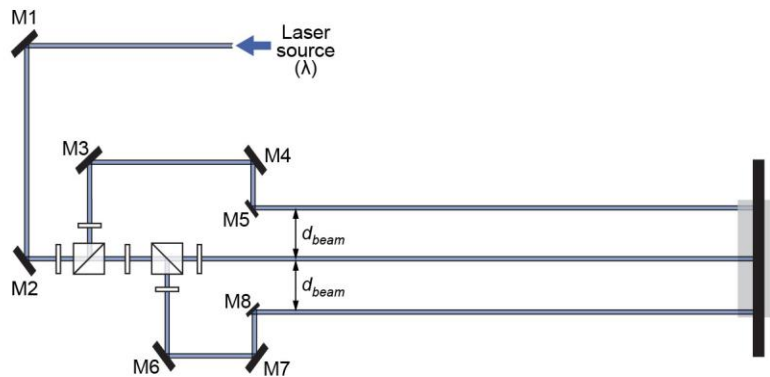


Figure 6.2: Alignment of the M3 to M8 mirrors to redirect the side beams along the z-axis with correct d_{beam} .

Next, the CL, OL1, OL2, photomask mount, and sample mount are added in this order to complete the prototype PIIES (Figure 6.3). Each lens is aligned by looking at the two reflections of the central beam produced by the two lens faces. The pitch, yaw, and lateral position of the lens are adjusted until the central beam and the two reflections are aligned. Lens positioning along the z-axis requires a different procedure. With the ELs in place, the CL is positioned along the z-axis such that the expanded beams are collimated. Then, without the ELs, OL1 is positioned along the z-axis such that the multiple beams propagate parallel to the z-axis after OL1. Finally, with the ELs in place, OL2 is positioned along the

z-axis such that the beams are collimated after OL2. Once the lenses are positioned, the ELs and CL are separated by a distance $f_{EL} + f_{CL}$, CL and OL1 are separated by a distance $f_{CL} + f_{OL1}$, and OL1 and OL2 are separated by a distance $f_{OL1} + f_{OL2}$. The PIIES is therefore an $8f$ optical system.

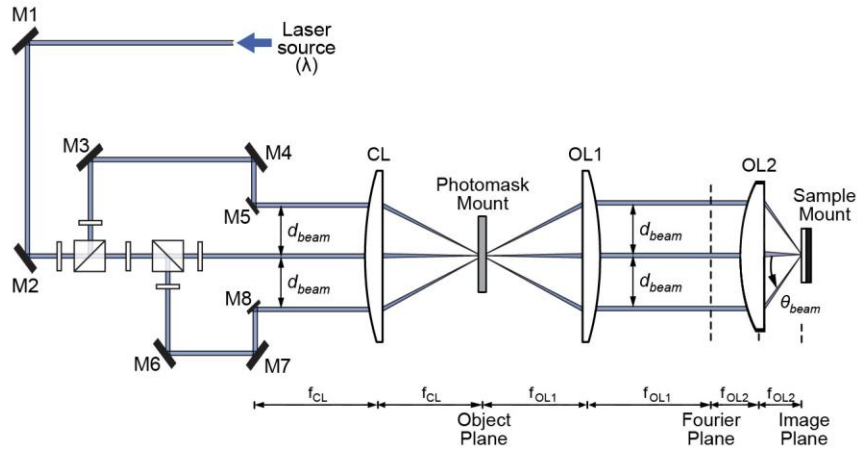


Figure 6.3: Alignment of the CL, OL1, OL2, photomask mount, and sample mount.

The photomask and sample mounts are then added to the PIIES. Both mounts are positioned using a similar technique. The pitch and yaw of the photomask (sample) mount are adjusted such that beams and their reflections on the photomask (a test sample) are evenly distributed around the optical axis upstream of the CL (OL2). Then, the photomask (test sample) is displaced along the z-axis until the beams are all diffracted simultaneously by a photomask (test sample) light-blocking feature. This ensures that the photomask (test sample) is positioned at the object (image) plane of the PIIES, where the multiple beams are focused and overlapping. If the CL (OL2) and the photomask (sample) mount are aligned correctly, the incident and reflected beams upstream of the CL (OL2) should be aligned. The complete PIIES with the ELs is shown in Figure 6.4.

Finally, using a Glan-Thompson polarizer and power meters, the polarization and intensities of the beams are adjusted by rotating the HWPs placed prior to and after the PBSC, respectively. These adjustments are done between the OL1 and OL2 when the beams are not expanded.

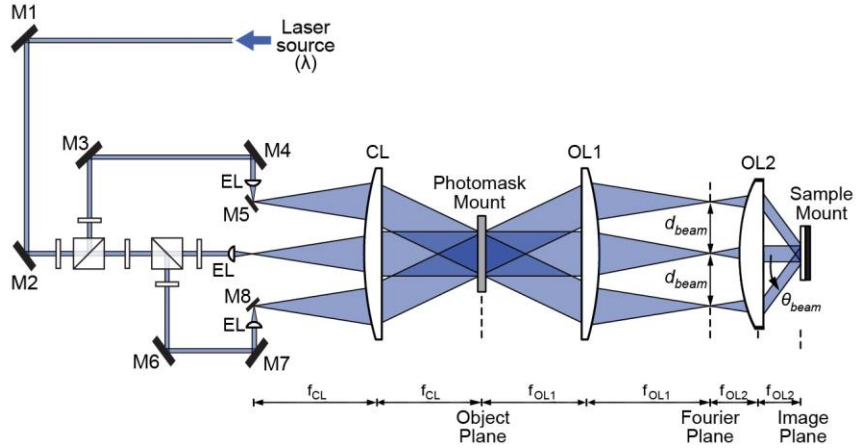


Figure 6.4: Addition of the ELs to complete the $8f$ prototype PIIES.

6.1.2 Photomask Design

The photomask contains custom-designed elements to be integrated within the interference pattern. The photomask is a $4in$, chrome-on-glass photomask fabricated by the Georgia Tech Institute for Electronics and Nanotechnology (IEN) mask shop. The various photomask elements are depicted in Figure 6.5.

The photomask contains seven elements corresponding to representative functional elements of photonic-crystal (PhC) devices plus the logo of the Georgia Institute of Technology (GT). The PhC functional elements are comprised of two waveguide couplers, a ring resonator, a $90deg$ -bend waveguide, a straight waveguide, a PhC circuitry, and a passband filter. Given their geometry, the photomask elements are intended to be

integrated within a square-lattice interference pattern. Except for the PhC circuitry and the GT logo, each element has two designs: a single-period-blocking design with $3.35\mu\text{m}$ -wide features intended to cover a single interference period, and a double-period-blocking design with $6.70\mu\text{m}$ -wide features intended to cover two interference periods. Since the PIIES system magnification M is 0.3, the targeted interference period is $3.35\mu\text{m} \times M \approx 1\mu\text{m}$.

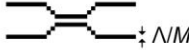
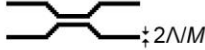
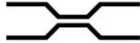
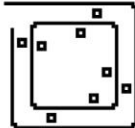
Photomask elements (Part Number)	Single-period-blocking designs	Double-period-blocking designs
Waveguide coupler 1 (P1)		
Waveguide coupler 2 (P2)		
Ring resonator (P3)		
90deg-bend waveguide (P4)		
Straight waveguide (P5)		
PhC circuit (P6)		
PhC passband filter (P7)		
Georgia Tech logo (P8)		

Figure 6.5: Schematic representations of the single- and double-period-blocking photomask elements contained in the photomask. The size scales are different in both columns

The single- and double-period-blocking elements are grouped as a pair as depicted in Figure 6.6(a). The pair is duplicated 100 times and arranged in a 10×10 array delimited by a frame as shown in Figure 6.6(b). For each photomask element, nine frames corresponding to nine different size scales ranging from 98% to 102% are included in the photomask. The photomask contains a total of 72 frames. Identification codes are added to each frame to recognize the photomask element (P1 to P8) and its size scale (S1 to S9). To facilitate the positioning of the photomask with unaided eyes, 5mm-tall numeric characters (1 to 8) are also incorporated to identify easily the lines containing the P1 to P8 photomask elements as shown in Figure 6.6(c).

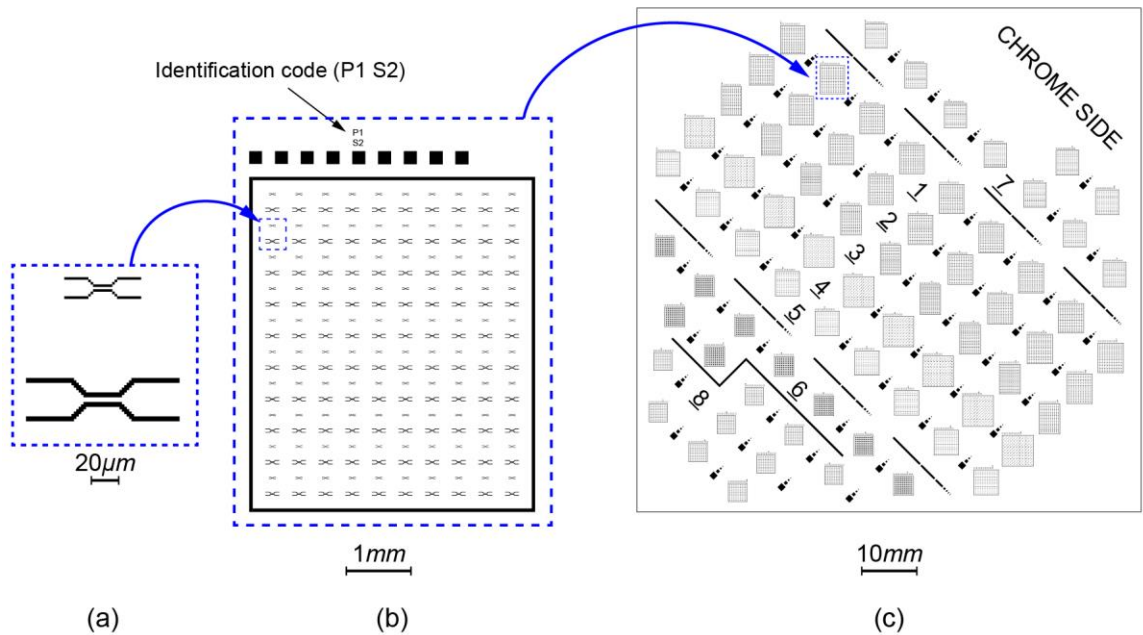


Figure 6.6: (a) Single- and double-period-blocking photomask elements are grouped as a pair. (b) 10×10 array of element pairs delimited by a solid frame and identification code. (c) Complete photomask containing 72 frames corresponding to the eight different photomask elements and their nine size scales.

6.1.3 Sample Processing

The samples to be exposed are prepared in the GT IEN Pettit cleanroom. The sample substrates are 1.25"-square optical-grade fused quartz slides. After being chemically cleaned in a 3:1 mixture of sulfuric acid (H_2SO_4) and hydrogen peroxide (H_2O_2) on a 150°C hotplate, the slides are stored in a cleanroom dry box. Prior to every experiment, the slides are cleaned again using an ultrasonic bath of acetone for 5min; rinsed with methanol, isopropanol, and deionized (DI) water; and finally dried for 5min on a hotplate at 150°C. Once dry, the slides are first coated with Microprime P-20 primer to increase photoresist adhesion and then with Microposit SC1813 positive-tone photoresist using a SCS G3P8 spin coater. Both the primer and the photoresist are coated at 3500rpm for 40sec. The samples are then softbaked for 3min on a hotplate at 115°C to remove photoresist solvent. The photoresist film is 1.5 μm thick as measured with a profilometer.

Covered in aluminum foil to avoid exposure from the ambient light, the samples are brought to the Optics Laboratory, where the prototype PIIES is installed. The output laser power is 170mW. The exposure time is about 1sec to 2sec. Once exposed, the photoresist is brought back to the cleanroom to be developed in an agitation bath of Microposit MF-319 developer for 30sec, rinsed with DI water, and dried with nitrogen. The developed sample is then evaluated using an optical microscope. For SEM imaging, the sample is further coated with ~20nm of gold/palladium using a Hummer 6 gold sputterer.

6.1.4 Sample Focusing Procedure

In the absence of an automatic focus system, a trial-and-error procedure requiring multiple exposures at various positions along the z-axis is employed to find the plane of best focus,

i.e. the plane where the photomask images are superposed and correctly integrated within the interference pattern. A single sample is exposed up to nine times to test nine different planes of focus. Between each exposure, the sample mount is translated along the z-axis by a constant defocusing step using the high-precision z-axis actuator of the sample mount. A coarse $15\mu\text{m}$ defocusing step is used first. The sample is also translated along the x- of y-directions by 8mm steps between the exposures such that the nine $\sim 6\text{mm}$ -diameter exposure spots are not overlapping as shown in Figure 6.7.

After the development and rinsing step, the nine exposure spots are analyzed with a microscope to determine which exposure plane is the closest to the plane of best focus. Because the plane of best focus is usually not found with a single sample, up to four samples are prepared to be exposed as well. For the next sample, the defocusing step is typically divided by two and the range of defocus along the z-axis is centered around the plane that provided the best results in the previous sample.

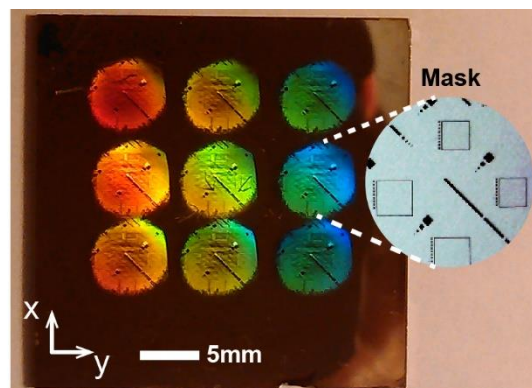


Figure 6.7: Picture of an exposed, developed, and gold-coated sample containing nine individual PIIL exposures. Light diffraction from the gratings and integrated large photomask features are visible.

6.2 Experimental results

6.2.1 Integration of Double-Period-Blocking Photomask Patterns within a Square-Lattice Periodic Microstructure

Through careful alignment of the prototype PIIES and focusing procedure, the integrations of the double-period-blocking $90deg$ -bend waveguide, first waveguide coupler, ring resonator, and straight waveguide within a 2D square-lattice interference pattern are first demonstrated. For these experimental results, the three-beam configuration at the image plane is depicted in Figure 6.8. The lateral beam displacement, d_{beam} , is $13.97mm$. According to the fitting function $\Lambda_{sq,fit}(d_{beam})$ derived in Section 5.2.2, the expected lattice period is $\Lambda_{sq,fit} = 1.022\mu m$. The intensities of the two beams labeled \mathbf{k}_1 and \mathbf{k}_2 propagating in the yz -plane, are adjusted to be half of that of the beam labeled \mathbf{k}_3 , which propagates in the xz -plane. The linear polarizations of the first and second beams are orthogonal and the linear polarization of the third beam bisects the other two. SEM images of the PIIL-produced microstructures are shown in Figure 6.90 and Figure 6.10.

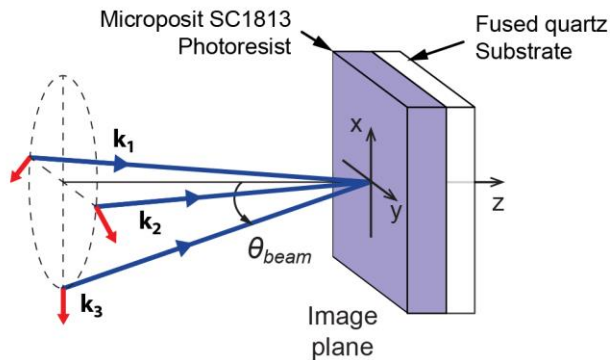


Figure 6.8: Beam configuration at the PIIES image plane for the pattern-integrated square-lattice results.

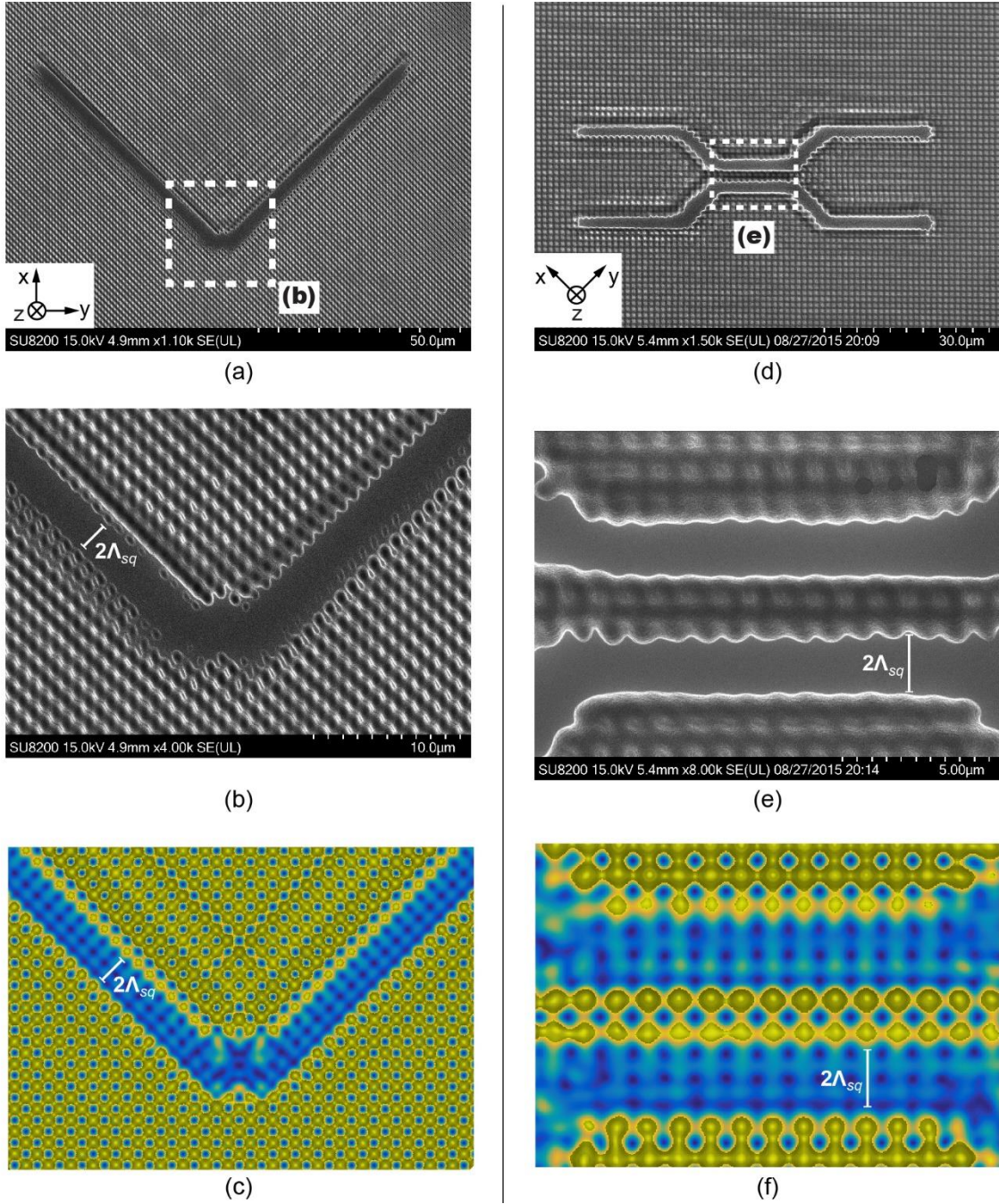


Figure 6.9: (a), (b), and (c). Low-magnification SEM image, high-magnification SEM image, and simulated PIIL exposure of the integration of the 90deg-bend waveguide within the square-lattice periodic microstructure, respectively. (d), (e), and (f). Low-magnification SEM image, high-magnification SEM image, and simulated PIIL exposure of the integration of the waveguide coupler within the square-lattice periodic microstructure, respectively.

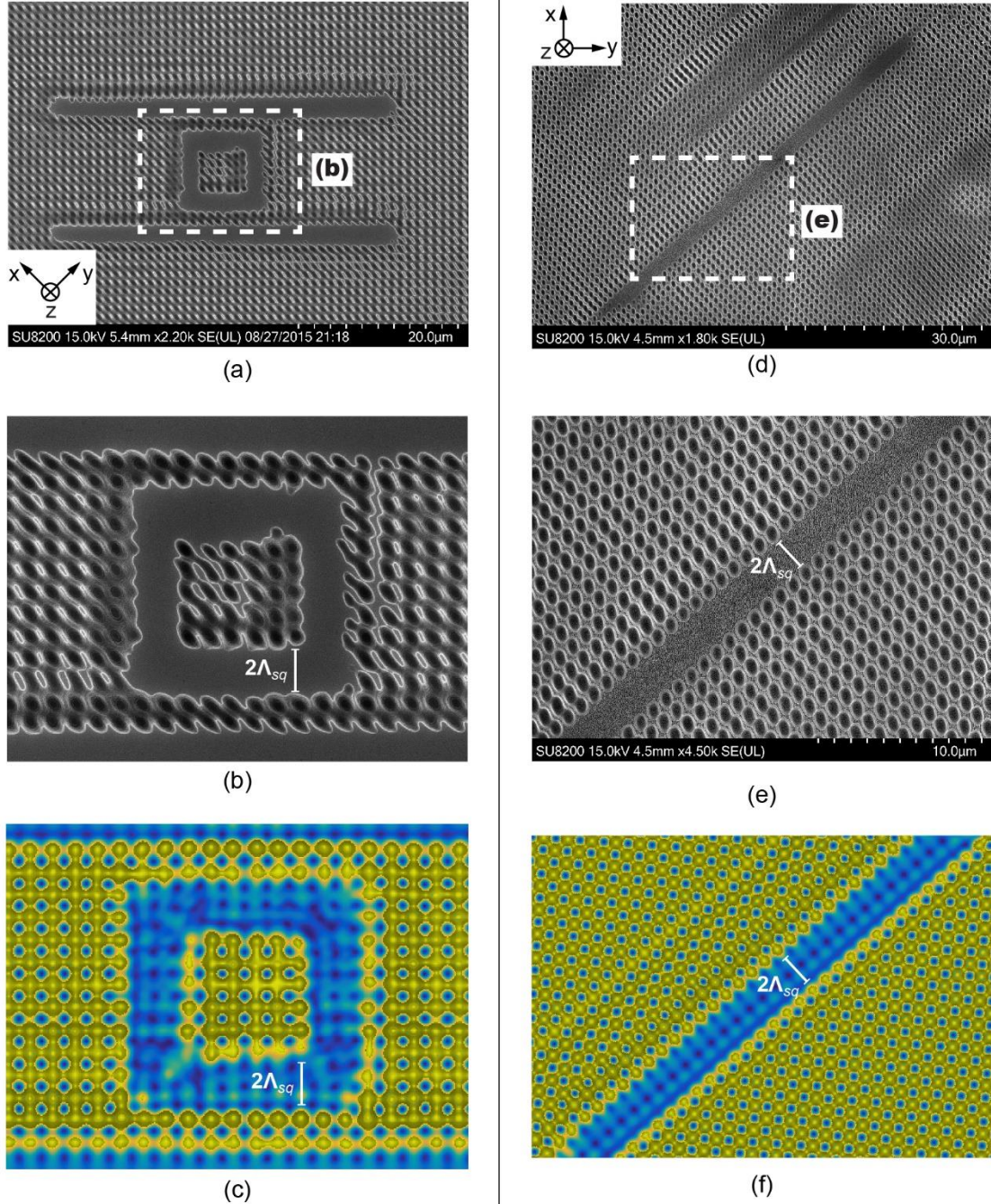


Figure 6.10: (a), (b), and (c). Low-magnification SEM image, high-magnification SEM image, and simulated PIIL exposure of the integration of the ring resonator within the square-lattice periodic microstructure, respectively. (d), (e), and (f). Low-magnification SEM image, high-magnification SEM image, and simulated PIIL exposure of the integration of the straight waveguide within the square-lattice periodic microstructure, respectively.

These experimental results demonstrate that PLB microstructures can be fabricated in a single exposure step by PIIL. The experimental results may seem unsatisfactory since the transitions between the integrated photomask patterns and the periodic lattice lacks sharpness. However, as discussed in Chapter 5, significant optical aberrations and overlay errors were expected due to the use of non-optimized optics and manual alignment of the system. Given the estimated alignment precision, these experimental results are actually very satisfactory. Noteworthy, the double bend in the $90deg$ -bend waveguide is distinguishable (Figure 6.90(b)), the periodic lattice between the two arms of the waveguide coupler is reproduced (Figure 6.90(e)), the periodic lattice inside the ring and between the ring and the waveguides in the ring resonator is present (Figure 6.10(b)), and the straight waveguide is well integrated (Figure 6.10(e)). Away from the integrated photomask elements, the periodic lattice is well reproduced as shown in Figure 6.11.

Depending on the exposure time, the photoresist is more or less exposed and thus, developed. For an exposure time, t_{exp} , smaller than $1.5sec$, the flat surface of the photoresist is still visible, but for longer exposure times, the surface exhibits a pattern of “hills” and “valleys”. Standing wave effects are also visible, in particular in Figure 6.11(b) and (c), for which the sample has been tilted by $15deg$. The lattice constants averaged over ten periods and along the two lattice vectors are given in Table 6.1. Between the two lattice directions, the measured lattice constants differ by less than 1%. Compared to the targeted lattice constant calculated with the fitting equations derived in Chapter 5, there are 3% to 5% relative period error e_{Λ} . The angle measured between the two lattice directions are listed in Table 6.1 as well, and the orientation error e_{θ} is less than $1deg$ compared to the targeted lattice angles.

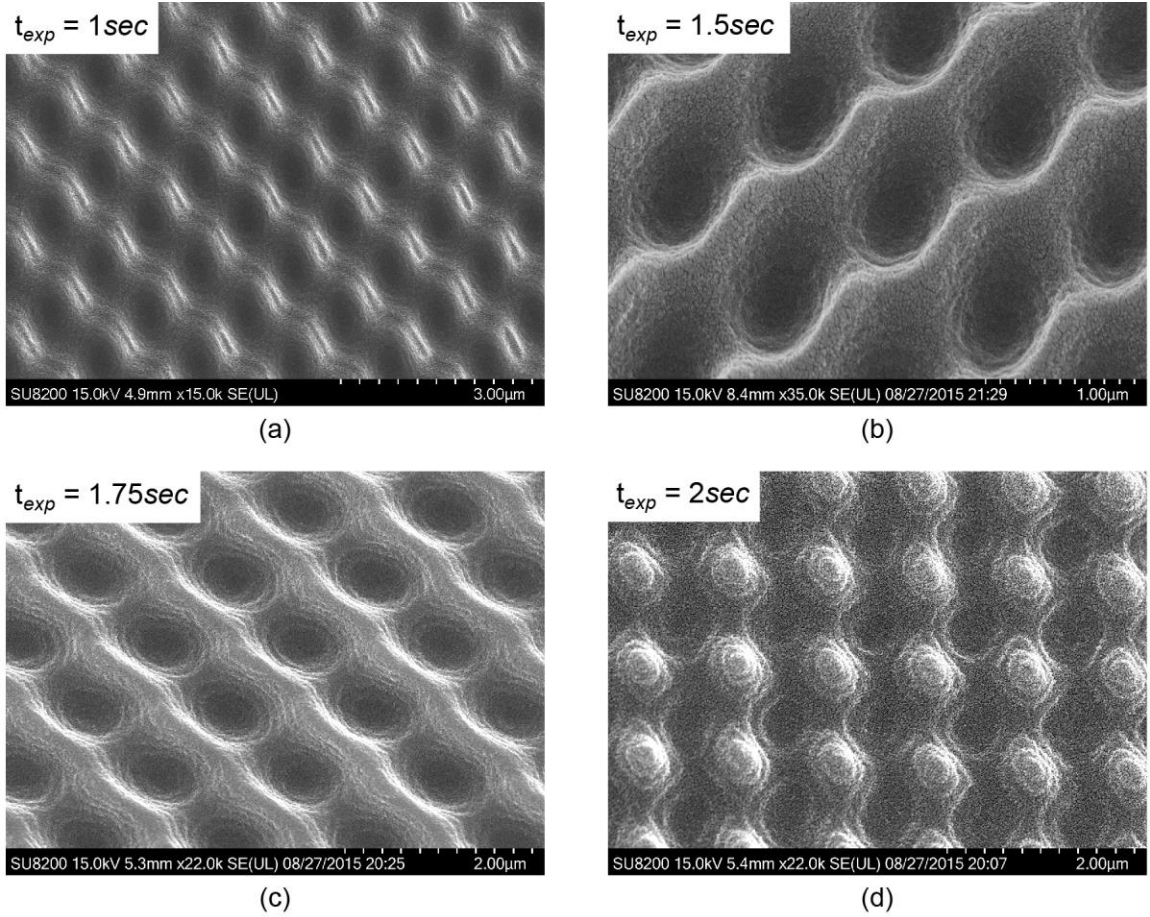


Figure 6.11: SEM images of the periodic square-lattice produced with (a) 1sec, (b) 1.5sec, (c) 1.75sec, and (d) 2sec exposure times.

Table 6.1: Experimental average lattice periods and lattice vector angles.

	$\Lambda_{sq} (\mu m)$	$e_{\Lambda} (\%)$	Lattice Vector Angle (deg)	$e_{\Theta} (deg)$
90deg-Bend	1.070	4.6	89.28	-0.72
Ring Resonator	1.073	5	90.50	0.5
Waveguide Coupler	1.058	3.5	90.84	0.84
Straight Waveguide	1.052	4.6	89.10	-0.9

Simulated PIIL exposures are also included in Figure 6.90 and Figure 6.10. The size scales in the simulated exposures are identical to those in the SEM images. The simulation results correspond to top-view of the 3D optical intensity distribution above a normalized intensity threshold of 0.4. For the simulations, the experimental parameters are used as simulation parameters and the lenses are assumed to be perfectly aligned. Of note, the Zernike coefficients calculated in Section 5.3.1 (and given in Appendix A) describing the PIIES optical aberrations due to the use of a wavelength different from the lens design wavelength are integrated in the simulations. Due to spherical aberrations, the three images of the photomask are not overlapping properly for a position of the photoresist surface, z_0 , of $0\mu m$. The defocus z_0 must be increased to $6\mu m$ such that the photomask images are reasonably aligned. The qualitatively good agreement between the experimental results and the simulated exposures indicates that the lack of sharpness is mainly due to spherical aberrations rather than misalignment of the PIIES components.

6.2.2 Integration of Single-Period-Blocking Photomask Patterns within a Square-Lattice Periodic Microstructure

SEM images of the integrated single-period-blocking photomask elements are shown in Figure 6.12. Due to their smaller feature size, the single-period-blocking elements are more challenging to image and align correctly and thus, are more difficult to integrate precisely within the lattice. Producing conclusive results with relatively complex elements such as the waveguide coupler and ring resonator has proved to be challenging as shown in Figures 6.12(a) and (b). However, satisfactory PIIL exposures have been obtained with the single-period-blocking $90deg$ -bend waveguide and straight waveguide.

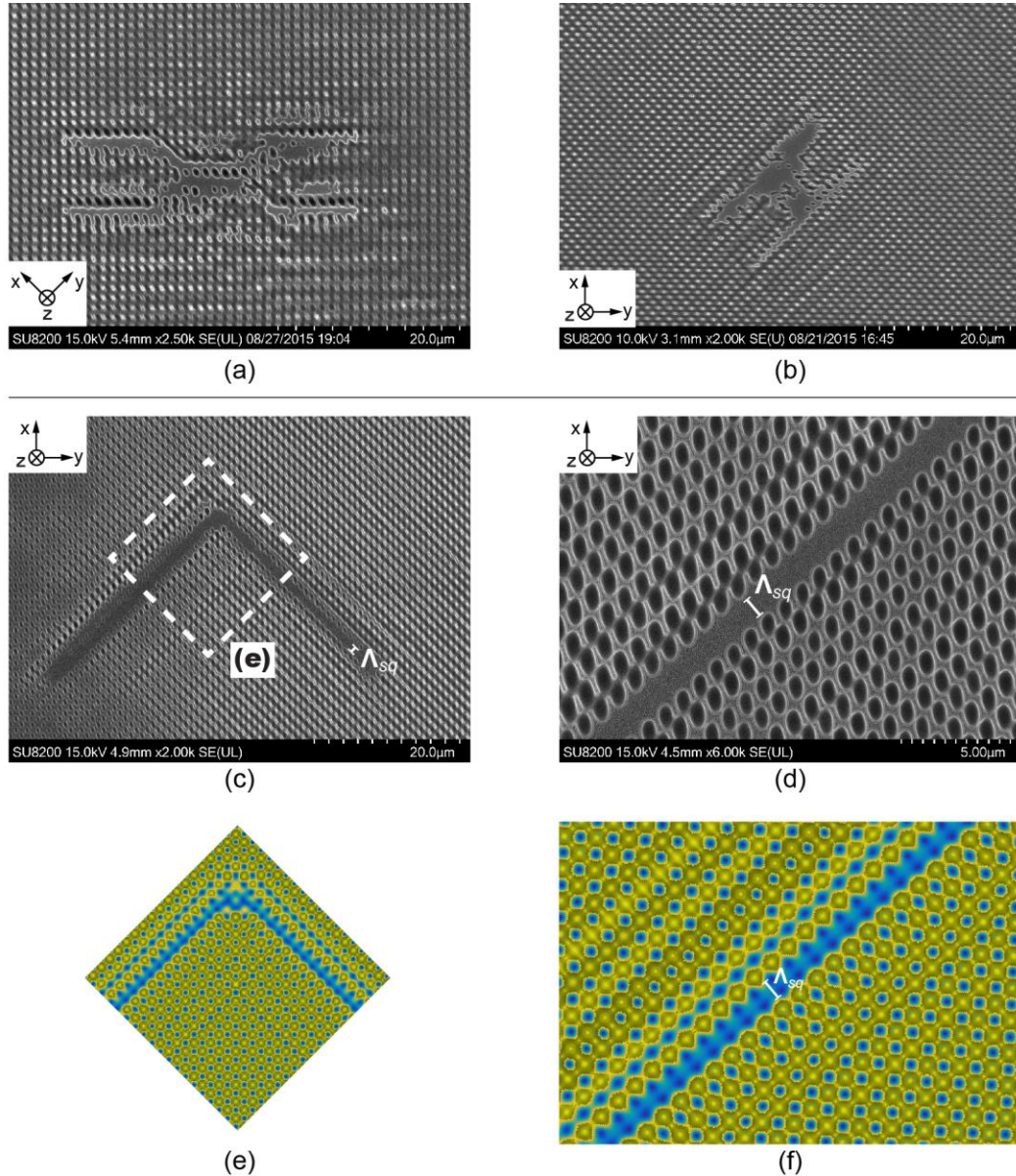


Figure 6.12: SEM image of PIIL exposures using the single-period-blocking (a) waveguide coupler, (b) ring resonator, (c) $90deg$ -bend waveguide, and (d) straight waveguide. (e) and (f) Simulated PIIL exposures corresponding to the (c) and (d), respectively.

These photomask patterns exhibit simpler geometries and are simpler to integrate. SEM images of these two photomask elements integrated within the square-lattice interference patterns are shown in Figures 6.12(c) and (d). Corresponding simulated PIIL exposures are shown in Figures 6.12(e) and (f). Noteworthy, lattice distortions located a few periods above the integrated *90deg*-bend and straight waveguides are visible in both the experimental and simulated exposures.

6.2.3 Integration of Single-Period-Blocking Photomask Patterns within a Hexagonal-Lattice Periodic Microstructure

Using another beam configuration depicted in Figure 6.13(a), the single-period-blocking straight waveguide was also integrated within a hexagonal-lattice interference pattern as shown in the SEM image in Figure 6.13(b). For this result, the interference beams have equal intensities, the beam polarizations are linear and lie in their plane of incidence, and the lateral beam displacement is increased to $d_{beam} = 15.24mm$. The lattice constant averaged over ten periods is $0.87\mu m$ and is less than 2% smaller than the expected lattice constant $\Lambda_{hex,fit} = 0.886\mu m$ obtained from the fitting function $\Lambda_{hex,fit}(d_{beam})$ derived in Section 5.2.2. Ghost motifs are perceptible in the waveguide in Figure 6.13(b) and also in the simulated PIIL exposure in Figure 6.13(c). These residual motifs are not uncommon [59, 87] and are likely due to non-ideal experimental conditions.

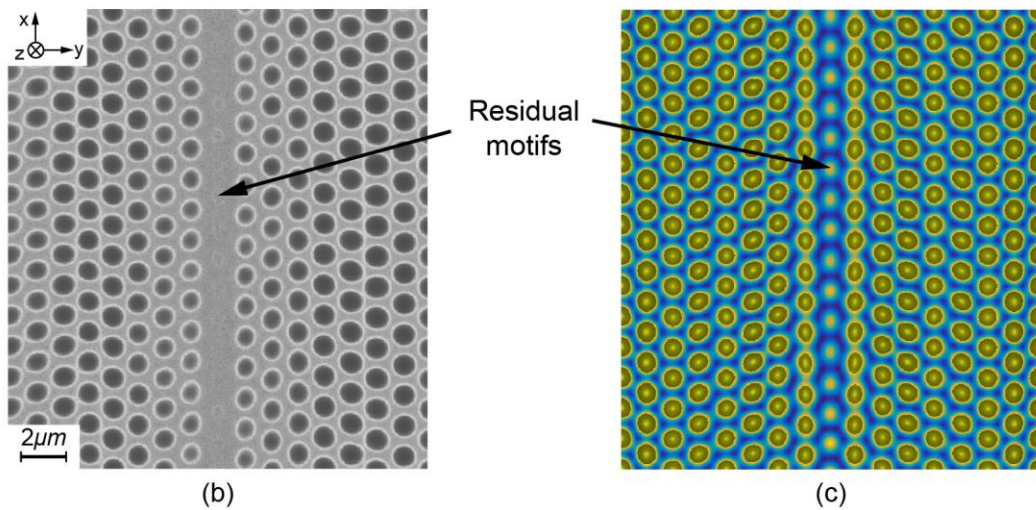
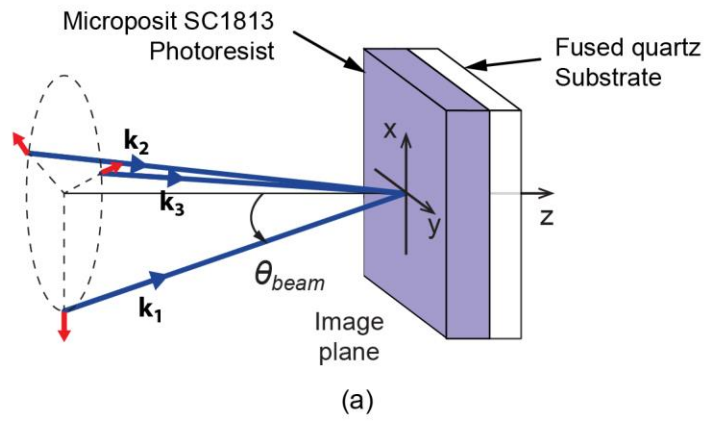


Figure 6.13: (a) Beam configuration at the PIIES image plane to generate the hexagonal-lattice 2D-PIIL experimental results. (b) SEM image of the single-period-blocking straight waveguide integrated within the lattice. (c) Corresponding simulated PIIL exposure. Residual motifs due to non-optimal conditions are visible in both experiments and simulations.

The microstructure topology has been further characterized by AFM using high-aspect-ratio tips (Bruker TESP-HAR). A 3D reconstruction of the periodic lattice and the corresponding simulated 3D optical intensity distribution within the photoresist are shown in Figures 6.14(a) and (b), respectively. The closest match between the AFM image and the simulated exposure is obtained for a normalized threshold intensity of 0.4. The simulated exposure in Figure 6.14(b) can be seen as underexposed photoresist remaining on the substrate after development. Depth profiles measured by AFM parallel to the waveguide in the xz -plane and across the waveguide in the yz -plane are superposed with the simulated PIIL exposures in Figures 6.14(c) and (d), respectively, and provide a good qualitative match between experiments and simulations.

The depth of the holes is $\sim 0.8\mu\text{m}$ indicating that the photoresist has not been exposed across its total thickness. Also, the hole depths range from $\sim 0.5\mu\text{m}$ to $\sim 0.9\mu\text{m}$ signifying that intensity fluctuations during the exposure impact the homogeneity of the hole depths. Noteworthy, intensity fluctuations along the z -axis in the simulations are caused by standing waves due to refractive index mismatch between the photoresist and the substrate. These fluctuations are not measured by the AFM tip due to the tapping nature of the technique. In the simulations, seven intensity oscillations can be counted for a hole, which is consistent with the theoretical number of standing waves calculated as $\sim 0.8\mu\text{m} / (\lambda_{exp} / 2n_{S1813}) \approx 7$ and with the number of standing waves visible in Figure 6.11.

6.2.4 Exposure Field Distortions

As described previously, the photomask elements are arranged in 10×10 arrays delimited by a frame. For the $90deg$ -bend waveguide elements, the frame dimension is $5.4\text{mm} \times 5.4\text{mm}$ and thus, is projected to a size of $\sim 1.6\text{mm} \times 1.6\text{mm}$ at the image plane.

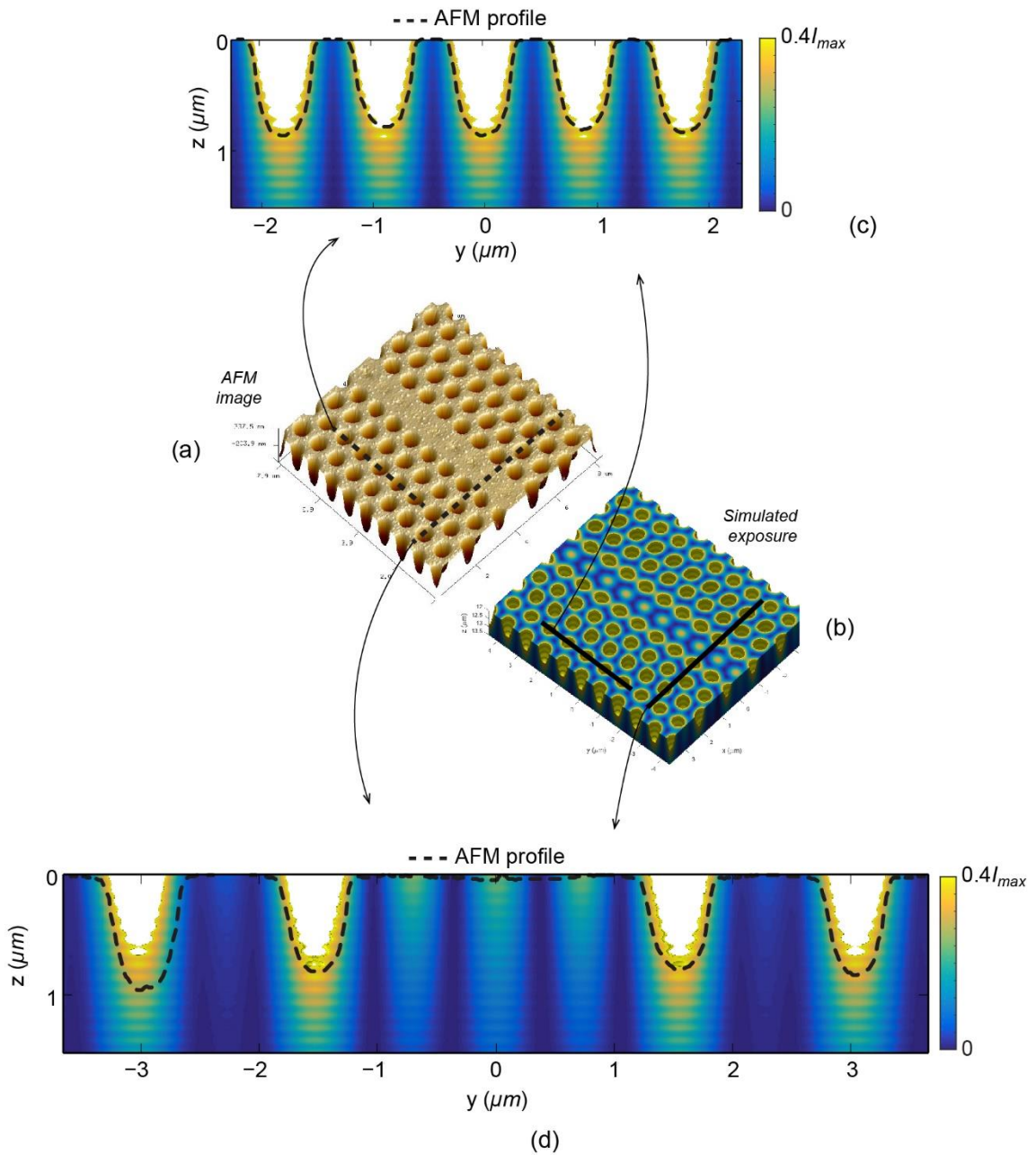


Figure 6.14: (a) 3D AFM image of the single-period-blocking straight waveguide integrated within the hexagonal lattice of holes. (b) Corresponding simulated PIIL exposure. (c) and (d) Cross-sectional view of the simulated PIIL exposures with the depth profile (black dashed lines) measured by AFM.

A low magnification microscope image of the PIIL exposure of this frame is shown in Figure 6.15(a). The three projections of the frame are visibly distorted and not superposed correctly. The distortions also apply for the elements in the array. As shown in the SEM image of the center of the array in Figure 6.15(b), overlay errors increase rapidly, resulting in satisfactory results for only one $90deg$ -bend waveguide. This experimental observation confirms the numerical analysis of the image field distortions. In Section 5.3.3, the RMS distortion error was smaller than $0.5\mu m$ for an exposure field area of only $0.2mm^2$ and centered on the optical axis.

The projection of the frame at the image plane produced by each beam can be simulated with ZEMAX and compared to the experimental exposure. The outlines of the three distorted frames extracted from Figure 6.15(a) are shown in Figure 6.15(c). The circle in the center corresponds to the location of the best lattice-integrated $90deg$ -bend waveguide. For comparison, the outlines of the projected frames have been separately simulated with ZEMAX and are shown superposed in Figure 6.15(d). The circle in Figure 6.15(d) corresponds to the center of the simulated distortion grids, where distortions are absent. The position of this circle has been adjusted to best fit the experimental data and thus, is not in the center of the frames. In both Figures 6.15(c) and (d), the size scales are identical. The green, blue, and red lines correspond to the outlines of the frames projected by the first, second, and third beam as defined in Figure 6.8. Experiments and simulations show a very good match, demonstrating that the current prototype PIIES has a very limited exposure field due to the non-optimal design of its projection lens. In a more advanced PIIES employing a photolithographic-grade projection lens made of multiple lens elements, distortions could be corrected over a larger field of exposure.

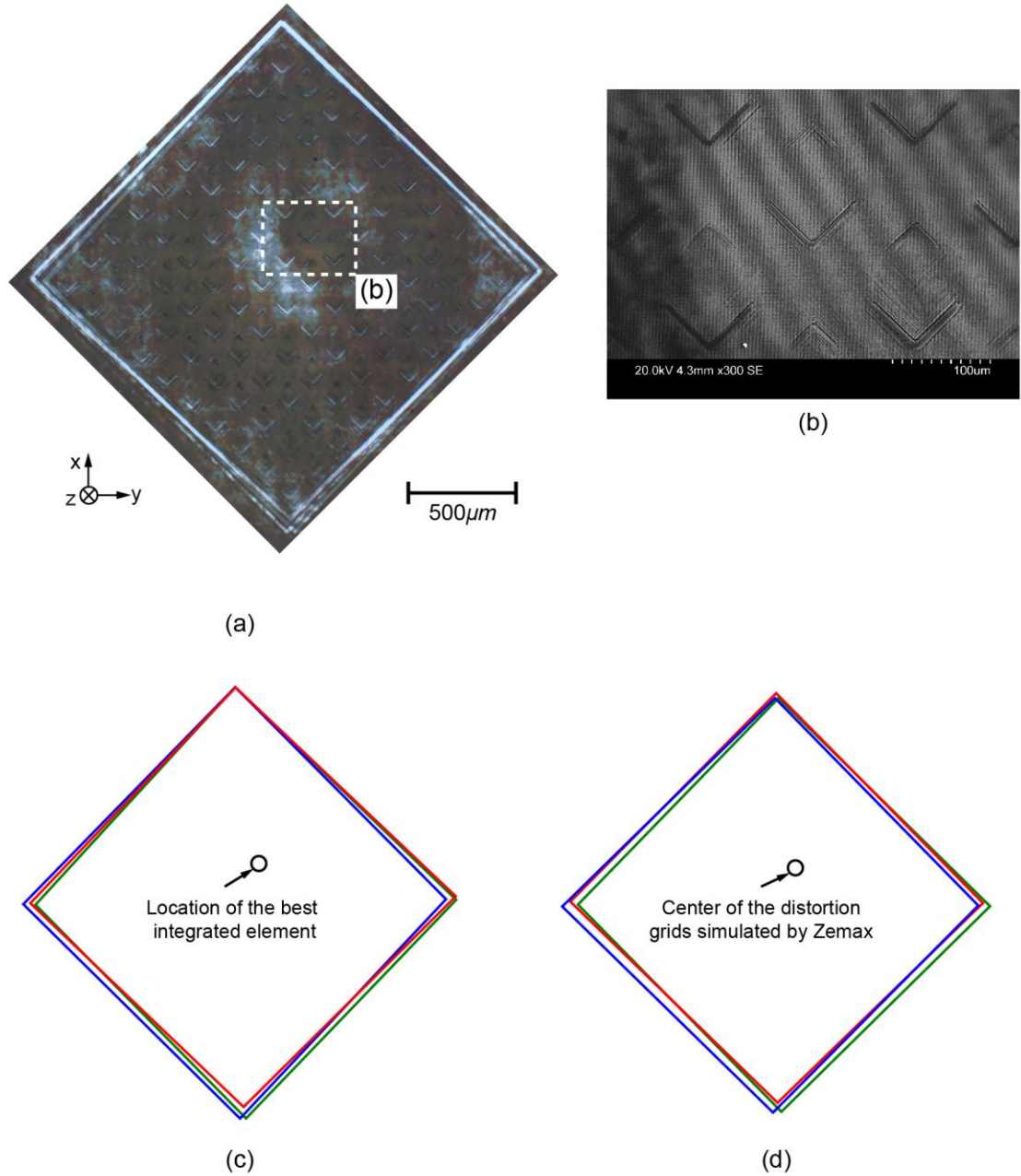


Figure 6.15: (a) Low-magnification microscope image of a complete frame containing a 10×10 array of $90deg$ -bend waveguides. (b) SEM image of the portion of the array containing the photomask elements that are the best integrated within the periodic lattice. (c) Representation of the outlines of the three frames extracted from (a). (d) Outlines of the projected frames simulated with ZEMAX. The center of the distortion grids for the three simulations are identical and fit the location of the best integrated element from the experiment.

6.3 Summary

In spite of the manual alignment and non-optimized optics of the PIIES, the PIIL concept was demonstrated. Single- and double-period-blocking elements were integrated within 2D square- and hexagonal-lattice periodic microstructures in a single-exposure step. SEM images reveal that the photomask patterns are imperfectly integrated within the interference pattern. However, these non-ideal results were expected and actually confirm conclusions drawn from the PIIES analysis performed in Chapter 5. As simulated, the useful exposure field is limited to a 0.2mm^2 area due to image field distortions. Furthermore, good qualitative agreement is found between the experimental and simulated PIIL exposures when the simulations account for optical aberrations in the form of the Zernike coefficients calculated with ZEMAX. Errors on the lattice period and orientation are also close to the errors estimated in Chapter 5. These results demonstrate the validity of the PIIES analysis and completeness of the PIIL vector model as a tool to simulate PIIL exposures.

Photomask patterns with simple geometries, such as the straight waveguide, have been sharply integrated with the periodic lattices. Single-period-wide waveguide has also been successfully integrated within a $1\mu\text{m}$ -period square-lattice and $0.87\mu\text{m}$ -period hexagonal-lattice periodic structures. Finally, AFM images agree also well with the simulated exposures of the volume of the photoresist and reveal the uncomplete exposure of the photoresist films.

CHAPTER 7

CONCLUSIONS AND FUTURE WORK

The objective of this thesis has been to quantify PIIL's fundamental capabilities and limitations in the fabrication of 2D and 3D periodic-lattice-based (PLB) microstructures through modeling, simulations, and experimental demonstrations. In this chapter, research results and accomplishments are summarized and discussed. Short- and long-term future research avenues are presented as well.

7.1 Conclusions

7.1.1 PIIL Concept and Modeling

As a logical progression from optical interference and holography, the new field of PIIL was introduced and conceptualized [88, 90]. PIIL addresses the lack of adequate microfabrication techniques for 2D and more complex 3D PLB microstructures. As a platform technology, PIIL is expected to impact numerous fields including photonics, bioengineering, microfluidics, and mechanical metamaterials. With its potential high-throughput, PIIL is applicable in research laboratories for rapid prototyping as well as in industrial settings that require high-throughput capital equipment.

To implement and demonstrate PIIL, an $8f$ confocal lens system has been presented. In this system, a photomask is coherently illuminated by multiple intensity-, polarization-, and direction-controlled laser beams. As the photomask projections are superposed at the system image plane, they produce a photomask-integrated interference pattern. Yet, it is reasonable to think that other optical system designs may be suitable to implement PIIL.

[90]. For example, the lenses could be rearranged such that the photomask is illuminated by partially coherent beams, thereby reducing speckle and diffraction effects during the exposure. However, partially coherent illumination may reduce the interference pattern contrast. Instead of the single-optical axis (SOA) PIIES presented in this thesis, multiple-optical-axis (MOA) PIIES may be workable as well, where each interfering/imaging beam propagate through an individual lens arrangement [90, 156, 157].

As commercial ray tracing and photolithography simulators have proved to be unsatisfactory in simulating PIIL, a novel vector model has been derived to calculate the optical intensity distribution within the photoresist film during a PIIL exposure [91]. This comprehensive model accounts for the off-axis propagation of the beams, the diffraction limit of the lenses, polarization changes due to high-NA optics, an energy conservation factor, Fresnel's equations, standing waves within the photoresist, photoresist absorption, defocus effects, and possible optical aberrations. The kinetics of the photoresist exposure may also be modeled to account for photoresist bleaching effects. While it is appropriate for the present PIIL system, this model would require modifications to be applicable to other PIIL systems.

Noteworthy, PIIL has the potential to produce 2D and 3D PLB microstructures with a wide range of lattice symmetry and lattice constants ranging from hundreds of nanometers to few micrometers. Furthermore, the dimensions of the integrated photomask pattern, which can have arbitrary geometries, may be as large as desired or as small as the interference period. Compared to existing microfabrication techniques, PIIL represents a particularly versatile approach.

7.1.2 PIIL Exposure Simulations for 2D PhC Devices

Using the PIIL vector model presented in Chapter 2, the fabrication by PIIL of three representative 2D PhC devices were simulated [95]. The PhC devices included a $90deg$ -bend waveguide, a passband filter, and a stopband filter. In addition, the transmission spectra of the PhC devices were calculated using the COMSOL Multiphysics software and compared to those of idealized PhC devices.

To reduce lattice distortions due to the integration of the photomask pattern, the innovative area of photomask optimization for PIIL was introduced [94]. This approach is inspired by optical proximity correction (OPC) [141] and resolution enhancement techniques in photolithography [142-146]. However, while OPC aims at pre-warping the photomask pattern to pre-compensate imaging imperfections due to the diffraction limit and optical aberrations, photomask optimization in PIIL aims at mitigating distortions within the periodic microstructure. Single-motif-blocking photomask patterns with various shapes and sizes were studied to determine what geometry minimizes lattice distortions. In the present study, a $0.9\Lambda_{sq}/M$ -wide $45deg$ -rotated square produces the smallest lattice distortions. Using this element as a building block, improved photomasks for the PhC devices were created. Yet, these improved photomasks do not represent optimized designs. The optimal solution to this problem may require inverse photolithography strategies as well as gray-scale and/or phase photomasks.

With the improved photomasks and by using realistic photolithographic parameters, the fabrication of the PhC devices was simulated and their performance appeared to be similar to that of idealized PhC devices. Since it is commonplace in research and development for idealized structures to have the best possible performance, it is noteworthy

when the realizable (“non-ideal”) fabricated structures have equivalent performance. It is normally assumed that the realizable structures will always have lesser performance. Usually, only in the limit of extensive refinements do the realizable structures’ performance approach that of the idealized structures. In these cases, the natural PIIL structures formed by wave interference seem to be superior to the artificially perfect idealized structures. These results are encouraging since using a smaller wavelength and larger lens NA would produce more ideal simulated PIIL exposures.

7.1.3 PIIL Exposure Simulations for 3D Periodic-Lattice-Based Microstructures

By combining simultaneously 3D-MBIL and projection photolithography, 3D-PIIL enables the rapid, single-exposure step, and large-area fabrication of custom-modified 3D periodic microstructures. Through simulations, the significant potential of 3D-PIIL in fabricating custom-modified 3D periodic microstructures was demonstrated [98]. By thoughtful photomask designing and positioning of the surface of the photoresist film relative to the image plane, 3D-PIIL capabilities range from integrating or shaping 3D periodic lattices to producing microcavities on top of, or fully embedded within, 3D periodic microstructures.

Yet, the present exposure simulations represent a non-exhaustive illustration of 3D-PIIL capabilities. To address various needs in bioengineering, microfluidics, or photonics, the interference period may be increased or decreased by changing the exposure wavelength, λ_{exp} , the NA, and the common beam incidence angle, θ_{beam} . Instead of the negative-tone SU8 used in the present results, a positive-tone photoresist may be employed to create inverted templates of the present examples. Also, photomask pattern optimization has not been investigated in the 3D-PIIL case. Optimized photomask patterns may be

designed to reduce distortions or control the aspect ratio of integrated microcavities in 3D-PIIL exposures. The photomask could be a 2D or 3D binary, grayscale, complex, or phase mask generated by a spatial light modulator that would create complex 3D functional elements within the 3D interference pattern [158-160].

Refraction effects at the interface between the air and the photoresist were discussed as well. Due to the change of the beam angle of propagation within the photoresist, the 3D periodic lattices are stretched along the normal of the photoresist surface. As a result, 3D cubic lattices are not feasible. Refraction effects may be overcome by using photoresist-refractive-index matching immersion fluids, although this solution presents some implementation challenges. Yet, cubic lattices are not necessarily the ideal structures for every application. The ellipsoidal shape and large aspect ratio of the interconnected pores may represent advantages.

7.1.4 PIIES Prototyping and Analysis

To implement PIIL, a prototype pattern-integrated interference exposure system (PIIES) was designed, prototyped, and analyzed [89, 101]. The light source is a 363.8nm argon-ion UV laser and the prototype PIIES is comprised of off-the-shelf lenses, mirrors, half-wave plates, polarizing beam splitter cubes, mounts, linear stages, and positioners. Custom-designed adapter plates and mounts were fabricated as well. Particular design efforts were made to reduce the form factor of some of the optics, thereby providing a sufficiently large beam displacement range and bringing the laser beams as close as possible.

Using the ray-tracing software ZEMAX and geometrical optics, the capabilities of the prototype PIIES were studied. With an exposure wavelength of 363.8nm, interference

periods ranging from sub-micron to a few microns are feasible. The sensitivity to beam misalignment of a two-beam interference period and fringe orientation was studied as well. Due to the manual nature of the PIIES alignment, a $\pm 2\%$ error on the interference period and $\pm 1deg$ error on the fringe orientation were determined for a typical beam configuration.

The imaging performance of the PIIES compound objective lens was investigated as well. Due to the $363.8nm$ wavelength employed, a large $0.46waves$ RMS optical path difference (OPD) was calculated, although the lenses are assumed perfectly aligned. Lens decentering and lens tilting further increase the RMS OPD. Yet, a $25\mu m$ lens decentering and $5mdeg$ lens tilting remain acceptable. The wavefront error is essentially due to spherical aberrations resulting in the imperfect projection of the photomask pattern at the image plane. Zernike coefficients describing the optical aberrations were calculated with ZEMAX and can be integrated within the PIIL model for simulations. Photomask projection and superposition are also limited due to image field distortions. RMS distortion errors smaller than $0.5\mu m$ are only feasible in an exposure area limited to $250\mu m \times 250\mu m$.

Interference pattern formation and photomask projection play equally important roles in PIIL. A large exposure field, accurate photomask pattern projection and superposition, and correct integration within the interference period require a photolithographic-grade projection lens. For rapid prototyping and to demonstrate experimentally the new field of PIIL, the present PIIES was developed with commercially-available and non-optimized optics and opto-mechanical components. To obtain more definitive PIIL results, an improved PIIES is needed.

7.1.5 PIIL Experimental Demonstration

In spite of the manual alignment and non-optimized optics of the PIIES, PIIL proof-of-concept results were produced [103, 104, 159]. Single- and double-period-blocking photomask patterns have been integrated within 2D square- and hexagonal-lattice periodic microstructures in a single-exposure step. Due to the basic projection lens design and off-axis propagation of the beams, field distortions at the image plane result in overlay errors and limit the experimentally useful exposure field. Experimental exposures are also impacted by spherical aberrations due to the non-ideal exposure wavelength. The photomask elements are imperfectly projected and their superposition is not ideally integrated within the periodic lattice. These aberrations have a stronger impact on results for single-period-blocking photomask elements that are more challenging to align. Yet, patterns with simple geometries, such as the straight waveguide, have been successfully integrated.

SEM and AFM images indicated that the photoresist was not developed through its complete thickness. Unlike commercial photolithographic systems, the prototype PIIES in its current form does not incorporate an exposure dose measurement tool. Partial photoresist development is possibly due to a lack of contrast in the interference pattern or insufficient energy dose during the exposure. Future research avenues include the optimization of the process to improve photoresist exposure and allow for substrate etching.

Finally, experiments match qualitatively well their corresponding simulated PIIL exposures when accounting for optical aberrations. This agreement demonstrates the completeness of the proposed PIIL vector model and is promising regarding the validity of

the 3D-PIIL simulations. Furthermore, the simulated PIIL exposures assumed a perfectly aligned system thus, it is reasonable to state that the imperfect experimental exposures result more from the non-optimized and elementary compound objective lens than from possible PIIES misalignment.

7.2 Future work

Although this thesis aimed at understanding the mathematical and physical underpinnings of PIIL, numerous research aspects remain unexplored. To understand better PIIL's capabilities and limitations, further research is needed. Potential near- and long-term avenues of research are presented in this Section.

7.2.1 Multiple-Optical-Axis Pattern-Integrated Interference Exposure System

The PIIES presented in this thesis represents one example of PIIL implementation. Since a PIIL system may be viewed as a progression of interference and holographic systems, numerous variations of these configurations are also possible candidate systems.

A multiple-optical-axis (MOA) PIIES represents an example of such systems. A MOA-PIIES employs multiple sets of condenser lens, objective lenses, photomask, and possibly Fourier filters for each individual beam. Example MOA configurations are shown in Figures 7.1(a) and (b), where only two beams are shown for clarity. Obviously, there may be three, four, or more beams in such systems to produce various 2D and 3D pattern-integrated periodic microstructures. The optical elements in each axis, including the photomasks, may be the same or may differ for more versatility. After the second objective lens, mirrors are required to deviate the collimated beam to the image plane and photosensitive material. Therefore, the photomasks and lenses must be tilted as shown so

that the images of the photomask lie in the plane of the photosensitive material. As a result, a uniform magnification is produced across the image and keystone distortions are avoided. For a common beam incidence angle of incidence at the image plane, θ_{beam} , the photomasks and lenses must also be inclined at an angle θ_{beam} . Alternatively, the lens configuration could be such that the optical axes are not collinear as depicted in Figure 7.2, eliminating the need for mirrors.

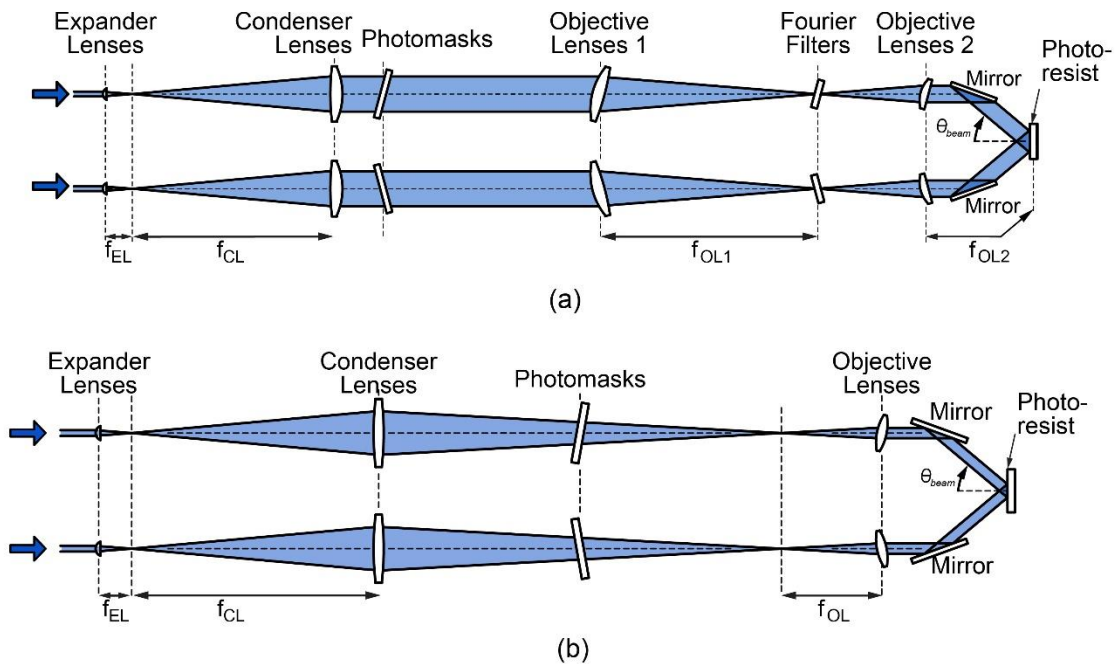


Figure 7.1: (a) MOA Fourier-transform PII system configuration. The photomask is coherently illuminated and a double-objective lens system is employed in each optical axis. (b) MOA PII system configuration employing a single objective lens in each axis. In both systems, the optical elements in each axis may be the same or may differ. Only two beams are shown for clarity but, there may be three, or more beams [90].

The two MOA-PIES configurations presented in Figure 7.1 have relative advantages and disadvantages. When a large demagnification factor is required, the double-objective lens system (Figure 7.1(a)) provides a more compact arrangement of the optical elements. Compared to single-optical-axis PIIES, MOA-PIES can also generate larger incidence

angles and thus produce smaller periodicities. Indeed, the common beam incidence angle at then image plane, θ_{beam} , is limited by the image-side NA in single-optical-axis PIIES. By using differing photomasks in each axis, MOA-PIIES can further generate a wider variety of custom-modified interference patterns [157]. On the other hand, single-optical-axis PIIES have simpler alignment procedures and reduced misalignment sensitivity since they require the alignment of a single photomask and fewer optical elements.

Although modeling and simulation work have been initiated to study MOA-PIIES [156, 157], additional theoretical, optical system design, and experimental research are needed for this alternative PIIL implementation.

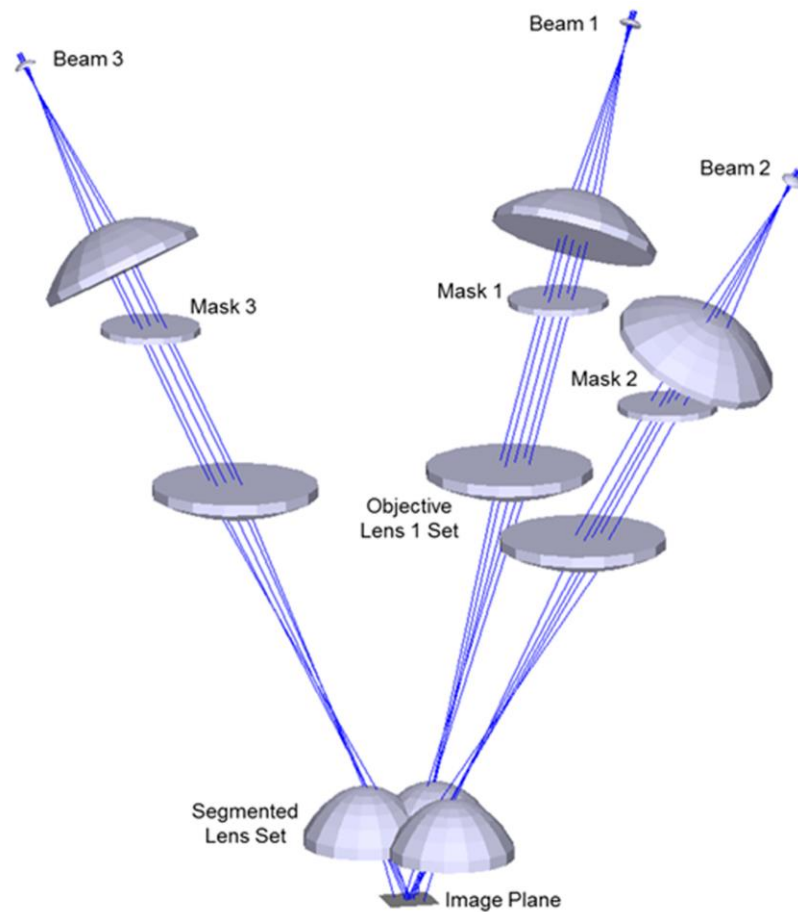


Figure 7.2: MOA-PIIES configuration without mirrors [157].

7.2.2 Partially Coherent Photomask Illumination in PIIL

Although comprehensive, the PIIL model reported in this thesis is only applicable to the PIIL conceptual system described in Chapter 2. If the illumination or lens configuration were modified, the model would also have to be adapted. One possible modification is the use of partially coherent illumination of the photomask. In this thesis, the laser beams are assumed to be collimated at the photomask plane, *i.e.* the photomask is coherently illuminated. This configuration is more convenient from a modeling and experimental procedure perspective. However, coherent illumination in photolithography is known to generate speckle and stronger diffraction effects [116]. To reduce these effects, partially coherent illumination is typically used in photolithography and its application to PIIL should be studied as well.

To account for partially-coherent illumination, the PIIL model can be modified by considering the sum-of-coherent-system model [161], where a partially coherent source is represented as the sum of several coherent sources. Yet, the partially coherent illumination would impact the formation of the interference pattern by reducing its contrast and this effect would have to be accounted for in the model. To address this issue, the PIIES lens configuration could be rearranged such that the beams are collimated at the image plane, while being partially coherent at the object plane. The use of partially coherent illumination would therefore require theoretical work for the development of an adapted model, PIIES design work with ZEMAX to determine an optimized lens arrangement, and a reexamination of the experimental PIIES alignment procedure.

7.2.3 Photomask Optimization

Similar to OPC that improves pattern fidelity in photolithography, photomask optimization in PIIL is introduced in this thesis to correct for undesirable distortions in the periodic lattice. A brute-force search approach was presented that yielded improved, but not optimized photomask patterns. A more rapid and systematic heuristic is needed to determine optimized photomask topologies and improve PIIL exposures.

For photolithography applications, photomasks can be optimized through scalar and vector gradient-based methods for both coherent and partially coherent illuminations [162-165]. Convergence is obtained using steepest descent or conjugate gradient approaches. At each iteration, photomask pixels that generate discrepancies are identified and modified so that the photomask image converges toward a target pattern. The algorithm is typically stopped when the pixel-by-pixel difference between the photomask image and target pattern is smaller than a certain threshold. Yet, gradient-based approaches typically require simplified equation models. The comprehensive PIIL model that combines a high-NA vector imaging model and the MBIL model may be too complex for gradient-based photomask optimization methods. Furthermore, photomask optimization for conventional photolithography and PIIL represent two different problems. For photolithography, how the photomask is updated after each iteration depends on the difference between the photomask image and the target pattern. In PIIL, however, the goal is to optimize the photomask while minimizing distortions in the periodic lattice. Initial research in this area showed that the photomask geometry and the algorithm tend to diverge when applied to PIIL. Future research will therefore have to determine a simplified PIIL model and a suitable algorithm for photomask optimization in PIIL.

If gradient-based optimization methods are not workable, other optimization techniques such as genetic algorithms may be considered. Although possibly slower, genetic algorithms can handle complex models and equations and have been used in optimizing MBIL exposures and photomask optimization [166, 167]. It is reasonable to think that they could be applicable to PIIL as well. Genetic algorithms are examples of evolutionary algorithms, which are inspired by natural selection in biology. At each iteration, the solutions forming a “population” are sorted based on a fitness factor. The fittest solutions are selected to “breed” a new “generation” of solutions. To avoid convergence toward a non-optimized solution, solutions that do not meet the fitness factor may also be selected to introduce some randomness in the new generation. Next, “crossover” and “mutation” genetic operators are employed. Crossovers consist in selecting two solutions as “parents” and combining them to generate a single “child” or “children”. The child solutions share attributes with their parent solutions. Mutations consist in randomly modifying the parent and child solutions. A new population of mutated parent and child solutions is then created and can be tested again with the fitness factor. The process is repeated until a termination figure of merit has been met. The convergence speed and optimality of the solution depend in part on the initial population, the definition of the fitness factor, and genetic operators.

For PIIL photomask optimization, the population would consist of pixelated photomasks with binary, gray-scale, or complex pixel values. The crossover may be bitwise operators (NOT, AND, OR, XOR, etc.), the mutation may be random pixel flipping, and the fitness factor and termination figure of merit may be the pixel-by-pixel difference between the optimized solution and the desired pattern. Future research will

have to determine appropriate fitness factors and genetic operators such that the algorithm converges toward an optimized solution.

7.2.4 Photoresist processing improvement

As discussed in Section 7.1.5, the photoresist film was not developed through its complete thickness in the experimental results. The present research focused on the prototype PIIES design, establishing an appropriate PIIES alignment procedure, and obtaining proof-of-concept results that demonstrate PIIL potential. Now that a stable and repeatable PIIES preparation procedure has been established, future research can focus on optimizing the PIIL exposure process including the exposure time. Photoresists with absorption coefficients smaller than that of the Microposit SC1813 may further be helpful in producing steeper photoresist walls as illustrated in the simulated exposures in Chapter 3. This future research will aim at exposing the photoresist to allow a pattern transfer to the substrate, either through etching and deposition/lift-off process.

7.2.5 3D-PIIL Experimental Demonstration

Simulated 3D-PIIL exposures show great promise for the single-exposure fabrication of custom-modified 3D periodic lattices. Future research will have to demonstrate 3D-PIIL capabilities experimentally. 3D-PIIL experiments have recently been initiated using $15\mu\text{m}$ -thick films of SU8-2015 negative-tone photoresist. The (3+1)-beam configuration presented in Chapter 4 is employed to produce a 3D face-centered rhombohedral lattice. The beam displacement, d_{beam} , is 17.78mm , which yields a $1.31\mu\text{m}$ -period in the xy-plane according to the fitting equations established in Chapter 5. SEM images of exposed SU8 films are shown in Figure 7.3. The measured lattice period in the xy-plane is $1.29\mu\text{m}$ and

matches well the estimated period. Yet, the 3D lattice is barely visible due to a lack of contrast and bicontinuity. To address this issue, future research will have to consider process improvement avenues including increasing the softbake time to remove residual solvent from the photoresist, reducing the post-exposure bake time to crosslink regions of highest concentration of exposure-generated acids only, and/or increasing the development time. In addition, future 3D-PIIL experiments may require adding a base to the SU8 to consume background acid concentration due to poor interference pattern contrast. For example, triethylamine has been demonstrated in 3D-MBIL to improve the contrast and quality of 3D periodic lattices recorded in SU8 [168-173].

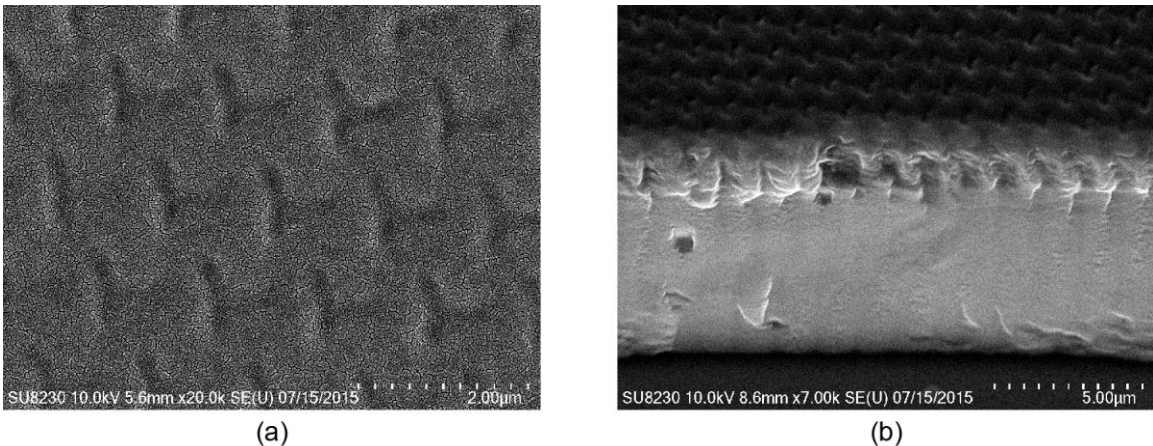


Figure 7.3: (a) Top-view and (b) 25deg-side-view SEM images of 3D-PIIL exposures.

7.3 Concluding Remarks

At the intersection of MBIL and projection lithography, the new concept of PIIL has been established as a successor of optical interference and holography, simulated with a multi-beam high-NA interference/image vector model, implemented in a prototype PIIES, and demonstrated experimentally with the fabrication of pattern-integrated 2D square- and

hexagonal periodic lattices. Of note, the experimental PIIL exposures are obtained with a non-optimized, manually-aligned *ad hoc* optical system. Reasons for the non-ideal results have been identified and can be addressed in future optimized PIIES. As numerous PIIL underpinnings remain unexplored, research avenues were proposed to understand further PIIL's full capabilities and limitations. Future research paths include the design of new PIIL systems, the development of photomask optimization strategies, the fabrication of functional devices, and the experimental demonstration of 3D-PIIL.

By enabling the rapid fabrication of large-format custom-modified 2D and 3D periodic microstructures, PIIL addresses several of the current issues in 3D microfabrication. In particular, the uniqueness of 3D-PIIL is expected to impact significantly nano- and microtechnologies. Various research and development areas in photonics, bioengineering, microfluidics, and mechanical metamaterials currently require a technology like PIIL for rapid prototyping or high-throughput manufacturing. As Professor Nadav Gutman in a *Spotlight on Optics* article stated [154],

“To the best of my knowledge, this is the only method that can be used to both create and pattern 3D periodic structure in a single step. The end result is a beautiful periodic 3D lattice, bounded by voids in the case of negative photo-resist or solid in the case of positive photo-resist.”

APPENDIX A

FRINGE ZERNIKE POLYNOMIALS AND COEFFICIENTS

In this thesis, the Zernike polynomials are expressed in polar terms, which are appropriate for rotationally symmetrical systems such as the PIIES. The polynomials are expressed as functions of the relative radial position ρ_P and polar angle θ_P over the exit pupil. Two equivalent formalisms exist: the fringe and standard Zernike polynomials. The polynomials and coefficients in these two formalisms only differ by a normalization factor. The first 37 fringe Zernike polynomials, which are orthogonal on a unit disc, are expressed as:

$Z_1(\rho_P, \theta_P) = 1$	Piston
$Z_2(\rho_P, \theta_P) = \rho_P \cos(\theta_P)$	x tilt
$Z_3(\rho_P, \theta_P) = \rho_P \sin(\theta_P)$	y tilt
$Z_4(\rho_P, \theta_P) = 2\rho_P^2 - 1$	power
$Z_5(\rho_P, \theta_P) = \rho_P^2 \cos(2\theta_P)$	3rd order astigmatism
$Z_6(\rho_P, \theta_P) = \rho_P^2 \sin(2\theta_P)$	3rd order 45deg astigmatism
$Z_7(\rho_P, \theta_P) = (3\rho_P^3 - 2\rho_P) \cos(\theta_P)$	3rd order x coma
$Z_8(\rho_P, \theta_P) = (3\rho_P^3 - 2\rho_P) \sin(\theta_P)$	3rd order y coma
$Z_9(\rho_P, \theta_P) = 6\rho_P^4 - 6\rho_P^2 + 1$	3rd order spherical
$Z_{10}(\rho_P, \theta_P) = \rho_P^3 \cos(3\theta_P)$	
$Z_{11}(\rho_P, \theta_P) = \rho_P^3 \sin(3\theta_P)$	
$Z_{12}(\rho_P, \theta_P) = (4\rho_P^4 - 3\rho_P^2) \cos(2\theta_P)$	5th order x coma

$Z_{13}(\rho_P, \theta_P) = (4\rho_P^4 - 3\rho_P^2) \sin(2\theta_P)$	5th order y coma
$Z_{14}(\rho_P, \theta_P) = (10\rho_P^5 - 12\rho_P^3 + 3\rho_P) \cos(\theta_P)$	5th order x coma
$Z_{15}(\rho_P, \theta_P) = (10\rho_P^5 - 12\rho_P^3 + 3\rho_P) \sin(\theta_P)$	5th order y coma
$Z_{16}(\rho_P, \theta_P) = 20\rho_P^6 - 30\rho_P^4 + 12\rho_P^2 - 1$	5th order spherical
$Z_{17}(\rho_P, \theta_P) = \rho_P^4 \cos(4\theta_P)$	
$Z_{18}(\rho_P, \theta_P) = \rho_P^4 \sin(4\theta_P)$	
$Z_{19}(\rho_P, \theta_P) = (5\rho_P^5 - 4\rho_P^3) \cos(3\theta_P)$	
$Z_{20}(\rho_P, \theta_P) = (5\rho_P^5 - 4\rho_P^3) \sin(3\theta_P)$	
$Z_{21}(\rho_P, \theta_P) = (15\rho_P^6 - 20\rho_P^4 + 6\rho_P^2) \cos(2\theta_P)$	7th order x coma
$Z_{22}(\rho_P, \theta_P) = (15\rho_P^6 - 20\rho_P^4 + 6\rho_P^2) \sin(2\theta_P)$	7th order y coma
$Z_{23}(\rho_P, \theta_P) = (35\rho_P^7 - 60\rho_P^5 + 30\rho_P^3 - 4\rho_P) \cos(\theta_P)$	7th order x coma
$Z_{24}(\rho_P, \theta_P) = (35\rho_P^7 - 60\rho_P^5 + 30\rho_P^3 - 4\rho_P) \sin(\theta_P)$	7th order y coma
$Z_{25}(\rho_P, \theta_P) = 70\rho_P^8 - 140\rho_P^6 + 90\rho_P^4 - 20\rho_P^2 + 1$	7th order spherical
$Z_{26}(\rho_P, \theta_P) = \rho_P^5 \cos(5\theta_P)$	
$Z_{27}(\rho_P, \theta_P) = \rho_P^5 \sin(5\theta_P)$	
$Z_{28}(\rho_P, \theta_P) = (6\rho_P^6 - 5\rho_P^4) \cos(4\theta_P)$	
$Z_{29}(\rho_P, \theta_P) = (6\rho_P^6 - 5\rho_P^4) \sin(4\theta_P)$	
$Z_{30}(\rho_P, \theta_P) = (21\rho_P^7 - 30\rho_P^5 + 10\rho_P^3) \cos(3\theta_P)$	
$Z_{31}(\rho_P, \theta_P) = (21\rho_P^7 - 30\rho_P^5 + 10\rho_P^3) \sin(3\theta_P)$	
$Z_{32}(\rho_P, \theta_P) = (56\rho_P^8 - 105\rho_P^6 + 60\rho_P^4 - 10\rho_P^2) \cos(2\theta_P)$	9th order x coma
$Z_{33}(\rho_P, \theta_P) = (56\rho_P^8 - 105\rho_P^6 + 60\rho_P^4 - 10\rho_P^2) \sin(2\theta_P)$	9th order y coma

$$Z_{34}(\rho_P, \theta_P) = (126\rho_P^9 - 280\rho_P^7 + 210\rho_P^5 - 60\rho_P^3 + 5\rho_P) \cos(\theta_P) \quad \text{9th order x coma}$$

$$Z_{35}(\rho_P, \theta_P) = (126\rho_P^9 - 280\rho_P^7 + 210\rho_P^5 - 60\rho_P^3 + 5\rho_P) \sin(\theta_P) \quad \text{9th order y coma}$$

$$Z_{36}(\rho_P, \theta_P) = 252\rho_P^{10} - 630\rho_P^8 + 560\rho_P^6 - 210\rho_P^4 + 30\rho_P^2 - 1 \quad \text{9th order spherical}$$

$$Z_{37}(\rho_P, \theta_P) = 924\rho_P^{12} - 2772\rho_P^{10} + 3150\rho_P^8 - 1680\rho_P^6 + 420\rho_P^4 - 42\rho_P^2 + 1 \quad \text{9th order spherical}$$

The quantities ρ_P and θ_P can be expressed as functions of the direction cosines α and β at the Fourier plane as

$$\rho_P = \sqrt{\alpha^2 + \beta^2} \quad (\text{A.1})$$

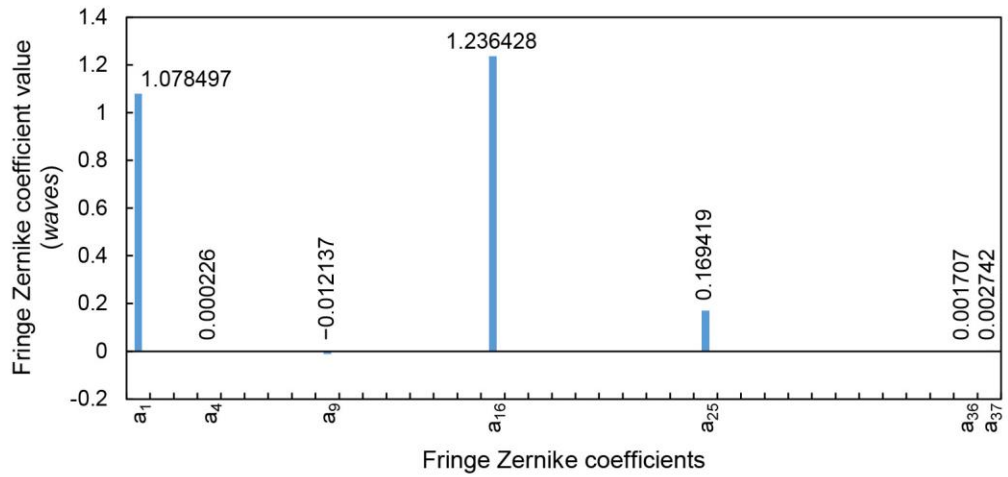
and

$$\theta_P = \tan^{-1}\left(\frac{\beta}{\alpha}\right). \quad (\text{A.2})$$

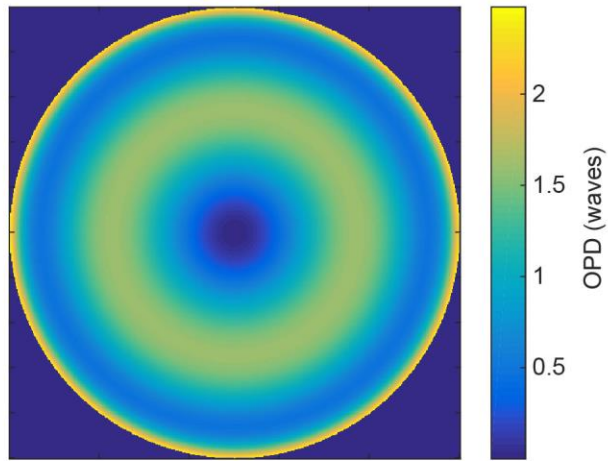
The function $W(\alpha, \beta)$ introduced in Section 2.3.2 describes the optical path difference (OPD) as function of the Zernike coefficients and is expressed as

$$W(\alpha, \beta) = \sum_{i=1}^{37} \frac{a_i Z_i(\alpha, \beta)}{\lambda}, \quad (\text{A.3})$$

where a_i is the fringe Zernike coefficient of the i^{th} fringe Zernike polynomial. The fringe Zernike coefficients for the PIIES compound objective lens are calculated with the ray-tracing software ZEMAX. Only the piston (a_1) and spherical aberration terms ($a_4, a_9, a_{16}, a_{25}, a_{36}, a_{37}$) comprise the OPD. These non-zero coefficients are plotted in Figure A.1(a). The OPD across the exit pupil is shown in Figure A.1(b).



(a)



(b)

Figure A.1: (a) Fringe Zernike coefficients calculated with ZEMAX (b) OPD across the exit pupil.

APPENDIX B

MATLAB SCRIPTS

MATLAB scripts implementing the PIIL vector model are given in this Appendix. The code presented here corresponds to the 3D-PIIL case discussed in Section 4.3.1 and simulation results shown in Figure 4.7(b) (4-beam configuration, photomask-integrated face-centered-rhombohedral lattice). The present MATLAB scripts include the main script and custom MATLAB functions. These functions include

- `Mask_Generation_Function` that returns the pixelated photomask pattern,
- `UnitMask_Generation_Function` that returns the single-motif-blocking pattern used in the design of the complete photomask,
- `shifted_fourier_transform` that returns Fourier transforms of the photomask shifted from the origin to account for the off-axis propagation of the beams,
- `fourier_transform_5beams` that calculates the image-side vector electric fields and returns the optical intensity distribution of the PIIL exposure at a certain depth within the photoresist film, and
- `stack_matrix_5beams` that returns the optical transfer functions.

B.1 Main script

In the main script, the user enters all the parameters needed for the simulations, including simulation parameters, photoresist characteristics, beam parameters, and photomask characteristics.

```

%% INITIALIZATION
disp('# INITIALIZATION #');

clc; % Clears command window
disp('Are you sure you want to start this program from')
disp('the beginning? Current workspace will be deleted.')
disp('Press Enter for Yes, Ctrl+C to cancel')
disp('-----')
pause

clear all

%% SIMULATION PARAMETERS
disp('# SIMULATION PARAMETERS #');

N_pitch = 15; % # of pixel for one period, must be odd
N = 36*N_pitch + 1; % # of periods across the image, must be
odd
lambda = 363.8e-9; % Source wavelength in [m]
pitch = 1000e-9; % Period at the sample/image plane
NA_im = 0.8; % Numerical aperture on image side
magn = 0.25; % Magnification of the system
n_imm = 1; % Immersion refractive index

% Verification of N for accuracy
if abs((1-(N/(2*N_pitch))/round(N/(2*N_pitch)))*100) > 0.1;
    N_temp=N; % Temporary N is created
    while abs((1-
(N_temp/(2*N_pitch))/round(N_temp/(2*N_pitch)))*100)>0.1;
        N_temp = N_temp+2*N_pitch;
    end

    disp(strcat('*WARNING* - N should be changed from:'));
    disp(strcat(num2str((N-1)/N_pitch), '*N_pitch+1 to:'));
    disp(strcat(num2str((N_temp-1)/N_pitch), '*N_pitch+1=',
num2str(round(N_temp)), ' for better accuracy.'));
    temp = input(strcat('Desired value x of x*N_pitch+1?'));
    disp('-----')
    if ~isequal(temp, []); N=temp*N_pitch+1; end
end

% # of pixel across the pupil in the Fourier plane
Number_of_pixels_across_pupil = 50;
if round(2*NA_im*N*pitch/(lambda*N_pitch)) <
Number_of_pixels_across_pupil;
    disp(' - *WARNING* Potential under-sampling in the Fourier plane')
    temp = input(strcat('N=', num2str((N+1)/N_pitch), '*N_pitch+1. Change
N for recommended value: "',
num2str(round(Number_of_pixels_across_pupil*lambda
/(2*NA_im*pitch))), '"*N_pitch+1=',
num2str(round(Number_of_pixels_across_pupil*lambda*N_pitch
/(2*NA_im*pitch))), '?'));
    disp('-----')
    %N is resized if considered too small

```

```

    if ~isequal(temp, []); N = temp*N_pitch+1; end
end

%% PHOTORESIST CHARACTERISTICS
disp('# PHOTORESIST CHARACTERISTICS #');

n_PR = 1.67; k_PR = 6e-5; n_sub = 1.47;
n_BARC = 1.67; BARC_depth = 0;

PR_depth = 10e-6; % Depth of the PR
range_depth = linspace(0, PR_depth, 21);
defocus = -PR_depth/2/n_PR; % Displacement of photoresist
surface along z-axis

%% BEAM CONDITIONING: NUMBER OF BEAMS, INCIDENCE & AZIMUTH. ANGLE,
SYMMETRIES
disp('# BEAM CONDITIONING #');

phi = [0 180 -60 60 0];
theta_im = asind(2*lambda/(sqrt(3)*pitch)); theta_im = [0
theta_im];
theta_pol = [1 1i 1 0 -0.5 sqrt(3)/2 -0.5 -sqrt(3)/2 0 0];
N_unit_scaled_x = N_unit; N_unit_scaled_y =
N/(sqrt(3)*N_unit)/round(N/(sqrt(3)*N_unit))*N_unit;

% Verification of sin(theta_im) smaller than NA
if sind(theta_im(2))>NA_im;
    disp('*** WARNING *** Beams are outside of the pupil.');
```

disp(strcat('sind(theta_im)=', num2str(sind(theta_im(2))), '>NA_im'));

temp = input(strcat('Press Ctrl+C'));

disp('-----')

```

end

%% IMAGE CHARACTERISTICS
disp('# IMAGE CHARACTERISTICS #');

pixel_resolution = pitch/N_pitch;
image_size = N*pixel_resolution;
image_axis = -image_size/2:image_size/(N-1):image_size/2;

pixel_resolution_x = pitch/N_unit_scaled_x;
image_size_x = N*pixel_resolution_x;
image_axis_x = -image_size_x/2:image_size_x/(N-1):image_size_x/2;

pixel_resolution_y = pitch/N_unit_scaled_y;
image_size_y = N*pixel_resolution_y;
image_axis_y = -image_size_y/2:image_size_y/(N-1):image_size_y/2;

%% PHOTOMASK CHARACTERISTICS
disp('# MASK CHARACTERISTICS #');
FunctElem = 'GT_squ_x3';
MaskShape = 'squ';
SizeRatio = 1;

%% PARAMETERS FOR TIME-DEPENDANT EXPOSURE
```

```

flagTime = 0; % 0 for no time-dependency, 1 otherwise
if      flagTime == 0; timeRange = 0;
elseif  flagTime == 1; timeStep = 0.05; timeRange =
timeStep:timeStep:1;
end

save constants pitch N N_pitch MaskShape FunctElem ...
    image_size lambda magn pixel_resolution NA_im ...
    theta_im phi flag_sym theta_pol defocus SizeRatio...
    A B C n_PR image_axis range_depth n_sub ...
    N_unit_scaled_x N_unit_scaled_y flagTime PR_depth ...
    BARC_depth n_BARC k_PR

%% CREATION OF THE MASK
disp('# CREATION OF THE MASK #');
mask = Mask_Generation_Function(SizeRatio);

%% CREATION OF THE FOURIER TRANSFORMS SHIFTED IN THE F. PLANE
disp('# FOURIER TRANSFORMS SHIFTED #');
[M1,M2,M3,M4,M5] =
shifted_fourier_transform(mask,theta_im,image_size,lambda,phi,N,NA_im,p
itch,N_pitch);

%% CALCULATION OF I
disp('# SIMULATIONS #');
I = zeros(N,N,length(range_depth)); % The 3D matrix that contains the
data of the illumination

for time = timeRange;
    t00 = clock; % To keep track of time
    for ii = 1:length(range_depth);
        t0 = clock;
        z = range_depth(ii);
        disp('-----')
        disp(strcat('Processing photoresist layer >',...
            num2str(round(z/PR_depth*100)), '% /',datestr(now)))

        I1 = fourier_transform_5beams_lite(z,M_pac,M1,M2,M3,M4,M5);
        I(:, :, ii) = I1;

        % Progress bar
        disp(strcat('Elapsed time is (in min):',
num2str(etime(clock,t0)/60));
            disp(strcat('Elapsed time (since beginning) is',
num2str(etime(clock,t00)/60), 'min'));
        end
    end
end

```

B.2 Mask_Generation_Function.m

Mask_Generation_Function returns the complete pixelated photomask pattern.

The photomask is created by a convolution operation between the single-motif-blocking pattern (UnitMask) and a matrix of 0s with 1s at the locations where the single-motif-blocking pattern is desired (Pattern).

```
function Mask = Mask_Generation_Function(SizeRatio)

load('constants.mat', '-regexp', '^(?!SizeRatio)\w');

%% Initialization of the matrices
UnitMask = UnitMask_Generation_Function(SizeRatio); % Generation of the
UnitMasks (unit blocking elements of the mask - square, disc, etc.)
Pattern = zeros(N); % Pattern will have ones at the location of the
UnitMasks

%% The UnitMask is only N_unit*N_unit large. This double loop will
reshape it to N*N, keeping the UnitMask in the center

% % UnitMask=padarray(UnitMask, [(N-length(UnitMask))/2, (N-
length(UnitMask))/2],1);
length_UnitMask = length(UnitMask);

UnitMask = padarray(UnitMask, [(N-length_UnitMask)/2+1, (N-
length_UnitMask)/2+1],1,'pre');
UnitMask = padarray(UnitMask, [(N-length_UnitMask)/2-1, (N-
length_UnitMask)/2-1],1,'post');

%% The pattern matrix is defined. It corresponds to a 1-value pixel at
the location where a unit cell is desired

if strcmp(FunctElem, 'GT_squ_x3');
    BlockPosition=[];
    Size = 3;
    for i=-3*Size:-3*Size+Size-1; for j=-4*Size:-1*Size+Size-1;
BlockPosition=[BlockPosition; [i j]];end;end %top of the G
    for i=-2*Size:1*Size+Size-1; for j=-4*Size:-4*Size+Size-1;
BlockPosition=[BlockPosition; [i j]];end;end %side of the G
    for i=1*Size:1*Size+Size-1; for j=-3*Size:-1*Size+Size-1;
BlockPosition=[BlockPosition; [i j]];end;end %side of the G
    for i=0*Size:0*Size+Size-1; for j=-1*Size:-1*Size+Size-1;
BlockPosition=[BlockPosition; [i j]];end;end %side of the G
    for i=-1*Size:-1*Size+Size-1; for j=-2*Size:3*Size+Size-1;
BlockPosition=[BlockPosition; [i j]];end;end %side of the G
    for i=0*Size:2*Size+Size-1; for j=1*Size:1*Size+Size-1;
BlockPosition=[BlockPosition; [i j]];end;end %side of the G
    % pause
end
```

```

% N_unit_scaled_ is required here to adjust the position of the
blocking elements
BlockPosition_y = (N+1)/2 + round(BlockPosition * N_unit_scaled_y);
BlockPosition_x = (N+1)/2 + round(BlockPosition * N_unit_scaled_x);

for k=1:size(BlockPosition,1)
    Pattern(BlockPosition_y(k,1)-1,BlockPosition_x(k,2)-1)=1; %-1 is
required because the ceil() function above forces positions to be
shifted up by one extra pixel
end

count = size(BlockPosition,1); % used to adjust the amplitude of the
mask at the end

% The Fourier transforms are multiplied and the inverse FT is derived,
% correspondign to the final mask
UnitMask_fft = fftshift(fft2(UnitMask));
Pattern_fft = fftshift(fft2(Pattern));
Mask_fft = UnitMask_fft.*Pattern_fft;

Mask = abs(ifftshift(ifft2(Mask_fft)));

Mask = (Mask-(count-1)); % necessary to adjust the amplitude of the
mask
Mask(Mask<0.5) = 0;
end

```

B.3 UnitMask_Generation_Function.m

UnitMask_Generation_Function returns the single-motif-blocking pattern that composes the photomask and that is used in Mask_Generation_Function.

```

function UnitMask = UnitMask_Generation_Function(SizeRatio)

load('constants.mat', '-regexp', '^(?!SizeRatio)\w');

ScaledSize=round(N_pitch*SizeRatio);
if mod(ScaledSize,2)==0, ScaledSize=ScaledSize-1;end % ScaledSize must
be odd

UnitMask=ones(N_pitch); %UnitMask is filled with ones, and then zeros
are added depending on the shape

if strcmp(MaskShape,'squ'); % For a square
    UnitMask=zeros(ScaledSize);
    % If the square is smaller than a period (SizeRatio<1)
    if ScaledSize<=N_pitch
        % Center the undersized square in the middle of the unit cell
and
        % fill 1's around it
    end
end

```

```

        UnitMask=padarray(UnitMask, [(N_pitch-ScaledSize)/2, (N_pitch-
ScaledSize)/2],1);
    end
end

if strcmp(MaskShape, 'disc') % disc, size=diameter
    UnitMask=ones(ScaledSize); %UnitMask is filled with ones, and then
zeros are added depending on the shape
    for i=1:ScaledSize
        for j=1:ScaledSize
            center=(ScaledSize+1)/2;
            if round(sqrt((i-center)^2+(j-
center)^2))<=(ScaledSize+1)/2;
                UnitMask(i,j)=0;
            end
        end
    end
end

if strcmp(MaskShape, 'rotsqu'); % rotated square
    UnitMask=ones(ScaledSize);
    for i=1:(ScaledSize+1)/2
        for j=(ScaledSize+1)/2-(i-1):(ScaledSize+1)/2+(i-1);
            UnitMask(i,j)=0;
        end
    end

    UnitMask=UnitMask.*rot90(UnitMask,2);

    if ScaledSize<=N_pitch
        UnitMask=padarray(UnitMask, [(N_pitch-ScaledSize)/2, (N_pitch-
ScaledSize)/2],1);
    end
end

if strcmp(MaskShape, 'hex'); % hexagon
    %ScaledSize=round(N_pitch*SizeRatio*2/sqrt(3));

    UnitMask=ones(ScaledSize); %a hexagon with size ScaledSize is
created. If ScaledSize<N_pitch, padarray is used to add ones around

    for i=1:(ScaledSize+1)/2 %for each line from the top to the bottom
        if i<round(1/2*(ScaledSize+1)/2)
            for j=ceil((ScaledSize+1)/2-i*sqrt(3)):(ScaledSize+1)/2
                UnitMask(i,j)=0;
            end

            elseif i>=round(1/2*(ScaledSize+1)/2)
                for j=ceil((ScaledSize+1)/2*(1-
sqrt(3)/2)):(ScaledSize+1)/2;
                    UnitMask(i,j)=0;
                end
            end
        end

    UnitMask = UnitMask.*fliplr(UnitMask);
    UnitMask = UnitMask.*rot90(UnitMask,2);

```

```

    if ScaledSize<=N_pitch
        UnitMask=padarray(UnitMask,[(N_pitch-ScaledSize)/2,(N_pitch-
ScaledSize)/2],1);
    end
end

if strcmp(MaskShape,'rothex'); % rotated hexagon
    UnitMask=ones(ScaledSize); %a hexagon with size ScaledSize is
created. If ScaledSize<N_pitch, padarray is used to add ones around

    for i=1:(ScaledSize+1)/2 %for each line from the top to the bottom
        if i<round(1/2*(ScaledSize+1)/2)
            for j=ceil((ScaledSize+1)/2-i*sqrt(3)):(ScaledSize+1)/2
                UnitMask(i,j)=0;
            end

            elseif i>=round(1/2*(ScaledSize+1)/2)
                for j=ceil((ScaledSize+1)/2*(1-
sqrt(3)/2)):(ScaledSize+1)/2;
                    UnitMask(i,j)=0;
                end
            end
        end
    end

    UnitMask=UnitMask.*fliplr(UnitMask); % Half of the hexagon is
created
    UnitMask=UnitMask.*rot90(UnitMask,2); % Complete hexagon is created
    UnitMask=rot90(UnitMask); % Rotated hexagon is created

    if ScaledSize<=N_pitch
        UnitMask=padarray(UnitMask,[(N_pitch-ScaledSize)/2,(N_pitch-
ScaledSize)/2],1);
    end
end
end

```

B.4 shifted_fourier_transform.m

shifted_fourier_transform returns the Fourier transforms of the photomask, which are shifted in the Fourier plane depending on the beam propagation characteristics.

```

function [ M1, M2, M3, M4, M5] = shifted_fourier_transform (mask,
theta_im, image_size, lambda, phi, N, NA_im, pitch, N_pitch )
%UNTITLED2 Summary of this function goes here
% Detailed explanation goes here

% the 1.001 is used because of some numerical artifact
source_shift=round(1.0001*sind(theta_im(2))*image_size/lambda*...
[[cosd(phi(2)) sind(phi(2))]);...

```

```

    [cosd(phi(3)) sind(phi(3))];...
    [cosd(phi(4)) sind(phi(4))];...
    [cosd(phi(5)) sind(phi(5))]];

if floor((N+1)/2-NA_im*N*pitch/(lambda*N_pitch)) <
max(abs(source_shift));
    disp('*** WARNING *** The pupil is too small - increase lattice
constant'); pause
end

M=fftshift(fft2((mask)));

M1=M;
M2=circshift(M,[source_shift(1,1) source_shift(1,2)]);
M3=circshift(M,[source_shift(2,1) source_shift(2,2)]);
M4=circshift(M,[source_shift(3,1) source_shift(3,2)]);
M5=circshift(M,[source_shift(4,1) source_shift(4,2)]);

end

```

B.5 `fourier_transform_5beams.m`

`fourier_transform_5beams` returns the optical intensity distribution of the PIIL exposure at a certain depth within the photoresist film. The calculation is based on the image-side complex vector electric fields calculated from the shifted Fourier transforms and the optical transfer functions (see next Section).

```

function [I] = fourier_transform_5beams (z,M_pac,M1,M2,M3,M4,M5)

load constants

%% INITIALIZATION OF MATRICES
E0 = zeros(N,N);
E1 = zeros(N,N,3);
E2 = zeros(N,N,3);
E3 = zeros(N,N,3);
E4 = zeros(N,N,3);
E5 = zeros(N,N,3);
Etotal = zeros(N,N,3);

[P0, P1, P2, P3, P4, P5] = stack_matrix_5beams(z,M_pac);

disp('# Calculating Etotal')
t1 = clock;

for i=1:3; % For each polarizations

```

```

E1(:,:,i) = ifft2(iffshift(M1.*P1(:,:,i)));%.*ScalingMatrix;
E2(:,:,i) = ifft2(iffshift(M2.*P2(:,:,i)));
E3(:,:,i) = ifft2(iffshift(M3.*P3(:,:,i)));
E4(:,:,i) = ifft2(iffshift(M4.*P4(:,:,i)));
Etotal(:,:,i) = ifft2(iffshift(...
    M1.*P1(:,:,i)...
    +M2.*P2(:,:,i)...
    +M3.*P3(:,:,i)...
    +M4.*P4(:,:,i))); % Calculate the total field Etotal
disp(strcat(num2str(round(i/3*100)), '% /',datestr(now))); %
Display updated status
end

disp(strcat('Elapsed time (in min):',num2str(etime(clock,t1)/60)));
disp('# Calculating I_PIIIL');
t1 = clock;

I = 0.5* real(Etotal(:,:,1).*conj(Etotal(:,:,1)))...
    + 0.5* real(Etotal(:,:,2).*conj(Etotal(:,:,2)))...
    + 0.5* real(Etotal(:,:,3).*conj(Etotal(:,:,3)));

I = rot90(I,2);
disp(strcat('Elapsed time (in min):',num2str(etime(clock,t1)/60)));

end

```

B.6 stack_matrix_5beams.m

stack_matrix_5beams returns the optical transfer functions derived from Flagello's high-NA vector imaging model.

```

function [P0, P1, P2, P3, P4, P5] = stack_matrix_5beams(z,M_pac)

t1 = clock;
load constants

%% INITIALIZATION OF MATRICES
P0 = zeros(N);
P1 = zeros(N,N,3);
P2 = zeros(N,N,3);
P3 = zeros(N,N,3);
P4 = zeros(N,N,3);
P5 = zeros(N,N,3);

A_matrix=zeros(N);
m_pac = min(min(min(M_pac(:,:,:))));

N_air=1;
if flagTime == 0; N_PR = n_PR-li*k_PR;
elseif flagTime == 1; N_PR = n_PR-li*lambda*1e6*(A*m_pac+B)/(4*pi());

```

```

end

N_bar = n_BAR;
N_sub = n_sub;

% Parameter normalization
d1      = PR_depth/lambda;
d_bar   = BARC_depth/lambda;
depth   = z/lambda;
defocus = defocus/lambda;

fx_vect = -N/(image_size*2):N/(image_size*(N-1)):N/(image_size*2);
fy_vect = fx_vect;
y_vect  = fy_vect/(NA_im/lambda);
x_vect  = fx_vect/(NA_im/lambda);
[Y_vect,X_vect] = meshgrid(y_vect,x_vect);
Pupil = sqrt(Y_vect.^2+X_vect.^2)<=1;
[row,col] = find(Pupil);

flag_txt=0; % used for the progression text

for m=min(col):max(col)
    for n=min(col):max(col)
        % Define the coordinates in the Fourier plane in [m^-1].
        fx = -N/(image_size*2)+(m-1)*N/(image_size*(N-1));
        fy = -N/(image_size*2)+(n-1)*N/(image_size*(N-1));

        % If the pixel is inside of the system pupil, defined by the
        diameter CA, the obliquity function is computed. The obliquity is 0
        otherwise.
        if sqrt(fx^2+fy^2)<=NA_im/lambda;
            x = fx/(NA_im/lambda);
            y = fy/(NA_im/lambda);

            A = atan2(y,x); % azimuthal angle relative to the x-axis
            theta_i=asin(sqrt(x^2+y^2)*NA_im);

            alpha = sin(theta_i)*cos(A); % Alpha (m,n)=alpha;
            beta  = sin(theta_i)*sin(A); % Beta (m,n)=beta;
            gamma = cos(theta_i); % Gamma (m,n)=gamma;

            gamma_layer = sqrt(1-sin(acos(gamma))^2/N_PR^2);
            gamma_sub    = sqrt(1-sin(acos(gamma))^2/N_sub^2);
            gamma_bar    = sqrt(1-sin(acos(gamma))^2/N_bar^2);

            phi_layer = 2*pi()*(d1-depth)*N_PR*gamma_layer

            % Optical admittances eta and phase delta
            eta_1_S = N_PR*gamma_layer;
            eta_1_P = N_PR/gamma_layer;

            eta_sub_S = N_sub*gamma_sub;
            eta_sub_P = N_sub/gamma_sub;

            eta_bar_S = N_bar*gamma_bar;
            eta_bar_P = N_bar/gamma_bar;

```

```

eta_air_S = N_air*gamma;
eta_air_P = N_air/gamma;

delta_1 = 2*pi()**(N_PR*gamma_layer*d1);
delta_bar_c = 2*pi()**(N_bar_c*gamma_bar_c*d_bar_c);

% B and C parameters
M_S = [cos(delta_1) li*sin(delta_1)/eta_1_S;...
       li*eta_1_S*sin(delta_1) cos(delta_1)];

M_P = [cos(delta_1) li*sin(delta_1)/eta_1_P; ...
       li*eta_1_P*sin(delta_1) cos(delta_1)];

M_bar_c_S = [cos(delta_bar_c) li*sin(delta_bar_c)/eta_bar_c_S;
...
            li*eta_bar_c_S*sin(delta_bar_c) cos(delta_bar_c)];

M_bar_c_P = [cos(delta_bar_c) li*sin(delta_bar_c)/eta_bar_c_P;
...
            li*eta_bar_c_P*sin(delta_bar_c) cos(delta_bar_c)];

temp = M_S * M_bar_c_S * [1;eta_sub_S];
B_S = temp(1); C_S = temp(2);
temp = M_P * M_bar_c_P * [1;eta_sub_P];
B_P = temp(1); C_P = temp(2);

temp = M_bar_c_S * [1;eta_sub_S];
B_sub_S = temp(1); C_sub_S = temp(2);

temp = M_bar_c_P * [1;eta_sub_P];
B_sub_P = temp(1); C_sub_P = temp(2);

% Transmission and reflection coefficients
tau_S_fraction = (2*eta_air_S / (B_S*eta_air_S + C_S)) /
(2*eta_1_S / (B_sub_S*eta_1_S + C_sub_S));
tau_P_fraction = (2*eta_air_P / (B_P*eta_air_P + C_P)) /
(2*eta_1_P / (B_sub_P*eta_1_P + C_sub_P));

r_II_S = (B_sub_S*eta_1_S - C_sub_S) / (B_sub_S*eta_1_S +
C_sub_S);
r_II_P = (B_sub_P*eta_1_P - C_sub_P) / (B_sub_P*eta_1_P +
C_sub_P);

% Film function matrix M

F_S = tau_S_fraction * ( exp(li*phi_layer) + r_II_S*exp(-
li*phi_layer));
F_P = tau_P_fraction * ( exp(li*phi_layer) + r_II_P*exp(-
li*phi_layer));
F_zP = N_air*gamma/(N_PR*gamma_layer) * tau_P_fraction * (
exp(li*phi_layer) -r_II_P * exp(-li*phi_layer));

M = [F_S*sin(A)^2+F_P*cos(theta_i)*cos(A)^2 F_S*-
cos(A)*sin(A)+F_P*cos(A)*sin(A)*cos(theta_i);...
     F_S*-cos(A)*sin(A)+F_P*cos(A)*sin(A)*cos(theta_i)
F_S*cos(A)^2 + F_P*cos(theta_i)*sin(A)^2;...
     F_zP*-alpha F_zP*-beta];

```

```

% Obliquity factor and defocus
O = [ (1-NA_im^2*magn^2*(x^2+y^2)) / (1-NA_im^2*(x^2+y^2))
]^(1/4);

%Defocus term
Defocus = exp(-1i*2*pi()* (defocus)*gamma);

% Zernike coefficients
rho = sqrt(x^2+y^2);

ZernikePolynomials = [...
1 ... % piston
rho*cos(A)
rho*sin(A)
2*rho^2-1 ...
rho^2*cos(2*A)
rho^2*sin(2*A) ...
(3*rho^3-2*rho)*cos(A) ...
(3*rho^3-2*rho)*sin(A)
6*rho^4-6*rho^2+1
rho^3*cos(3*A) ...
rho^3*sin(3*A) ...
(4*rho^4-3*rho^2)*cos(2*A)
(4*rho^4-3*rho^2)*sin(2*A)
(10*rho^5-12*rho^3+3*rho)*cos(A)
(10*rho^5-12*rho^3+3*rho)*sin(A)
20*rho^6-30*rho^4+12*rho^2-1 ...
rho^4*cos(4*A) ...
rho^4*sin(4*A) ...
(5*rho^5-4*rho^3)*cos(3*A) ...
(5*rho^5-4*rho^3)*sin(3*A) ...
(15*rho^6-20*rho^4+6*rho^2)*cos(2*A)
(15*rho^6-20*rho^4+6*rho^2)*sin(2*A)
(35*rho^7-60*rho^5+30*rho^3-4*rho)*cos(A)
(35*rho^7-60*rho^5+30*rho^3-4*rho)*sin(A) ...
70*rho^8-140*rho^6+90*rho^4-20*rho^2+1 ...
rho^5*cos(5*A) ...
rho^5*sin(5*A) ...
(6*rho^6-5*rho^4)*cos(4*A) ...
(6*rho^6-5*rho^4)*sin(4*A) ...
(21*rho^7-30*rho^5+10*rho^3)*cos(3*A) ...
(21*rho^7-30*rho^5+10*rho^3)*sin(3*A) ...
(56*rho^8-105*rho^6+60*rho^4-10*rho^2)*cos(2*A)
(56*rho^8-105*rho^6+60*rho^4-10*rho^2)*sin(2*A)
(126*rho^9-280*rho^7+210*rho^5-60*rho^3+5*rho)*cos(A)
(126*rho^9-280*rho^7+210*rho^5-60*rho^3+5*rho)*sin(A)
252*rho^10-630*rho^8+560*rho^6-210*rho^4+30*rho^2-1
924*rho^12-2772*rho^10+3150*rho^8-1680*rho^6+420*rho^4-
42*rho^2+1];

ZernikeCoefficients = [1.078497 0 0 0.000226 0 0 0 0 -
0.012137 0 0 0 0 0 1.236428 0 0 0 0 0 0 0 0.169419 0 0 0 0 0 0 0
0 0 0.001707 0.002742];

```

```

        Z = exp(-1i*2*pi()*ZernikePolynomials(1:37) *
ZernikeCoefficients(1:37)');

%           Z = 1; % Uncomment if no aberrations

[X,Y] = meshgrid(1:100,1:100); P = atan2(Y,X);

%Final matrix and derivation of the polarization amplitudes
-
%3*2 x 2*1 = 3*1 vector elements

E_1 = M * [(theta_pol(1));(theta_pol(2))] * O * Defocus *
Z;
E_2 = M * [(theta_pol(3));(theta_pol(4))] * O * Defocus * Z
;
E_3 = M * [(theta_pol(5));(theta_pol(6))] * O * Defocus * Z
;
E_4 = M * [(theta_pol(7));(theta_pol(8))] * O * Defocus * Z
;
E_5 = M * [(theta_pol(9));(theta_pol(10))] * O * Defocus * Z
;

    for i=1:3;
        P1(m,n,i) = E_1(i);
        P2(m,n,i) = E_2(i);
        P3(m,n,i) = E_3(i);
        P4(m,n,i) = E_4(i);
        P5(m,n,i) = E_5(i);
    end
end
end

if round(m/N*100)>=flag_txt+20;
    disp(strcat(num2str(round(m/N*100)), '% /',datestr(now)));
    flag_txt = round(m/N*100);
end

end

```

REFERENCES

- [1] M. Maldovan and E. L. Thomas, *Periodic Materials and Interference Lithography for Photonics, Phononics and Mechanics*, Wiley, 2009.
- [2] K. Busch, G. von Freymann, S. Linden, S. F. Mingaleev, L. Tkeshelashvili, and M. Wegener, "Periodic nanostructures for photonics," *Phys. Rep.*, vol. 444, pp. 101-202, Jun. 2007.
- [3] J. D. Joannopoulos, S. G. Johnson, J. N. Winn, and R. D. Meade, *Photonic Crystals Molding the Flow of Light, Second Edition*, Princeton University Press, 2008.
- [4] G. Parker and M. Charlton, "Photonic crystals," *Phys. World*, vol. 13, pp. 29-34, Aug. 1, 2000.
- [5] A. Adibi, Y. Xu, R. K. Lee, A. Yariv, and A. Scherer, "Properties of the slab modes in photonic crystal optical waveguides," *J. Lightwave Technol.*, vol. 18, pp. 1554-1564, Nov. 2000.
- [6] A. Jafarpour, E. Chow, C. M. Reinke, J. Huang, A. Adibi, A. Grot, L. W. Mirkarimi, G. Girolami, R. K. Lee, and Y. Xu, "Large-bandwidth ultra-low-loss guiding in bi-periodic photonic crystal waveguides," *Appl. Phys. B*, vol. 79, pp. 409-414, 2004.
- [7] M. M. Beaky, J. B. Burk, H. O. Everitt, M. A. Haider, and S. Venakides, "Two-dimensional photonic crystal Fabry-Perot resonators with lossy dielectrics," *IEEE Trans. Microw. Theory Tech.*, vol. 47, pp. 2085-91, Nov. 1999.
- [8] P. Kramper, M. Kafesaki, C. M. Soukoulis, A. Birner, F. Muller, U. Gosele, R. B. Wehrspohn, J. Mlynek, and V. Sandoghdar, "Near-field visualization of light confinement in a photonic crystal microresonator," *Opt. Lett.*, vol. 29, pp. 174-176, Jan. 15, 2004.
- [9] T. Kim and C. Seo, "A novel photonic bandgap structure for low-pass filter of wide stopband," *IEEE Microw. Wirel. Compon. Lett.*, vol. 10, pp. 13-15, Jan. 2000.
- [10] R. C. Rumpf, A. Mehta, P. Srinivasan, and E. G. Johnson, "Design and optimization of space-variant photonic crystal filters," *Appl. Opt.*, vol. 46, pp. 5755-5761, Aug. 10, 2007.

- [11] A. Mehta, R. Rumpf, Z. Roth, and E. G. Johnson, "Simplified fabrication process of 3-D photonic crystal optical transmission filter," *Proc. SPIE*, vol. 6462, p. 6462D, 2007.
- [12] B. Z. Steinberg, A. Boag, and R. Lisitin, "Sensitivity analysis of narrowband photonic crystal filters and waveguides to structure variations and inaccuracy," *J. Opt. Soc. Am. A*, vol. 20, pp. 138-146, Jan. 2003.
- [13] Y.-D. Wu, T.-T. Shih, and J.-J. Lee, "High-quality-factor filter based on a photonic crystal ring resonator for wavelength division multiplexing applications," *Appl. Opt.*, vol. 48, pp. F24-F30, Sep. 1, 2009.
- [14] T. Kamalakis and T. Sphicopoulos, "Numerical study of the implications of size nonuniformities in the performance of photonic crystal couplers using coupled mode theory," *IEEE J. Quantum Electron.*, vol. 41, pp. 863-871, Jun. 2005.
- [15] C. Y. Liu and L. W. Chen, "Tunable photonic crystal waveguide coupler with nematic liquid crystals," *IEEE Photon. Technol. Lett.*, vol. 16, pp. 1849-1851, Aug. 2004.
- [16] A. Mekis and J. D. Joannopoulos, "Tapered couplers for efficient interfacing between dielectric and photonic crystal waveguides," *J. Lightwave Technol.*, vol. 19, pp. 861-865, Jun. 2001.
- [17] Y. Tanaka, H. Nakamura, Y. Sugimoto, N. Ikeda, K. Asakawa, and K. Inoue, "Coupling properties in a 2-D photonic crystal slab directional coupler with a triangular lattice of air holes," *IEEE J. Quantum Electron.*, vol. 41, pp. 76-84, Jan. 2005.
- [18] M. Thorhauge, L. H. Frandsen, and P. I. Borel, "Efficient photonic crystal directional couplers," *Opt. Lett.*, vol. 28, pp. 1525-7, Sep. 1, 2003.
- [19] Q. F. Xu and M. Lipson, "All-optical logic based on silicon micro-ring resonators," *Opt. Express*, vol. 15, pp. 924-929, Feb 2007.
- [20] T. A. Ibrahim, R. Grover, L. C. Kuo, S. Kanakaraju, L. C. Calhoun, and P. T. Ho, "All-optical AND/NAND logic gates using semiconductor microresonators," *IEEE Photon. Technol. Lett.*, vol. 15, pp. 1422-1424, Oct. 2003.
- [21] B. Momeni and A. Adibi, "Demultiplexers harness photonic-crystal dispersion properties," *Laser Focus World*, vol. 42, pp. 125-128, Jun. 2006.
- [22] C. Caloz, A. K. Skrivervik, and F. E. Gardiol, "An efficient method to determine Green's functions of a two-dimensional photonic crystal excited by a line source - the phased-array method," *IEEE Trans. Microw. Theory Tech.*, vol. 50, pp. 1380-91, May 2002.

- [23] M. Belotti, J. F. Galisteo-Lopez, S. De Angelis, M. Galli, I. Maksymov, L. C. Andreani, D. Peyrade, and Y. Chen, "All-optical switching in 2D silicon photonic crystals with low loss waveguides and optical cavities," *Opt. Express*, vol. 16, pp. 11624-11636, Jul. 21, 2008.
- [24] M. Notomi, A. Shinya, S. Mitsugi, G. Kira, E. Kuramochi, and T. Tanabe, "Optical bistable switching action of Si high-Q photonic-crystal nanocavities," *Opt. Express*, vol. 13, pp. 2678-2687, Apr. 4, 2005.
- [25] S. Chakravarty, J. Topol'ancik, P. Bhattacharya, S. Chakrabarti, Y. Kang, and M. E. Meyerhoff, "Ion detection with photonic crystal microcavities," *Opt. Lett.*, vol. 30, pp. 2578-2580, Oct. 1, 2005.
- [26] K. Inoue and K. Ohtaka, *Photonic Crystals: Physics, Fabrication and Applications*, Springer, 2010.
- [27] D. Threm, Y. Nazirizadeh, and M. Gerken, "Photonic crystal biosensors towards on-chip integration," *J. Biophotonics*, vol. 5, pp. 601-616, Aug. 2012.
- [28] J. B. Pendry and D. R. Smith, "The quest for the superlens," *Sci. Am.*, vol. 295, pp. 60-67, Jul. 2006.
- [29] M. W. Klein, C. Enkrich, M. Wegener, and S. Linden, "Second-harmonic generation from magnetic metamaterials," *Science*, vol. 313, pp. 502-504, Jul. 28, 2006.
- [30] D. Schurig, J. J. Mock, B. J. Justice, S. A. Cummer, J. B. Pendry, A. F. Starr, and D. R. Smith, "Metamaterial electromagnetic cloak at microwave frequencies," *Science*, vol. 314, pp. 977-980, Nov. 10, 2006.
- [31] J. Jang, S. J. Jhaveri, B. Rasin, C. Koh, C. K. Ober, and E. L. Thomas, "Three-dimensionally-patterned submicrometer-scale hydrogel/air networks that offer a new platform for biomedical applications," *Nano Lett.*, vol. 8, pp. 1456-1460, Apr. 5, 2008.
- [32] P. Sung-Gyu, L. Seung-Kon, M. Jun Hyuk, and Y. Seung-Man, "Holographic fabrication of three-dimensional nanostructures for microfluidic passive mixing," *Lab Chip*, vol. 9, pp. 3144-50, 2009.
- [33] S. Jeon, J. Park, R. Cirelli, S. Yang, C. Heitzman, P. Braun, P. Kenis, and J. Rogers, "Fabricating complex three-dimensional nanostructures with high-resolution conformable phase masks," *Proc. Natl. Acad. Sci.*, vol. 101, pp. 12428-12433, Aug. 24, 2004.
- [34] E. L. Hedberg-Dirk and U. A. Martinez, "Large-scale protein arrays generated with interferometric lithography for spatial control of cell-material interactions," *J. Nanomater.*, vol. 2010, p. 176750, May 2010.

- [35] F. P. W. Melchels, A. M. C. Barradas, C. A. van Blitterswijk, J. de Boer, J. Feijen, and D. W. Grijpma, "Effects of the architecture of tissue engineering scaffolds on cell seeding and culturing," *Acta Biomater.*, vol. 6, pp. 4208-4217, Nov. 2010.
- [36] X. Y. Zheng, H. Lee, T. H. Weisgraber, M. Shusteff, J. DeOtte, E. B. Duoss, J. D. Kuntz, M. M. Biener, Q. Ge, J. A. Jackson, S. O. Kucheyev, N. X. Fang, and C. M. Spadaccini, "Ultralight, ultrastiff mechanical metamaterials," *Science*, vol. 344, pp. 1373-1377, Jun. 2014.
- [37] G. M. Burrow and T. K. Gaylord, "Multi-beam interference advances and applications: nano-electronics, photonic crystals, metamaterials, subwavelength structures, optical trapping, and biomedical structures," *Micromachines*, vol. 2, pp. 221-257, Jun. 2011.
- [38] C. O. Cho, J. Jeong, J. Lee, H. Jeon, I. Kim, J. D. H., Y. S. Park, and J. C. Woo, "Photonic crystal band edge laser array with a holographically generated square-lattice pattern," *Appl. Phys. Lett.*, vol. 87, p. 161102, Oct. 10, 2005.
- [39] G. Mertens, R. B. Wehrspohn, H. S. Kitzerow, S. Matthias, C. Jamois, and U. Gosele, "Tunable defect mode in a three-dimensional photonic crystal," *Appl. Phys. Lett.*, vol. 87, p. 241108, Dec. 2005.
- [40] A. C. van Popta, M. J. Brett, and J. C. Sit, "Double-handed circular Bragg phenomena in polygonal helix thin films," *J. Appl. Phys.*, vol. 98, p. 083517, Oct. 15, 2005.
- [41] G. M. Gratson, M. J. Xu, and J. A. Lewis, "Microperiodic structures - Direct writing of three-dimensional webs," *Nature*, vol. 428, pp. 386-386, Mar. 2004.
- [42] M. Deubel, G. Von Freymann, M. Wegener, S. Pereira, K. Busch, and C. M. Soukoulis, "Direct laser writing of three-dimensional photonic-crystal templates for telecommunications," *Nat. Mater.*, vol. 3, pp. 444-447, Jul. 2004.
- [43] F. García-Santamaría, H. T. Miyazaki, A. Urquía, M. Ibisate, M. Belmonte, N. Shinya, F. Meseguer, and C. López, "Nanorobotic manipulation of microspheres for on-chip diamond architectures," *Adv. Mater.*, vol. 14, pp. 1144-1147, 2002.
- [44] M. H. Qi, E. Lidorikis, P. T. Rakich, S. G. Johnson, J. D. Joannopoulos, E. P. Ippen, and H. I. Smith, "A three-dimensional optical photonic crystal with designed point defects," *Nature*, vol. 429, pp. 538-542, Jun. 3, 2004.
- [45] C. Moormann, J. Bolten, and H. Kurz, "Spatial phase-locked combination lithography for photonic crystal devices," *Microelectron. Eng.*, vol. 73-74, pp. 417-422, Sep. 2004.
- [46] C. J. M. van Rijn, "Laser interference as a lithographic nanopatterning tool," *J. Microlithogr., Microfabr., Microsyst.*, vol. 5, p. 11012, Jan. 2006.

- [47] T. Liu, M. Fallahi, J. V. Moloney, and M. Mansuripur, "Fabrication of two-dimensional photonic crystals with embedded defects using blue-laser-writer and optical holography," *IEEE Photon. Technol. Lett.*, vol. 18, pp. 1100-1102, May 1, 2006.
- [48] M. Fritze, T. M. Noomstein, B. Tyrrell, and M. Rothschild, "Extending 193nm immersion with hybrid optical maskless lithography," *Solid State Technol.*, vol. 49, pp. 41-46, 2006.
- [49] J. Scrimgeour, D. N. Sharp, C. F. Blanford, O. M. Roche, R. G. Denning, and A. J. Turberfield, "Three-dimensional optical lithography for photonic microstructures," *Adv. Mater.*, vol. 18, pp. 1557-1560, Jun. 2006.
- [50] X. Chen, A. Frauenglass, and S. R. J. Brueck, "Interferometric lithography pattern delimited by a mask image," in *Proc. SPIE*, vol. 3331, pp. 496-502, 1998.
- [51] Y. K. Lin, A. Harb, K. Lozano, D. Xu, and K. P. Chen, "Five beam holographic lithography for simultaneous fabrication of three dimensional photonic crystal templates and line defects using phase tunable diffractive optical element," *Opt. Express*, vol. 17, pp. 16625-16631, Sep. 14, 2009.
- [52] J. Li, Y. Liu, X. Xie, P. Zhang, B. Liang, L. Yan, J. Zhou, G. Kurizki, D. Jacobs, K. S. Wong, and Y. Zhong, "Fabrication of photonic crystals with functional defects by one-step holographic lithography," *Opt. Express*, vol. 16, pp. 12899-12904, Aug. 18, 2008.
- [53] X. S. Xie, Y. K. Liu, M. D. Zhang, J. Y. Zhou, and K. S. Wong, "Manipulating spatial light fields for micro- and nano-photonics," *Physica E*, vol. 44, pp. 1109-1126, Apr. 2012.
- [54] P. Q. Zhang, X. S. Xie, Y. F. Guan, J. Y. Zhou, K. S. Wong, and L. Yan, "Adaptive synthesis of optical pattern for photonic crystal lithography," *Appl. Phys. B*, vol. 104, pp. 113-116, Jul. 2011.
- [55] Y. Zhong, J. Ma, K. S. Wong, Z. Chen, and J. Zhou, "Fabrication large area photonic crystals with periodic waveguide by one-step holographic lithography based on spatial light modulator," in *Proc. SPIE*, vol. 8418, p. 84181F, 2012.
- [56] M. Kumar and J. Joseph, "Embedding a nondiffracting defect site in helical lattice wave-field by optical phase engineering," *Appl. Opt.*, vol. 52, pp. 5653-5658, Aug. 10, 2013.
- [57] M. Kumar and J. Joseph, "Embedding multiple nondiffracting defect sites in periodic lattice wavefield by optical phase engineering," *J. Nanophotonics*, vol. 8, p. 083894, Jan. 2014.

- [58] A. Kelberer, M. Boguslawski, P. Rose, and C. Denz, "Embedding defect sites into hexagonal nondiffracting wave fields," *Opt. Lett.*, vol. 37, pp. 5009-5011, Dec. 1, 2012.
- [59] J. Xavier and J. Joseph, "Complex photonic lattices embedded with tailored intrinsic defects by a dynamically reconfigurable single step interferometric approach," *Appl. Phys. Lett.*, vol. 104, p. 081104, Feb. 2014.
- [60] J. H. Jang, C. K. Ullal, M. Maldovan, T. Gorishnyy, S. Kooi, C. Y. Koh, and E. L. Thomas, "3D micro- and nanostructures via interference lithography," *Adv. Funct. Mater.*, vol. 17, pp. 3027-3041, Nov. 5, 2007.
- [61] P. V. Braun, S. A. Rinne, and F. Garcia-Santamaria, "Introducing defects in 3D photonic crystals: State of the art," *Adv. Mater.*, vol. 18, pp. 2665-2678, Oct. 2006.
- [62] W. Mao, Y. Zhong, J. Dong, and H. Wang, "Crystallography of two-dimensional photonic lattices formed by holography of three noncoplanar beams," *J. Opt. Soc. Am. B*, vol. 22, pp. 1085-91, May 2005.
- [63] L. Z. Cai, X. L. Yang, and Y. R. Wang, "All fourteen Bravais lattices can be formed by interference of four noncoplanar beams," *Opt. Lett.*, vol. 27, pp. 900-2, Jun. 1, 2002.
- [64] N. D. Lai, J. H. Lin, and C. C. Hsu, "Fabrication of highly rotational symmetric quasi-periodic structures by multiexposure of a three-beam interference technique," *Appl. Opt.*, vol. 46, pp. 5645-5648, Aug. 10, 2007.
- [65] E. R. Dedman, D. N. Sharp, A. J. Turberfield, C. F. Blanford, and R. G. Denning, "Photonic crystals with a chiral basis by holographic lithography," *Phot. Nano. Fund. Appl.*, vol. 3, pp. 79-83, Dec. 2005.
- [66] W. Y. Tam, "Icosahedral quasicrystals by optical interference holography," *Appl. Phys. Lett.*, vol. 89, p. 251111, Dec. 18, 2006.
- [67] M. Kumar and J. Joseph, "Optical generation of a spatially variant two-dimensional lattice structure by using a phase only spatial light modulator," *Appl. Phys. Lett.*, vol. 105, p. 051102, Aug. 2014.
- [68] M. Kumar and J. Joseph, "Digitally reconfigurable complex two-dimensional dual-lattice structure by optical phase engineering," *Appl. Opt.*, vol. 53, pp. 1333-1338, Mar. 1, 2014.
- [69] M. Campbell, D. N. Sharp, M. T. Harrison, R. G. Denning, and A. J. Turberfield, "Fabrication of photonic crystals for the visible spectrum by holographic lithography," *Nature*, vol. 404, pp. 53-56, Mar. 2, 2000.

- [70] J. S. King, E. Graugnard, O. M. Roche, D. N. Sharp, J. Scrimgeour, R. G. Denning, A. J. Turberfield, and C. J. Summers, "Infiltration and inversion of holographically defined polymer photonic crystal templates by atomic layer deposition," *Adv. Mater.*, vol. 18, pp. 1561-1565, Jun. 2006.
- [71] N. Tetreault, G. Von Freymann, M. Deubel, M. Hermatschweiler, F. Perez-Willard, S. John, M. Wegener, and G. A. Ozin, "New route to three-dimensional photonic bandgap materials: Silicon double inversion of polymer templates," *Adv. Mater.*, vol. 18, pp. 457-460, Oct. 11, 2006.
- [72] M. L. Dakss, L. Kuhn, P. F. Heidrich, and B. A. Scott, "Grating coupler for efficient excitation of optical guided waves in thin films," *Appl. Phys. Lett.*, vol. 16, pp. 523-525, Jun. 15, 1970.
- [73] R. Gronheid and M. J. Leeson, "Extreme ultraviolet interference lithography as applied to photoresist studies," *J. Micro-Nanolithogr. MEMS MOEMS*, vol. 8, p. 021205, 2009.
- [74] V. Berger, O. Gauthier-Lafaye, and E. Costard, "Fabrication of a 2D photonic bandgap by a holographic method," *Electron. Lett.*, vol. 33, pp. 425-426, Feb. 27, 1997.
- [75] M. Miyake, Y. C. Chen, P. V. Braun, and P. Wiltzius, "Fabrication of three-dimensional photonic crystals using multibeam interference lithography and electrodeposition," *Adv. Mater.*, vol. 21, pp. 3012-3015, Aug. 7, 2009.
- [76] T. Kondo, S. Matsuo, S. Juodkazis, and H. Misawa, "Femtosecond laser interference technique with diffractive beam splitter for fabrication of three-dimensional photonic crystals," *Appl. Phys. Lett.*, vol. 79, pp. 725-727, Aug. 6, 2001.
- [77] X. Mai, R. Moshrefzadeh, U. J. Gibson, G. I. Stegeman, and C. T. Seaton, "Simple versatile method for fabricating guided-wave gratings," *Appl. Opt.*, vol. 24, pp. 3155-3161, Oct. 1, 1985.
- [78] L. Wu, Y. Zhong, C. T. Chan, K. S. Wong, and G. P. Wang, "Fabrication of large area two- and three-dimensional polymer photonic crystals using single refracting prism holographic lithography," *Appl. Phys. Lett.*, vol. 86, p. 241102, Jun. 7, 2005.
- [79] Y. Lin, D. Rivera, and K. P. Chen, "Woodpile-type photonic crystals with orthorhombic or tetragonal symmetry formed through phase mask techniques," *Opt. Express*, vol. 14, pp. 887-892, Jan. 23, 2006.
- [80] J. He, X. Fang, Y. Lin, and X. Zhang, "Polarization control in flexible interference lithography for nano-patterning of different photonic structures with optimized contrast," *Opt. Express*, vol. 23, pp. 11518-11525, May 4, 2015.

- [81] J. L. Stay, G. M. Burrow, and T. K. Gaylord, "Three-beam interference lithography methodology," *Rev. Sci. Instrum.*, vol. 82, p. 23115, Feb. 24, 2011.
- [82] C. Lu and R. H. Lipson, "Interference lithography: a powerful tool for fabricating periodic structures," *Laser Photon. Rev.*, vol. 4, pp. 568-580, Jul. 2010.
- [83] J. Murakowski, G. J. Schneider, and D. Prather, "Fabrication of 3-dimensional photonic crystals with embedded defects," *Proc. SPIE*, vol. 5347, pp. 181-189, 2004.
- [84] K. O. Hill, B. Malo, F. Bilodeau, D. C. Johnson, and J. Albert, "Bragg gratings fabricated in monomode photosensitive optical fiber by UV exposure through a phase mask," *Appl. Phys. Lett.*, vol. 62, pp. 1035-1037, Mar. 8, 1993.
- [85] L. M. Goldenberg, Y. Gritsai, O. Sakhno, O. Kulikovska, and J. Stumpe, "All-optical fabrication of 2D and 3D photonic structures using a single polymer phase mask," *J. Opt.*, vol. 12, p. 015103, 2010.
- [86] Y. Lin, A. Harb, D. Rodriguez, K. Lozano, D. Xu, and K. P. Chen, "Holographic fabrication of photonic crystals using multidimensional phase masks," *J. Appl. Phys.*, vol. 104, p. 113111, Dec. 4, 2008.
- [87] J. Lutkenhaus, D. George, B. Arigong, H. L. Zhang, U. Philipose, and Y. K. Lin, "Holographic fabrication of functionally graded photonic lattices through spatially specified phase patterns," *Appl. Opt.*, vol. 53, pp. 2548-2555, Apr. 20, 2014.
- [88] G. M. Burrow, "Pattern-Integrated Interference Lithography: Single-Exposure Formation of Photonic Crystal Lattices with Integrated Functional Elements," Ph.D. thesis, Electrical and Computer Engineering, Georgia Institute of Technology, 2012.
- [89] G. M. Burrow, M. C. R. Leibovici, J. W. Kummer, and T. K. Gaylord, "Pattern-integrated interference lithography instrumentation," *Rev. Sci. Instrum.*, vol. 83, p. 063707, May 2012.
- [90] T. K. Gaylord, M. C. R. Leibovici, and G. M. Burrow, "Pattern-integrated interference [Invited]," *Appl. Opt.*, vol. 52, pp. 61-72, Jan. 1, 2013.
- [91] M. C. R. Leibovici and T. K. Gaylord, "Pattern-integrated interference lithography: Vector modeling and 1D, 2D, and 3D device structures," *J. Vac. Sci. Technol. B*, vol. 31, p. 06F501, Oct. 24, 2013.
- [92] M. C. R. Leibovici and T. K. Gaylord, "Pattern-integrated interference lithography: vector modeling of the single-exposure recording of integrated photonic-crystal structures," in *EIPBN*, pp. P04-05, 2013.

- [93] M. C. R. Leibovici and T. K. Gaylord, "Simulation of photonic-crystal devices fabricated via pattern-integrated interference lithography," in *Frontiers in Optics*, p. FW1F.5, 2013.
- [94] M. C. R. Leibovici and T. K. Gaylord, "Photomask optimization strategies for pattern-integrated interference lithography," *Appl. Opt.*, (in preparation, 2015).
- [95] M. C. R. Leibovici and T. K. Gaylord, "Performance simulation of 2D photonic-crystal devices fabricated by pattern-integrated interference lithography," *Opt. Lett.*, vol. 39, pp. 3798-3801, Jul. 1, 2014.
- [96] M. C. R. Leibovici and T. K. Gaylord, "Simulation of photonic-crystal devices fabricated by pattern-integrated interference lithography," in *Frontiers in Optics*, p. FW1A.6, 2014.
- [97] T. K. Gaylord and M. C. R. Leibovici, "Pattern-integrated interference lithography for 2D and 3D photonic crystals (invited)," in *Frontiers in Optics*, p. FTh2F.1, 2013.
- [98] M. C. R. Leibovici and T. K. Gaylord, "Custom-modified three-dimensional periodic microstructures by pattern-integrated interference lithography," *J. Opt. Soc. Am. A*, vol. 31, pp. 1515-1519, Jul. 2014.
- [99] M. C. R. Leibovici and T. K. Gaylord, "Three-dimensional periodic structures via pattern-integrated interference lithography," in *Frontiers in Optics*, p. FW1A.4, 2014.
- [100] M. C. R. Leibovici and T. K. Gaylord, "Pattern-integrated interference exposure system: capabilities and optimization," in *Frontiers in Optics*, p. FTu3A.26, 2012.
- [101] M. C. R. Leibovici, S. K. Vadivel, and T. K. Gaylord, "Evaluation of multi-beam imaging system performance," *Appl. Opt.*, (in preparation, 2015).
- [102] S. K. Vadivel, M. C. R. Leibovici, and T. K. Gaylord, "Pattern-Integrated Interference Exposure System Alignment Procedure," *Appl. Opt.*, (in preparation, 2015).
- [103] G. M. Burrow, M. C. R. Leibovici, and T. K. Gaylord, "Pattern-integrated interference lithography: Single-exposure fabrication of photonic-crystal structures," *Appl. Opt.*, vol. 51, pp. 4028-4041, Jun. 20, 2012.
- [104] M. C. R. Leibovici and T. K. Gaylord, "Photonic-crystal waveguide structure by pattern-integrated interference lithography," *Opt. Lett.*, vol. 40, pp. 2806-2809, Jun. 15, 2015.
- [105] T. Young, *A Course of Lectures on Natural Philosophy and the Mechanical Arts*, London: Printed for J. Johnson, 1807.

- [106] J. L. Stay, "Multi-Beam-Interference-Based Methodology for the Fabrication of Photonic Crystal Structures," Ph.D. thesis, Electrical and Computer Engineering, Georgia Institute of Technology, 2009.
- [107] D. Gabor, "Microscopy by reconstructed wave-fronts," *Proc. R. Soc. London, Ser. A*, vol. 197, pp. 454-487, 1949.
- [108] E. N. Leith and J. Upatnieks, "Reconstructed wavefronts and communication theory," *J. Opt. Soc. Am.*, vol. 52, pp. 1123-1130, Oct. 1962.
- [109] E. N. Leith and J. Upatnieks, "Wavefront reconstruction with diffused illumination and three-dimensional objects," *J. Opt. Soc. Am.*, vol. 54, pp. 1295-1301, Nov. 1964.
- [110] J. W. Goodman, *Introduction to Fourier Optics*, San Francisco: McGraw-Hill, 1968.
- [111] R. J. Collier, C. B. Burckhardt, and L. H. Lin, *Optical Holography*, New York: Academic Press, 1971.
- [112] N. H. Farhat, *Advances in Holography vol. 3*, New York: Marcel Dekker, 1976.
- [113] H. J. Caulfield, *Handbook of Optical Holography*, New York: Academic Press, 1979.
- [114] R. B. Millington, A. G. Mayes, J. Blyth, and C. R. Lowe, "A hologram biosensor for proteases," *Sens. Actuators, B*, vol. 33, pp. 55-9, 1996.
- [115] J. Wallace, "Optical data storage: 500GByte volume-holographic disc can be written at Blu-ray speed," *Laser Focus World*, vol. 47, pp. 13-14, Sep. 2011.
- [116] J. R. Sheats and B. W. Smith, *Microlithography: Science and Technology*, New York: Marcel Dekker, 1998.
- [117] W. G. Oldham, S. N. Nandgaonkar, A. R. Neureuther, and M. O'Toole, "A general simulator for VLSI lithography and etching processes: Part I - Application to projection lithography," *IEEE Trans. Electron Dev.*, vol. 26, pp. 717-722, Apr. 1979.
- [118] C. A. Mack, "PROLITH - A comprehensive optical lithography model," in *Proc. SPIE*, vol. 538, pp. 207-220, 1985.
- [119] "FRED Optical Engineering Software," ed: Photon Engineering, v11.40.
- [120] M. Switkes and M. Rothschild, "Resolution enhancement of 157 nm lithography by liquid immersion," in *Proc. SPIE*, vol. 4691, pp. 459-465, 2002.

- [121] B. W. Smith, A. Bourov, H. Y. Kang, F. Cropanese, Y. F. Fan, N. Lafferty, and L. Zavyalova, "Water immersion optical lithography at 193 nm," *J. Microlithogr., Microfabr., Microsyst.*, vol. 3, pp. 44-51, Jan. 2004.
- [122] A. Yen, S. S. Yu, J. H. Chen, C. K. Chen, T. S. Gau, and B. J. Lin, "Low- k_1 optical lithography for 100 nm logic technology and beyond," *J. Vac. Sci. Technol. B*, vol. 19, pp. 2329-2334, Nov.-Dec. 2001.
- [123] M. S. Hibbs and R. R. Kunz, "193-nm full-field step-and-scan prototype at MIT Lincoln Lab," in *Proc. SPIE*, vol. 2440, pp. 40-48, 1995.
- [124] T. M. Bloomstein, M. W. Horn, M. Rothschild, R. R. Kunz, S. T. Palmacci, and R. B. Goodman, "Lithography with 157 nm lasers," in *41st International Conference on Electron, Ion, and Photon Beams Technology and Nanofabrication*, vol. 15, pp. 2112-2116, 1997.
- [125] A. Yen, M. L. Schattenburg, and H. I. Smith, "Proposed method for fabricating 50-nm-period gratings by achromatic holographic lithography," *Appl. Opt.*, vol. 31, pp. 2972-2973, jun. 1, 1992.
- [126] H. H. Solak, C. David, J. Gobrecht, V. Golovkina, F. Cerrina, S. O. Kim, and P. F. Nealey, "Sub-50 nm period patterns with EUV interference lithography," *Microelectron. Eng.*, vol. 67-68, pp. 56-62, Jun. 2003.
- [127] D. G. Flagello, T. Milster, and A. E. Rosenbluth, "Theory of high-NA imaging in homogeneous thin films," *J. Opt. Soc. Am. A*, vol. 13, pp. 53-64, Jan. 1996.
- [128] J. L. Stay and T. K. Gaylord, "Three-beam-interference lithography: Contrast and crystallography," *Appl. Opt.*, vol. 47, pp. 3221-3230, Jun. 20, 2008.
- [129] J. L. Stay and T. K. Gaylord, "Contrast in four-beam-interference lithography," *Opt. Lett.*, vol. 33, pp. 1434-1436, Jul. 1, 2008.
- [130] M. S. Yeung, "Modeling high numerical aperture optical lithography," in *Proc. SPIE*, vol. 922, pp. 149-67, 1988.
- [131] F. H. Dill, A. R. Neureuther, J. A. Tuttle, and E. J. Walker, "Modeling projection printing of positive photoresists," *IEEE Trans. Electron Dev.*, vol. 22, pp. 456-641, Jul. 1975.
- [132] A. Mekis, J. C. Chen, I. Kurland, S. Fan, P. R. Villeneuve, and J. D. Joannopoulos, "High transmission through sharp bends in photonic crystal waveguides," *Phys. Rev. Lett.*, vol. 77, pp. 3787-3790, Oct. 28, 1996.
- [133] P. Kramper, A. Birner, M. Agio, C. M. Soukoulis, F. Muller, U. Gosele, J. Mlynek, and V. Sandoghdar, "Direct spectroscopy of deep two-dimensional photonic crystal microresonator," *Phys. Rev. B*, vol. 64, p. 233102, Dec. 15, 2001.

- [134] T. P. White, L. C. Botten, R. C. McPhedran, and C. M. d. Sterke, "Ultracompact resonant filters in photonic crystals," *Opt. Lett.*, vol. 28, pp. 2452-2454, Dec. 15, 2003.
- [135] T. Ogawa, A. Sekiguchi, and N. Yoshizawa, "Advantages of a SiO_xNy:H anti-reflective layer for ArF excimer laser lithography," *Jpn. J. Appl. Phys. Part 1 - Regul. Pap. Short Notes Rev. Pap.*, vol. 35, pp. 6360-6365, Dec 1996.
- [136] R. Ferrini, D. Leuenberger, R. Houdré, H. Benisty, M. Kamp, and A. Forchel, "Disorder-induced losses in planar photonic crystals," *Opt. Lett.*, vol. 31, pp. 1426-1428, May 15, 2006.
- [137] M. Skorobogatiy, "Modeling the impact of imperfections in high-index-contrast photonic waveguides," *Phys. Rev. E*, vol. 70, p. 046609, Oct. 2004.
- [138] A. F. Koenderink, A. Lagendijk, and W. L. Vos, "Optical extinction due to intrinsic structural variations of photonic crystals," *Phys. Rev. B*, vol. 72, p. 153102, Oct 2005.
- [139] L. L. Lima, M. Alencar, D. P. Caetano, D. R. Solli, and J. M. Hickmann, "The effect of disorder on two-dimensional photonic crystal waveguides," *J. Appl. Phys.*, vol. 103, p. 123102, Jun. 2008.
- [140] M. Notomi, K. Yamada, A. Shinya, J. Takahashi, C. Takahashi, and I. Yokohama, "Extremely large group-velocity dispersion of line-defect waveguides in photonic crystal slabs," *Phys. Rev. Lett.*, vol. 87, p. 253902, Dec. 2001.
- [141] N. Cobb, A. Zakhor, and E. Miloslavsky, "Mathematical and CAD framework for proximity correction," in *Proc. SPIE*, vol. 2726, pp. 208-222, 1996.
- [142] J. F. Chen, K. Wampler, and T. L. Laidig, "Optical proximity correction method for intermediate-pitch features using sub-resolution scattering bars on a mask " U.S. Patent 5,821,014, 1998.
- [143] A. E. Rosenbluth, S. Bukofsky, M. Hibbs, K. F. Lai, A. Molless, R. N. Singh, and A. Wong, "Optimum mask and source patterns to print a given shape," in *Proc. SPIE*, vol. 4346, pp. 486-502, 2001.
- [144] M. D. Levenson, N. S. Viswanathan, and R. A. Simpson, "Improving resolution in photolithography with a phase-shifting mask," *IEEE Trans. Electron Dev.*, vol. 29, pp. 1828-1836, Dec. 1982.
- [145] L. Liebmann, I. Graur, W. Leipold, J. Oberschmidt, D. O'Grady, and D. Regaill, "Alternating phase shifted mask for logic gate levels, design and mask manufacturing," in *Proc. SPIE*, vol. 3679, pp. 27-37, 1999.
- [146] B. J. Lin, "The attenuated phase-shifting mask," *Solid State Technol.*, vol. 35, pp. 43-47, Jan. 1992.

- [147] R. C. Rumpf and E. G. Johnson, "Fully three-dimensional modeling of the fabrication and behavior of photonic crystals formed by holographic lithography," *J. Opt. Soc. Am. A*, vol. 21, pp. 1703-1713, Sep. 2004.
- [148] X. L. Zhu, Y. G. Xu, and S. Yang, "Distortion of 3D SU8 photonic structures fabricated by four-beam holographic lithography with umbrella configuration," *Opt. Express*, vol. 15, pp. 16546-16560, Dec. 10, 2007.
- [149] W. Y. Tam, "Woodpile and diamond structures by optical interference holography," *J. Opt. Soc. Am. A*, vol. 9, pp. 1076-1081, Nov. 2007.
- [150] Y. K. Pang, J. C. W. Lee, C. T. Ho, and W. Y. Tam, "Realization of woodpile structure using optical interference holography," *Opt. Express*, vol. 14, pp. 9113-9119, Oct. 2, 2006.
- [151] K. Y. Lee, N. LaBianca, S. A. Rishton, S. Zolgharnain, J. D. Gelorme, J. Shaw, and T. H. P. Chang, "Micromachining applications of a high resolution ultrathick photoresist," *J. Vac. Sci. Technol. B*, vol. 13, pp. 3012-3016, Nov. 1995.
- [152] J. Q. Chen, W. Jiang, X. N. Chen, L. Wang, S. S. Zhang, and R. T. Chen, "Holographic three-dimensional polymeric photonic crystals operating in the 1550 nm window," *Appl. Phys. Lett.*, vol. 90, p. 93102, Feb. 26, 2007.
- [153] C. K. Ullal, M. Maldovan, M. Wohlgenuth, E. L. Thomas, C. A. White, and S. Yang, "Triply periodic bicontinuous structures through interference lithography: a level-set approach," *J. Opt. Soc. Am. A*, vol. 20, pp. 948-954, May 2003.
- [154] N. Gutman. (2014, August). *Custom-modified three-dimensional periodic microstructures by pattern-integrated interference lithography*. Available: <http://www.opticsinfobase.org/spotlight/summary.cfm?uri=josaa-31-7-1515>
- [155] F. S. Inc., "Zemax Optical Design Program," ed: Focus Software, Inc., Tucson, Arizona, 2003.
- [156] D. E. Sedivy and T. K. Gaylord, "Characterization of multiple-optical-axis implementation of pattern-integrated interference lithography," in *Frontiers in Optics*, p. FTh3F.2, 2013.
- [157] D. E. Sedivy and T. K. Gaylord, "Modeling of multiple-optical-axis pattern-integrated interference lithography systems [Invited]," *Appl. Opt.*, vol. 53, pp. D12-D20, May 2014.
- [158] T. K. Gaylord and M. C. R. Leibovici, "Three-dimensional pattern exposure system: Computer-generated-volume-holographic Fourier-plane mask and method for making same," U. S. Provisional Patent Application no. 62/065,380, assigned to Georgia Tech Research Corporation, filed Oct. 17, 2014, Georgia Tech Record of Invention No. 6830, Oct. 9, 2014.

- [159] T. K. Gaylord and M. C. R. Leibovici, "Exposure system that produces general three-dimensional patterns: Computer-generated volume hologram or spatial light modulator in object-plane space and method of specifying same," U. S. Provisional Patent Application no. 62/104,473, assigned to Georgia Tech Research Corporation, filed Jan. 16, 2015, Georgia Tech Record of Invention No. 6880, Dec. 2, 2014.
- [160] H. Ren, H. Lin, X. Li, and M. Gu, "Three-dimensional parallel recording with a Debye diffraction-limited and aberration-free volumetric multifocal array," *Opt. Lett.*, vol. 39, pp. 1621-1624, Mar. 2014.
- [161] B. E. A. Saleh and M. Rabbani, "Simulation of partially coherent imagery in the space and frequency domains and by modal expansion," *Appl. Opt.*, vol. 21, pp. 2770-2777, Aug. 1, 1982.
- [162] X. Ma and G. R. Arce, "Pixel-based simultaneous source and mask optimization for resolution enhancement in optical lithography," *Opt. Express*, vol. 17, pp. 5783-93, Mar. 30, 2009.
- [163] X. Ma and G. Arce, "Binary mask optimization for inverse lithography with partially coherent illumination," *J. Opt. Soc. Am. A*, vol. 25, pp. 2960-2970, Dec. 2008.
- [164] A. Poonawala and P. Milanfar, "Mask design for optical microlithography - An inverse imaging problem," in *IEEE Trans. Image Process.*, vol. 16, pp. 774-788, Mar. 2007.
- [165] X. Ma, Y. Li, and L. Dong, "Mask optimization approaches in optical lithography based on a vector imaging model," *J. Opt. Soc. Am. A*, vol. 29, pp. 1300-1312, 2012.
- [166] C. Yang, X. Wang, S. Li, and A. Erdmann, "Source mask optimization using real-coded genetic algorithms," in *Proc. SPIE*, vol. 8683, p. 86831T, 2013.
- [167] J. W. Rinne and P. Wiltzius, "Design of holographic structures using genetic algorithms," *Opt. Express*, vol. 14, pp. 9909-9916, Oct. 16, 2006.
- [168] D. George, J. Lutkenhaus, D. Lowell, U. Philipose, H. Zhang, Z. Poole, K. Chen, and Y. Lin, "Fabrication of 4, 5, or 6-fold symmetric 3D photonic structures using single beam and single reflective optical element based holographic lithography," in *Proc. SPIE*, vol. 9350, p. 93501K, 2015.
- [169] S. Yang, M. Megens, J. Aizenberg, P. Wiltzius, P. M. Chaikin, and W. B. Russel, "Creating periodic three-dimensional structures by multibeam interference of visible laser," *Chem. Mater.*, vol. 14, pp. 2831-2833, 2002.

- [170] D. Xu, K. P. Chen, K. Ohlinger, and Y. Lin, "Holographic fabrication of diamondlike photonic crystal template using two-dimensional diffractive optical elements," *Appl. Phys. Lett.*, vol. 93, pp. 031101-1-3, 2008.
- [171] Z. Poole, D. Xu, K. P. Chen, I. Olvera, K. Ohlinger, and Y. Lin, "Holographic fabrication of three-dimensional orthorhombic and tetragonal photonic crystal templates using a diffractive optical element," *Appl. Phys. Lett.*, vol. 91, pp. 251101-1-3, 2007.
- [172] J. H. Moon and S. Yang, "Creating three-dimensional polymeric microstructures by multi-beam interference lithography," *J. Macromol. Sci., Polym. Rev.*, vol. 45, pp. 351-373, Oct.-Dec. 2005.
- [173] J. H. Moon, J. Ford, and S. Yang, "Fabricating three-dimensional polymeric photonic structures by multi-beam interference lithography," *Polym. Adv. Technol.*, vol. 17, pp. 83-93, 2006.

VITA

Matthieu Leibovici was born in 1987 in Paris, France. He received his Diplôme d'Ingénieur from the Ecole Supérieure d'Electricité (SUPELEC) in 2010. While studying at SUPELEC, he entered the Georgia Institute of Technology in 2009 and received his Masters of Science in Electrical and Computer Engineering in 2011. In parallel with his Ph.D. studies, Matthieu received a Certificate in Technology Innovation through the TI:GER entrepreneurship program from the Scheller College of Business at the Georgia Institute of Technology.